Tumor cell clusters form intercellular nanolumina which promote collective metastasis via epigen accumulation

Emma Wrenn

A dissertation

submitted in partial fulfillment of the

requirements for the degree of

Doctor of Philosophy

University of Washington

2021

Reading Committee:

Kevin Cheung, Chair

Barry Gumbiner

Valeri Vasioukhin

Program Authorized to Offer Degree:

Molecular and Cellular Biology

University of Washington

Abstract

Tumor cell clusters form intercellular nanolumina which promote collective metastasis via epigen accumulation

Emma Wrenn

Chair of the Supervisory Committee:
Kevin Cheung
Department of Pharmacology

During development and wound healing, communities of epithelial cells can accomplish dramatic cellular rearrangements and tissue remodeling through coordinated, intercellular signaling. Recent studies have demonstrated that when tumor cells remain organized in multicellular cohorts during metastasis, they have a greatly increased likelihood of forming secondary tumors compared to single cells. These studies support the hypothesis that cancer cells may accomplish metastatic colonization through similar collective or cooperative mechanisms. However, specific molecular properties underlying the high metastatic efficiency of tumor cell clusters remain largely unknown. The purpose of my doctoral research was to identify such mechanisms, with the goal of finding new therapeutic targets against collective metastasis.

To address this question, I developed techniques to manipulate single and clustered tumor cells and perform downstream molecular analyses. I devised a method of suspension organoid culture which allowed me to propagate and transduce large quantities of tumor cell clusters from the MMTV-PyMT mouse model of breast cancer for ex vivo and in vivo analyses. Using this system, I found that aggregation of single tumor cells into clusters generates >100-fold increases in macrometastasis formation (normalized to injected cell number). RNA-sequencing throughout tumor cell aggregation revealed that clustering strongly induces the expression of EGFR-related genes, including EGFR ligands. The most cluster-upregulated gene was *Epgn* (protein name: epigen), the most recently discovered EGFR ligand. Notably, *Epgn* knockdown profoundly reduced the outgrowth of lung metastases formed by injected tumor cell clusters.

To better understand epigen's function in tumor cell clusters, I began by assessing its localization. Epigen was predominantly localized to cell-cell boundaries within tumor cell clusters. Super-resolution and electron microscopy showed that epigen frequently localized within intercellular spaces between cells. These cavities, which we refer to as "nanolumina", are lined with microvilli-like protrusions and bounded by cell-cell junctions. Nanolumenal junctions reduce the diffusion of epigen into the local microenvironment, allowing clusters to accumulate high concentrations of epigen between cells to facilitate potent intercellular growth signaling. Cell clusters from the aggressive basal-like 2 subset of human triple negative breast cancer also highly expressed *EPGN* and contained extensive intercellular nanolumina. Importantly, epigen suppression likewise reduced metastatic outgrowth by these clusters, supporting the human disease relevance of this signaling modality.

TABLE OF CONTENTS

LIST OF FIGURES

LIST OF TABLES

LIST OF VIDEOS

ACKNOWLEDGMENTS

To my advisor. First, I would like to acknowledge my advisor, Kevin Cheung. Thank you for taking a chance on me as your first graduate student, and devoting an incredible amount of time to training, mentoring, and supporting me. As I move forward in my career, I can only hope to emulate your work ethic, creativity, and enthusiasm for science.

To my supervisory committee: Cyrus Ghajar, Barry Gumbiner, Patrick Paddison, and Valeri Vasioukhin. Thank you so much for your encouragement, constructive criticism, and advice. Your guidance was invaluable during the last several years, and you each are remarkable scientific role models.

To the lab. I would like to thank all the members of the Cheung Lab who have helped me in countless ways, scientific and otherwise, throughout the years. This dissertation is the culmination of a collaborative effort from several people in the lab including Ami Yamamoto, Erin Greenwood, Breanna Moore, Margaux McBirney, Sarah Huang, and Aaron Thomas.

To the MCB program. Thank you so much to the excellent staff and directors of the Molecular & Cellular Biology program. Your commitment to creating such a kind and supportive program culture is deeply appreciated.

To my first partners in research. I would also like to thank the first research team I was lucky enough to join, the Weimbs Lab at UCSB, and especially Kevin Kipp, Elyse Verstelle, and Claudia Jette. I don't know where I would be today if I hadn't stumbled into a position in that lab and met each of you.

To my friends in Seattle. Your contributions to my happiness and well-being are too numerous to describe here. I cannot thank you enough, so I will not try to. But I would like to briefly express my gratitude to Julia Berkson, Sarah Crist, Becca Martin, Mollie McDonell, Anja Ollodart, Dylan Udy, and Elyse Verstelle. You are all amazing people and I feel lucky to know you.

To the Wrenn family. I feel so incredibly fortunate to be part of our hilarious, piratical, adventurous, accepting, and loving clan.

To my sister, Elly. I owe countless thanks to my sister, who always knows the exact right moment to silently bring me candy for emergency stress-relief, and who valiantly battles monsters by my side every week at D&D.

To my brother, Miller. Mark Twain once said, “Sufficient unto the day is one baby. As long as you are in your right mind don't you ever pray for twins. Twins amount to a permanent riot.” I feel immensely fortunate to have been your accomplice for our 28+ year riot full of mischief, adventure, twin talks, philosophical debates, and fierce loyalty. I deeply admire your creativity, towering intellect, and inimitably hilarious sense of humor. Thank you for all your support and sage advice.

To my parents. Thank you for indulging all my scientific endeavors from such an early age, often at great personal inconvenience – I apologize again for bringing strange bugs, eggs, and various invertebrates home for further study. Dad – I so respect your integrity and generosity, our family is lucky to have you as their “Baba”. Mom – I couldn’t have gotten through graduate school without your reminders to practice self-care, usually by binge-watching British detective shows together. No girl and her mom are like us, I cannot adequately express how grateful I am for your encouragement and support.

Chapter 1. INTRODUCTION: THE BIOLOGY OF TUMOR CELL CLUSTERS THROUGHOUT METASTASIS

1.1 DISSERTATION OUTLINE

The goal of my doctoral research was to uncover molecular mechanisms underlying the enhanced metastatic potential of tumor cell clusters compared to single cells. Here, in Chapter 1, I aim to put my research project in context by summarizing what is currently known about the process of collective metastasis. Next, I describe my development of ex vivo organoid suspension culture techniques to facilitate rapid propagation and transduction of mammary tumor organoids for large-scale experiments (Chapter 2, pg. 47). Using these culture methods, I then analyzed the transcription of single vs. clustered tumor cells using RNA-sequencing, followed by shRNA knockdown to identify genes that were (1) upregulated in tumor cell clusters vs. single cells, and (2) critical for the metastatic outgrowth of tumor cell clusters in the lung. These experiments led me to identify epigen (gene name: *Epgn*) as one such pro-metastatic gene enriched in clusters. Super-resolution and electron microscopy revealed epigen's mode of action; tumor cell clusters form intercellular cavities with restricted junctional permeability, which we term nanolumina, in which they accumulate high concentrations of epigen. Epigen diffuses between cells, activating EGFR signaling and strongly promoting metastatic outgrowth (described in detail in Chapter 3, pg. 82). Finally, I summarize my findings, their implications for our understanding of collective metastasis, and possible future directions (Chapter 4, pg. 160).

1.2 INTRODUCTION: STUDYING COLLECTIVE MECHANISMS OF METASTASIS

The metastatic process is often depicted as a cascade of events, classically described as the journey of a solitary cancer cell which manages to generate a secondary tumor through pro-metastatic intrinsic properties (Celià-Terrassa and Kang, 2016; Gupta et al., 2019; Massague and Obenauf, 2016; Talmadge and Fidler, 2010). In this single-cell model, a tumor cell breaks off from the primary tumor, ostensibly through epithelial-to-mesenchymal transitions (EMT) or partial EMT mechanisms (Yang et al., 2020). Then, that cell works its way through the basement membrane and stroma, often assisted by the secretion of matrix-cleaving proteases (Kessenbrock et al., 2010; Liotta et al., 1980; Liotta et al., 1986). It then migrates through endothelial cells to enter the vascular circulation (Massague and Obenauf, 2016). But even if that cell successfully enters and exits the circulation, it still may not succeed at metastasizing if it arrives in an unsupportive niche with negative extrinsic cues. Patrolling immune cells, metabolic changes and reactive oxygen species, lack of pro-survival ECM molecules, and other factors can all coalesce to promote the death of tumor cells. Alternatively, non-tumor cells in the tumor microenvironment can collaborate with tumor cells to promote their growth or survival. This complex web of superimposed inherent and environmental factors determines success during the “metastatic cascade” (Talmadge and Fidler, 2010).

But recent findings have recast one long-standing tenet of this model — that metastases arise exclusively from the invasion and dissemination of single cells. Tumor cells have often been presupposed to travel through the body individually. But, in most common epithelial cancer types. multicellular strands or nests of tumor cells are far more frequently detected near primary tumors (Bronsert et al., 2014; Friedl and Wolf, 2003).

Elegant studies have since shown that cooperation between cells in multicellular clusters can increase their capacity to generate distant metastases, in a process referred to as collective (Al Habyan et al., 2018; Khalil et al., 2017; Wrenn et al., 2020b) or cluster-based (Jolly et al., 2017; Kai et al., 2018; Saxena et al., 2020) metastasis. When they migrate in groups tumor cells may be able to assess their environment more sensitively, generate supracellular organization, and work together to accomplish invasion. Clustering can also help cells avoid induction of cell death in the physically and molecularly hostile vascular environment during circulation. Finally, when they seed a distant metastatic site, clustered tumor cells can signal to one another in a variety of ways to collectively promote immune evasion, survival, and growth. The additive effect of these advantages over single cells throughout the metastatic cascade can be striking – in several models of cancer, tumor cell clusters generate metastases with far greater efficiency than single cells **(Table 1.1)**. Below, I will describe what is currently known about the disparate mechanisms of tumor single cell and cluster biology, and what implications these divergences have for our understanding and treatment of metastasis.

1.2.1 *Caveats to describing the "metastatic cascade"*

One thing to keep in mind throughout this chapter is that the "metastatic cascade" is often laid out as a series of linear steps, as I have often done below for the purposes of organization. But tumor cells can skip, repeat, and modify steps, or proceed through parallel mechanisms (Katt et al., 2018). For instance, passive shedding of cells directly into disrupted blood vessels (Chang et al., 2000; Silvestri et al., 2020) or intravascular proliferation (Al-Mehdi et al., 2000; Lapis et al., 1988) can result in "skipping" of the

invasion, intravasation, or extravasation steps in the cascade. Tumors can also cycle back between steps. For example, a distant metastasis can restart the whole cascade, resulting in the seeding of additional metastases or re-seeding of other tumor sites (Gundem et al., 2015; Kim et al., 2009). It is important to keep this non-linearity and flexibility in mind as we consider the relative significance of each “step” in the cascade.

1.3 FREQUENT OBSERVATIONS OF COLLECTIVE ORGANIZATION

1.3.1 *Epithelial-like tumors often invade as clustered groups of cells*

An early step in metastasis is local invasion of tumor cells into the surrounding tissues. Many normal epithelial tissues (and neoplastic derivatives such as carcinoma in situ) exist as multicellular collectives fenced behind a basement membrane. Invasive carcinoma is defined by the breach of basement membrane and migration of tumor cells into the surrounding tissue microenvironment and is associated with markedly higher rates of metastatic progression (Cichon et al., 2010; Hu et al., 2008; Yu et al., 2011). Accordingly, the mechanism of tumor invasion has been an area of intensive research for decades (Friedl and Alexander, 2011; Friedl et al., 1995; Lambert et al., 2017; Liotta and Kohn, 2001).

In human tumors, pathologists have long noted the presence of tumor “nests” adjacent to primary tumors. One such study in 1960 noted that the tissue bed surrounding tumors was often populated by groups of cells more frequently than single tumor cells, and speculated that these nests might be able to give rise to further tumor growth and dissemination (Leighton et al., 1960). The authors suggested that these aggregates were

functioning as integrated units which worked cooperatively through supracellular organization and interactions with the microenvironment, not merely physical groupings of fully independent single cells. They went so far as to recommend development of “aggregate disrupting” agents to sensitize tumor nests to treatment.

Quantitative morphometric studies of invasion are challenging because they require either multiple parallel sections or thick reconstructions of tumor borders to determine if disseminated single cells are truly isolated. 3D reconstructions often reveal hidden connections between single cells and nearby tumor cells, revealing they are actually clusters, or between clusters and the main tumor body, revealing they are actually extensions from the primary tumor (Bronsert et al., 2014; Enderle-Ammour et al., 2017; Jensen et al., 2015; Kudo et al., 2013; Tian et al., 2020; Yoshizawa et al., 2020). In one such study, 3D reconstructions were used to directly quantify the presence of single and clustered tumor buds at tumor stromal borders in human pancreatic, colorectal, lung, and breast adenocarcinomas. After assessing over 5000 tumor buds and over 260,000 cancer cells, they did not observe any individual cells that were not connected to other tumor cells, indicating 100% of adjacent invaded tumor cells were part of collective units (Bronsert et al., 2014). Likewise, another study examined ductal and lobular human breast cancer samples to assess 3D morphology of peritumoral cancer cells (Khalil et al., 2017). Over 99% of invasive ductal carcinoma cells were in multicellular groups in the peritumoral area, and extent of collective invasion correlated with poorer prognosis.

Clusters can also be detected in the process of collectively invading into local lymphovascular channels, and this is frequently associated with poor prognosis. This feature, termed lymphovascular invasion (LVI), denotes the presence of tumor cells in

peritumoral vessels or vessels within the tumor mass (Mohammed et al., 2011) and frequently manifests as cohesive multicellular emboli (Aleskandarany et al., 2015; Mohammed et al., 2011). The presence of tumor emboli within lymphatic or blood vessels is correlated with poorer prognosis in pancreatic ductal adenocarcinoma (Takahashi et al., 2020), urothelial carcinoma (Cheng et al., 2009), sporadic colorectal cancer (Lim et al., 2010), and breast cancer (Hamy et al., 2018; Schoppmann et al., 2004). In inflammatory breast carcinoma tumor emboli are particularly abundant in dermal lymphatics. These emboli strongly express the cell adhesion molecule E-cadherin, associate with the *peau de l'orange* phenotype observed clinically, and are prone to metastasize (Jolly et al., 2017; Kleer et al., 2000; Robertson et al., 2010).

At the same time, there are notable counterexamples in which invading tumor cells favor discohesion and single cell dissemination. Invasive lobular carcinomas, a breast cancer subtype accounting for 5-15% of cases (Weigelt et al., 2010), are associated with loss of function mutations in E-cadherin, single file morphology, and tendency toward individualization to rounded cancer cells (though collective organization of lobular carcinoma is reported in some studies) (Bruner and Derksen, 2018; Ciriello et al., 2015; Khalil et al., 2017). Another breast cancer subtype, metaplastic carcinoma, accounting for <5% of breast cancers (Weigelt et al., 2010), is associated with highly mesenchymal spindle cell morphology and gene expression indicative of epithelial mesenchymal transition (EMT) (Hennessy et al., 2009; McCart Reed et al., 2019; Taube et al., 2010). Taken together recent morphometric studies suggest a major, but importantly not universal, tendency toward multicellular organization in cancers derived from epithelial tissues.

1.3.2 *Circulating tumor cell clusters vary greatly in their size and prevalence in the circulation*

The main routes of escape for tumor cells from the primary tumor are drainage via blood vessels and via lymphatics. Since the first descriptions of circulating tumor cells (CTCs) in the blood (Ashworth, 1869), there has been extensive interest in enumerating and isolating rare circulating tumor cells, including circulating tumor cell clusters (CTC clusters). Technological developments in the last 15 years have greatly facilitated direct isolation and analysis of bona fide circulating tumor cells in patients (Aceto et al., 2015; Au et al., 2017; Ferreira et al., 2016; Giuliano et al., 2018; Pantel and Alix-Panabières, 2019). Studies of patient blood samples across the most common cancer types have since conclusively demonstrated that both single and clustered tumor cells are present in the vasculature (Aceto et al., 2014; Chang et al., 2016; Hou et al., 2012; Lee et al., 2017; Long et al., 2016; Mu et al., 2015; Paoletti et al., 2015; Vona et al., 2004; Wang et al., 2017; Zhang et al., 2017; Zheng et al., 2017).

The number of CTCs is highly variable per patient. In some cases, metastatic patients will have CTC counts in the 100s to 1000s per 7.5 mL blood draw (Hou et al., 2012; Jansson et al., 2016; Krebs et al., 2011). However, many metastatic patients will have few or no detectable CTCs. In breast cancer, for example, multiple studies show that roughly 50% of metastatic patients will have fewer than 5 detectable CTCs per 7.5mL of blood (Cristofanilli et al., 2004; Cristofanilli et al., 2019; Larsson et al., 2018; Szczerba et al., 2019). Although circulating tumor cells are most often collected via tubes of blood, more invasive approaches such as indwelling catheters that capture circulating tumor cells can further increase yield of these rare entities (Kim et al., 2019). Whether variability in CTC abundance is a result of differences in ability to collect CTCs between patients or

reflect true differences in CTC frequency remains to be worked out. But it is clear that CTCs are rare entities which are difficult to isolate and characterize.

In this context, circulating tumor cell (CTC) clusters are even rarer than single CTCs, accounting for roughly 1 to 17% of detected CTCs in patients. CTC cluster detection varies greatly depending on the tumor type, stage, and CTC enumeration methodology (Amintas et al., 2020; Cho et al., 2012; Micalizzi et al., 2017; Szczerba et al., 2019). The reported proportions of patients with detected CTC clusters range widely, for example from 5 to 54% in breast cancer (Cho et al., 2012; Jansson et al., 2016; Larsson et al., 2018; Mu et al., 2015; Paoletti et al., 2015; Szczerba et al., 2019; Wang et al., 2017), 18 to 81% in pancreatic ductal adenocarcinoma (Amantini et al., 2019; Buscail et al., 2019; Catenacci et al., 2015; Chang et al., 2016), and 26 to 50% in lung cancer (Hou et al., 2012; Manjunath et al., 2019; Murlidhar et al., 2017; Sawabata et al., 2020). The size of CTC clusters is also highly variable; clusters over 20 cells have been identified in the blood of patients across the most common cancer types, though they are more commonly reported as clumps of between 2 to 6 cells (Long et al., 2016; Molnar et al., 2001; Sarioglu et al., 2015). Importantly, accruing evidence suggests that patient populations in which these CTC clusters are detected often have greater rates of disease progression and poorer treatment response.

1.3.3 *Circulating tumor cell clusters correlate with poorer clinical outcomes*

Across the most common types of cancer, CTC clusters are associated with worse clinical outcomes including disease progression and early mortality. A potential confounding variable is that the frequency of single CTCs tends to co-vary with the frequency of CTC

clusters. For example, retrospective analysis of samples collected in a large breast cancer clinical trial found that single and clustered CTC counts correlated such that CTC cluster count was not an independent prognostic factor, unlike total CTC count (Paoletti et al., 2019). Still, in other studies the presence of CTC clusters remains an independent prognostic factor by Cox proportional hazards, yielding prognostic information beyond the presence of single CTCs alone **(Table 1.2)**. A study in pancreatic cancer found that the mean number of detected CTC clusters per blood draw increased with disease progression from 0 to 9.2 to 15.2 to 71.2 through stages I-IV, respectively (Chang et al., 2016). Other studies have likewise demonstrated that CTC cluster counts are time-dependent in patients, often increasing with disease progression and decreasing with response to therapy (Larsson et al., 2018; Wang et al., 2017; Yu et al., 2013). Broadly, the presence of clusters or an increase in their prevalence are concerning indicators of poor patient prognoses.

Increasing numbers of CTC clusters have also been postulated to directly cause patient morbidity even if they fail to generate distant metastases. CTC clusters can occlude vessels, as in pulmonary lymphangitic carcinomatosis when lung lymphatic vessels become obstructed and inflamed, in turn leading to respiratory distress (Klimek, 2019). Moreover, occlusion of vessels by tumor emboli in the brain can lead to cerebral infarction and has been speculated as a possible explanation for the preferential seeding of metastases in watershed regions, which are sites of narrowing of the vascular network to 50-150 μm arterioles (Delattre et al., 1988; Hwang et al., 1996; Walker and Kapoor, 2007). Thus, CTC clusters can have directly negative consequences on patient outcome in addition to seeding new secondary tumors.

CTC clusters are also found as heterotypic aggregates between tumor cells and platelets or immune cells encountered in the blood, but sometimes also with cells from the primary tumor microenvironment like fibroblasts and macrophages which have been carried along into the circulation (Aceto, 2020; Duda et al., 2010; Heeke et al., 2019; Jiang et al., 2017; Micalizzi et al., 2017; Sarioglu et al., 2015). A recent study found that 8.6% of collected breast cancer CTCs were homotypic clusters but 3.4% were heterotypic white blood cell-CTC clusters, with the remaining 88% corresponding to single cell CTCs. In these heterotypic clusters, roughly 25% of attached white blood cells were predicted to be T-cells. Of the remaining 75% a large majority were neutrophils, which may have adhered to CTCs using VCAM1. Neutrophils conferred greater expression of cell-cycle genes and enhanced aggression in these circulating tumor cells (Szczerba et al., 2019). Neutrophils are also implicated in extravasation of tumor cells through their secretion of IL-8 which modulates endothelial barriers (Chen et al., 2018). These studies and others suggest that disrupting communication and aggregation between certain immune compartments and tumor cells in the circulation might benefit patients.

Platelets attached to CTCs can also play several important roles in promoting metastasis (Camerer et al., 2004; Dasgupta et al., 2017; Labelle and Hynes, 2012). By coating CTCs, platelets can shield them from immune cells, from the physical stress of circulation, and inconveniently from some CTC detection methods when platelets mask tumor cell surface epitopes (Egan et al., 2014; Heeke et al., 2019; Jiang et al., 2017). Cluster-platelet aggregation can also promote transendothelial migration and extravasation (Xiong et al., 2020). Moreover, platelet-derived TGFβ and NF-κB signaling increased mesenchymal gene expression in CTCs and enhanced metastasis in a recent

study (Labelle et al., 2011). These heterogeneous interactions with non-tumor blood cells can give CTCs a greater ability to survive in the bloodstream and generate new metastases.

1.3.4 *Human studies and mouse models harbor evidence of metastases seeded by multiple cells*

While clinical studies demonstrate that the presence of circulating clusters is often associated with poorer prognosis and metastatic progression, this does not provide direct evidence that metastases originate from circulating clusters of tumor cells. To answer this question, experimental models of metastasis are helpful to unambiguously trace the contribution of clusters to metastasis formation. Two such studies were recently carried out using breast cancer mouse models with primary tumors labeled with multiple fluorescent proteins to identify polyclonal (i.e. multi-color) metastases founded by multiple cells. By measuring the proportion of multi-color CTC clusters vs. single color individual CTCs, as well as identifying the fraction of metastases with multiple fluorescent tags (i.e. founded by multiple cells), the authors were able to back-calculate the metastatic potential of clusters vs. single cells in these systems. They found that CTC clusters were predicted to generate 50 to 97% of all metastases despite accounting for a small fraction of all CTCs (Aceto et al., 2014; Cheung et al., 2016). Thus, the metastatic potential of CTC clusters was predicted to be 20 to >50-fold higher than that of single cells in these models. In another study using a multi-color mouse model of pancreatic cancer, 80% of macrometastases to the diaphragm or peritoneum were seeded by multiple cells, despite only ~15% of CTCs circulating as clusters (Maddipati and Stanger, 2015). Studies in other

models have similarly identified enhanced aggression of clusters and polyclonal metastasis formation in breast, colorectal, and ovarian cancer (Echeverria et al., 2018; Janiszewska et al., 2019; Kok et al., 2021; Liu et al., 2019c; Lo et al., 2020; Mizukoshi et al., 2020; Naffar-Abu Amara et al., 2020) **(Table 2)**. These experimental findings all point to greatly increased metastatic efficiency in circulating tumor cell clusters and demonstrate that, at least in some cancer models, they give rise to the majority of metastases despite their rarity (Cheung and Ewald, 2016).

In human tumors, DNA sequencing and phylogenetic analysis of metastases compared to primary tumors can reveal if metastases were clonally seeded by a single cell or instead seeded by multiple cell clones from the primary tumor (Birkbak and McGranahan, 2020; Hunter et al., 2018). Still, an important consideration when interpreting these findings is that polyclonal seeding could occur either by metastasis of multiclonal clusters or serial seeding of single cells. Conversely, seeding by monoclonal clusters or later clonal sweeps could result in monoclonal metastases despite a multicellular origin. Polyclonal metastases have been identified in prostate cancer (Gundem et al., 2015), lung cancer (Hu et al., 2020), colorectal cancer (Dang et al., 2020; Leung et al., 2017; Ulintz et al., 2018; Wei et al., 2017), ovarian cancer (McPherson et al., 2016), gastric cancer (Hirotsu et al., 2020), and intrahepatic cholangiocarcinoma (Dong et al., 2018). In rapid autopsy studies of metastatic breast cancer patients, 63 to 73% of patients had evidence of polyclonal metastasis (Siegel et al., 2018; Ullah et al., 2018). Further, this polyclonal organization can be observed from the first phases of neoplasia. In breast cancer, the invasion of genetically multiclonal clusters of cells is observed when ductal carcinoma in situ (DCIS) cells breach the mammary duct and

escape into surrounding tissues (Casasent et al., 2018; Pareja et al., 2020). Genomic analysis has additionally demonstrated polyclonal seeding of lymph node metastases in colorectal and breast cancer (Ulintz et al., 2018; Ullah et al., 2018). These genetic findings further support a model of metastatic dissemination propagated by multiclonal groups of cells, rather than individual clones.

Still, these observational human studies cannot determine what proportion of polyclonal metastases were seeded simultaneously by clusters of cells, or serially by single cells. In mouse models of breast cancer, however, polyclonal metastases derived from cluster-based seeding were observed more frequently than metastases arising from serial seeding of individual cells. In three recent studies, tumor cells with different fluorescent tags were separately inoculated into the left and right mammary fat pads to generate two single-color tumors. If serial seeding of metastases were a frequent event, a high proportion of the metastases would be expected to be multi-color, that is derived from single cells from both the left and right tumor. However, when lung metastases were assessed, only 0 to 14% of them were two-color (Aceto et al., 2014; Cheung et al., 2016; Liu et al., 2019c; Lo et al., 2020). These experiments indicate that the majority of polyclonal seeding in these models is not derived from serial seeding of cells but rather from cells which group together at the primary tumor site. While further and deeper sequencing of metastatic tumors will better elucidate seeding patterns, these experimental studies suggest that tumor cell clusters may be an important source for polyclonal metastases in human patients.

1.4 COOPERATIVE INTERACTIONS DURING COLLECTIVE CELL METASTASIS

Cooperation is the observation that individuals within a group coordinate their activities, resulting in collective benefit. In nature, cooperation is observed across biological time and length scales ranging from the population dynamics of T-cells (Antonioli et al., 2019; Polonsky et al., 2018) to hair follicle regrowth (Chen et al., 2015) to nest-site selection of honeybees (Seeley and Visscher, 2004). In each of these examples, communities of individuals use cooperation to their advantage to overcome obstacles, share information, or neutralize threats. For example, during tissue development and wound repair intercellular cooperation between local niche cells and stem cells maintain the correct balance of renewal and proliferation. This dialogue is shaped by the physical topology of cells and their cell-cell contacts, extrinsic environmental signals like injury or inflammation, and bidirectional niche cell/stem cell signaling (Mesa et al., 2015; Park et al., 2016; Riquelme et al., 2008; Xin et al., 2016).

The field of microbiology serves as another instructive example; recent findings have upended the model that bacteria behave as “lone agents” and instead identified important cooperative behaviors like biofilm formation mediated by intercellular communication and quorum sensing (Ben-Jacob et al., 2012; Lambert et al., 2011; Papenfort and Bassler, 2016). Unlike stem cell/niche cell interactions with sender-receiver dynamics, in this instance all cells are competent to produce a quorum signal. When enough cells in the population express that signal its concentration passes a key threshold, inducing a community-level switch in phenotype. Tuning the degree of “self communication” vs. social or “neighbor communication” can generate emergent signaling

circuits and population-level responses in natural or synthetic biological systems (Antonioli et al., 2019; Doganer et al., 2016; Youk and Lim, 2014).

Further, in ecology cooperative interactions can be used to explain population dynamics that differ from logistic growth models. These divergences can be generated by “Allee effects” in which interactions amongst members of a population, such as cooperative feeding and shared contributions to defence, generate threshold effects whereby populations must reach an intermediate size before achieving maximum growth (Korolev et al., 2014).

In the field of cancer research however, we are only recently appreciating the degree to which cooperativity can promote disease progression (Tabassum and Polyak, 2015). Cancer cells are often associated with “selfish” behavior and uncontrollable growth arising from mutations releasing cells from the constraints of their original developmental programming (Archetti and Pienta, 2019). But the recognition that cancer cells maintain physical contact as clusters throughout the metastatic cascade, and that doing so can greatly increase their likelihood of successful colonization, indicates that intercellular cooperation might confer advantages during this process.

1.4.1 *Cellular specialization and intercellular communication in tumor cell collectives during invasion*

Locally invading cancer cells face a multitude of challenges as they disperse from the primary tumor. Within a 3D context, these include pathfinding, coping with changing local environments, matrix remodeling, and metabolic demand (Yamada and Sixt, 2019). An individual invasive cell must acquire properties to overcome all these obstacles, often

simultaneously, while retaining the capacity to later proliferate and expand into a secondary tumor. In clusters, these demands can be surmounted in part through cell specialization and intercellular communication.

A common motif across both normal collective migration and collective invasion by cancer cells is the emergence of distinct cellular states along the axis of migration; that is to say, there are “front” and “rear” cells within clusters which can have important differences in their phenotypes. At the extreme end of this spectrum, migrating clusters can arrange into single-file chains which is observed in melanoma and breast cancer invasion (Friedl and Wolf, 2003; Khalil et al., 2017). Nonlinear nest-like groups of cells can also arrange themselves with one or more “leader” cells at the front-most edge of the cluster directing migration and remaining connected to several “followers” behind. Leaders, as their name implies, are usually thought to determine the direction of migration of the cluster. They can accomplish this by sensing the microenvironment through ECM-integrin signaling and responding to chemoattractants, and in turn can modify the path in front of them through traction forces or secretion of matrix metalloproteinases (Mayor and Etienne-Manneville, 2016). Follower cells, in turn, may assist leader cells via pro-survival signaling and maintaining the direction of migration, and can provide much of actual traction force needed for movement (Konen et al., 2017; Trepat et al., 2009; Yamada and Sixt, 2019).

There are many different forms this leader-follower pattern can take depending on the biological context. During lateral line morphogenesis in zebrafish, multiple leader cells and followers within the migrating cluster maintain distinct but cooperative phenotypes through differential expression of chemokine and growth factor receptors (Aman and

Piotrowski, 2008; Mishra et al., 2019). Another example during development is *Drosophila* border cell migration, in which non-motile polar cells activate JAK/STAT signaling in leading border cells to promote their motility (Mishra et al., 2019; Silver and Montell, 2001). In mammals, a prototypic example of this organization occurs during normal vascular sprouting; “tip” cells connected by cell-cell junctions to “stalk” cells lead multicellular cohorts of endothelial cells via VEGF chemotaxis (Gerhardt et al., 2003).Though the number of cells in each group and the molecular distinctions between them vary greatly, this leader-follower dichotomy is repeatedly observed across different species in both normal and disease contexts (Cheung et al., 2013; Mayor and Etienne-Manneville, 2016; Nagai et al., 2020).

Functional experiments have confirmed that this leader-follower organization can be important for successful invasion and metastasis. A study in breast cancer found that basal cells expressing keratin-14 frequently led collectively invading strands in both mouse models and human tumor samples. Keratin-14 knockdown significantly reduced collective invasion and subsequent metastasis by clusters, indicating that disrupting the leader cell-associated gene expression of tumor cell clusters can greatly suppress their metastatic potential (Cheung et al., 2013). Another study found that laser ablation of leader cells interrupted forward invasion of collective strands in 3D culture (Zhang et al., 2019). However, within 12 hours a new leader cell typically emerged and resumed invasion. The authors noted that new leader cells arose from follower cells and replaced existing leader cells even without laser ablation, suggesting that follower-leader states can dynamically interchange. Denser collagen matrices, which required greater energy consumption by leader cells, also hastened the emergence of new leader cells to replace

the previous “tired” leaders (Zhang et al., 2019). A number of other studies have likewise found that removal of leader cells or disruption of their function significantly impairs collective migration (Gao et al., 2017; Khalil et al., 2020; Kim et al., 2017a; Yang et al., 2019).

Many experimental techniques have been developed to further isolate and characterize the molecular properties of leader and follower cells. These approaches help identify leader vs. follower distinctions that confer disparate functions and facilitate cooperativity, including differences in transcription, metabolism, epigenetic modifications, senescence, and gene mutations (Commander et al., 2020; Kim et al., 2017a; Konen et al., 2017; Summerbell et al., 2020; Zhang et al., 2019; Zoeller et al., 2019). For example, after culturing cells transduced with the photoconvertible fluorophore Dendra2 in 3D ex vivo culture systems which promote collective invasion (Konen et al., 2017), photoconverted leader cells have been separated from non-leader cells by flow sorting for further phenotypic and genomic analyses. When specific markers for leader cells are known, such as Keratin-14 in breast and ovarian cancer, leader cells can instead be identified by differential expression through gene promoter-driven fluorescence expression or antibody-based methods (Bilandzic et al., 2019; Cheung et al., 2013; Cheung et al., 2016; Hwang et al., 2019b; Quan et al., 2020; Yang et al., 2019). Live imaging alternatively allows actively migrating leader cells to be analyzed in situ without disrupting their dynamic interactions with follower cells. Pairing live time-lapse microscopy with other techniques such as fluorescent metabolic indicators (Commander et al., 2020; Zhang et al., 2019), traction force microscopy (Riahi et al., 2015; Trepat et al., 2009), organelle-specific dyes (Commander et al., 2020), and co-culture with non-tumor cells

(Gaggioli et al., 2007; Hanley et al., 2020; Hwang et al., 2019a) can provide additional layers of information clarifying the role of leader cells during collective migration and invasion.

Similar experimental systems can also be used interrogate cooperative interactions between leader and follower cells to identify the signaling or communication that emerges when clustered cells segregate into these two identities. Cell mixing or co-culture experiments, leader or follower cell-specific gene knockdown, conditioned media treatment, and other techniques have been used to identify the molecular sources of leader-follower cooperative phenotypes. Experiments assessing isolated vs. mixed leader and follower cells have been particularly informative; one study found that mixing increasing proportions of purified leader cells with follower cells resulted in a dose-dependent increase in invasion. Leader-cell conditioned media could also induce invasion of follower cells, supporting the hypothesis that secreted factors facilitate leader-follower communication (Konen et al., 2017). In lung cancer cells, VEGF was upregulated in leader cells, which in turn stimulated the motility of follower cells (Konen et al., 2017). These purified leader cells grew slowly compared to follower cells, but their growth was rescued by follower-conditioned media, suggesting both compartments generate important secreted signals. And, in thyroid cancer cells, CXCL12 secretion by leader cells increased the survival and anoikis-resistance of co-cultured cells (Kim et al., 2017a). Communication between leaders and followers may also occur through modulation of existing soluble signaling molecule gradients. During melanoma migration, follower cells breakdown local LPA to form a chemotactic sink, generating an outward-facing chemotactic gradient that invasive cells follow (Muinonen-Martin et al., 2014). Thus

follower-leader cells can participate in multiple modes of bidirectional signaling to modulate or support each other's phenotypes.

In addition to secreted molecules, leader and follower cells can communicate directly at or through cell-cell junctions. One group recently demonstrated gap junction intercellular communication (GJIC) between leader and follower cells using fluorescence recovery after photobleaching. Leader and follower cells containing calcein dye were photobleached, but quickly recovered fluorescent calcein signal donated by neighboring cells indicating active intercellular transfer (Khalil et al., 2020). Cell-cell junctions can also facilitate juxtacrine signaling of receptors and ligands on adjacent cells. For instance, juxtacrine Notch1-Dll4 signaling between leader and follower cells can prevent the initiation of additional leader cells (Riahi et al., 2015). Cell-cell junction molecules themselves can also communicate important information between leaders and followers. E-cadherin signaling between motile cells and polar cells during border cell migration communicates the direction of movement through positive feedback with Rac (Cai et al., 2014). As leader cells move forward, tension accumulates at cadherin junctions with follower cells. This tension can transduce a number of downstream signals, including relocalization of cytoskeletal proteins like merlin, ultimately increasing the migratory polarization of migrating cells (Das et al., 2015). In some instances, leader cells can also generate a peripheral actomyosin cable which prevents the initiation of new leader cells amongst their followers (Reffay et al., 2014). These findings affirm the concept that migrating clusters are often not just physically linked, but in many instances are communicating through mechanical or chemical signals downstream of cell-cell adhesion.

Though leader-follower arrangements have been identified in multiple cancer types, there are intriguing exceptions in which leader cells are not detected, or in which or steering and pathfinding are actually driven by cells at the rear of the cluster (Theveneau and Linker, 2017). A recent study found that colorectal cancers can form large multicellular spheres with reversed (apical surface, basal core) polarity which migrate in an amoeboid-like manner without generating adhesive cellular protrusions or forming leader cells (Zajac et al., 2018). Another example is the normal development of mammary ducts, which is accomplished by the collective migration and bifurcation of multilayered bulb-like structures called terminal end buds (TEBs) which similarly lack protrusions and leader cells (Paine and Lewis, 2017). Developmental TEB migration shares common features with breast cancer invasion. In both cases multicellular groups of cells invade through the mammary stroma, secrete MMPs to facilitate migration, generate mixed luminal/basal cell populations, have reduced apical-basal polarization, and are assisted by local non-epithelial cells including fibroblasts and macrophages (Avagliano et al., 2020; Cheung et al., 2013; Kessenbrock et al., 2010; Lee and Vasioukhin, 2008; Paine and Lewis, 2017; Scheele et al., 2017; Wiseman et al., 2003). These studies highlight that collective migration can be carried out through various means of supracellular organization. But a unifying theme across disparate mechanisms of collective invasion and migration is that the diversity of phenotypic states within cell clusters can generate intercellular cooperativity and important pro-invasive features.

Still, yet another form of intercellular cooperation during invasion is through interaction with local non-tumor cells, extensively reviewed elsewhere (Binnewies et al., 2018; Egeblad et al., 2010; Hirata and Sahai, 2017; Lyssiotis and Kimmelman, 2017;

Sahai et al., 2020). For instance, two-way paracrine signaling in which cancer cells secrete CSF1 and macrophages secrete EGF promotes breast cancer cell invasion (Patsialou et al., 2009). Macrophages can additionally contribute to invasion through breakdown or modification of the ECM (Sanchez et al., 2019) or direct cytosolic transfer to tumor cells (Hanna et al., 2019; Roh-Johnson et al., 2017). Fibroblasts can promote collective invasion in several ways, including forming migration tracks within the ECM (Gaggioli et al., 2007), increasing expression of invasive and leader-cell associated genes (Hanley et al., 2020; Matsumura et al., 2019), and forming heterotypic N-cadherin/E-cadherin contacts with cancer cells which allow fibroblasts to promote and even lead collective invasion (Labernadie et al., 2017). Broadly, cooperative interactions amongst tumor/tumor or tumor/non-tumor cell collectives are increasingly appreciated to be critical mediators of invasion.

1.4.2 *Cell-cell adhesion induces pro-survival signaling during early metastatic colonization*

Cell-matrix attachment, namely through integrin-ECM interactions (Miranti and Brugge, 2002), is a fundamental regulator of epithelial cell survival (Miranti and Brugge, 2002; Strilic and Offermanns, 2017; Taddei et al., 2012). Loss of integrin-ECM signaling results in downstream signals including the release of sequestered Bim protein, which can then translocate to the mitochondria and promote intrinsic apoptosis, or upregulation of Fas and Fas-L expression, which activate extrinsic apoptosis (Taddei et al., 2012). When cancer cells lose these signals in settings either without sufficient ECM, such as vascular or lymphatic channels, or without appropriate ECM, such as distant tissues with distinct

and non-permissive matrix components, they become susceptible to programmed cell death (Celià-Terrassa and Kang, 2016; Strilic and Offermanns, 2017). But in certain contexts, cell-cell adhesion can override pro-apoptotic signals, preserving metastatic cell survival in these environments (Al Habyan et al., 2018; Kantak and Kramer, 1998; Liu et al., 2019c; Zhao et al., 2010)

In some cases, cell-cell adhesion helps cells evade death by activating integrin signaling. In clustered carcinoma cells the cell-surface protein PVRL4, which can bind PVRL1 on adjacent cells (Pavlova et al., 2013), activates $\alpha 6\beta 4$ integrin signaling. This in turn maintains expression of lipid repair enzyme GPX4, preventing lipid peroxidation and subsequent cell death via ferroptosis (Brown et al., 2018). Clustering of integrins with other receptors at cell-cell contacts can also activate downstream pro-survival signaling. For example, integrins can interact directly with EGFR or its ligands at cell-cell contact sites, and activate downstream signaling (Nakamura et al., 1995; Yu et al., 2000). This ECM-independent induction of signaling is particularly important in fluid metastatic microenvironments, such as when ovarian cancer cells metastasize by shedding into the peritoneal fluid. Upregulation of E or N-cadherin and formation of multicellular aggregates protects ovarian cancer cells from anoikis in this liquid environment by activating PI3K and EGFR signaling (Hudson et al., 2008; Klymenko et al., 2017; Rayavarapu et al., 2015; Reddy et al., 2005). By either promoting integrin activation or bypassing it to activate downstream oncogenic signaling pathways, cell-cell adhesion provides an alternative route to pro-survival signaling when ECM contact is absent or non-permissive.

Oxidative stress is another major initiator of cell death during metastasis, and can greatly lower the metastatic potential of tumor cells (Piskounova et al., 2015). Clustering

helps cells mitigate reactive oxygen species (ROS) by several mechanisms. Clustering of detached cells can promote mitophagy, resulting in the clearance of damaged mitochondria and reduced ROS (Labuschagne et al., 2019). Recent studies in mouse models of breast cancer found that reducing expression of E-cadherin or p120-catenin increases local invasion, but ultimately reduces successful metastasis (Ilina et al., 2020; Kurley et al., 2020; Padmanaban et al., 2019). E-cadherin downregulated tumor cells had increased levels of oxidative stress and apoptosis and poorer overall metastasis formation. E-cadherin expression ultimately reduced ROS-promoting signals via modulation of TGFβ signaling, promoting survival and increasing metastatic colonization (Padmanaban et al., 2019). Though molecular mechanisms are still being uncovered, these studies suggest that cell-cell adhesion in tumor cell clusters can help circumvent major causes of apoptosis during metastasis such as ECM detachment and oxidative

1.4.3 *Multicellularity can modify certain tumor-immune cell interactions, promoting immune evasion*

During dissemination and colonization, tumor cells can be targeted for destruction by immune cells patrolling tissues. Indeed immune escape is a critical step for successfully forming overt metastases (Leone et al., 2018; Mohme et al., 2017). Tumor cells can escape immune cells through many different mechanisms, making sensitizing tumors to the immune system challenging. These mechanisms include secreting cytokines or growth factors that can recruit tumor-promoting immune cells or inhibit the activity of anti-tumor immune cells; cells can evade immune cells by avoiding antigen presentation; or tumor cells can co-opt nearby non-tumor cells, inducing them to become

immunosuppressive (Binnewies et al., 2018; Sun et al., 2018). Each of these heterotypic interactions, or combinations thereof, can help tumors escape one of the body's most potent protections against metastasis (Binnewies et al., 2018).

It is still largely unknown whether single cells or clusters utilize distinct mechanisms of immune escape. Still, there are hints at cluster-specific mechanisms of immune evasion, particularly in regard to natural killer (NK) cells. NK cells play a key role in the targeting of metastases, and their infilitration into tumors often correlates with better patient prognoses (Chiossone et al., 2018; López-Soto et al., 2017; Malladi et al., 2016; Souza-Fonseca-Guimaraes et al., 2019). One recent study found that natural killer cells effectively killed single tumor cells, but not clusters. This depended partly on clusters' ability to downregulate NK cell activating ligands, which include EMT promoting genes, and upregulate NK inhibitory ligands, which include cell-cell adhesion genes (Lo et al., 2020). In fact many cell-cell adhesion molecules function as NK cell inhibitory signals; classical E, N, and R-cadherins are ligands for the inhibitory KLRG1 receptor expressed on NK cells (Li et al., 2009; Pegram et al., 2011). Downregulation of cell-cell adhesion, as in EMT, increases sensitivity to NK killing (Lo et al., 2020; López-Soto et al., 2013). This suggests that NK cells may be fundamentally better suited to kill aberrant post-EMT single cells rather than tumor cell clusters. However, a different study found that NK cells were able to specifically target and induce apoptosis in basal leader cells in collectively invading breast cancer strands, which could be exacerbated by antibody-dependent cell-mediated cytotoxicity. But after prolonged exposure to tumor cell clusters, NK cells were reprogrammed to a metastasis promoting state (Chan et al., 2020). Further studies are

needed to assess how collectively invading clusters or micrometastases evade targeting by NK cells and shift them into more permissive cell states.

In addition to NK cells, the pro and anti-tumorigenic attributes of macrophages, T-cells, neutrophils, and other immune populations are known to be major determinants of metastatic colonization (Binnewies et al., 2018; Kitamura et al., 2015). We do not yet understand if and how their response to single cells or multicellular clusters differs, though recent studies point at some potentially interesting lines of questioning. One such study used an unbiased shRNA screen to identify CD44, which can mediate breast cancer tumor cell cluster cell-cell adhesion (Liu et al., 2019c), as a novel positive regulator of the inhibitory immune checkpoint gene *PDL1* (Kong et al., 2020). Another class of cell-cell adhesion molecules identified in tumor cell clusters, nectins, also may promote immune evasion. Nectin-2 can bind to TIGIT expressed on T-cells, resulting in T-cell inhibition (Gorvel and Olive, 2020; Yu et al., 2009). Immune suppression downstream of tumor cell cluster formation remains unclear and understudied. But given recent clinical successes using anti-PD-L1 treatments and immune checkpoint inhibitors (Sun et al., 2018), understanding the induction of immunosuppressive signals in tumor cell clusters has important clinical relevance.

1.4.4 *Intercellular signaling promotes metastatic colonization and outgrowth by tumor cell clusters*

The reproducible observations in many models that tumor cell clusters are intrinsically more proliferative and less apoptotic than single tumor cells suggests that cellular signaling pathways regulating those states are altered by clustering. Correspondingly, in

normal cells, cell-cell adhesion has long been known to strongly influence proliferation and survival (Benham-Pyle et al., 2015; Garcia et al., 2018; Livshits et al., 2012). Early findings suggested that single cells from certain tissues are apoptotic by default, unless rescued by the “social signaling” of adjacent cells – a mechanism which prevents lone cells from surviving in incorrect tissue locations (Raff, 1992). Other early studies in embryonic development noted “community effects”, in which direct interactions with neighboring cells were critical for promoting survival and differentiation (Gurdon, 1988). Using transplant experiments, researchers found that transplanting single cells early in development into different tissues could induce them to differentiate into the tissue present at that site. However, if cells were transplanted as a group they retained their original tissue type (Gurdon et al., 1993). Extensive studies since have shown that adhesion to neighboring cells, and the geometry of those adhesions, have profound effects on survival, proliferation, and differentiation of developing tissues (Gilmour et al., 2017; Xin et al., 2016).

Likewise, it has been speculated that cell-cell interaction is a prerequisite needed to achieve certain community-level effects and cooperative “decision making” in tumor cell communities (Ben-Jacob et al., 2012; Deisboeck and Couzin, 2009; Hickson et al., 2009; Jolly et al., 2018; Korolev et al., 2014). However, many of the specific mechanisms of intercellular signaling active in disseminated clusters, micrometastases, and overt metastases remain to be elucidated. But increasing evidence indicates that by disseminating as a cohesive group, tumor cells in clusters may be able to activate cell-cell signaling networks that promote metastasis.

(1) Paracrine and interclonal signaling

Paracrine signaling between cells plays a key role in development in which morphogen gradients, chemoattractants, and other secreted molecules determine the placement and formation of tissues (Wartlick et al., 2011). These paracrine signals can operate over incredibly long distances, sometimes forming gradients across an entire organism. Alternatively, they can operate in a spatially restricted, short-range manner such as JAK/STAT signaling during border cell migration (Silver and Montell, 2001) or tethering of TGFβ to the extracellular matrix (Müller and Schier, 2011). Though long-distance secretion and paracrine interactions can have an important role in cancer (Fujita et al., 2016; Peinado et al., 2017), short-range signal exchanges are also possible between adjacent tumor cells. Paracrine signaling between nearby cells in this manner maintains high local signal concentrations and effective signaling induction (Müller and Schier, 2011). This can result in a minority of cells in the cluster shifting the phenotype of their neighbors. For example Twist1 and Snail1 expressed in EMT-high breast cancer cells can induce EMT gene expression and promote aggression in neighboring non-EMT cells though paracrine secretion and activation of Hedhehog signaling (Neelakantan et al., 2017). Thus the close spatial proximity of cells in a tumor cell cluster can facilitate a particularly rapid and spatially concentrated form of paracrine signaling.

Heterogeneity within clusters may result in producer-receiver dynamics in paracrine signaling circuits when subgroups within the cluster differentially express ligands and receptors. These kinds of interclonal interactions can result in emergent cooperative, neutral, or competitive dynamics between tumor cells (Kok et al., 2021; Martín-Pardillos et al., 2019; Marusyk et al., 2014; Tabassum and Polyak, 2015).

Intercellular receptor-ligand interactions have been implicated in promoting primary or metastatic tumor cell cooperation and outgrowth via Wnt secretion (Cleary et al., 2014), cytokine production (Cleary et al., 2014; Janiszewska et al., 2019), and EGFR ligand exchange (Hobor et al., 2014; Naffar-Abu Amara et al., 2020; Wrenn et al., 2020b). A recent study using breast cancer xenograft models found that polyclonal mixtures of IL11 and FIGF secreting clones generated significantly greater metastatic growth than either clone alone (Janiszewska et al., 2019). Another study isolated clonal populations from an ovarian patient derived xenograft cell line. A multiclonal mixture generated significantly greater tumor burden after injection than 10 of 11 constituent clones injected alone – the only clone with an equivalent rate of growth had a particularly high degree of ERBB2 amplification which supported its anchorage-independent growth. However, alone that ERBB2-high clone could not generate solid peritoneal metastases unless exposed to the growth factor amphiregulin which was secreted by other clones (Naffar-Abu Amara et al., 2020). These findings highlight the powerful effects of beneficial interclonal interactions on metastatic outgrowth.

(2) Direct signaling at cell-cell junctions

One emergent property of tumor cell clusters is that cells in such close proximity can signal directly to their adherent neighbors at sites of cell-cell contact (Toda et al., 2019). Perhaps the most obvious cluster-dependent signaling mechanism which this could enable is juxtacrine signaling, in which membrane-bound molecules on two apposing cells bind one another. Notch signaling, for example, is a well-described mechanism of juxtacrine signaling which can promote metastatic success (Boareto et al., 2016;

Jackstadt et al., 2019; Li et al., 2017). During normal development and homeostasis, membrane bound Notch ligands bind the Notch receptor, resulting in receptor cleavage and transport of the C-terminal domain of the receptor to the nucleus where it can alter cellular transcription (Siebel and Lendahl, 2017). The Notch pathway encompasses five different ligands and four different receptors, resulting in many potential combinations with specific signaling outputs (Meurette and Mehlen, 2018).

In tumor cells, Notch ligands like JAG1 have been implicated in increased tumor cell growth and dissemination (Choi et al., 2008; Riahi et al., 2015) as well as lumen formation in colon cancer cells (Kawai et al., 2020). In triple negative breast cancer, Notch overexpression increased the proportion of K14+ to K14- cells nearly 3-fold by increasing rates of symmetric division (Granit et al., 2018). In another recent study using lung cancer cells, JAG1 was highly enriched in leader cells and anti-JAG1 antibody treatment reduced collective invasion (Summerbell et al., 2020). And in ovarian tumor cell clusters, juxtacrine interactions between JAG1 and NOTCH3 result in increased proliferation (Choi et al., 2008). Notch signaling can also occur through heterotypic interactions with cells in the TME (Meurette and Mehlen, 2018) or modify the TME itself, including through downstream TFGβ signaling and neutrophil recruitment (Jackstadt et al., 2019). In addition to the Notch pathway, ligands from several other pathways known to promote growth or metastasis such as ERBB, Ephrin, Hedgehog, and integrin signaling can each function in a juxtacrine manner (Friedl and Mayor, 2017; Lu et al., 2014; Pettigrew et al., 2014; Singh and Harris, 2005).

Adjacent tumor cells can also form gap junctions which permit the direct diffusion of signaling molecules between their cytosols (Hitomi et al., 2015). Intercellular

communication through gap junctions has been shown to increase migration in prostate cancer cells (Zhang et al., 2015), to promote stemness in glioblastoma cells (Hitomi et al., 2015), to facilitate intercellular calcium transients in invasive glioma cells (Gritsenko et al., 2020; Osswald et al., 2015), to enhance EGF gradient sensing during collective migration (Ellison et al., 2016), and to promote anchorage-independent growth of breast cancer cells (Gava et al., 2018). Gap junction proteins can also form hemi-channels which modify metastatic behavior through signaling in the extracellular space. A recent study found that invading leader cells released adenosine into the extracellular space through connexin-43 hemichannels, and adenosine then activated Akt signaling through the adenosine receptor 1 (ADORA1) to promote collective invasion (Khalil et al., 2020). The unique ability of gap junctions to facilitate direct cytosol-to-cytosol transmission or rapid cytosol-to-extracellular space release makes them an intriguing target to disrupt tumor cell-cell communication (Aasen et al., 2016).

(3) 3D cell arrangment and morphology-dependent signaling

Development of 3D culture models has improved our ability to recapitulate the all-encompassing interactions of tumor cells with one another and their environment during ex vivo experiments (Shamir and Ewald, 2014; Simian and Bissell, 2017). In addition to allowing 3D cell-cell or cell-matrix adhesions to form, 3D culture also facilitates important changes in shape as tumor cells combine to form complex structures resembling spheres, cysts, strands, or buds (Jamieson et al., 2017; Padmanaban et al., 2020; Sachs et al., 2018; van de Wetering et al., 2015). In normal cells such shape changes can alter cellular functions greatly (Gilmour et al., 2017), as when lateral line cells form rosettes with a

central lumen concentrating FGFs to regulate collective migration (Durdu et al., 2014), when gut epithelia buckle to form concentrated pockets of Shh signaling (Shyer et al., 2015), or when cell-cell contacts in embyros fracture and break the axis of symmetry (Dumortier et al., 2019). Given the critical role cell placement and shape plays in normal homeostasis and development, it seems likely that these features could similarly shape tumor biology and signaling during metastasis.

We recently described a form of pro-metastatic signaling in tumor cell clusters similarly dependent on their collective 3D architecture, summarized in detail in Chapter 3 (pg. 82). We find that breast cancer tumor cell clusters form “nanolumina”, open intercellular spaces lined by microvilli-like structures and gated at either end by cell-cell junctions (Wrenn et al., 2020b). These intercellular cavities have been previously observed in normal and tumor mammary epithelia (Ewald et al., 2012; Mazzucchelli et al., 2019; Tarin, 1969), but not ascribed with major functional importance or signaling properties. We identified a critical function for nanolumina during primary and metastatic tumor outgrowth, during which they act as concentrated reservoirs of the growth factor epigen (*Epgn*), whose expression is induced upon clustering, which promotes tumor cell cluster proliferation. Cell-cell junctions restrict the permeability of nanolumina, preventing entrance of some molecules and egress of others. This creates a private signaling compartment where pro-growth signals like epigen can be maintained and exchanged between cells at high concentrations. Therefore, the collective production and sensing of epigen by tumor cells in clusters represents a pro-growth signaling mechanism dependent on their 3D morphology and multicellular organization.

Importantly, we found that targeting this intercellular structure can reduce metastatic outgrowth. Epigen suppression or treatment with IFNγ to induce nanolumenal paracellular permeability both significantly suppressed metastatic outgrowth, with *Epgn* knockdown reducing metastatic outgrowth of tumor cell clusters in the lungs by over 94%. Interestingly, dependence on epigen signaling and nanolumenal morphology varied amongst subtypes of breast cancer. We found that high epigen expression and nanolumina with restricted permeability were present in basal-like 2 triple negative breast cancers but not mesenchymal-like triple negative breast cancers. Basal-like 2 breast cancers have poor treatment response and a limited number of available therapies (Lehmann et al., 2011; Masuda et al., 2013; Wang et al., 2019). Reducing epigen expression or disrupting nanolumenal permeability reduced metastatic outgrowth in clusters generated from basal-like 2 cancer cells. These findings indicate that tumor cell clusters from specific subtypes of breast cancer, but not others, may rely on cooperative nanolumenal signaling generated by their 3D topology. We have much yet to learn about the role of nanolumina and nanolumenal trafficking of signaling molecules during metastasis. Further examination of these structures, including assessing their prevalence across other normal and malignant tissues, may generate important insights as to how multicellular morphology regulates signaling.

In summary, the heterogeneity, direct cell-cell contacts, and 3D arrangement of cells in a tumor cell clusters can each facilitate modified or novel mechanisms of intercellular signaling during metastatic colonization that are not achievable by single cells. In addition to improving our understanding of the means by which cells can

metastasize, these emergent signaling mechanisms may represent potential therapeutic targets in patients with cluster-based dissemination.

1.5 UNRESOLVED QUESTIONS REGARDING SINGLE CELL VS. COLLECTIVE METASTASIS

1.5.1 *How do bulky clusters enter and exit the bloodstream? Do they use the same mechanisms as single cells?*

The exact details of tumor cell intravasation across different cancer types are still unclear, though the mechanisms used during metastasis are increasingly better understood (Bockhorn et al., 2007; Reymond et al., 2013). Cells may either approach blood vessels through random migration, or through active chemotaxis as in breast cancer when perivascular macrophages secrete EGF which attracts tumor cells (Roussos et al., 2011). To actually enter the circulation they pass through surrounding basement membrane and past the tightly connected endothelial cells which form the vessel walls in a process of transendothelial migration known as diapedesis. Migration through these layers is difficult, but can be improved through different mechanisms; cells may secrete proteases like MT4MMP which can disrupt vessel integrity (Chabottaux et al., 2009), or squeeze through existing holes in the basement membrane (Baluk et al., 2003; Madsen and Sahai, 2010). Likewise local production of factors such as VEGF and TGFβ can weaken the endothelial barrier in mouse models of cancer, facilitating easier entry (Anderberg et al., 2013). Intravasation of tumor cells may also be assisted by other cells, particularly macrophages (Patsialou et al., 2009; Roh-Johnson et al., 2014). The collusion of perivascular

macrophages, tumor cells, and cells expressing the actin regulatory MENA protein has been implicated in creating “doorways” through which tumor cells can pass into blood vessels (Karagiannis et al., 2017; Pignatelli et al., 2016). Thus, single tumor cells have a number of means by which to enter the circulation, with or without collaborating non-tumor cells.

However, the molecular and cellular events giving rise to multicellular tumor emboli are less clear. During diapedesis, cells squeeze through narrow openings ~3 μm wide between endothelial junctions (Madsen and Sahai, 2010), a feat that seems difficult if not impossible for a 5-cell circulating cluster. An alternative hypothesis is that clusters may instead be shed directly into fragile adjacent or tumor-transecting blood vessels without the need for diapedesis (Bockhorn et al., 2007). Cluster shedding may also be facilitated by the formation of mosaic vessels, in which tumor cells displace endothelial cells and allow direct contact of the tumor mass with the bloodstream (Chang et al., 2000; Silvestri et al., 2020). Bypassing the need for transendothelial migration may protect tumor cells from the stress of migrating through ECM, pericytes, and endothelial cells, and instead allow tumor cell clusters immediate entry into the circulation despite their increased size.

Once in the circulation, tumor cells are surrounded by red blood cells and leukocytes and flowing at high speeds through vessels as large as the aorta and as small as <10 μm wide capillaries (Au et al., 2017; Au et al., 2016). This environment generates substantial shear force which can increase cellular stress or even cause necrosis and cell fragmentation (Follain et al., 2020). Tumor cells must rapidly adapt to or exit this environment to move to the next phase of metastatic seeding (Follain et al., 2020; Gensbittel et al., 2021). In order to extravasate, tumor cells first slow down significantly

either by generating adhesions with the endothelial walls or by vessel occlusion (Katt et al., 2018). In zebrafish models, which facilitate time lapse intravital imaging of cell circulation throughout an entire organism, tumor cells preferentially arrest in vessels with flow velocities below roughly 400-600 μm/second (Follain et al., 2018). There is also some evidence that clusters travel through vessels more slowly, facilitating longer interactions with endothelial cells (Choi et al., 2015; Patil et al., 2019). Some models suggest that clusters can also take advantage of different mechanisms of circulatory exit. Clusters may use endothelial remodeling to extravasate, in which endothelia enclose the arrested tumor cell cluster then expel it into the tissue (Allen et al., 2019; Follain et al., 2018). This mechanism was also observed to facilitate the extravasation of clusters of cardiac stem cells (Allen et al., 2017). CTC clusters were far more likely to use endothelial remodeling to extravasate than single cells in zebrafish models, and far more proliferative than single cells after extravasation (Allen et al., 2019). Despite intriguing differences in their means of exit, actual rates of extravasation between single cells and clusters appear similar (Allen et al., 2019). And while zebrafish provide an excellent model for live imaging of an intact circulatory system, further intravital observations of cluster entry and exit from the circulation in mammalian models will strengthen the human disease relevance of these models.

1.5.2 *What is the relative efficiency of cluster-based and single-cell metastasis at each step of the cascade?*

Multiple studies have used experimental metastasis assays to show that clustering of tumor cells increases their potential to generate distant metastases up to 500-fold more

than equal numbers of single tumor cells **(Table 1.1).** But taking a step back, it is less obvious why clustering should provide increased efficiency compared with single tumor cells at earlier steps of metastasis. For example, one might predict that invasion of clusters is far less efficient simply because the small size of single cells allows them to navigate more restrictive environments (Mak et al., 2013; McGregor et al., 2016; Wolf et al., 2013). In agreement, measured speeds of collective invasion are quite slow when compared to single cell migration; clusters often travel just 0.1-1 μm per minute (Clark and Vignjevic, 2015; Friedl et al., 2012). But, while slower, migratory clusters may be better than single cells at following chemotactic cues. Clusters of mammary cells can sense gradients of EGF that are undetectable by single cells (Ellison et al., 2016) In glioma, inhibition of intercellular cooperation through downregulation of p120 cadherin impairs migratory persistence (Gritsenko et al., 2020). Lymphoid malignancies can also form multicellular aggregates that undergo faster and more directional chemotaxis as clusters (Malet-Engra et al., 2015). This increased sensitivity is partly due to the increased size of cell clusters, which allows them to sample a larger range of signal gradients. Clusters of cells could also accomplish directional migration by generating and sensing their own chemokine gradients, instead of relying solely on long-range signals (Donà et al., 2013). In principle, collective invasion could represent a balance between competing demands. Larger clusters may be slower and less able to negotiate dense environments, but they can generate cooperative intercellular signals.

Still, the relative rarity of CTC clusters compared to individual CTCs in patients indicates that, though collective organization is often heavily favored in the peritumoral area, individualized cells outnumber clustered cells once in the circulatory system. The

increased barriers to intravasation by clusters mentioned above are one plausible contributor to this shift. Another reason for the low steady-state proportion of CTC clusters in the blood could be more rapid arrest; the measured half-life of CTC clusters in a mouse model of breast cancer was shorter than single cells, at 6-10 minutes vs. 25-30 minutes (Aceto et al., 2014). One breast cancer study found that the ratio of cells from tumor-draining vessels (local circulation) vs. heart puncture (systemic circulation) was over two-fold higher for CTC clusters than CTC single cells, suggesting enhanced rates of early arrest for tumor cell clusters (Szczerba et al., 2019). Still, clusters may be able to deform into single-file shapes that permit passage through narrow vessels and capillaries (Au et al., 2016). Overall, these findings suggest that both single and clustered CTCs are cleared from the blood stream fairly rapidly, usually on the order of minutes to hours (Aceto et al., 2014; Meng et al., 2004; Sasportas and Gambhir, 2014).

But differences in metastatic success continue diverging considerably once cells have left the circulatory system. Prior studies, using mostly single tumor cells, have shown that the vast majority of cells are expected to die or enter dormancy within days of initial seeding (Chambers et al., 2002; Glaves et al., 1988; Labelle and Hynes, 2012; Luzzi et al., 1998; Yoshida et al., 1993). Recently, we observed that for every 1,000,000 single MMTV-PyMT breast cancer cells injected into mice, only 2.4 macrometastases formed after 3 weeks (Wrenn et al., 2020b). In contrast, for every 1,000,000 clustered cells, injected as small ~5-10 cell clusters, we observed over 1260 macrometastases. Closer examination at earlier time points revealed only ~3% of the number of cells present in the lungs shortly after tail vein injection of single cells were detectable in the lungs 48 hours after injection. In contrast, in cluster-injected mice ~30% of the number of arrested

clusters present shortly after injection were present in the lungs 48 hours after injection. This ten-fold increase in early survival and persistence at metastatic sites could give clustered cells a major advantage over single tumor cells when seeding lung tissues.

During the final step of metastasis, colonization, disseminated tumor cells must not only survive but proliferate to establish overt metastases. Though it is possible for cells to begin proliferating shortly after seeding a metastatic site, some cancers are characterized by long latent periods in which metastatic cells remain viable, but dormant, after dispersal to other tissues (Carlson et al., 2019; Ghajar, 2015; Ghajar et al., 2013; Risson et al., 2020). Dormant single cells are detected more commonly than clusters, and the presence of cell-cell adhesion in fact can promote escape from dormancy (Ruppender et al., 2015). Degree of cell-cell adhesion may also regulate entrance into a proliferative state; in a recent study we found that breast cancer tumor cell clusters in 3D culture were largely growth arrested below a threshold size of ~10 cells, but above that size experienced rapid outgrowth (Wrenn et al., 2020a). As mentioned previously, a wide variety of cell-cell adhesion dependent mechanisms of signaling can feed into signaling pathways which regulate clusters' proliferation. We identified the growth factor epigen as one such signal shared between clustered cells at metastatic sites. When *Epgn* was knocked down, injected clusters were equally as competent as control clusters to seed the lungs and persist for 3 weeks. However, *Epgn* knockdown reduced the outgrowth of those clusters in this metastatic environment over 15-fold. The signals regulating outgrowth in disseminated clusters and micrometastases are still mysterious, but our findings show that in some contexts intercellular signaling can be a major contributor to the massively increased outgrowth of metastasizing clusters vs. single cells.

1.5.3 *How can cluster-based metastasis be interrupted therapeutically?*

The unique properties of tumor cell clusters that promote metastasis could provide promising potential targets for clinical disruption. One such strategy would comprise treatments which block collective invasion by inhibiting leader cell activity. Leader cells may be targeted in multiple ways, such as suppressing leader-cell specific protein functions (Cheung et al., 2013; Moffitt et al., 2019) or exploiting their metabolic vulnerabilities (Commander et al., 2020; Zhang et al., 2019). Tumor cells with leader cell characteristics, e.g. basal keratin positive tumor cells, are also associated with micro-metastases at distant sites (Cheung et al., 2013; Lawson et al., 2015). Therapeutic targeting of leader cells could prevent invasion at the primary site, and possibly curb formation of metastases in distant organs, though this hypothesis remains to be tested rigorously.

A number of studies have also posited that killing or at least disaggregating CTC clusters in the circulation could benefit patients (Choi et al., 2015; Gkountela et al., 2019; Wei et al., 2018). Still, caveats to this strategy need to be carefully considered. Disaggregating CTC clusters could produce more potential seeds of metastasis, since they might be broken apart into viable single cells or simply smaller clusters. Additionally, CTC clusters are identified and held together by common cell-cell adhesion molecules such as E-cadherin (Cheung et al., 2016; Na et al., 2020; Padmanaban et al., 2019), Epcam (Allard et al., 2004), CD44 (Liu et al., 2019c), desmosomal proteins (Aceto et al., 2014), or claudins (Li et al., 2019). Targeting any of these genes would be challenging given that normal cells expressing the same genes could also be impacted. But further study may reveal distinct properties of tumor cell-cell adhesions, such as specific

activation states (Na et al., 2020), that allow them to be targeted with less collateral damage to normal epithelia.

Inhibiting the growth of micrometastases is also an important strategy to reduce metastasis-associated mortality. This is largely because metastasis outgrowth can generate fatal health outcomes, but also because for many patients their primary tumor may have already seeded micrometastases before diagnosis and treatment (Katt et al., 2018; Loberg et al., 2007; Mina and Sledge, 2011). Therefore it may be too late for anti-invasion or anti-CTC therapies to prevent metastatic seeding. We might be able to harness the immune system to target disseminated clusters and micrometastases to prevent their expansion. The last decade has seen immense progress in cancer immunotherapy through checkpoint blockade therapies, CAR-T cells, and other personalized immunotherapies (Riley et al., 2019). It is plausible that the immune system could be modified to better target cluster-based metastasis, for example by ex vivo engineering of NK cells to more effectively kill clusters (Chan et al., 2020; Daher and Rezvani, 2018; Lo et al., 2020; Shimasaki et al., 2020). But more detailed molecular insights into the activating and immunosuppressive signals generated by tumor cell clusters are needed first to develop these therapeutic approaches.

Another promising strategy may be to focus on the cooperation amongst cells that collectively promotes their metastatic potential, instead of targeting the individual cells themselves. For instance, therapeutics that block critical secreted paracrine molecules, disrupt juxtracrine interactions, or destroy nanolumina and other structures that facilitate intercellular communication may be effective. Resetting these clustered cell states to resemble those of individual cells may be able to mitigate the greatly increased metastatic

efficiency that cells acquire after establishing cell-cell cohesion. Alternatively, the highly interconnected nature of cancer cell collectives may be leveraged to sensitize them to therapy; cells connected by gap junctions, for example, can transmit damage signals from irradiated to non-irradiated cancer cells, increasing the potency of radiotherapy through a bystander effect (Azzam et al., 2003; Brücher and Jamall, 2014).

Disrupting cell-cell communication, or exploiting it to transmit anti-metastatic signals, may bring cells below molecular thresholds needed to acquire a highly proliferative, aggressive phenotype (Korolev et al., 2014). Importantly, as we have outlined above, intercellular cooperativity promotes metastasis throughout the entire metastatic cascade. Therefore multiple anti-collective therapies may be developed and used throughout the invasion, circulation, and colonization phases of metastasis. Still, It remains to be seen whether such strategies could be adapted to destroy collectively metastasizing cancers. But as more critical intercellular interactions are identified in cancer cell collectives, some may turn out to be fruitful clinical targets.

1.6 CONCLUDING SUMMARY

Here I have featured recent findings in the emerging field of collective metastasis regarding the manners in which single cell and cluster-based metastasis diverge. Already these findings suggest several key advantages generated specifically by cell-cell adhesion during metastasis. These emergent properties, dependent on the physical and biochemical coupling of tumor cells, occur throughout the metastatic cascade from beginning to end **(Figure 1.1)**:

(1) **Dispersal from the primary tumor:** The collective migration of strands or nests of tumor cells is widely observed in human tumors, often more frequently than single cell dissemination. These invasive clusters may generate intracluster heterogeneity and leader-follow cell dynamics.

(2) **Vascular circulation:** Clusters may enter and exit the vasculature without needing to squeeze through endothelial junctions via mosaic vessel formation or endothelial remodeling. Circulating tumor cell clusters are less common than single CTCs, but often have higher viability and shorter transit times. Tumor cell clusters maintain higher viability in the circulatory system through anti-anoikis and pro-survival signaling, as well as through the formation of heterotypic aggregates with non-tumor cells which can promote survival, stemness, or proliferation.

(3) **Seeding and surviving in new tissues:** Tumor single cells and clusters are both able to seed distant organs and tissues. However, clusters appear to have increased survival and persistence early phase of metastasis colonization. This may be due to both anti-apoptotic signaling mediated by cell-cell adhesion, and evasion of immune populations such as NK cells.

(4) **Outgrowth into a secondary tumor**: Tumor cell clustering is associated with increased proliferation after metastatic seeding, though dormant clusters can exist in patients. Pro-metastatic outgrowth signaling may be generated in tumor cell clusters through a variety of intercellular signaling mechanisms dependent on cell-cell adhesion such as paracrine, juxtacrine, or nanolumenal signaling.

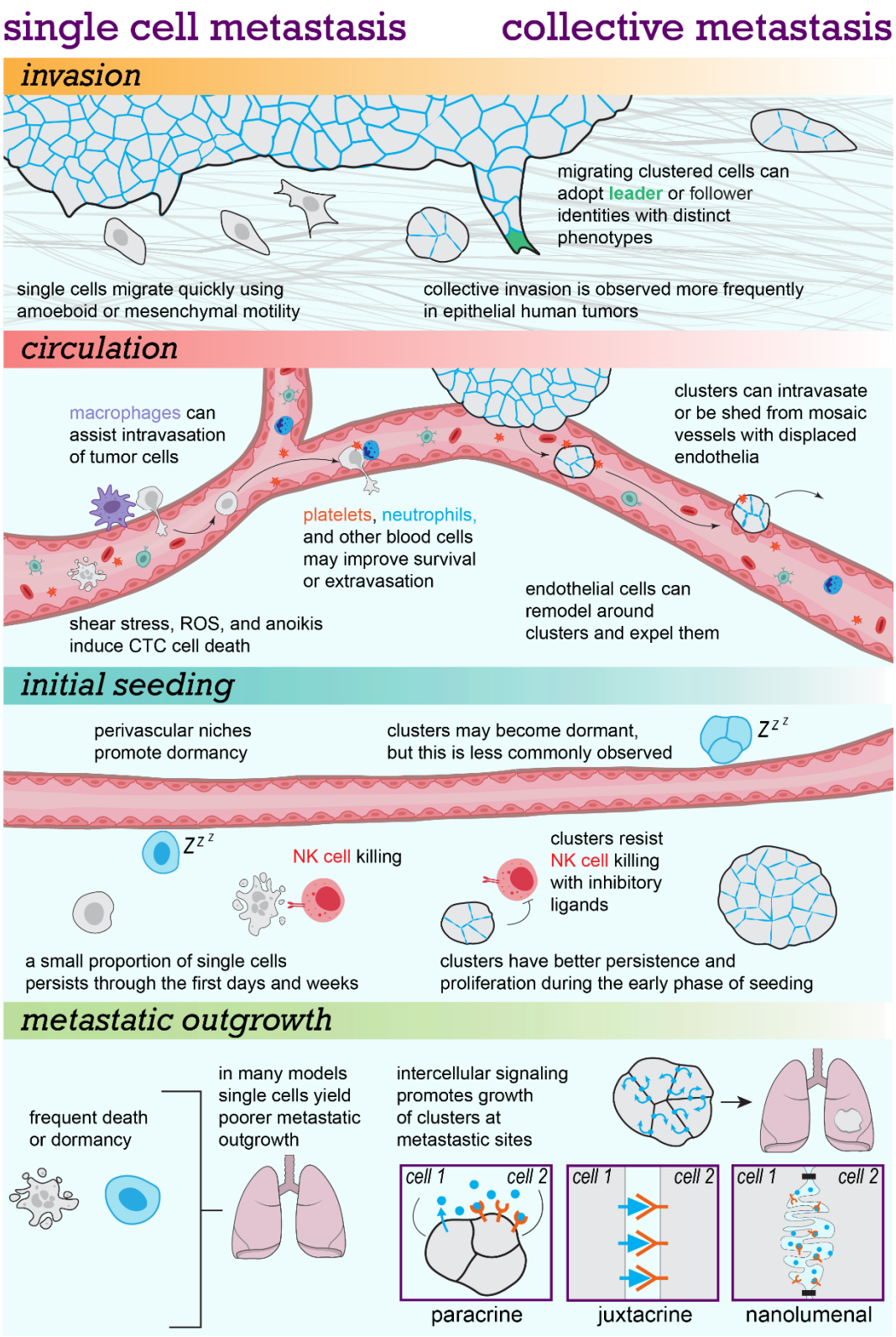

Figure 1.1. Our emerging understanding of cluster-based metastasis suggests key divergences from single-cell based mechanisms throughout the metastatic cascade.

Table 1.1. Summary of experiments comparing the metastatic potential of single and clustered tumor cells.

Citation	Model	Method	Findings
(Watanabe, 1954)	Mouse bronchogenic carcinoma	Jugular injection into mice	92% take rate for clusters, 0% for single cells
(Fidler, 1973)	B16 mouse melanoma	Tail vein injection into mice	~3-fold more lung metastases formed in cluster-injected mice after 2 weeks
(Liotta et al., 1976)	T-241 fibrosarcoma	Tail vein injection into mice	13 to 25-fold more lung metastases formed in cluster-injected mice after 12 days
(Aceto et al., 2014)	MDA-MB-231-LM2 human breast cancer cell line	Orthotopic transplant into mice	~50-fold more lung metastases formed by CTC clusters from tumor transplants relative to single CTCs
	4T1 mouse breast cancer cell line	Orthotopic transplant into mice	~23-fold more lung metastases formed by CTC clusters from tumor transplants relative to single CTCs
(Maddipati and Stanger, 2015)	KCPX mouse model of pancreatic cancer	Intraperitoneal injection into mice	>2-fold more metastases formed in cluster-injected mice after 3 weeks
	KCPX mouse model of pancreatic cancer	Retro-orbital injection into mice	>15-fold more lung metastases formed in cluster-injected mice after 3 weeks
	KCPX mouse model of pancreatic cancer	Multi-color spontaneous mouse tumor model	80% of large metastatic lesions to peritoneum and diaphragm arose from multiple cells
(Cheung et al., 2016)	MMTV-PyMT mouse model of Luminal B breast cancer	Orthotopic transplant into mice	Estimated >97% of lung metastases were derived from clusters (95% CI: 74-100%)
	MMTV-PyMT mouse model of Luminal B breast cancer	Tail vein injection into mice	>100-fold more lung metastases formed by cluster-injected mice after 3 weeks
(Zajac et al., 2018)	Colorectal cancer PDX	Intraperitoneal injection	>20-fold higher tumor burden in cluster-injected mice after 40 days
(Allen et al., 2019)	B16F10 mouse melanoma cell line	Tail vein injection into mice	~2-fold higher BLI signal of cluster-injected mice after 10 days
	A375 human melanoma cell line	Tail vein injection into mice	~3-fold higher BLI signal of cluster-injected mice after 10 days
(Liu et al., 2019c)	Breast cancer PDX	Orthotopic transplant into mice	54% of lung metastases were polyclonal 6-8 weeks after transplant (based on 2-color fluorescence)
	Breast cancer PDX	Tail vein injection into mice	>5-fold higher BLI signal of cluster-injected mice after 8 weeks
(Lo et al., 2020)	4T1 mouse breast cancer cell line	Tail vein injection into mice	~8-fold higher BLI signal of cluster-injected Balb/c mice after 7 days vs. single cells
	AT3 mouse breast cancer cell line	Tail vein injection into mice	~500-fold higher BLI signal of cluster-injected C57BL/6 mice after 25 days vs. single cells
(Wrenn et al., 2020)	MMTV-PyMT mouse model of Luminal B breast cancer	Tail vein injection into mice	141 to 532-fold more lung metastases formed in cluster-injected mice after 3 weeks
(Wrenn et al., 2020)	MMTV-PyMT mouse model of Luminal B breast cancer	Intracardiac injection into mice	7.6-fold more metastases to systemic organs in cluster injected mice after 6 weeks

Table 1.2. Clinical correlation of CTC clusters with poorer patient prognosis.

Citation	Cancer type	# of patients	OS HR (95% CI)	PFS HR (95% CI)	Were clusters an independent prognostic factor?
(Jansson et al., 2016)	Breast[a]	50	7.0 (1.7 - 28.0)	1.8 (0.5-6.5)	Yes
(Wang et al., 2017)	Breast[b]	128	4.69 (1.9 - 11.6)	3.02 (1.7 - 5.3)	Yes
(Larsson et al., 2018)	Breast[b]	156	4.07 (2.0 - 8.3)	2.64 (1.5 -4.8)	Yes
(Paoletti et al., 2019)	Breast[b]	549	15.1 (11.3 - 18.1) vs. 19.9 (17.1 - 21.8) †	-	No
(Costa et al., 2020)	Breast[b]	54	4.46 (1.6 - 12.8)	3.95 (1.8 -8.7)	Yes
(Zheng et al., 2017)	Gastric[b]	86	4.49 (1.7 - 12.0)	2.87 (1.2 - 6.8)	Yes
(Sawabata et al., 2020)	Lung[b]	104	8.92 (2.4 - 32.9)	4.43 (1.1 - 18.1)	Yes
(Hou et al., 2012)	Lung (SCLC)[b]	97	2.94 (1.7 - 5.2)	2.07 (1.2 - 3.5)	Yes
(Long et al., 2016)	Melanoma[b]	128	5.1 (2.0 - 19.0)	-	Yes
(Chang et al., 2016)	PDAC[b]	63	8.18 (2.1 - 32.7) ††	486.66 (12.4 - 12884.9) ††	Yes
(Okegawa et al., 2018)	Prostate[b]	98	4.2 (2.4 - 5.6)	4.4 (2.4 -7.3)	Yes

Summary of recent studies assessing the prognostic significance of circulating tumor cell clusters. OS = overall survival. PFS = progression free survival. HR = hazard ratio. CI = confidence interval. - = not reported. [a] = longitudinal time-dependent analysis of CTC cluster presence. [b] = baseline analysis of CTC cluster presence. † = median survival in months (with 95% CI) of patients with vs. without detected CTC clusters. †† = analysis of patients with unfavorable CTC cluster counts (greater than the mean of all cases: >30 clusters/2 mL blood).

Chapter 2. DEVELOPING ORGANOID SUSPENSION CULTURE TECHNIQUES TO FACILITATE LARGE-SCALE ASSAYS

A version of the following work was published in: Wrenn ED, Moore BM, Greenwood E, McBirney M, Cheung KJ. Optimal, Large-Scale Propagation of Mouse Mammary Tumor Organoids. J Mammary Gland Biol Neoplasia. 2020 Oct 26:1–14. doi: 10.1007/s10911-020-09464-1. Epub ahead of print. PMID: 33106923; PMCID: PMC7587543.

ABSTRACT

Tumor organoids mimic the architecture and heterogeneity of *in vivo* tumors and enable studies of collective interactions between tumor cells as well as with their surrounding microenvironment. Although tumor organoids hold significant promise as cancer models, they are also more costly and labor-intensive to cultivate than traditional 2D cell culture. We sought to identify critical factors regulating organoid growth ex vivo, and to use these observations to develop a more efficient organoid expansion method to facilitate larger-scale experiments. Using time-lapse imaging of mouse mammary tumor organoids in 3D culture, we observed that outgrowth potential varies non-linearly with initial organoid size. Maximal outgrowth occurred in organoids with a starting size between ~10 to 1000 cells. Based on these observations, we developed a suspension culture method that maintains organoids in the size range associated with maximum growth, enabling expansion from 1 million to over 100 million cells in less than 2 weeks and less than 3 hours of hands-on time. This method facilitates the rapid, cost-effective expansion of organoids for CRISPR

and lentiviral-transduction based studies, or other assays requiring a large amount of organoid starting material.

2.1 INTRODUCTION

A wealth of studies have demonstrated that 3D organotypic culture systems can faithfully recapitulate diverse aspects of the tissue architecture, heterogeneity, and spatial complexity of the *in vivo* microenvironment (Lancaster and Knoblich, 2014; Shamir and Ewald, 2014; Simian and Bissell, 2017; Takebe and Wells, 2019; Tuveson and Clevers, 2019). In recent years, organoids have been usefully applied to understanding diverse developmental and disease processes ranging from early embryogenesis (Shahbazi et al., 2016; Xiang et al., 2020) to COVID-19 viral replication in different tissue types (Zhou et al., 2020) to complex genotype-phenotype processes in degenerative brain diseases (Ghatak et al., 2019; Smits et al., 2019).

Organoids have also emerged as important models for cancer (Drost and Clevers, 2018; Liu et al., 2019b; Shamir and Ewald, 2014; Tuveson and Clevers, 2019). Tumor organoids can be isolated from experimental mouse models as well as human patient primary and metastatic tumors, allowing for the representation of a wide range of tumor phenotypes and genotypes. To observe and perturb complex interactions amongst tumor cells, normal cells, and stroma, multicellular tumor organoids are embedded in a variety of 3D matrix platforms (Aisenbrey and Murphy, 2020; Debnath and Brugge, 2005; Debnath et al., 2003; Giandomenico et al., 2019; Lee et al., 2007; Misra et al., 2019; Neal et al., 2018; Nguyen-Ngoc et al., 2015). In this way, investigators have used tumor organoids in 3D culture to uncover essential aspects of tumor formation, metastasis, intercellular tumor-tumor and tumor-microenvironmental interactions, and therapeutic

drug resistance (Cattaneo et al., 2020; Cheung and Ewald, 2016; Cheung et al., 2013; de Witte et al., 2020; Hubert et al., 2016; Padmanaban et al., 2019; Wrenn et al., 2020b).

Though tumor organoids hold significant promise, they also face technical challenges distinct from studies in immortalized cancer cell lines. 2D culture of cell lines enables robust, cost-effective expansion of starting material. This is particularly important for experiments that require a high starting input, such as genome-wide or drug library screening. In contrast, 3D organoid culture typically requires passaging variably sized organoids in a polymerized gel, usually a basement membrane-rich extract such as Matrigel, every 1-2 weeks. The logistical and financial burdens of 3D culture are sometimes under-appreciated, but are important factors affecting the adoption of organoid techniques into mainstream use.

In this study, we characterize the parameters affecting tumor organoid outgrowth. We find that organoid growth is optimal within an intermediate size range. We find that commonly used protocols for passaging by partial enzymatic digestion do not maintain organoids in this ideal range, resulting in suboptimal outgrowth. We identify conditions that allow tumor organoids to expand robustly in suspension, precluding the need for plating or depolymerization of solid Matrigel droplets, and allowing us to expand organoid lines by over 100-fold in less than 2 weeks.

2.2 RESULTS

2.2.1 *Intermediate size organoids expand optimally*

Individual organoids vary in their starting size in 3D culture, but how starting organoid size affects eventual outgrowth potential is not well understood. Here we

performed time-lapse imaging of tumor organoids isolated from the MMTV-PyMT mouse model of aggressive breast cancer, which has invasive and metastatic properties that can be modeled in organoid culture (Cheung et al., 2013; Cheung et al., 2016; Diermeier et al., 2016; Guy et al., 1992; Lin et al., 2003; Padmanaban et al., 2020; Padmanaban et al., 2019). We embedded freshly derived MMTV-PyMT tumor organoids in basement membrane-rich extract (3D Matrigel) and directly observed the growth kinetics of 522 individual organoids **(Figure 2.1A-B)**. For each organoid, we measured the starting and ending areas to obtain an estimate of outgrowth. Importantly, organoid outgrowth varied considerably; some organoids had high growth rates in 3D matrigel, while others grew poorly or even shrank over time. Closer examination revealed that single tumor cells frequently underwent cell death, consistent with prior observations (Cheung et al., 2016; Wrenn et al., 2020b). More surprisingly, very small organoids (< 300 μm^2 area) and very large organoids (>30K μm^2) also showed inferior outgrowth compared with organoids at intermediate sizes (~300-30,000 μm^2) **(Figure 2.1C)**.

To extend this observation, we measured cell proliferation and cell death in individual organoids embedded in 3D matrigel. First, we measured mitotic rate in organoids by staining for nuclear mitosis marker phospho-Histone H3. Consistent with our outgrowth estimates, we observed that intermediate-sized organoids had the highest proportion of cells in mitosis **(Figure 2.1D)**. Next, we treated organoids after 4 days in 3D matrigel with cell-impermeable propidium iodide to assess organoid viability. We observed that very large organoids frequently had extensive non-viable regions within the organoid core **(Figure 2.1E)**. No observed organoids below 10,000 μm^2 had such non-viable core regions.

Taken together, these data indicate that organoid expansion is nonlinear and strongly associated with initial organoid size. Single MMTV-PyMT cells rarely grow in 3D culture, and frequently undergo cell death. Intermediate sized organoids have increased mitotic rates, increased viability, and strong outgrowth in 3D culture. Very large organoids have decreased mitotic rates, increased core cell death, and poorer overall growth rates. To translate starting and final organoid areas from **Figure 2.1B** into approximate starting and ending cell numbers we empirically determined the average organoid cell area, accounted for non-viable cores formation as reported in **Figure 2.1E**, and generated a non-linear regression model (see **Methods** for details). Based on these calculations, we estimate that the starting size of organoids that generates maximal growth is between ~10 cells (95% CI 10.5-12.9) to ~1000 cells (95% CI 1029.3-1268.2) per organoid **(Figure 2.1F)**.

2.2.2 *Suspension culture supplemented with basement membrane-rich extract produces optimal organoid outgrowth*

Organoids are commonly cultivated fully surrounded by a 3D matrix, most often encapsulated within a droplet of basement membrane extract such as Matrigel (Drost et al., 2016; Nguyen-Ngoc et al., 2015; Padmanaban et al., 2019). In these systems, organoids are typically split by gentle enzymatic digestion or by trituration, then re-embedded in fresh 3D matrix. We reasoned that this conventional approach was likely suboptimal because of our finding that intermediately sized organoids have maximal growth potential. Under-digestion during traditional organoid passaging produces overly large organoids with low growth rates and which are prone to form non-viable cores.

Additionally, over-digestion produces many single cells and small (<10 cell) clusters prone to cell death and growth arrest, respectively (**Figure 2.2A:** left panel). Because the optimal level of digestion depends on many factors including organoid size, amount of 3D matrix, and cultivation time, the size of digested organoids is difficult to control and to keep consistent from passage to passage.

We hypothesized that a suspension culture system could more optimally generate organoids in the ideal intermediate size range for optimal outgrowth (**Figure 2.2A**: right panel). In this system, we dissociate organoids to single cells and then reaggregate them in suspension at specific cell densities to form intermediate sized clusters (**Figure 2.1F**, ~10-1000 cells). By digesting completely to single cells, the degree of digestion and the concentration of cells can be controlled from passage to passage, while allowing for reaggregation in suspension to reform clusters. To optimize our suspension protocol, we first determined whether basement membrane matrix was required for outgrowth **(Figure 2.2B)**. The extracellular matrix surrounding tumor cells fulfills two key roles: supplying signaling molecules such as integrin ligands and growth factors, and providing a physical framework that supports and exerts force on cells (Kai et al., 2019). 98% of the protein content of Matrigel is composed of laminin, collagen IV, and entactin (Aisenbrey and Murphy, 2020). To determine whether these components were sufficient to induce organoid growth, we tested outgrowth of MMTV-PyMT organoids in organoid media only; media supplemented with 2% Matrigel, which remains liquid; or media supplemented with recombinant laminin, entactin, and collagen IV. Outgrowth was highest using media + 2% Matrigel compared with all other conditions **(Figure 2.2B)**. These findings indicate that (1) matrix structure provided by polymerized Matrigel is dispensable for robust outgrowth,

(2) there appear to be additional components in Matrigel, beyond laminin/entactin/collagen IV, which are required for organoid expansion, and that (3) a 2% concentration of Matrigel provides the necessary signals for outgrowth while allowing easy sample manipulation as the media remains completely fluid.

Having devised a suspension culture system which could support high organoid outgrowth, we next sought to identify the ideal seeding density that would maximize growth by forming optimally sized aggregates. We tested cell seeding at $0.5x10^5$ to $2.5x10^5$ viable single cells per mL in non-adherent 6 well plates. 150,000 viable cells/mL consistently delivered the highest outgrowth in matched organoid cultures from the same mice **(Figure 2.2C)**. Seeding at 150,000 viable cells/mL also resulted in robust growth of normal mouse mammary organoids as well as organoids from the MMTV-Neu and C3(1)TAg mouse models of breast cancer **(Table 2.1)**. In summary, we find that aggregating tumor organoid cells at 150,000 viable cells/mL in media supplemented with 2% Matrigel generates the optimal rate of outgrowth per passage.

Organoids in either suspension or 100% Matrigel had similar proportions of cells expressing Keratin-14 **(Figure 2.2D)**, confirming that this suspension culture method does not interrupt the formation of K14+ basal cells in tumor organoids. No significant differences in morphology were observed in organoids cultivated in suspension vs. 100% Matrigel **(Figure 2.2E)**, using previously published morphologic criteria for organoids (Jamieson et al., 2017). In both conditions most organoids formed dense, budded structures and no hollow, cystic structures were observed. In our experience MMTV-PyMT organoids predominantly form cysts after long periods of culture without media renewal. Though there are likely to be important differences in organoids cultured in

suspension or in 3D gels, most obviously through changes in mechanotransduction pathways, these findings indicate that other organoid features are preserved.

Finally, we sought to compare the efficiency of our suspension culture method head-to-head with traditional embedded 3D culture methods. MMTV-PyMT organoids were either plated in 100% Matrigel droplets, briefly enzymatically dissociated and then plated in 100% Matrigel droplets, or seeded at 150,000 viable cells/mL in suspension + 2% Matrigel **(Figure 2.2F)**. DIC images were taken of each culture at day 1 and the sizes of tumor organoids, tumor single cells, and suspension aggregates were measured **(Table 2.2)**. Overall, we observed that the vast majority of whole organoids seeded in 100% Matrigel were above the threshold we predict would yield optimal growth. Brief enzymatic dissociation improved the size distribution of organoids embedded in 3D Matrigel, resulting in a higher proportion of cells in optimally sized clusters **(Table 2.2)**. However, many large organoids which had shed outer layers of cells remained >1000 cells in size. We also observed a large number of single cells shed from organoids after brief enzymatic digestion. Over time, some of these single cells merged with adjacent neighbors to form small clusters, however many remained as single cells and failed to undergo substantial growth **(Figure 2.2F)**. When plated using our suspension method at 150,000 viable cells/mL, MMTV-PyMT cells formed many small, optimally sized clusters within 1 day of plating which underwent strong outgrowth over 4 days in culture **(Table 2.2, Figure 2.2F)**.

Using the growth rate prediction model shown in **Figure 2.1F**, we calculated the predicted change in cell number per passage for each of these methods based on organoid area measurements **(Table 2.2)**. Based on these predictions we estimated the

fold-growth per passage by viable cell number to be approximately 4.3-fold, 6.1-fold, and 13.0-fold for whole organoids in 3D Matrigel, partly dissociated organoids in 3D Matrigel, and our suspension culture method, respectively **(Figure 2.2G)**. Next, we assessed the actual fold-growth per passage in each culture method using matched organoids from the same mice. The median fold-growth per passage was 1.3-fold, 4.6-fold, and 13.0-fold (by viable cell number) for the whole embedded, partly dissociated, and suspension culture methods, respectively **(Figure 2.2G)**. Overall, these real-world data fairly closely match our predictions based on the growth parameters identified in **Figure 2.1F** and confirm that our suspension culture method supports more optimal growth than traditional 3D culture techniques.

MMTV-PyMT organoid lines consistently generated strong fold-growth in suspension culture after passaging. Individual growth rates varied between lines generated from different mice **(Table 2.1)**, consistent with heterogeneity of spontaneous tumor initiation and outgrowth of this model in vivo. This variation in growth is an important consideration when planning experiments. We recommend repeating experiments in at least 3 separate organoid lines derived from different mice to increase the likelihood of robust results. Relative differences, for example between non-targeting control and sgRNA transduced organoids, can then be compared between the different organoid lines to take into account differences in intrinsic growth rates.

2.2.3 *This suspension organoid culture method facilitates large scale organoid expansion and efficient lentiviral transduction*

It is relatively simple and inexpensive to expand millions or tens of millions of cells from immortal cancer cell lines in 2D culture. In comparison, when culturing organoids in 3D basement membrane-rich gels it can be tedious and expensive to generate more than a few million viable cells as starting inputs. As a result, commonly used assays that work best with large numbers of cells such as immunoblots, biochemical assays, and medium to high-throughput screens are much more challenging to perform using organoids.

We realized that our suspension culture system had several useful properties that could enable large-scale expansion for such assays. First, our system maintains organoids in suspension. This avoids the requirement to first free organoids from a polymerized gel, making passaging and sample collection far less time-consuming. As a result, organoid culture can be scaled up by increasing the volume of suspension culture and using readily available large-volume cell culture flasks. Second, our system expands organoids more rapidly than fully embedded systems, reducing the time to achieve sufficient outgrowth of cells to generate starting material. Third, our system uses 2% Matrigel, which significantly reduces the cost of basement membrane extract during large-scale experiments.

As a demonstration of the scaling capability of this method, we cultured up to 50 mL of organoids using cell culture flasks coated with 1% agarose to generate a non-adherent surface. Using this suspension + 2% Matrigel culture method in non-adherent cell culture flasks, we expanded 1 million organoid cells to over 100 million cells in 2 weeks **(Figure 2.3A)**. To expand 1 million starting cells to >150 million, the number that has been reported to achieve sufficient coverage for a genome-wide CRISPR screen

(Joung et al., 2017), the estimated cost is much more expensive and much more labor-intensive using traditional 3D culture compared to this suspension culture method **(Table 2.3)**.

To expand such large numbers of cells required at least 2 passages, and we anticipated that this protocol would be most useful if organoids could be repeatedly passaged to maintain laboratory stock cultures. Consequently, we sought to determine whether repeated passaging negatively affected important organoid features and phenotypes. We assessed viability and fold growth of matched MMTV-PyMT organoid lines after 2, 5, or 7 passages in 2% Matrigel suspension culture. No significant changes in either viability or fold growth were observed **(Figure 2.3B)**. The longest we cultivated organoid lines was 10 passages (approximately 30 population doublings); up to passage 10 organoid lines did not reach growth arrest or experience lower fold-growth per passage than earlier passages (n=2).

Next, we assessed cell lineage; breast cancer tumors contain Keratin-14 positive basal cells, generally enriched on the organoid periphery, as well as Keratin-8 positive luminal cells (Cheung et al., 2013). After repeated passaging in suspension, organoids maintained similar levels and distributions of K14 protein expression **(Figure 2.3C)**. Lastly, we assessed genomic stability, as long periods of growth and passaging can also introduce genomic alterations (Liu et al., 2019d). Copy number variations were assessed using low coverage whole genome sequencing, relative to a normal mouse control, in un-passaged and passaged PyMT organoids. We observed fairly modest changes in copy number variations after passaging (chromosome-level $\log_2$ copy # ratio range vs. unpassaged = -0.36 to 0.2, 100kb bin-level $\log_2$ copy # ratio range vs. unpassaged = -

1.16 to 1.48), and no chromosome-level duplications or deletions were identified **(Figure 2.3D-F).** Though it is likely that passaging will alter organoids at least to some degree, these results suggest that certain properties of MMTV-PyMT organoids such as growth rate, viability, genotypic stability, and basal/luminal lineage specification remain fairly consistent throughout repeated passaging in suspension.

Having generated a protocol to rapidly expand very large numbers of organoids, we next sought to test the utility of this protocol for lentiviral transduction, a useful technique which is challenging in traditional 3D culture (Maru et al., 2016). We previously developed magnetic particle transduction methods for organoids as a means to enhance transduction efficiency in limited organoid samples (Cheung et al., 2013; Padmanaban et al., 2020). However, an optimal organoid expansion protocol enables a more cost-efficient transduction method for large numbers of organoids. Lentiviral particles were generated in HEK 293FT cells and concentrated to 1/100th the starting lentiviral supernatant volume. To maximize cell-virus contact, MMTV-PyMT organoids were first dissociated to single cells before plating in suspension + 2% Matrigel. Protamine sulfate was then added to the media, a polycation which greatly increases lentiviral transduction efficiency (Balak et al., 2019; Cornetta and Anderson, 1989). Using this method, we were able to generate a highly EGFP expressing MMTV-PyMT organoid line **(Figure 2.3G)**.

Next, we sought to confirm that CRISPR-Cas9 could be used in this system for effective gene targeting. The MMTV-PyMT-EGFP organoids were transduced again, using the same protocol, with either non-targeting or EGFP targeting sgRNAs. Organoids were maintained in media + 2% matrigel with puromycin for 10 days to select for transduced cells and permit enough time for maximal Cas9 activity (Shalem et al., 2014).

After selection, we observed strong EGFP signal reduction only in the sgEGFP transduced condition **(Figure 2.3G)**. This experiment provides a proof-of-concept that MMTV-PyMT organoids in long-term suspension culture can be used to generate stable knockout, knockdown, or overexpression cultures through lentiviral transduction (Dominguez et al., 2016; Joung et al., 2017).

Lastly, we sought to confirm that organoids cultivated, passaged, transduced, and selected in 2% suspension culture retained the ability to form primary tumors and metastases *in vivo*. MMTV-PyMT organoids were generated, passaged in 2% Matrigel suspension, and transduced with a GFP-encoding lentiviral construct. Cells were selected in puromycin for at least 5 days. Selected organoids were then dissociated to single cells and allowed to reaggregate overnight in 2% Matrigel suspension to form small clusters. The following day, reaggregated clusters were orthotopically transplanted into the mammary fat pads of immunocompromised NSG mice which were collected 6 weeks later when they had formed large tumors. We observed 100% take rates (n=10/10 mice) and imaging of tumor sections confirmed high retention of GFP fluorescence **(Figure 2.3H)**.

As a second approach, reaggregated clusters were injected by tail vein into immunocompromised NSG mice, and lungs were collected 3 weeks later. Likewise, we observed 100% take rates (n=8/8 mice) and numerous lung metastases that were GFP+ by stereomicroscopy **(Figure 2.3I)**. We conclude that our propagation method can be used to prepare and transduce large numbers of organoids prior to in vivo experiments, facilitating validation and phenotypic analysis of sgRNA, shRNA, or overexpression organoid lines in pre-clinical models. Together, these methods form an efficient pipeline for large-scale cultivation, ex vivo manipulation, and in vivo analysis of tumor organoids.

2.3 DISCUSSION

Here, we describe a protocol for the rapid cultivation of large numbers of mouse mammary tumor organoids. We show that organoid size is partially predictive of organoid outgrowth, and that maximal outgrowth occurs at an intermediate size corresponding to between ~10 to 1000 cells per organoid. As a result, passaging organoids via partial digestion to generate fragments yields suboptimal outgrowth. To overcome this challenge, we developed a suspension culture protocol in which organoids are fully dissociated to single cells, and then subsequently aggregated to form organoids in the ideal intermediate size range. This protocol enables larger-scale and rapid outgrowth of mouse mammary tumor organoids for a variety of assays requiring large cell numbers. Although not directly tested here, it is plausible that the size vs. outgrowth relationships described here may occur in normal organoids or organoids from other mouse models of cancer. We recommend that researchers interested in testing this culture system in their preferred organoid model similarly compare fold growth, viability, cellular heterogeneity, and genomic stability in traditional 3D culture vs. 2% Matrigel suspension using the techniques we have applied to MMTV-PyMT tumor organoids.

This culture system offers a number of practical advantages over traditional embedded 3D culture, greatly reducing financial cost and hands-on time for large-scale experiments. It also diverges from other breast cancer suspension culture techniques in several important ways. Mammosphere or tumorsphere assays have also been used to cultivate breast cancer cells in suspension. In these assays, cells are plated as single cells and often prevented from re-aggregating, for example by addition of methylcellulose to the media (Lee et al., 2016; Sheridan et al., 2015). Multiple growth factors are typically

needed to coax the clonal outgrowth of spheres of cells. While these conditions are ideal to test the presence of rare cancer stem cell or progenitor cells, our data suggest that this approach can also result in high dropout of individual clones in models which have poor survival or growth as single cells, such as MMTV-PyMT. In contrast, our method encourages aggregation of single cells to induce the optimal level of multicellularity supporting organoid survival and outgrowth.

Nonetheless, it is important to acknowledge several limitations to this method. Firstly, the cultivation of tumor organoids in suspension is non-organotypic. Tumor cells do not typically exist in fluid-based environments *in vivo*, apart from tumor cells in the circulation or in bodily fluids like pleural effusions and malignant ascites. Suspension culture lacks the rigid physical structure of fully embedded systems, which could modulate mechanotransduction and other signaling pathways which have been shown to be relevant during tumor progression and metastasis (Fattet et al., 2020; Martino et al., 2018). We therefore suggest using this method primarily for organoid expansion and hypothesis generation. For further validation and organoid analyses, we recommend transferring organoids into fully embedded 3D matrices and animal models to better recapitulate the tumor microenvironment. Secondly, the introduction of additional mutations over time can cause confounding effects on experiments, particularly those assessing the phenotype of shRNAs or sgRNAs. MMTV-PyMT has relatively high genomic stability (Rennhack et al., 2019), making organoids from this model ideal for large-scale, long-term propagation. We encourage regular genetic analysis when applying this long-term cultivation method to other organoid models with higher genomic instability. Thirdly, this method is applicable at this time only to organoids isolated from

mice. It is well known that human organoids grow significantly slower than mouse organoids. We do not resolve that problem here but suggest this to be an essential direction of future research.

In this study, we show that the size of tumor cell communities can have non-linear effects on proliferation and cell death. Collective cellular organization is known to promote invasive and metastatic potential in diverse tumor types (Aceto et al., 2014; Cheung and Ewald, 2016; Cheung et al., 2016; Friedl and Gilmour, 2009; Gkountela et al., 2019; Haeger et al., 2020; Labuschagne et al., 2019; Liu et al., 2019c; Padmanaban et al., 2019; Wrenn et al., 2020b). An interesting question is whether the growth kinetics observed here as a function of organoid size in 3D culture might also have relevance for the outgrowth of microscopic and macroscopic metastases *in vivo,* which are known to display different properties at different size regimes (Cheung et al., 2016; Davis et al., 2020; Lawson et al., 2015; Savage et al., 2017). Thus, our study advocates for further systematic analyses of the factors supporting collective organization, signaling, and outgrowth in tumor cells.

2.4 ACKNOWLEDGMENTS

We thank Patrick Paddison for providing sgRNA reagents and lentiviral packaging plasmids. We thank Andrew Ewald and Sasha Stanton for providing mouse tumors. We thank David MacPherson and Nan Wu for CNV sample preparation and analysis. This work was supported by grants from the Department of Defense W81XWH-18-1-0098, NIH R37CA234488, the Burroughs Wellcome Fund Career Award for Medical Scientists 1013355.01, the Phi Beta Psi Sorority, the Breast Cancer Research Foundation BCRF-

18-035, the V Foundation V2017-014, Seattle Translational Tumor Research, and the Fred Hutch/University of Washington Cancer Consortium (P30 CA015704). This research was also supported by Fred Hutch Comparative Medicine Shared Resources. The authors declare no competing interests.

AUTHOR CONTRIBUTIONS

EDW and KJC drafted the manuscript. KJC supervised the project and secured funding. EDW, BMM, EG, and MM designed and conducted experiments.

2.5 FIGURES

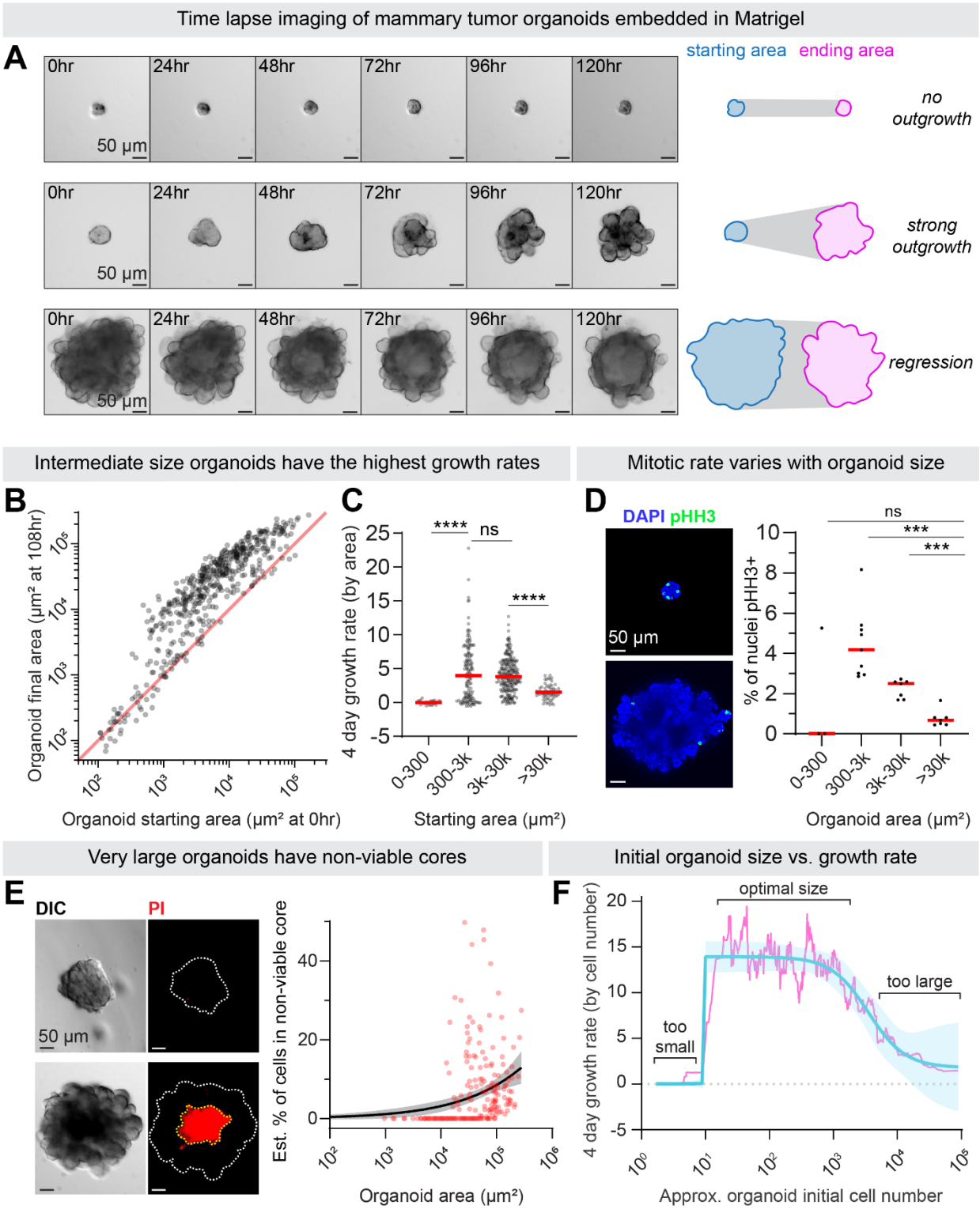
Time lapse imaging of mammary tumor organoids embedded in Matrigel
A
0hr
24hr
48hr
72hr
96hr
120hr
50 µm
starting area
ending area
no outgrowth
strong outgrowth
regression
Intermediate size organoids have the highest growth rates
B
Organoid final area (µm² at 108hr)
Organoid starting area (µm² at 0hr)
C
4 day growth rate (by area)
****
ns
****
0-300
300-3k
3k-30k
>30k
Starting area (µm²)
Mitotic rate varies with organoid size
D
DAPI pHH3
50 µm
% of nuclei pHH3+
ns
***
***
Organoid area (µm²)
Very large organoids have non-viable cores
E
DIC
PI
50 µm
Est. % of cells in non-viable core
Organoid area (µm²)
Initial organoid size vs. growth rate
F
optimal size
too large
too small
4 day growth rate (by cell number)
Approx. organoid initial cell number

Figure 2.1. Maximal organoid growth occurs within a size threshold which promotes proliferation and minimizes cell death.

(A) Time lapse imaging of MMTV-PyMT organoids in 3D Matrigel. Right, summary of growth as change in area. See also **Video 2.1**. **(B)** Organoid initial area and final area (after 4 days of time lapse imaging in 3D Matrigel) were measured to estimate growth over time. n=522 organoids from 8 mice**.** Red line = fold change of 1 (no growth). **(C)** Organoid area growth rate ([final area-initial area]/initial area) from 4 days of time-lapse imaging in 3D Matrigel binned by initial organoid area. n=8 mice, 522 organoids. P-values = unpaired t-tests. **(D)** Mitotic rate assessed by phospho-Histone H3 immunofluorescence in organoids of varying sizes in 3D Matrigel. Each dot is one mouse, n=349 organoids. Red line = median. P-values = unpaired t-tests. **(E)** Propidium iodide staining of non-viable cells in organoids of varying sizes in 3D Matrigel. The PI+ core area was measured and converted to a volume to estimate the % of cells in the non-viable core region, relative to the total organoid volume. Each dot is an organoid (n=267 organoids, n=2 mice). Line = non-linear regression. Band = 95% CI of non-linear regression. **(F)** Organoid cell number growth rate was calculated from 4 days of time lapse imaging in Matrigel ([final volume-initial volume]/initial volume). Based on the non-linear regression calculated in E, growth rates were corrected to account for organoid core death (detailed equations in Methods section). Blue line = non-linear regressions. Pink line = rolling average. Band = 95% CIs of regressions. n=522 organoids from 8 mice.

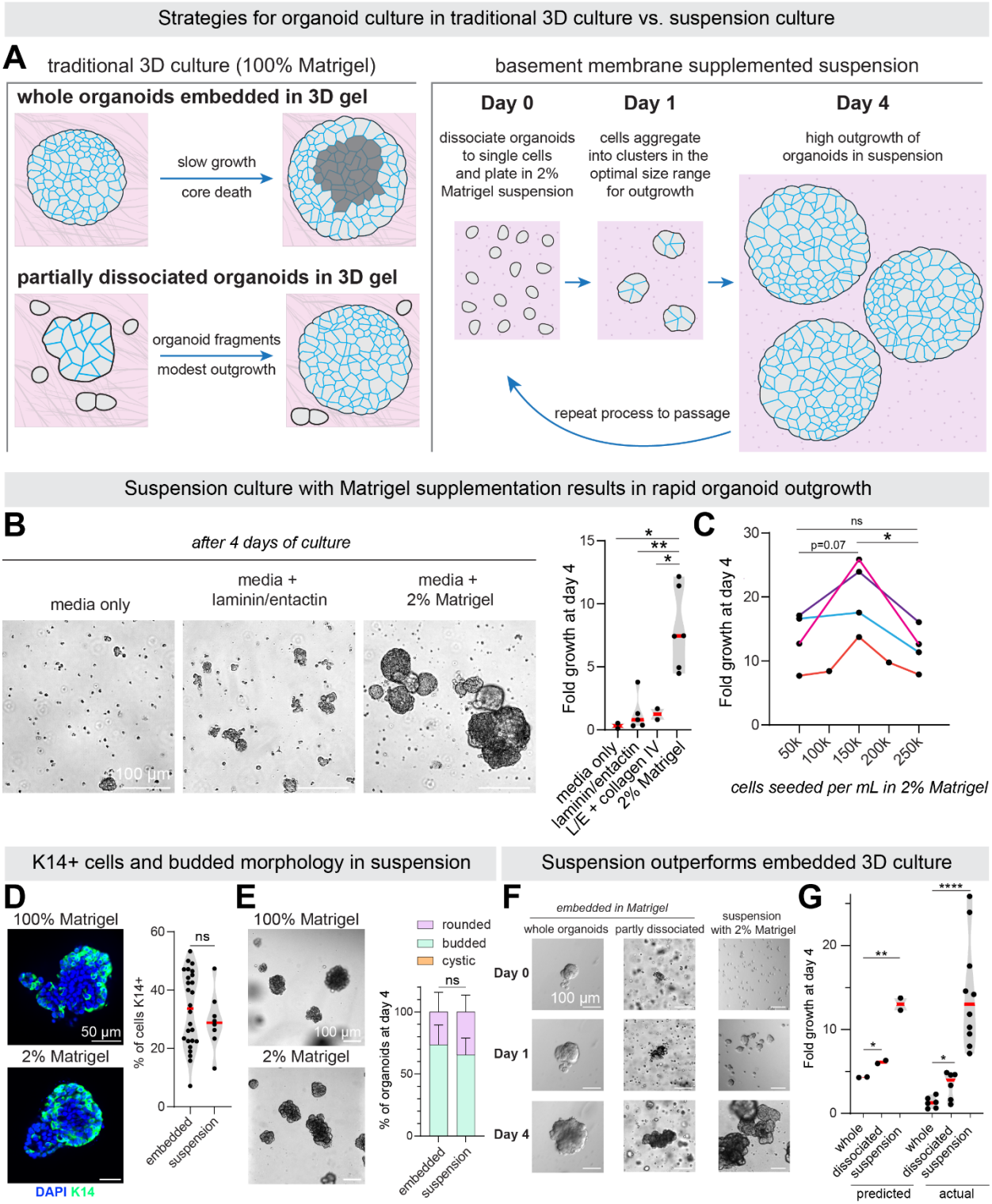
Strategies for organoid culture in traditional 3D culture vs. suspension culture
A
traditional 3D culture (100% Matrigel)
whole organoids embedded in 3D gel
slow growth
core death
partially dissociated organoids in 3D gel
organoid fragments
modest outgrowth
basement membrane supplemented suspension
Day 0
dissociate organoids to single cells and plate in 2% Matrigel suspension
Day 1
cells aggregate into clusters in the optimal size range for outgrowth
Day 4
high outgrowth of organoids in suspension
repeat process to passage
Suspension culture with Matrigel supplementation results in rapid organoid outgrowth
B
after 4 days of culture
media only
media + laminin/entactin
media + 2% Matrigel
100 µm
Fold growth at day 4
media only
laminin/entactin
L/E + collagen IV
2% Matrigel
C
p=0.07
ns
Fold growth at day 4
50k
100k
150k
200k
250k
cells seeded per mL in 2% Matrigel
K14+ cells and budded morphology in suspension
Suspension outperforms embedded 3D culture
D
100% Matrigel
50 µm
2% Matrigel
DAPI K14
% of cells K14+
embedded
suspension
E
100% Matrigel
100 µm
2% Matrigel
rounded
budded
cystic
% of organoids at day 4
F
embedded in Matrigel
whole organoids
partly dissociated
suspension with 2% Matrigel
Day 0
Day 1
Day 4
100 µm
G
Fold growth at day 4
whole
dissociated
suspension
predicted
actual

Figure 2.2 Suspension culture supplemented with basement membrane-rich extract facilitates rapid expansion of tumor organoids.

(A) Schematic of organoid culture methods. Traditionally, organoids are either plated intact in 3D gels or briefly mechanically or enzymatically disrupted to generate organoid fragments, as well as debris and single cells, before plating in 3D culture. Right, we present an alternative culture method where single tumor cells are aggregated in non-adherent suspension supplemented with basement membrane-rich extract to form multicellular aggregates optimally sized for rapid outgrowth. **(B)** DIC images (left) and fold growth by viable cell number (right), of MMTV-PyMT organoids after 4 days in organoid media only, media supplemented with 2% Matrigel, media + 100 μg/mL laminin/entactin, or media + 70 μg/mL laminin/entactin + 30 μg/mL collagen IV. Each dot is a biological replicate. P-values = unpaired t-tests. **(C)** To determine the optimal density to seed MMTV-PyMT single cells for aggregation in 2% Matrigel suspension culture, cells were plated at $0.5x10^5$ to $2.5x10^5$ viable cells/mL to form small clusters. After 4 days, fold-growth by viable cell number was measured. n = 4 mice, each line is a biological replicate. P-values = paired t-tests. **(D)** Left, Keratin-14 immunofluorescence images of MMTV-PyMT organoids cultured embedded in 100% Matrigel vs. cultured in suspension supplemented with 2% Matrigel. Right, quantification of the % of cells K14+ (basal). n=2 mice (suspension), n=3 mice (embedded), n=4161 cells analyzed. P-value = unpaired t-test. **(E)** Images of organoids after 4 days in culture embedded in 100% Matrigel or seeded in suspension culture supplemented with 2% Matrigel. Right, summary of organoid morphology at D4. “Rounded” refers to organoids

with smooth spherical borders, vs. “budded” organoids with multicellular budded protrusions. No organoids scored had hollow, cystic morphology in either condition. n=3 mice, n= 285 organoids in suspension, 259 organoids embedded in 100% Matrigel. P-value = unpaired t-test. **(F)** DIC images of MMTV-PyMT organoids 0 days, 1 day, and 4 days after initial plating in the methods described in (A). Whole organoids or briefly dissociated (5’ Accumax treated) organoids were plated in 3D matrigel, or single cells were allowed to aggregated at 150,000 viable cells/mL in organoid media + 2% Matrigel. **(G)** From the area measurements of **Figure 2.2F** (see **Table 2.2**) and the growth parameters identified in **Figure 2.1F**, estimated fold growth for each culture method was predicted (see Methods section for piecewise function). Then actual fold growth of MMTV-PyMT organoids by viable cell number after 4 days in each of the 3 culture methods was measured. Each dot is a mouse. P-values = unpaired t-tests.

Growth and survival during long-term culture in suspension with 2% Matrigel

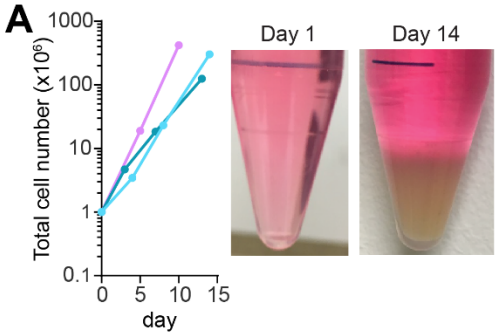

B

Passage #	% viability (95% CI)	Fold growth (95% CI)
2	93.8% (91.1%-96.5%)	12.4 (6.3-18.5)
5	90.5% (81.7%-99.2%)	11.6 (2.3-21.0)
7	91.1% (82.6%-99.5%)	9.8 (3.5-16.0)

Cell lineage

Copy number variations of passaged vs. unpassaged organoids

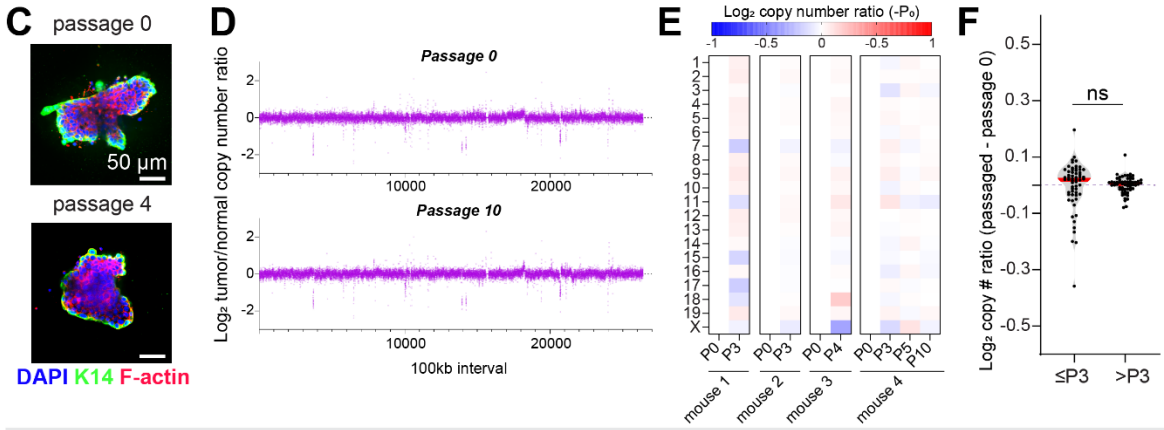

Efficient lentiviral transduction in Matrigel supplemented suspension culture

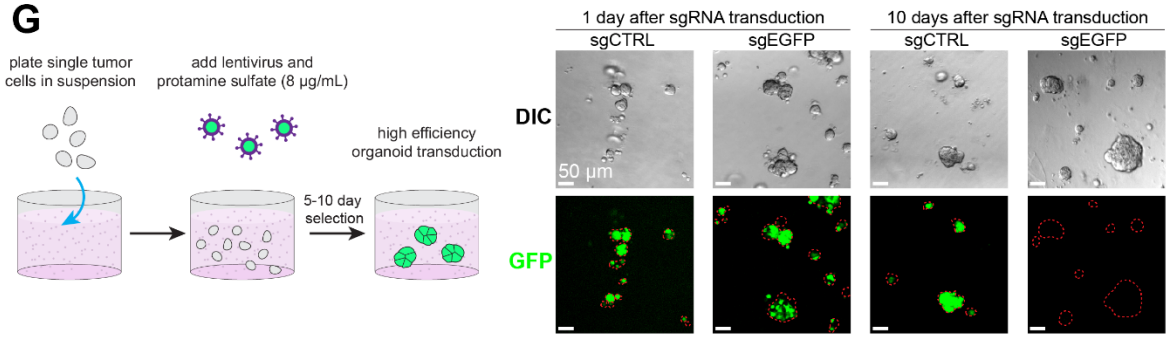

Suspended cultured and transduced organoids form primary tumors and metastases in vivo

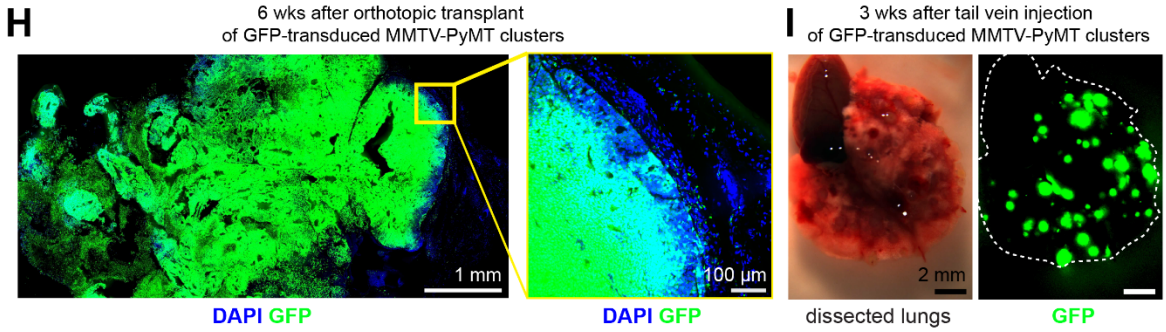

Figure 2.3 Suspension culture supplemented with basement membrane-rich extract facilitates stable long-term culture and efficient lentiviral transduction.

(A) Using the 2% Matrigel suspension culture method, a starting input of 1 million tumor organoid cells (n=3 mice, each line is a biological replicate, each dot is a passage) were expanded and passaged for 2 weeks. Right, image of >300 million MMTV-PyMT cells expanded from 1 million initial cells after 2 weeks. **(B)** Percent viability and fold growth by viable cell number of MMTV-PyMT cells at passage number 2, 5, or 7 in 2% Matrigel suspension culture. n = 4 mice. No significant differences were detected between passages for growth or viability (unpaired t-tests, $p>0.05$). **(C)** Immunofluorescence for basal cell marker Keratin-14 in MMTV-PyMT organoids freshly isolated from primary tumors (passage 0) or after 4 passages in 2% Matrigel suspension culture. Representative images from n=2 mice. **(D)** Log_2 tumor/normal copy number variations from low coverage whole genome sequencing (plotted as 100 kilobase bins) of MMTV-PyMT organoids from the same mouse shortly after isolation (passage 0) or after 10 passages in 2% Matrigel suspension culture. **(E)** Heatmap of passaged log_2 copy number ratios (tumor/normal) minus passage 0 log_2 copy number ratios (mean per chromosome). **(F)** Passaged log_2 copy number ratios (tumor/normal) minus passage 0 log_2 copy number ratios (mean per chromosome). Each dot is a chromosome, n=4 mice, n= 6 passages. Red line = median. **(G)** Left, schematic of lentiviral transduction of organoids in suspension. MMTV-PyMT tumor organoids were lentivirally transduced with PGK-EGFP at MOI ~10 in suspension. Then tumor organoids were lentivirally transduced with non-targeting (sgCTRL) or EGFP targeting (sgEGFP) lentiCRISPRv2 constructs. Right, DIC

and GFP images after 10 days of puromycin selection showing effective EGFP knockout. **(H)** MMTV-PyMT organoids were cultured in suspension + 2% Matrigel and transduced with a GFP encoding lentivirus as in (G). After puromycin selection, PyMT-GFP clusters were orthotopically transplanted into the mammary fat pads of NSG mice. Tumors were collected 6 weeks later. n=10 mice, n=20 tumors. **(I)** MMTV-PyMT organoids were cultured in suspension + 2% Matrigel and transduced with GFP encoding lentivirus as in G. After puromycin selection, PyMT-GFP clusters were injected by tail vein into NSG mice. 3 weeks later lungs were harvested to assess metastatic outgrowth via stereomicroscopy. n=8 mice.

2.6 TABLES AND SUPPLEMENTAL ITEMS

Table 2.1. Fold growth of different normal and tumor mouse mammary organoids.

Fold growth by viable cell number of organoids from normal FVB mouse mammary glands (n=6) or from the C3(1)TAg (n=3), MMTV-Neu (n=2), or MMTV-PyMT (n=10) mouse models of breast cancer. Cells seeded at 150,000 viable cells/mL in suspension with 2% Matrigel on day 0.

Mouse model	Median fold growth per passage	95% CI of median fold growth
Normal FVB mammary gland	7.2	4.6 - 14.8
C3(1)TAg tumor	6.1	6.1 - 8.0
MMTV-Neu tumor	9.2	7.4 - 11.0
MMTV-PyMT tumor	13.0	8.0 - 24.0

Table 2.2. Proportion of cells and organoids in different initial size bins one day after plating in each culture method.

Day 1 organoid area measurements were taken from organoids cultured using the 3 methods outlined in **Figure 2.2A**, then converted into approximate cell number as in **Figure 2.1F**. n=2 biological replicates, n (# of area measurements) = 120 whole embedded, 423 partly dissociated then embedded, 487 suspension culture. Units (single cells, small clusters, or large clusters) were then binned into sub-optimal (<10 or >1000 cell) and optimal (100 to 1000 cell) sizes. The percentage by cell number (calculated from predicted organoid volume) and by number of measured units (cells or clusters) in each bin are presented.

	% of organoids in size range (mean ± SD)			% of cells in size range (mean ±SD)		
	Whole organoids	Partly dissociated	Suspension (150k/mL)	Whole organoids	Partly dissociated	Suspension (150k/mL)
<10 cells	7.0 ± 4.4	58.3 ± 9.3	70.6 ± 12.4	0.0026 ± 0.0023	0.308 ± 0.013	13.26 ± 7.77
10-1000 cells	34.3 ± 1.4	33.5 ± 11.7	29.4 ± 12.4	1.13 ± 0.068	9.14 ± 4.59	86.74 ± 7.77
>1000 cells	58.7 ± 3.0	8.20 ± 2.43	0 ± 0	98.7 ± 0.07	90.55 ± 4.60	0 ± 0

Table 2.3. Estimated cost to expand 1 million MMTV-PyMT cells to >150 million cells as organoids.

Approximate cost (as of June 2020) of expanding 1 million cells to 167 million cells (i.e. the number of cells needed for a genome-wide CRISPR screen) either by plating in 100 µL Matrigel droplets in 24 well plates and lightly dissociating organoids after removal from gel to passage (traditional method) or by plating in suspension supplemented with 2% Matrigel and passaging to 150,000 viable cells/mL.

	Traditional 3D culture (embedded in 100% Matrigel)				*Suspension with 2% Matrigel culture*		
	Item	**Quantity**	**Cost**		**Item**	**Quantity**	**Cost**
	24 well plate	19 plates	$57.93		6 well plate, non-adherent	1 plate	$15.04
	GFR Matrigel	42.24 mL	$1314.17		T175 flask, agarose coated	1 flask	$10.95
	Organoid media	422 mL	$257.86		Organoid media + 2% Matrigel	84 mL	$103.04
Total cost			**$1,629.96**				**$129.03**
Hours of labor			**≥ 12 hrs**				**≤ 3 hrs**
# of days to reach target			**16**				**8**

Video 2.1. Growth dynamics of mammary tumor organoids embedded in 3D Matrigel.

Left, hourly DIC time lapse images of 3 organoids of different sizes (from **Figure 2.1A**) cultured embedded in 100% Matrigel. Right, summary of growth rate ([current area-initial area]/initial area) measured every 10 hours.

2.7 METHODS

Mouse mammary tumor organoid culture

Animal protocols were approved by the Fred Hutchinson Institutional Animal Care and Use Committee. FVB/N-Tg(MMTV-PyVT)634Mul/J (MMTV-PyMT) were maintained and tumor growth was monitored every 2 days. Adult female mice were used for all experiments. In this study, we isolated intact epithelial fragments from tumors to generate freshly derived tumor tissue organoids (Padmanaban et al., 2020). A variety of growth factors and ligands can be used in this culture setting to promote growth, but a simple media composed of DMEM/F12, ITS-X, and 2.5 nM FGF is frequently used to maintain both normal mammary and tumor organoids (Cheung et al., 2013; Nguyen-Ngoc et al., 2015; Padmanaban et al., 2020; Wrenn et al., 2020b). However other supplements can be included to promote growth or alter the cellular composition of organoids (Jardé et al., 2016), particularly when culturing human tumor organoids which often grow poorly ex vivo (Rosenbluth et al., 2020; Sachs et al., 2018).

Organoids were isolated from MMTV-PyMT, C3(1)TAg, or MMTV-Neu mouse mammary tumors as previously described (Nguyen-Ngoc et al., 2015). Mammary tumors were dissected, mechanically disrupted with a scalpel, and then digested in a collagenase-trypsin solution for 30-60 minutes shaking at an angle at 100-150 rpm at 37^{o}C. The digestion solution (in 20 mL of DMEM/F12) contained 2 mg/mL collagenase (Sigma C2139), 2mg/mL trypsin (Gibco 27250–018), 5% fetal bovine serum, 5 µg/mL human insulin (Sigma-Aldrich I9278), 50 µg/mL gentamicin (Gibco 15750-060). Tumor fragments were centrifuged for 10 minutes at 1500 rpm, resuspended in 4 mL DMEM/F12 and treated with 40 µL (2000 U/mL) of DNAse (Sigma D4263) for 3 minutes then pelleted

and resuspended in 10mL DMEM/F12. The solution was centrifuged for 4 seconds at 1500 rpm (453g) to isolate multicellular organoids, then resuspended in 10 mL DMEM/F12. This was repeated for a total of 4 washes to remove contaminating single cells and debris, leaving behind primarily multicellular epithelial organoids (Nguyen-Ngoc et al., 2015; Padmanaban et al., 2020). Mice were harvested as the largest tumor neared 1.5 cm in diameter.

For 3D culture, 100-200 clusters were embedded in 100 µL of growth-factor reduced Matrigel (Corning 354230), the Matrigel was allowed to polymerize for 30-60 minutes at 37ºC, then 1 mL of organoid media (DMEM-F12, 2.5 nM FGF2, insulin-transferrin selenium, & penicillin/streptomycin) was added. For recombinant ECM media supplementation, laminin/entactin (Corning 354259) and collagen IV (Corning 354233) were used. For suspension culture, clusters were cultured in non-adherent 6 well plates (Fisher Scientific 07-200-601) in 2-4 mL organoid media + 2% (v/v) Corning Growth Factor Reduced Matrigel. Tips and tubes used to handle organoids were first coated in 2.5% bovine serum albumin (Sigma-Aldrich A9576) in DPBS to prevent loss of material. To passage cells in 2% Matrigel suspension, organoids were pelleted and resuspended in Accumax (Innovative Cell Technologies, AM105) for 20 minutes in a 37ºC water bath, pipetted every 10 minutes with a BSA coated pipette to generate a single cell suspension. Cells were counted with Trypan blue on a hemocytometer to ensure high viability and a low number of residual clusters. Cells were pelleted and resuspended in warm OGM + 2% Matrigel at 150,000 viable cells/mL and plated in non-adherent plates or flasks. Matrigel was added to the media at 4ºC, mixed thoroughly, then warmed at 37ºC for at least 10 minutes before organoid resuspension.

For large-scale suspension culture, T175 flasks were coated in 1% agarose (dissolved in boiling Milli-Q filtered water and then cooled to ~50^{o}C before pouring along bottom of flask until ~3mm thick) to prevent cell adhesion. MMTV-PyMT cells were plated at 150,000 viable cells/mL in 75 mL OGM+2% Matrigel in T-175 flasks coated with 1% agarose, passaged every 4-6 days back to 150,000 viable cells/mL at the desired volume.

Fresh organoid preparations were typically >70% viable. Organoids passaged in 2% Matrigel supplemented suspension maintained higher viability **(~80-95%, Figure 2.2).** Taking into account single cells that fail to aggregate and small clusters, both of which are more likely to apoptose, we estimate a drop-out rate of <10% after initial passage in suspension culture **(Table 2.2).**

Immunofluorescence and non-viable cell labeling

Organoids were fixed with 4% paraformaldehyde in DPBS (10 min), permeabilized 30 minutes with 0.5% Triton-X, and blocked 1 hr at room temperature with 10% FBS/1% BSA/0.1% Triton-X in DPBS. Primary antibodies were added in block solution and incubated at 4^{o}C overnight. Alexa Fluor conjugated secondary antibodies (1:200) were incubated for 2-3 hrs at room temperature with 5% host serum. Confocal images were acquired using an Andor CSU-W confocal spinning disk on a Leica DMi8 inverted microscope. Antibodies used: phospho-Histone H3 Ser10 (CST 9701), Keratin-14 (BioLegend 905301), and Keratin-8 (DHSB TROMA-I). For live imaging of non-viable cells, propidium iodide (Thermo Scientific P1304MP) was added at 1 µg/mL to the organoid media. At least 15 minutes later, DsRed and DIC images were acquired. To assess K14-/K14+ cell populations in suspension culture vs. embedded 100% Matrigel culture, organoids cultured in 2% Matrigel suspension for at least 48 hours were

embedded in 100% Matrigel and fixed immediately for immunofluorescence. K14 scoring was blinded, DAPI+ cells with at least 50% membrane positivity were scored as K14 positive.

Time-lapse imaging of organoids

Single or clustered cells were plated in growth factor reduced basement membrane-rich gels. Differential interference contrast (DIC) images were captured hourly using a Leica SPE at 10X magnification. Exposure times were <30ms for BF/DIC. Temperature was maintained at 37^{o}C and CO_2 at 5%. Images were acquired using a Leica DMi8 TCS SPE. To assess organoid growth, the μm^2 area of organoids was assessed at 0 hrs and 108 hrs of time lapse imaging in FIJI software.

Lentivirus production and transduction

Lentivirus was produced in HEK293FT cells using PsPax and MD2.G packaging plasmids. Supernatants were concentrated using Lenti-X (Takara 631232), resuspended in 1/100th the supernatant volume of PBS, and frozen at -80^{o}C. Viruses were titered using a ZeptoMetrix p24 ELISA (Fisher Scientific 22-156-700). Tumor organoids were dissociated to single cells in Accumax and resuspended at 150,000 viable cells/mL in organoid media + 2% (v/v) Matrigel. Protamine sulfate (Fisher ICN15197105) was added at 8 µg/mL to enhance transduction efficiency before adding concentrated lentivirus. For plasmids with PuroR, 2 days after transduction puromycin was included in the media at 1-2 µg/mL for selection. CRISPR sgRNA transduced cells were kept in puromycin for 10 days before assessing sgRNA efficacy.

Low-coverage whole genome sequencing

MMTV-PyMT organoids were flash frozen in liquid nitrogen at specific passage numbers (unpassaged organoids = passage 0). MMTV-PyMT tumor organoid genomic DNA was collected using the QIAGEN DNEasy Blood & Tissue Kit (69504), following manufacturer's instructions. For whole genome analysis of CNV variation, low-coverage whole-genome sequencing of organoid genomic DNA was performed. The NEBNext DNA Library Prep Master Mix Set for Illumina (New England BioLabs; catalog E6040L) was used to generate DNA libraries from 1,000 ng genomic DNA. Single-read data (50 bp) were generated using an Illumina HiSeq 2500. Reads were aligned to the mm9 build of the murine genome using the Burrows Wheeler Aligner (Li and Durbin, 2010), and we used CNVseq (Xie and Tammi, 2009) to examine copy numbers.

Orthotopic transplantation of PyMT-GFP clusters

MMTV-PyMT-mTomato organoids were transduced with a GFP encoding lentivirus (Transomic NT4) and selected with 1μg/mL puromycin for at least 5 days. Organoids were then dissociated to single cells using Accumax, and reaggregated overnight at 250,000 viable cells/mL in organoid media + 2% Matrigel (using non-adherent 6 well plates). Clusters were then resuspended in 50% basement Matrigel in DMEM/F12 (vol/vol) on ice for mammary fat pad injection. 9-10 week old Nod scid gamma (NSG) immunocompromised mice were anesthetized with 2.5% isoflurane and the surgical site was sterilized with ethanol and chlorhexidine. A 1 cm midline incision was made, allowing the #4 mammary fat pad to be exposed. 50,000 clustered MMTV-PyMT-GFP cells per gland were injected into the left and right #4 mammary glands. The surgical area was locally infiltrated with 0.25% bupivacaine for pain relief. Surgical wounds were closed with

9 mm autoclips and tissue glue. Triple antibiotic ointment was applied to the incision. Mice were monitored closely with autoclip removal two weeks after surgery. Tumors were measured every 2 days, and mice were sacrificed before tumors reached 15 mm in diameter. At endpoint, mice were euthanized and primary tumors were fixed in 4% PFA for 4 hrs, then transferred to 25% sucrose in DPBS overnight at 4^{o}C before embedding in OCT and storing at -80^{o}C. 50 µm sections stained with DAPI were used to assess retention of GFP expression in MMTV-PyMT tumors.

Tail vein injection of PyMT-GFP clusters

MMTV-PyMT-mTomato organoids were transduced with a GFP encoding lentivirus (Transomic NT4) and selected with 1µg/mL puromycin for at least 5 days. Organoids were then dissociated to single cells using Accumax, and reaggregated overnight at 150,000 viable cells/mL in media +2% Matrigel (v/v). The following day, after cells had reaggregated, 200,000 viable clustered cells per mouse were injected by tail vein into Nod scid gamma (NSG) immunocompromised mice in 200 µL of PBS using a 27g needle. 3 weeks after tail vein injection, mice were euthanized and lungs imaged under a dissecting microscope to assess GFP+ PyMT metastatic outgrowth.

Statistical Analysis

Graphs, non-linear regressions, and statistical tests were generated using GraphPad Prism 8. Red lines denote medians, unless otherwise noted. Experiments conducted on different days or using samples from different mice were considered biological replicates. All statistical tests are two-sided. $p \leq 0.05$ was considered significant. P-values: “ns” $p > 0.05$, *$p \leq 0.05$, **$p \leq 0.01$, ***$p \leq 0.001$, ****$p \leq 0.0001$.

Piecewise function for estimating organoid growth rate from initial cell number

FIJI software was used to measure the μm^2 area of cells or clusters to measure organoid growth rate, defined as [(final organoid volume)-(initial organoid volume)/(initial organoid volume)]. To estimate organoid volume, an approximate radius was calculated from organoid area ($A=\pi r^2$). Then, approximate organoid volume was calculated ($V=(4/3)\pi r^3$). From immunofluorescence, we estimated that average MMTV-PyMT cell radius as ~4.92 μm (95% CI: 4.66-5.00). To convert organoid volume to approximate cell number, volume was divided by 498.2 μm^3 (volume of one cell with radius 4.92 μm). Growth rate by volume ([final organoid volume-initial organoid volume]/initial organoid volume) was calculated for each organoid to approximate growth rate by cell number. Based on measurements in **Figure 2.1F**, we generated a non-linear regression to estimate the proportion of cells in non-viable organoid cores. Growth rates were adjusted to exclude the predicted number of cells in non-viable cores. A simple linear regression was used to model the growth rates of 1-10 cell organoids (usually growth arrested). For organoids >10 cells, we generated non-linear regression to predict final growth rate. Equations used to model growth summarized on the following page:

Estimated # of cells per organoid $= \left[\frac{4}{3}\pi\left(\sqrt{\frac{Organoid\ Area\ \mu m^2}{\pi}}\right)^3\right] \div 498.2\ \mu m^3$

Predicted proportion outside non-viable core

x = *estimated organoid cell number*

$f(x)$ = *predicted proportion of cells outside viable core*

$$f(x) = 1 - ([predicted\ cell\ \#]^{0.2695} \times (319301945^{0.2695} + [predicted\ cell\ \#]^{0.2695})$$

Cell # growth rate = $\frac{\text{(final cell \# corrected for viability)} - \text{(initial cell \# corrected for viability)}}{\text{initial cell \# corrected for viability}}$

Predicted cell number growth rate based on initial organoid size

$x =$ *initial estimated organoid cell number*

$g(x)$ = *predicted organoid growth rate*

Simple linear regression for $x < 10$*, 4-part nonlinear regression (variable slope)*

for $x \geq 10$

$$g(x)\begin{cases} GR = 0.007606x + 0.0002078 & if\ x \geq 1, < 10 \\ GR = 13.93 + (1.79 - 13.93) \div (1 + (\frac{3493}{x})^{1.5}) & if\ x \geq 10 \end{cases}$$

Chapter 3. NANOLUMENAL SIGNALING REGULATES METASTATIC OUTGROWTH

A version of the following work was published in: Wrenn ED, Yamamoto A, Moore BM, Huang Y, McBirney M, Thomas AJ, Greenwood E, Rabena YF, Rahbar H, Partridge SC, Cheung KJ. Regulation of Collective Metastasis by Nanolumenal Signaling. Cell. 2020 Oct 15;183(2):395-410.e19. doi: 10.1016/j.cell.2020.08.045. Epub 2020 Oct 1. PMID: 33007268.

ABSTRACT

Collective metastasis is defined as the cohesive migration and metastasis of multicellular tumor cell clusters. Disrupting various cell-cell adhesion genes markedly reduces cluster formation and colonization efficiency, yet the downstream signals transmitted by clustering remain largely unknown. Here, we use mouse and human breast cancer models to identify a collective signal generated by tumor cell clusters supporting metastatic colonization. We show that tumor cell clusters produce the growth factor epigen and concentrate it within nanolumina – intercellular compartments sealed by cell-cell junctions and lined with microvilli-like protrusions. Epigen knockdown profoundly reduces metastatic outgrowth in vivo and promotes a collective migratory state ex vivo. Tumor cell clusters from basal-like 2, but not mesenchymal-like, triple-negative breast cancer cell lines have increased epigen expression, sealed nanolumina, and impaired outgrowth upon nanolumenal junction disruption.

3.1 INTRODUCTION

Though metastasis is often conceived of as a single cell process, multicellular tumor cell clusters have been directly observed at tumor invasive fronts, within the systemic circulation, and colonizing distant organs (Aceto et al., 2015; Cheung and Ewald, 2016; Friedl and Gilmour, 2009; Friedl and Mayor, 2017). Until recently, the functional importance of clusters for metastatic seeding has remained unclear. Studies have since shown that multicellular clusters give rise to between 50-97% of metastases in different models (Aceto et al., 2014; Cheung et al., 2016). Notably, circulating tumor cell clusters are associated with rapid disease progression and increased mortality in many different cancer types (Au et al., 2017; Giuliano et al., 2018; Hou et al., 2012). Yet compared with the process of single cell metastasis (Derynck and Weinberg, 2019; Lambert et al., 2017; Massague and Obenauf, 2016), the molecular mechanisms driving dissemination and outgrowth of multicellular clusters are less well understood.

An important question is whether multicellular organization gives rise to unique cellular and molecular properties that promote metastasis and are targets for therapy. Recent studies have identified some of the features distinguishing single and clustered tumor cells: increased chromatin accessibility at the binding sites of stemness-promoting transcription factors (Gkountela et al., 2019); the ability of clusters to maintain cell-cell adhesion while squeezing through narrow vasculature, extravasating and proliferating at secondary sites; and the increased capacity of clusters to survive reactive oxygen stress (Labuschagne et al., 2019; Padmanaban et al., 2019), an acute challenge for disseminating cells (Piskounova et al., 2015; Schafer et al., 2009; Tasdogan et al., 2020). In several of these studies, disrupting cell adhesion reduces cluster formation and

integrity and greatly diminishes the metastatic potential of these tumor cells (Aceto et al., 2014; Choi et al., 2015; Gkountela et al., 2019; Liu et al., 2019c; Padmanaban et al., 2019). These studies advance the concept that therapeutically targeting tumor cell cluster adhesion may be able suppress collective metastasis.

An alternative approach is to focus on the signals arising downstream of tumor cell cluster formation. This strategy is supported by evidence that multicellularity and cell-cell adhesion regulate signaling in normal contexts to accomplish tissue remodeling during developmental morphogenesis and wound healing (Friedl and Mayor, 2017; Gurdon, 1988; Mishra et al., 2019; Raff, 1992). Intercellular cooperation and signaling in these systems are still incompletely understood, but are known to involve synchronized shifts in the composition of cellular junctions (Pei et al., 2019; Theveneau and Mayor, 2012; White and Plachta, 2015), spatially-restricted and long-range paracrine signaling (Durdu et al., 2014; Müller and Schier, 2011), contact-mediated juxtacrine signaling (Siebel and Lendahl, 2017), and patterning by the local microenvironment (Bruno et al., 2017; Chen et al., 2016; Inman et al., 2015; Xin et al., 2016). Thus, in addition to forming adhesions, clustering of tumor cells could give rise to complex signaling mechanisms distinct from those utilized by single cells.

Further, metastasis has been conceptualized as a series of switch-like transitions (Lambert et al., 2017; Massague and Obenauf, 2016) that involve the collaboration of tumor cell communities (Archetti and Pienta, 2019; Egeblad et al., 2010; Tabassum and Polyak, 2015; Zhou et al., 2017). Although a number of theoretical studies have posited that cancer cells could promote metastatic transitions through cooperative signaling mechanisms (Archetti and Pienta, 2019; Ben-Jacob et al., 2012; Deisboeck and Couzin,

2009; Hickson et al., 2009; Korolev et al., 2014), direct molecular evidence for collective signaling between tumor cells during metastasis remains scarce.

In the present study, we used mouse and human models of breast cancer metastasis to identify collective signals generated by tumor cell clusters during metastatic outgrowth. We show that mouse and human tumor cell clusters harbor nanolumina—intercellular signaling compartments sealed by cell-cell junctions. Within nanolumina, we identify a diffusible growth factor, epigen, which promotes metastatic outgrowth. Importantly, we find that epigen expression and nanolumen formation are enriched in a subtype of aggressive, triple-negative human breast cancers.

3.2 RESULTS

3.2.1 *An experimental system to identify metastasis-promoting signals generated by aggregation*

To identify metastasis-promoting signals generated by aggregation, we first developed an experimental system to temporally control cluster formation and monitor downstream molecular events **(Figure 3.1A)**. We began our studies with an aggressive mouse model of breast cancer, MMTV-PyMT, (Guy et al., 1992; Lin et al., 2003) in which collective invasion and multicellular metastasis have been reported (Cheung et al., 2013; Cheung et al., 2016; Nguyen-Ngoc et al., 2015). When MMTV-PyMT tumor organoids were enzymatically dissociated and cultured in suspension, individual tumor cells spontaneously assembled into loosely attached cell aggregates by 6 hrs and more compact clusters by 24 hrs, with a mean number of cells per cluster of 4.4 (SD ± 4.2) and 5.4 (SD ± 5.2), respectively **(Supplemental Figure 3.1A,**

Video 3.1). MMTV-PyMT membrane-Tomato labeled tumor organoids were dissociated to single cells, then four input suspensions were generated: single cells (aggregated for 0hrs), cells aggregated for 6 hrs, cells aggregated for 24 hrs, and cells aggregated for 24 hrs then re-dissociated back to single cells. 3 weeks after injection, loosely attached (6 hrs) clusters had formed 141-fold and compact (24 hrs) clusters formed 532-fold more lung metastases than an equal number of single cells **(Figure 3.1B, Supplemental Figure 3.1B)**. Well-organized (24hr) clusters re-dissociated back into single cells were negligibly metastatic **(Figure 3.1B)**, indicating that the metastasis-promoting processes occurring during aggregation do not persist through another round of dissociation but instead depend on a multicellular state.

Further, we observed that both single cells and clusters were trapped in the lungs of mice shortly after tail vein injection **(Supplemental Figure 3.1C)**. But over consecutive days, clusters had increased persistence compared to single cells **(Supplemental Figure 3.1D-E)**. A small number of single cells persisted in the lungs at 3 wks post-injection but micrometastases were not detected, in contrast to the large number of macrometastases in cluster-injected conditions. To assess metastatic potential in organs other than the lung, mTomato-PyMT single cells or clusters were injected into the left cardiac ventricle of NSG mice. Intracardiac injection of clustered tumor cells generated significantly more metastases to multiple organs including the brain, lungs, and liver than injection of single cells **(Supplemental Figure 3.1F-G)**.

Concordant with these in vivo observations, MMTV-PyMT tumor cell clusters had >4.7-fold higher outgrowth than single cells in 3D basement membrane-rich gels **(Supplemental Figure 3.2A)**. Proliferation was highest in clusters with tumor cells directly contacting multiple neighbors **(Supplemental Figure 3.2B-C)**. To assess differences in apoptosis, mixed populations of single cells and clusters embedded together in 3D basement membrane-rich gels were monitored in the presence of a caspase 3/7 fluorescent biosensor. MMTV-PyMT clusters had >2.2-fold higher survival than single cells after 96 hours **(Supplemental Figure 3.2D)**. Further, 8 of 10 individual human breast cancer tumor specimens, including those from metastases to brain and bone, had 2.5 to >70-fold higher survival as clusters **(Supplemental Figure 3.2E-F, Table 3.1)**. Together, these data establish a system to dissect the metastasis-promoting signals downstream of tumor cell cluster formation.

3.2.2 *The growth factor epigen is the most induced gene upon clustering and supports efficient metastatic outgrowth in the lung*

To identify molecular differences between single cells and clusters that underlie their disparate metastatic potentials, we performed an RNA-seq time-course of MMTV-PyMT cells throughout their aggregation from single cells (0 hrs after dissociation) to highly metastatic clusters (6 to 48 hrs after dissociation) **(Figure 3.1A, C)**. This revealed sequential upregulation of different biological pathways: at 0 hrs, HIF1 and interferon stress signaling pathways; at 6 hrs, wound-healing and MAPK associated genes; at 12 hrs, ribosome biogenesis; and at 24 and 48 hrs, genes involved in cell cycle and fatty acid metabolism **(Figure 3.1C, Table 3.2)**.

Analysis of early clusters (6 hrs) compared to single cells revealed that clustering rapidly induced expression of low-affinity EGFR ligands epigen and amphiregulin **(Figure 3.1D)**. Epigen was the most differentially expressed of all mRNAs **(Table 3.3)**. Compared to high-affinity ligands like EGF, low-affinity EGFR ligands are associated with prolonged signaling, altered effector responses, and different ligand-EGFR complex conformations (Freed et al., 2017). uPar (*Plaur*) which can participate in ligand-independent EGFR activation (Liu et al., 2002; Smith and Marshall, 2010) was also highly induced in clusters. Therefore, we hypothesized that growth factor production and EGFR activation could support the superior metastatic colonization of clusters.

To test the role of EGFR associated genes in collective metastatic outgrowth, we used lentiviral RNAi to deplete *Egfr*, *Epgn*, *Areg*, and *Plaur* in MMTV-PyMT tumor cell clusters **(Supplemental Figure 3.3A)**. Knockdowns suppressed outgrowth in 3D culture but did not disrupt the ability of tumor cells to aggregate, supporting the hypothesis that these factors act downstream of clustering **(Supplemental Figure 3.3B-C)**. Next, for each condition, equal numbers of clustered cells were injected by tail vein. 3 weeks later, we observed significantly less macrometastatic burden relative to control by Egfr-kd, Areg-kd, and Epgn-kd **(Supplemental Figure 3.1E-F)**. Strikingly, Epgn-kd reduced metastatic outgrowth in the lungs by >94% and significantly reduced the size, but not total number, of lung metastases **(Supplemental Figure 3.1H-I)**. Further, lung metastases had reduced reporter GFP expression in Epgn-kd but not non-targeting Ctrl-kd cluster injected mice, possibly from pressure to escape epigen knockdown **(Supplemental Figure 3.1J-K)**. The similar number of total metastases in Ctrl-kd and Epgn-kd conditions suggests that epigen is not required to seed and persist in the lungs. However, the

dramatically reduced size of these metastases indicates that cluster outgrowth after seeding largely depends on epigen expression.

3.2.3 *Epigen suppression switches tumor cell clusters from a proliferative to a migratory state*

We next sought to determine the biological processes regulated by epigen expression. RNA seq of Ctrl-kd and Epgn-kd MMTV-PyMT clusters, generated by 24 hrs of aggregation of single cells, revealed that Epgn-kd clusters downregulate cell cycle genes, but upregulate migration-related genes **(Figure 3.2A, Table 3.4).** Additionally, their transcription most closely resembles nascent, non-proliferative clusters (6-12 hrs) from our aggregation time course RNA-sequencing, instead of later proliferative clusters (24-48 hrs), despite Epgn-kd cells having aggregated for 24 hours **(Figure 3.1C, Figure 3.2B)**. Gene set analysis revealed that Epgn-kd induces expression of genes in cadherin, desmosome, tight junction, and matrix metalloproteinase families **(Figure 3.2C)**. Although Epgn-kd induced expression of some EMT-associated genes, Epgn-kd organoids showed persistent expression of epithelial genes including *Epcam* and *Cdh1* **(Figure 3.2C)**, and expression of multiple cytokeratins associated with basal/myoepithelial and invasive leader cells including *Krt5*, *Krt14,* and *Krt17* **(Supplemental Figure 3.3E-F)** (Cheung et al., 2013; Cheung et al., 2016).

To functionally test the effects of epigen suppression on collective outgrowth and migration, Ctrl-kd and Epgn-kd clusters were embedded in 3D basement membrane-rich gels and monitored by time-lapse microscopy **(Figure 3.2D)**. Compared with Ctrl-kd clusters, Epgn-kd clusters showed increased migration but reduced outgrowth and proliferation **(Fig. 3.2D-G, Supplemental Figure 3.3D).** Epgn-kd clusters migrated not as

individual cells but as E-cad+/K14+/K17+ clusters **(Figure 3.2H, Supplemental Figure 3.3F)**. We further confirmed that a second epigen shRNA reduced epigen expression and outgrowth **(Supplemental Figure 3.3G-H)**, and that outgrowth was rescued by an shRNA-resistant human epigen construct **(Supplemental Figure 3.3I)**. These data indicate that epigen suppression can promote the transition of clustered tumor cells to more migratory, but less proliferative, state.

3.2.4 *Epigen acts as a collective signaling factor shared non-cell-autonomously within clusters*

There are several possible mechanisms by which epigen could induce cluster outgrowth **(Figure 3.3A)**. For example, epigen could be secreted from clusters into their local microenvironment, facilitating long-range paracrine signaling (model 1). Epigen could act in an autocrine manner, inducing proliferation in the same cell that expresses it (model 2). Epigen could induce paracrine growth factors downstream of receptor activation (model 3). Or, epigen could be a non-cell-autonomous growth factor whose signaling range is restricted to each tumor cell cluster (model 4).

If epigen acts as a long-range secreted molecule with no local restriction (model 1), then co-culture with non-transduced clusters should partly rescue the outgrowth defect of nearby Epgn-kd clusters. However, time-lapse imaging indicated that Epgn-kd clusters co-cultured with non-transduced clusters had similar outgrowth rates as those cultured in 3D gels alone **(Figure 3.3B-C)**. In addition, immunofluorescence revealed that epigen was largely restricted to intercellular areas in clusters from MMTV-PyMT, MMTV-Neu, and C3(1)-TAg mouse models of breast cancer, and intercellular immunofluorescence

signal was depleted upon epigen knockdown **(Figure 3.3D-E**, **Supplemental Figure 3.4A-C)**. Likewise, mTomato-PyMT clusters transduced with an epigen-mGFP fusion construct had enriched GFP signal at intercellular regions **(Figure 3.3F)**. These data indicate that epigen acts primarily as a short-range signal with strong enrichment at cell-cell boundaries.

We next sought to test different cluster-restricted models of epigen signaling (models 2 through 4). If epigen ligand is shared non-cell-autonomously amongst neighboring cells, adding epigen-expressing cells to a cluster should rescue the outgrowth of adjacent epigen deficient cells. Epgn-kd cells were mixed with non-transduced cells to form mosaic clusters with varying proportions of cells from each population **(Figure 3.3G)**. After 6 days, clusters were dissociated and the number of Epgn-kd cells was counted to assess their outgrowth in each condition relative to their starting cell number. Mixing non-transduced cells and Epgn-kd cells in a 9:1 ratio increased the outgrowth of Epgn-kd cells 3-fold higher than when cultured alone **(Figure 3.3H)**. Further, Epgn-kd cells aggregated with Ctrl-kd cells at a 1:1 ratio migrated markedly less than pure Epgn-kd clusters **(Supplemental Figure 3.4E)**.

These data suggest that epigen induces outgrowth of neighboring cells non-cell-autonomously. Consistent with this hypothesis, recombinant epigen induced outgrowth in a dose-dependent manner **(Supplemental Figure 3.4D)**. However, an alternative explanation is that epigen does not directly promote outgrowth but rather induces expression of a second growth signal transmitted to neighboring cells downstream of receptor binding (model 3). To test this, we performed mosaic mixing experiments with non-transduced cells and Egfr-kd cells. Egfr-kd cells in mosaic clusters did not grow

significantly more than when cultured as pure Egfr-kd clusters **(Figure 3.3H)**, demonstrating that non-transduced cells do not produce a second signal downstream of EGFR activation that can non-cell-autonomously rescue Egfr-kd outgrowth. Thus, epigen's intercellular enrichment, short-range restriction, and non-cell-autonomous activity all indicate that epigen acts within clusters as a shared, collective growth signal (model 4).

3.2.5 *Secreted epigen is concentrated within intercellular nanolumina*

We next used transmission electron microscopy (TEM) to characterize the physical properties at the site of epigen accumulation in MMTV-PyMT clusters. To our surprise, we observed that intercellular membranes, rather than being closely apposed, were often separated by hollow cavities which were bounded by electron-dense cell-cell junctions and lined by microvilli-like protrusions **(Figure 3.4A, Supplemental Figure 3.4F)**. We refer to these intercellular cavities as "nanolumina." Epigen knockdown did not alter nanolumina morphology, indicating that high epigen expression is not required for nanolumina formation **(Supplemental Figure 3.4G)**.

We hypothesized that the nanolumina observed in tumor cell clusters could concentrate soluble signaling molecules such as epigen **(Figure 3.4B)**, not unlike the luminal signaling compartments observed in collectively migrating zebrafish lateral line primordium (Durdu et al., 2014). Alternatively, epigen could localize to areas of direct cell-cell contact and activate EGFR in a membrane-restricted juxtracrine manner, as has been reported for some EGFR ligands (Singh and Harris, 2005). Consistent with the first model, stimulated emission depletion microscopy revealed concentration of epigen within

intercellular spaces **(Figure 3.4C)**. Immunoelectron microscopy also confirmed the presence of epigen within nanolumenal cavities and along nanolumenal membranes but not at direct cell-cell junctions **(Figure 3.4D-E)**. Epigen was not restricted to areas expressing the apical marker Muc1, suggesting that these are not fully apically polarized lumina **(Supplemental Figure 3.4H)**. Together with the non-cell-autonomous effects of epigen on cluster outgrowth, these findings suggest that epigen diffuses within shared nanolumina between clustered cells.

The accumulation of epigen within nanolumina implied a mechanism for preventing ligand diffusion out of clusters. To characterize junctional permeability, we treated clusters with sulfo-NHS-biotin which labels membrane surface proteins but is excluded from the cytosol. At baseline, biotin was excluded from areas of cell-cell contact, predominantly labeling areas of cell-matrix contact **(Figure 3.4F)**. Disruption of junctions by calcium chelation, Latrunculin A, or ochratoxin A allowed biotin to leak between clustered cells **(Figure 3.4F, Supplemental Figure 3.4I)**. Likewise, calcium chelation reduced epigen immunofluorescence in clusters **(Figure 3.4G)**. Although we could not measure the nanolumenal concentration of epigen directly, we estimated it to be >5000-fold higher than the extra-cluster concentration based on ELISA measurements of cluster lysates and culture supernatants (223 vs. 0.04 ng/mL, **Supplemental Figure 3.4J**). Thus, nanolumina preserve a high local concentration of epigen between clustered cells.

These findings suggested a critical role for EGFR signaling in nanolumina. To assess the dominant receptor tyrosine kinase pathway active in clusters in an unbiased manner, we performed protein array analysis of 39 phospho-RTKs in single cell vs. cluster lysates. ERBB family members pTyr-EGFR and pTyr-HER2, which can heterodimerize

with EGFR, were the most cluster-upregulated phospho-RTKs **(Supplemental Figure 3.5A)**. We observed induction of EGFR effectors pERK1/2 and pAKT in clustered tumor cells **(Supplemental Figure 3.5B-D)**. In addition, pEGFR and HER2 localized to intercellular areas between clustered tumor cells **(Supplemental Figure 3.5E-F)**. Using immunoelectron microscopy, we confirmed pEGFR and HER2 localized along nanolumenal membranes, as would be expected of transmembrane receptors **(Supplemental Figure 3.5G-H)**.

3.2.6 *Epigen suppression reduces outgrowth of primary tumors and spontaneous metastases*

Having identified the site and mechanism of epigen signaling ex vivo, we next assessed epigen expression and nanolumina formation during metastasis. MMTV-PyMT mTomato+ clusters were transplanted into mammary fat pads of non-fluorescent NSG mice. Intercellular epigen was usually highly expressed at cell-cell boundaries within primary tumors and in locally disseminated tumor cell clusters **(Figure 3.5A-B)**. Likewise, distant metastases consistently expressed intercellular epigen **(Figure 3.5D-F, Supplemental Figure 3.6D)**, pEGFR, and HER2 **(Supplemental Figure 3.6E-F)**. In contrast, epigen was absent or weakly expressed in locally disseminated single cells **(Fig. 3.5B)** and in surrounding non-tumor tissues **(Figure 3.5A-F, Supplemental Figure 3.6D)**.

We observed that locally disseminated tumor cell clusters generally adopted two morphologies: strand-like with extensive protrusions, or nest-like with rounded cluster borders. Near primary tumors, protrusive clusters had lower epigen expression than their non-protrusive counterparts **(Figure 3.5C).** Pan-cytokeratin, keratin-14, and keratin-17

staining confirmed that these highly protrusive tumor strands were of epithelial origin, not contaminating stromal cells **(Supplemental Figure 3.6C)**. Likewise, protrusive clusters adjacent to brain metastases expressed epigen at lower levels than their non-protrusive counterparts **(Figure 3.5F)**.

TEM of MMTV-PyMT primary tumors revealed extensive intercellular nanolumina similar to those observed in clusters ex vivo **(Figure 3.5G)**. When tumors were exposed to sulfo-NHS-biotin prior to fixation, biotin was found throughout tumor-adjacent stroma but was largely excluded from tumor cell nests **(Figure 3.5H)**. We observed modestly increased biotin permeability in protrusive compared with non-protrusive clusters (**Figure 3.5I).** To assess nanolumenal permeability at secondary sites, tumor cell clusters were injected by tail vein into NSG mice. 2 weeks later, lungs were harvested and exposed to NHS-sulfo-biotin. Lung metastases appeared less biotin permeable than the adjacent lung tissue (**Figure 3.5J**). Thus, restricted biotin permeability and intercellular epigen accumulation are observed across primary tumors, local cell clusters, and lung metastases in the MMTV-PyMT model.

To assess the functional role of epigen in vivo, Ctrl-kd and Epgn-kd clusters were orthotopically transplanted into the mammary fat pads of NSG mice. Over the ensuing 6 weeks, we observed significantly slower growth of Epgn-kd tumors vs. control tumors **(Figure 3.5K)** and a slight increase in locally disseminated clusters in the adjacent stroma **(Supplemental Figure 3.6G)**. Epgn-kd lung metastases were significantly less proliferative **(Supplemental Figure 3.6H)** and smaller **(Supplemental Figure 3.6I)** than Ctrl-kd metastases. Although Epgn-kd mice harbored fewer macrometastases **(Figure 3.5L)**, the total number of metastases was similar between Ctrl-kd and Epgn-kd mouse

lungs **(Supplemental Figure 3.6J)**, supporting a larger effect on metastatic outgrowth than initial seeding. This mirrors our earlier findings that Epgn-kd clusters could effectively seed the lungs after tail vein injection but grew poorly **(Supplemental Figure 3.1H-I)**. Epgn-kd-GFP tumors also lost expression of GFP expression far more frequently than Ctrl-kd-GFP tumors **(Supplemental Figure 3.6K)**, again indicating pressure to revert to Epgn-high phenotypes. Thus, epigen suppression reduces MMTV-PyMT primary tumor and metastatic outgrowth in vivo, consistent with our ex vivo findings.

3.2.7 *Epigen expression and nanolumina formation are associated with basal-like 2 triple-negative breast cancer*

We next sought to determine the generality of our findings to human breast cancer. Tumor cell clusters were collected from a breast cancer patient recruited to an IRB approved study at Fred Hutchinson Cancer Research Center. At the time of enrollment, the patient had ER+/PR+/HER2- breast cancer that was metastatic to orbit, lung, liver, and bone. CTC clusters were detected at the second and third time points, coinciding with clinical evidence of disease progression **(Figure 3.6A-B)**. Palliative paracentesis revealed malignant ascites containing cytokeratin-positive/CD45-negative tumor cell clusters **(Figure 3.6C)** and phosphorylated EGFR at intercellular contacts **(Figure 3.6C)** Further, TEM revealed nanolumina with microvilli-like protrusions in ascites-derived tumor cell clusters **(Figure 3.6D)**. Malignant ascites were also collected from a second patient with metastatic ER+/PR+/HER2- breast cancer. At the time of paracentesis, she was treated with letrozole and abemaciclib, and had metastatic disease to bone, liver, chest wall, stomach, and peritoneum. Similarly, tumor cell clusters collected from this patient

demonstrated intercellular pEGFR as well as intercellular nanolumina **(Supplemental Figure 3.7A-B).**

As a second approach, we examined epigen expression in two RNA-seq compendia of human breast cancer cell lines (Barretina et al., 2012; Klijn et al., 2015). Triple-negative cell lines have been previously classified based on their gene expression into subgroups: basal-like 1 (BL1), basal-like 2 (BL2), mesenchymal-like (M-like), and luminal androgen receptor (LAR) (Lehmann et al., 2011; Lehmann et al., 2016). We observed a strong association between *EPGN* expression and the basal-like 2 subgroup, whereas mesenchymal-like breast cancer cell lines had the lowest *EPGN* expression **(Figure 3.6E, Supplemental Figure 3.7C)**. Triple-negative breast cancers frequently overexpress EGFR which is associated with poorer prognosis (Nielsen et al., 2004). BL2 triple-negative breast cancers have increased growth factor signaling and basal/myoepithelial gene expression, as well as poor (0-22%) response rates to chemotherapy (Lehmann et al., 2016; Masuda et al., 2013; Ring et al., 2016). In addition, the highest epigen expressing HER2+ cell lines were associated with the recently described basal-like (HER2E) subset of HER2+ cell lines (Watson et al., 2018). Likewise, basal-like HER2+ patient tumors have increased expression of RTKs, including EGFR, and HER2 relative to luminal HER2+ tumors (TCGA, 2012).

TEM revealed considerable morphological differences between three BL2, epigen-high cell lines (HCC70, CAL851, and HDQP1) and three M-like, epigen-low cell lines (MDA-MB-231, MDA-MB-436, BT549). BL2 cell clusters contained nanolumina with extensive microvilli-like protrusions, often sealed by electron-dense junctional complexes **(Figure 3.6F)**. In contrast, M-like cell clusters were loosely organized and largely lacked

junctionally-sealed intercellular spaces. Further, BL2 cell clusters were largely biotin-impermeable, whereas biotin readily leaked into the intercellular spaces of M-like clusters **(Figure 3.6G)**. Transcriptional analysis of these 6 cell lines (Barretina et al., 2012) revealed that BL2, epigen-high lines were enriched for genes related to epithelial development and migration; branching morphogenesis of the placental labyrinthine layer (Rinkenberger and Werb, 2000); and tight junction genes including *CLDN7*, *MARVELD3*, and the transcription factor *GRHL2* **(Figure 3.6H-I, Table 3.5)**. Mesenchymal-like cell lines, on the other hand, were enriched for genes related to collagen metabolism and FGFR signaling relative to BL2 lines **(Supplemental Figure 3.7D, Table 3.5)**. These data show that epigen enrichment and nanolumina occur in aggressive metastatic breast cancers, and reveal large differences in nanolumina formation, junctional permeability, and morphogenesis-related gene expression between BL2 and M-like cells.

3.2.8 *HCC70 outgrowth depends on epigen expression and is sensitive to IFNγ which induces nanolumen permeability*

HCC70 was the highest *EPGN* expressing cell line in both RNA-seq datasets (Barretina et al., 2012; Klijn et al., 2015). When compared to a transcriptomic dataset of metastatic solid tumors (MET500), HCC70 cells modeled the gene expression of basal-like breast cancers more closely than other tested cell lines (Liu et al., 2019a; Robinson et al., 2017). We observed that HCC70 clusters expressed epigen, pEGFR, and the tight junction protein occludin, but not HER2 **(Figure 3.7A).** *EPGN* knockdown in HCC70 clusters significantly reduced their outgrowth ex vivo **(Figure 3.7B-C)**. No significant differences in migration or outgrowth were observed in 2D **(Supplemental Figure 3.7E-**

F). Transduction with an *EPGN* sgRNA likewise reduced HCC70 cluster outgrowth **(Supplemental Figure 3.7G)**.

To assess epigen's role in metastatic outgrowth, Epgn-kd HCC70 cell clusters were injected by tail vein into immunocompromised NSG mice. 3 weeks later, the Epgn-kd clusters had formed significantly smaller metastases than Ctrl-kd clusters **(Figure 3.7D)**. Thus, epigen supports metastatic outgrowth in human basal-like 2 HCC70 cells. We conclude that epigen dependence and nanolumina formation can occur in both mouse and human models of breast cancer.

The existence of nanolumina suggested that this structure could be targeted to reduce collective signaling during metastasis. The cytokine IFNγ can enhance paracellular diffusion (Bruewer et al., 2003; Madara and Stafford, 1989) and increase epithelial flux to amplify immune responses (Turner, 2009), independent of apoptosis induction. We hypothesized that IFNγ could weaken the barriers sealing nanolumina and inhibit cluster outgrowth. Consistent with this hypothesis, IFNγ treatment strongly reduced HCC70 tumor cell cluster outgrowth (IC50= 0.58 ng/mL) **(Figure 3.7E).** IFNγ reduced proliferation but did not increase cell death in HCC70 clusters **(Figure 3.7F, Supplemental Figure 3.7H)**. IFNγ treatment also increased biotin permeability of HCC70 clusters **(Figure 3.7G)** and altered nanolumenal morphology **(Figure 3.7H)**. Additionally, HCC70 clusters had reduced mRNA expression of tight junction related genes *RAB25* and *CLDN7* after IFNγ treatment **(Figure 3.7I)**. Conversely, MDA-MB-231 clusters were far less sensitive to IFNγ treatment **(Figure 3.7E)**, lowly expressed *RAB25* and *CLDN7* **(Supplemental Figure 3.7I),** and were highly biotin-permeable with or without IFNγ treatment **(Supplemental Figure 3.7J)**.

Next, we tested the effects of IFNγ on metastatic outgrowth. After 6 days of IFNγ (2 ng/mL) treatment, equal viable cell numbers of HCC70 clustered cells were injected by tail vein into NSG mice **(Figure 3.7J)**. 3 weeks later, HCC70 metastases in the lungs were identified using a human-specific antibody (Lawson et al., 2015). IFNγ pre-treated clusters formed significantly smaller metastases than untreated controls **(Figure 3.7K-L)**. Although a cytokine like IFNγ is likely to have pleotropic effects beyond nanolumina disruption, these data indicate that the collective metastatic outgrowth of tumor cell clusters can be therapeutically targeted.

3.3 DISCUSSION

Metastasis is regulated by factors both internal to the cancer cell as well as arising from interactions with its tumor microenvironment (Fidler and Kripke, 2015; Lambert et al., 2017; Massague and Obenauf, 2016). Our study reveals an additional dimension: the shared intercellular exchange of growth factors between clustered tumor cells using an interstitial compartment. Here we find that multicellular clusters form nanolumina – intercellular spaces that accumulate a high local concentration of epigen **(Supplemental Figure 3.7K)**. In this way, tumor cell clusters create a pro-growth internal microenvironment through non-cell-autonomous signaling.

Recent studies have demonstrated that tumor cells can cooperatively support polyclonal growth and metastasis through secreted paracrine signals between genetically distinct clones (Cleary et al., 2014; Janiszewska et al., 2019; Marusyk et al., 2014). Here we describe a similar but distinct mechanism in which cooperative signaling is generated

by the physical architecture of nanolumina. In this regard, our findings share parallels with the concentration of FGF within lumens in migrating lateral line primordia (Durdu et al., 2014), though the compartments we observe here are typically nanometer-scale in diameter and do not appear apically polarized. Recent findings have similarly emphasized the impact of 3D topology on signaling during development and in generating synthetic biological systems (Durdu et al., 2014; Gilmour et al., 2017; Shyer et al., 2015; Simian and Bissell, 2017; Toda et al., 2018; Xavier da Silveira Dos Santos and Liberali, 2018). Our study supports the parallel ability of 3D multicellular architecture to shape signaling during metastasis.

Nanolumenal signaling could also play a role in normal development and homeostasis. In normal mammary epithelia there are interdigitating structures similar to the nanolumina characterized here, but whose function has remained unknown (Ewald et al., 2012). Likewise, the enrichment of genes related to labyrinthine placental morphogenesis (Rinkenberger and Werb, 2000) in BL2 cancer cells may hint at a developmental role for nanolumina that is being co-opted during metastasis, analogous to the co-option of EMT programs in mesenchymal cancer cells (Dongre and Weinberg, 2019; Nieto et al., 2016). Future studies are needed to interrogate nanolumen signaling in normal and cancer contexts, and to develop therapeutic strategies that target these signaling compartments.

3.4 ACKNOWLEDGMENTS

We thank the following people: S. Beronja and P. Paddison for providing shRNA and sgRNA reagents; A. Ewald and S. Stanton for providing mouse tumors; C. Tran for

research coordinator support at SCCA; A. Hsieh, J. Cooper, and V. Vasioukhin for critical feedback on this work. This study was supported by grants from the Department of Defense Breast Cancer Research Program (BCRP; W81XWH–18–1–0098), the NIH/NCI (R37CA234488), the Burroughs Wellcome Fund Career Award for Medical Scientists, the Breast Cancer Research Foundation (BCRF-18-035), the V Foundation (V Foundation Scholar Award), the Phi Beta Psi Sorority, Seattle Translational Tumor Research, and the Shared Resources of the FHCRC/UW Cancer Consortium (P30 CA015704). Most of all, we thank the patients participating in this study for their generosity.

AUTHOR CONTRIBUTIONS

EDW and KJC drafted the manuscript. EDW, KJC, AY, BMM, YH, MM, AJT, and EG conceived and performed experiments. YFR, HR, and SP provided human breast tumor tissue from the biospecimen repository. EDW, AJT, MM, and YFR prepared human breast cancer patient tissue samples. KJC secured funding and supervised the project.

Declaration of interests: EDW and KJC are inventors on a pending patent application related to this work.

3.5 FIGURES

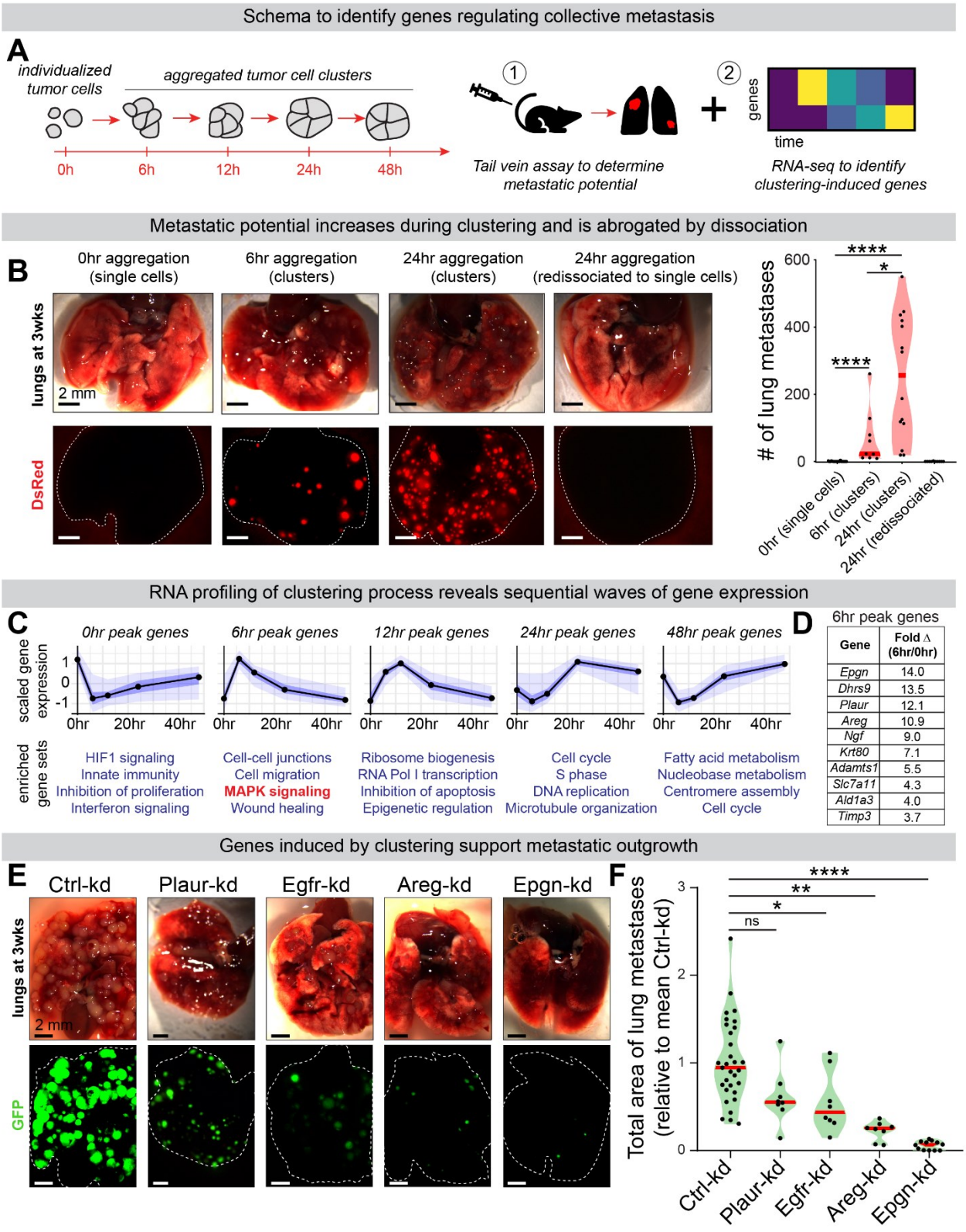
Schema to identify genes regulating collective metastasis
A
individualized tumor cells
aggregated tumor cell clusters
0h
6h
12h
24h
48h
1
2
genes
time
Tail vein assay to determine metastatic potential
RNA-seq to identify clustering-induced genes
Metastatic potential increases during clustering and is abrogated by dissociation
B
0hr aggregation (single cells)
6hr aggregation (clusters)
24hr aggregation (clusters)
24hr aggregation (redissociated to single cells)
lungs at 3wks
2 mm
DsRed
# of lung metastases
0hr (single cells)
6hr (clusters)
24hr (clusters)
24hr (redissociated)
RNA profiling of clustering process reveals sequential waves of gene expression
C
0hr peak genes
6hr peak genes
12hr peak genes
24hr peak genes
48hr peak genes
scaled gene expression
enriched gene sets
HIF1 signaling
Innate immunity
Inhibition of proliferation
Interferon signaling
Cell-cell junctions
Cell migration
MAPK signaling
Wound healing
Ribosome biogenesis
RNA Pol I transcription
Inhibition of apoptosis
Epigenetic regulation
Cell cycle
S phase
DNA replication
Microtubule organization
Fatty acid metabolism
Nucleobase metabolism
Centromere assembly
Cell cycle
D
6hr peak genes
Gene
Fold Δ (6hr/0hr)
Epgn 14.0
Dhrs9 13.5
Plaur 12.1
Areg 10.9
Ngf 9.0
Krt80 7.1
Adamts1 5.5
Slc7a11 4.3
Ald1a3 4.0
Timp3 3.7
Genes induced by clustering support metastatic outgrowth
E
Ctrl-kd
Plaur-kd
Egfr-kd
Areg-kd
Epgn-kd
lungs at 3wks
2 mm
GFP
F
Total area of lung metastases (relative to mean Ctrl-kd)
ns

Figure 3.1. RNA-seq analysis of tumor cell aggregation identifies epigen as a cluster-upregulated gene supporting metastatic outgrowth

(A) MMTV-PyMT tumor organoids dissociated to single cells spontaneously aggregate into clusters in suspension. Single cells or aggregates were subjected to (1) tail vein metastasis assays and (2) RNA-seq to identify genes altered by aggregation. **(B)** MMTV-PyMT mTomato+ tumor organoids were dissociated to single cells and aggregated for 0, 6, and 24 hrs. At 24 hrs, some clusters were re-dissociated back to single cells. At each time point 200,000 cells were injected by tail vein into NSG mice. Left: lungs 3 weeks later. Right: # of mTomato+ metastases. n (# mice) = 19 (0hr), 9 (6hr), 14 (24hr), 10 (re-dissociated). P-values = Mann-Whitney tests. **(C)** MMTV-PyMT cells were collected for RNA-seq at 0, 6, 12, 24, and 48 hrs of aggregation. n = 455, 780, 367, 320, 482 genes peaking at each time point, respectively (false discovery rate [FDR] ≤ 0.05). n=3. Above: Mean-variance normalized gene expression. Black line = median. 50% CI = dark blue, 95% CI= light blue. Below: Gene ontology enrichment (Metascape, p-value <0.0001). **(D)** The top ten cluster-induced genes (by t-statistic, ranked by fold change, 0 hrs vs. 6 hrs aggregation). n=3. **(E)** Non-targeting control or shRNA transduced PyMT tumor cell clusters were injected by tail vein into NSG mice (200,000 clustered cells/mouse). Representative images of lungs 3 week later. **(F)** Total GFP+ lung metastatic burden per mouse, relative to mean Ctrl-kd metastatic burden for each injection replicate. n (# of mice): Ctrl-kd = 31, Egfr-kd = 8, Areg-kd = 8, Epgn-kd = 12, Plaur-kd = 8. One-way ANOVA p<0.0001. P-values = Dunnett's Test.

See also **Supplemental Figure 3.1-3** and **Table 3.2-3**

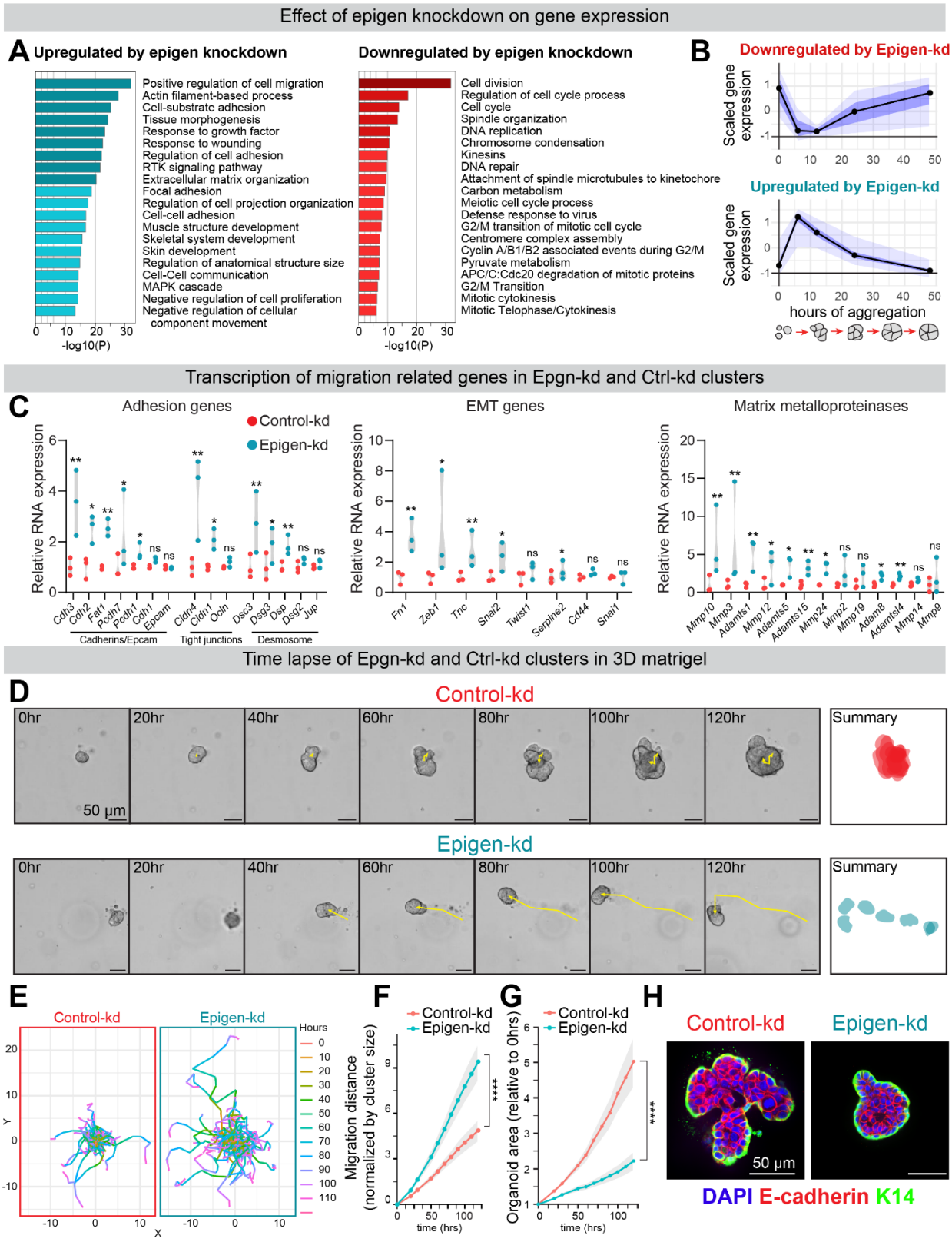
Effect of epigen knockdown on gene expression
A
Upregulated by epigen knockdown
Positive regulation of cell migration
Actin filament-based process
Cell-substrate adhesion
Tissue morphogenesis
Response to growth factor
Response to wounding
Regulation of cell adhesion
RTK signaling pathway
Extracellular matrix organization
Focal adhesion
Regulation of cell projection organization
Cell-cell adhesion
Muscle structure development
Skeletal system development
Skin development
Regulation of anatomical structure size
Cell-Cell communication
MAPK cascade
Negative regulation of cell proliferation
Negative regulation of cellular component movement
0 10 20 30
-log10(P)
Downregulated by epigen knockdown
Cell division
Regulation of cell cycle process
Cell cycle
Spindle organization
DNA replication
Chromosome condensation
Kinesins
DNA repair
Attachment of spindle microtubules to kinetochore
Carbon metabolism
Meiotic cell cycle process
Defense response to virus
G2/M transition of mitotic cell cycle
Centromere complex assembly
Cyclin A/B1/B2 associated events during G2/M
Pyruvate metabolism
APC/C:Cdc20 degradation of mitotic proteins
G2/M Transition
Mitotic cytokinesis
Mitotic Telophase/Cytokinesis
0 10 20 30
-log10(P)
B
Downregulated by Epigen-kd
Scaled gene expression
1
0
-1
0 10 20 30 40 50
Upregulated by Epigen-kd
Scaled gene expression
1
0
-1
0 10 20 30 40 50
hours of aggregation
Transcription of migration related genes in Epgn-kd and Ctrl-kd clusters
C
Adhesion genes
Control-kd
Epigen-kd
Relative RNA expression
0 2 4 6
Cdh3 Cdh2 Fat1 Pcdh7 Pcdh1 Cdh1 Epcam Cldn4 Cldn1 Ocln Dsc3 Dsg3 Dsp Dsg2 Jup
Cadherins/Epcam
Tight junctions
Desmosome
EMT genes
Relative RNA expression
0 2 4 6 8 10
Fn1 Zeb1 Tnc Snai2 Twist1 Serpine2 Cd44 Snai1
Matrix metalloproteinases
Relative RNA expression
0 5 10 15 20
Mmp10 Mmp3 Adamts1 Mmp12 Adamts5 Adamts15 Mmp24 Mmp2 Mmp19 Adam8 Adamts4 Mmp14 Mmp9
Time lapse of Epgn-kd and Ctrl-kd clusters in 3D matrigel
D
Control-kd
0hr 20hr 40hr 60hr 80hr 100hr 120hr
50 μm
Summary
Epigen-kd
0hr 20hr 40hr 60hr 80hr 100hr 120hr
Summary
E
Control-kd
Epigen-kd
Hours
0 10 20 30 40 50 60 70 80 90 100 110
Y
X
F
Control-kd
Epigen-kd
Migration distance (normalized by cluster size)
****
time (hrs)
G
Control-kd
Epigen-kd
Organoid area (relative to 0hrs)
****
time (hrs)
H
Control-kd
Epigen-kd
50 μm
DAPI E-cadherin K14

Figure 3.2. **Epigen suppression switches tumor cell clusters from a proliferative state to a migratory state.**

(A) Gene ontology analysis of differentially expressed genes in Epgn-kd clusters vs. Ctrl-kd clusters (aggregated 24 hrs; Metascape, FDR ≤ 0.05). **(B)** Comparison of aggregation induced genes (from **Figure 3.1C**) to genes differentially expressed in Epgn-kd vs. Ctrl-kd clusters (FDR ≤ 0.01). n=39 Epgn-kd downregulated genes, 107 upregulated genes. Black line = median. 50% CI = dark blue, 95% CI = light blue. **(C)** RNA expression of selected gene families in Ctrl-kd and Epgn-kd MMTV-PyMT clusters. n=3, adjusted p-values. **(D)** Time-lapse images of clusters in 3D basement membrane-rich gels. Right, summary of cluster size and location over 120 hrs. **(E)** Cumulative migration distance of individual clusters in 3D culture, normalized to initial cluster size. n (# of clusters): Ctrl-kd = 106, Epgn-kd = 102. n =4 biological replicates. P-values = unpaired t-tests. **(F)** Cumulative migration distance, normalized to initial cluster size, for Ctrl-kd and Epgn-kd clusters in 3D culture. n (# of clusters): Ctrl-kd = 106, Epgn-kd = 102. n = 4 biological replicates. P-values = unpaired t-tests. **(G)** Area measurements, relative to starting cluster area, of Ctrl-kd and Epgn-kd clusters in 3D culture. Mean with 95% CI. n (# of clusters): Ctrl-kd = 106, Epgn-kd = 102. n = 4 biological replicates. P-values = unpaired t-tests. **(H)** Keratin-14 and E-cadherin immunofluorescence of clusters in 3D culture.

See also **Supplemental Figure 3.3** and **Table 3.4**.

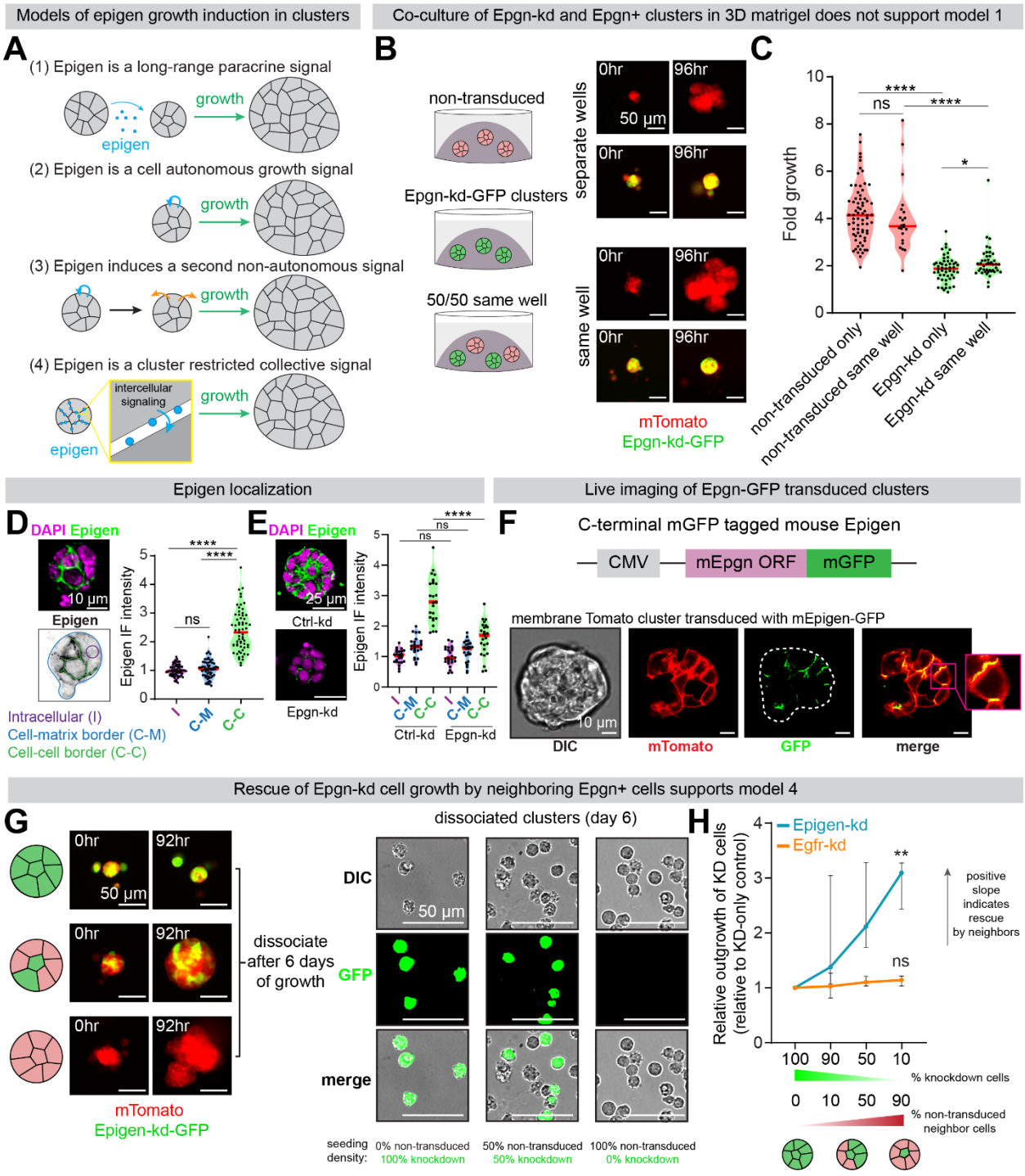
Models of epigen growth induction in clusters
Co-culture of Epgn-kd and Epgn+ clusters in 3D matrigel does not support model 1
A
(1) Epigen is a long-range paracrine signal
growth
epigen
(2) Epigen is a cell autonomous growth signal
growth
(3) Epigen induces a second non-autonomous signal
growth
(4) Epigen is a cluster restricted collective signal
intercellular signaling
growth
epigen
B
non-transduced
Epgn-kd-GFP clusters
50/50 same well
separate wells
same well
0hr
96hr
50 μm
mTomato
Epgn-kd-GFP
C
Fold growth
****
ns
****
*
non-transduced only
non-transduced same well
Epgn-kd only
Epgn-kd same well
Epigen localization
Live imaging of Epgn-GFP transduced clusters
D
DAPI Epigen
10 μm
Epigen
Epigen IF intensity
****
****
ns
I
C-M
C-C
Intracellular (I)
Cell-matrix border (C-M)
Cell-cell border (C-C)
E
DAPI Epigen
25 μm
Ctrl-kd
Epgn-kd
Epigen IF intensity
****
ns
ns
Ctrl-kd
Epgn-kd
F
C-terminal mGFP tagged mouse Epigen
CMV
mEpgn ORF
mGFP
membrane Tomato cluster transduced with mEpigen-GFP
10 μm
DIC
mTomato
GFP
merge
Rescue of Epgn-kd cell growth by neighboring Epgn+ cells supports model 4
G
0hr
92hr
50 μm
dissociate after 6 days of growth
mTomato
Epigen-kd-GFP
dissociated clusters (day 6)
DIC
GFP
merge
50 μm
seeding density:
0% non-transduced
100% knockdown
50% non-transduced
50% knockdown
100% non-transduced
0% knockdown
H
Epigen-kd
Egfr-kd
Relative outgrowth of KD cells (relative to KD-only control)
**
ns
positive slope indicates rescue by neighbors
100 90 50 10
% knockdown cells
0 10 50 90
% non-transduced neighbor cells

Figure 3.3 Epigen acts as a collective signaling factor shared non-cell-autonomously within clusters

(A) Possible mechanisms by which epigen is a signal for cluster outgrowth. **(B)** Epgn-kd and non-transduced clusters were cultured individually or co-cultured in the same 3D gel. Right, time lapse images of each condition. **(C)** Time-lapse fold outgrowth measurements of (B). n = 71 non-transduced clusters alone, 22 in co-culture. n= 51 Epgn-kd clusters alone, 44 in co-culture. n = 2 biological replicates. P-values = Mann-Whitney test. **(D)** Immunofluorescence of epigen in a MMTV-PyMT cluster ex vivo. Below, schematic of IF quantification. Right, quantification of epigen signal. n = 3 biological replicates, n = 63 clusters. P-values = Mann-Whitney tests. **(E)** Immunofluorescence of epigen in Ctrl-kd and Epgn-kd clusters. Right, quantification of mean intensity in different regions. n = 2 biological replicates, 30 clusters per condition. P-values = Mann-Whitney test. **(F)** Live imaging of a mTomato PyMT cluster expressing epigen-mGFP. **(G)** Left, time lapse images of Epgn-kd-GFP and non-transduced mTomato-PyMT cells aggregated at different ratios to form pure or mosaic clusters. Right, dissociated cells after 6 days of culture. **(H)** Relative outgrowth of Epgn-kd or Egfr-kd cells when mixed with different proportions of non-transduced cells. Epgn-kd n = 3 biological replicates (36,022 cells). Egfr-kd n=4 biological replicates (19,911 cells). Median and 95% CI. P-values = unpaired t-tests vs. 100% knockdown clusters.

See also **Supplemental Figure 3.4**.

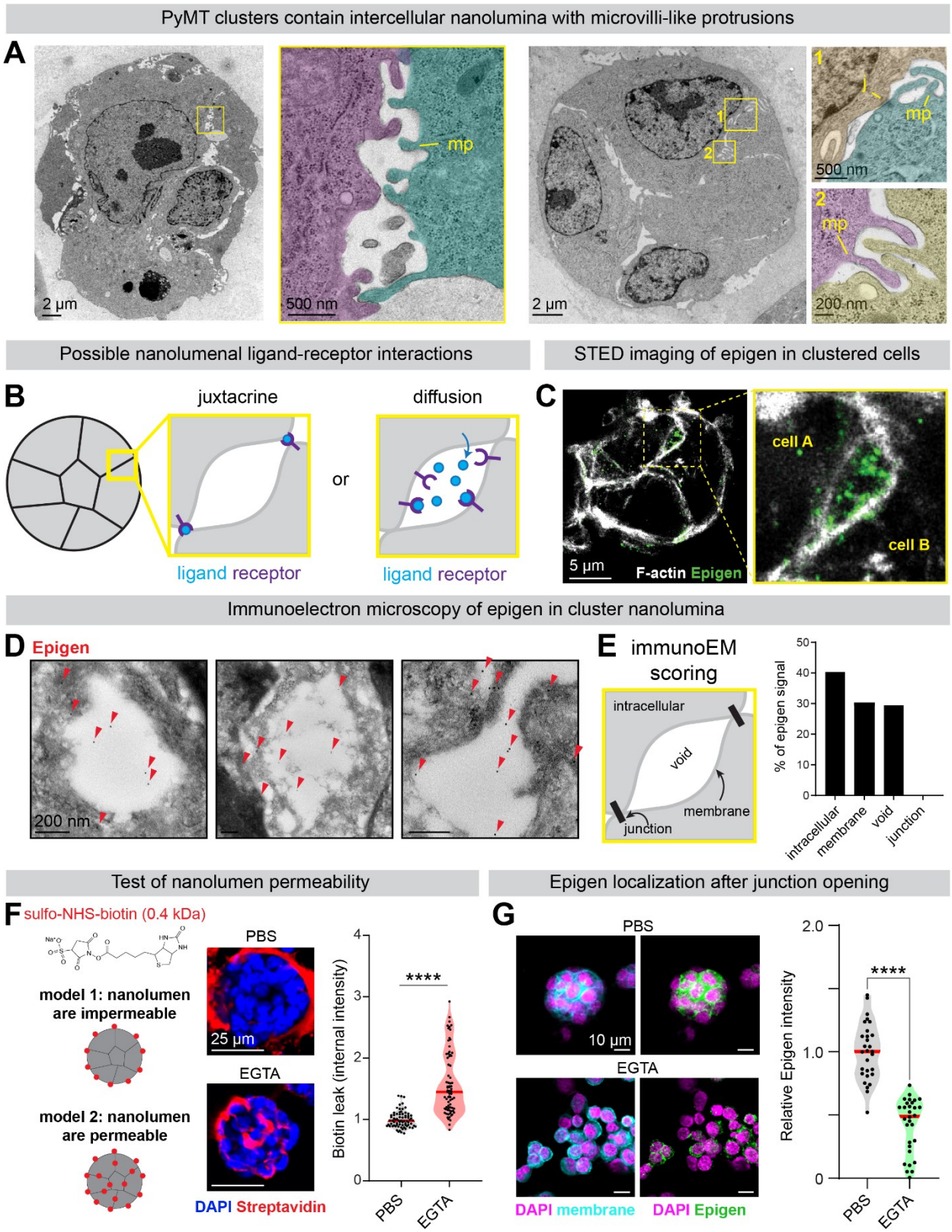
PyMT clusters contain intercellular nanolumina with microvilli-like protrusions
A
2 µm
mp
500 nm
1
2
200 nm
Possible nanolumenal ligand-receptor interactions
STED imaging of epigen in clustered cells
B
juxtacrine
diffusion
or
ligand receptor
ligand receptor
C
cell A
cell B
5 µm
F-actin Epigen
Immunoelectron microscopy of epigen in cluster nanolumina
D
Epigen
200 nm
E
immunoEM scoring
intracellular
void
membrane
junction
% of epigen signal
intracellular
membrane
void
junction
Test of nanolumen permeability
Epigen localization after junction opening
F
sulfo-NHS-biotin (0.4 kDa)
model 1: nanolumen are impermeable
model 2: nanolumen are permeable
PBS
25 µm
EGTA
DAPI Streptavidin
Biotin leak (internal intensity)
****
PBS
EGTA
G
PBS
10 µm
EGTA
DAPI membrane
DAPI Epigen
Relative Epigen intensity
****
PBS
EGTA

Figure 3.4. Epigen is stored and concentrated within intercellular nanolumina.

(A) TEM images of MMTV-PyMT clusters (pseudo-colored). MP = microvilli-like protrusions. J = cell-cell junction. **(B)** Models of intercellular epigen signaling as a membrane-restricted juxtacrine ligand or a diffusible paracrine ligand. **(C)** Epigen immunofluorescence stimulated emission depletion microscopy images in a MMTV-PyMT cluster. **(D)** Immunogold labeling of epigen in MMTV-PyMT clusters. Arrows = gold labeling. **(E)** Schematic of features scored for immunogold signal. Right, quantification of epigen immunogold signal. n=268 gold particles. **(F)** To assess junctional permeability, clusters were incubated with sulfo-NHS-biotin. EGTA was used as a positive control to disrupt cell-cell junctions. Right, quantification of streptavidin-FITC fluorescence. n = 3 biological replicates. n = 75 clusters per condition. P-values = Mann-Whitney tests. **(G)** Immunofluorescence of epigen in clusters +/- 1mM EGTA treatment. Right, median epigen intensity per cluster. n=3 biological replicates, 59 clusters. P-value = Mann-Whitney test.

See also **Supplemental Figure 3.4-5**.

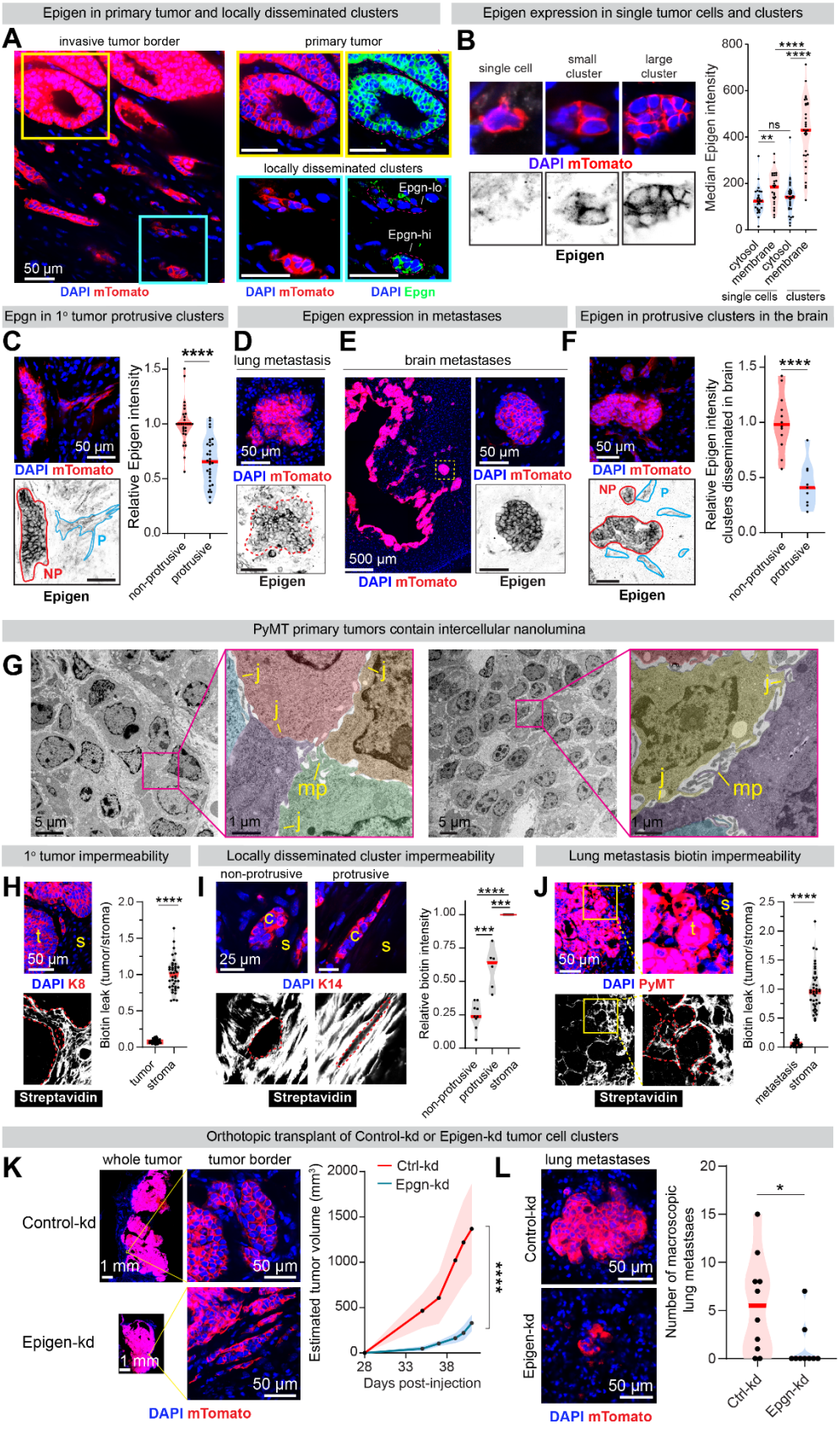
Epigen in primary tumor and locally disseminated clusters
Epigen expression in single tumor cells and clusters
A
invasive tumor border
primary tumor
locally disseminated clusters
Epgn-lo
Epgn-hi
50 µm
DAPI mTomato
DAPI mTomato
DAPI Epgn
B
single cell
small cluster
large cluster
DAPI mTomato
Epigen
Median Epigen intensity
800
600
400
200
0
****
****
ns
**
cytosol
membrane
cytosol
membrane
single cells
clusters
Epgn in 1° tumor protrusive clusters
Epigen expression in metastases
Epigen in protrusive clusters in the brain
C
50 µm
DAPI mTomato
NP
P
Epigen
Relative Epigen intensity
1.5
1.0
0.5
0.0
****
non-protrusive
protrusive
D
lung metastasis
50 µm
DAPI mTomato
Epigen
E
brain metastases
500 µm
DAPI mTomato
50 µm
DAPI mTomato
Epigen
F
50 µm
DAPI mTomato
NP
P
Epigen
Relative Epigen intensity clusters disseminated in brain
1.5
1.0
0.5
0.0
****
non-protrusive
protrusive
PyMT primary tumors contain intercellular nanolumina
G
5 µm
1 µm
j
mp
5 µm
1 µm
1° tumor impermeability
Locally disseminated cluster impermeability
Lung metastasis biotin impermeability
H
t
s
50 µm
DAPI K8
Streptavidin
Biotin leak (tumor/stroma)
2.0
1.5
1.0
0.5
0.0
****
tumor
stroma
I
non-protrusive
protrusive
c
s
25 µm
DAPI K14
Streptavidin
Relative biotin intensity
1.00
0.75
0.50
0.25
0.00
****
***
***
non-protrusive
protrusive
stroma
J
t
s
50 µm
DAPI PyMT
Streptavidin
Biotin leak (tumor/stroma)
2.5
2.0
1.5
1.0
0.5
0.0
****
metastasis
stroma
Orthotopic transplant of Control-kd or Epigen-kd tumor cell clusters
K
whole tumor
tumor border
Control-kd
Epigen-kd
1 mm
50 µm
1 mm
50 µm
DAPI mTomato
Estimated tumor volume (mm³)
2000
1500
1000
500
0
Ctrl-kd
Epgn-kd
****
28
33
38
Days post-injection
L
lung metastases
Control-kd
Epigen-kd
50 µm
50 µm
DAPI mTomato
Number of macroscopic lung metastsaes
20
15
10
5
0
*
Ctrl-kd
Epgn-kd

Figure 3.5. Epigen suppression reduces both primary and metastatic tumor outgrowth.

(A) Immunofluorescence of epigen in a mTomato-PyMT primary tumor and adjacent clusters 10 weeks after orthotopic transplant in non-fluorescent NSG mouse. **(B)** Quantification of epigen expression in locally disseminated single tumor cells and non-protrusive tumor cell clusters. n = 27 single cells, 33 clusters. n=2 tumors. P-values = Mann-Whitney tests. **(C)** Immunofluorescence of epigen in locally disseminated clusters adjacent to a primary tumor. NP=non-protrusive, P=protrusive. Right, relative epigen intensity. n=3 tumors. n=29 non-protrusive, 31 protrusive clusters (clusters with intermediate morphology were not scored). P-value = Mann-Whitney test. **(D)** Epigen immunofluorescence of a spontaneous lung metastasis 10 weeks after mTomato-PyMT organoid orthotopic transplant. **(E)** Epigen immunofluorescence in brain metastases 6 weeks after mTomato-PyMT cluster intracardiac injection. **(F)** Epigen immunofluorescence in the brain 6 wks after intracardiac mTomato-PyMT cluster injection. n=3 mice. n = 12 non-protrusive, 9 protrusive clusters. P-value = Mann-Whitney test. **(G)** TEM of an MMTV-PyMT tumor. Pseudo-color highlights different cells. MP = microvilli-like protrusions. J = cell-cell junctions. **(H)** Immunofluorescence of Keratin-8 (K8) and FITC-streptavidin in MMTV-PyMT primary tumors treated with sulfo-NHS-biotin. Right, FITC-streptavidin quantification. n=3 tumors, 50 tumor areas (“t”), 50 stromal (“s”) areas. P-value = Mann-Whitney test. **(I)** Immunofluorescence of Keratin-14 and FITC-streptavidin in locally disseminated clusters from tumors fixed after sulfo-NHS-biotin treatment. Right, for each cluster, internal FITC-streptavidin signal relative to adjacent

stroma. n=15 clusters (9 non-protrusive, 6 protrusive), n=2 tumors. P-values = Mann-Whitney tests. **(J)** Immunofluorescence of PyMT and FITC-streptavidin in mouse lungs 2 weeks after tail vein injection of MMTV-PyMT clusters, lungs treated with sulfo-NHS-biotin before fixation. Right, FITC-streptavidin quantification. n=3 mice, 50 metastasis areas ("t"), 32 stromal areas ("s"). P-value = Mann-Whitney test. **(K)** Primary tumors 6 weeks after orthotopic transplant of Ctrl-kd or Epgn-kd PyMT clusters. Right, estimated tumor volume. n=10 Ctrl-kd mice, 9 Epgn-kd mice. P-value = Mann-Whitney test. **(L)** Left, lung metastases 6 weeks after orthotopic transplant. Right, # of visible GFP+ lung macrometastases per mouse. n=10 Ctrl-kd mice, 9 Epgn-kd mice. P-value = Mann-Whitney test.

See also **Supplemental Figure 3.6**.

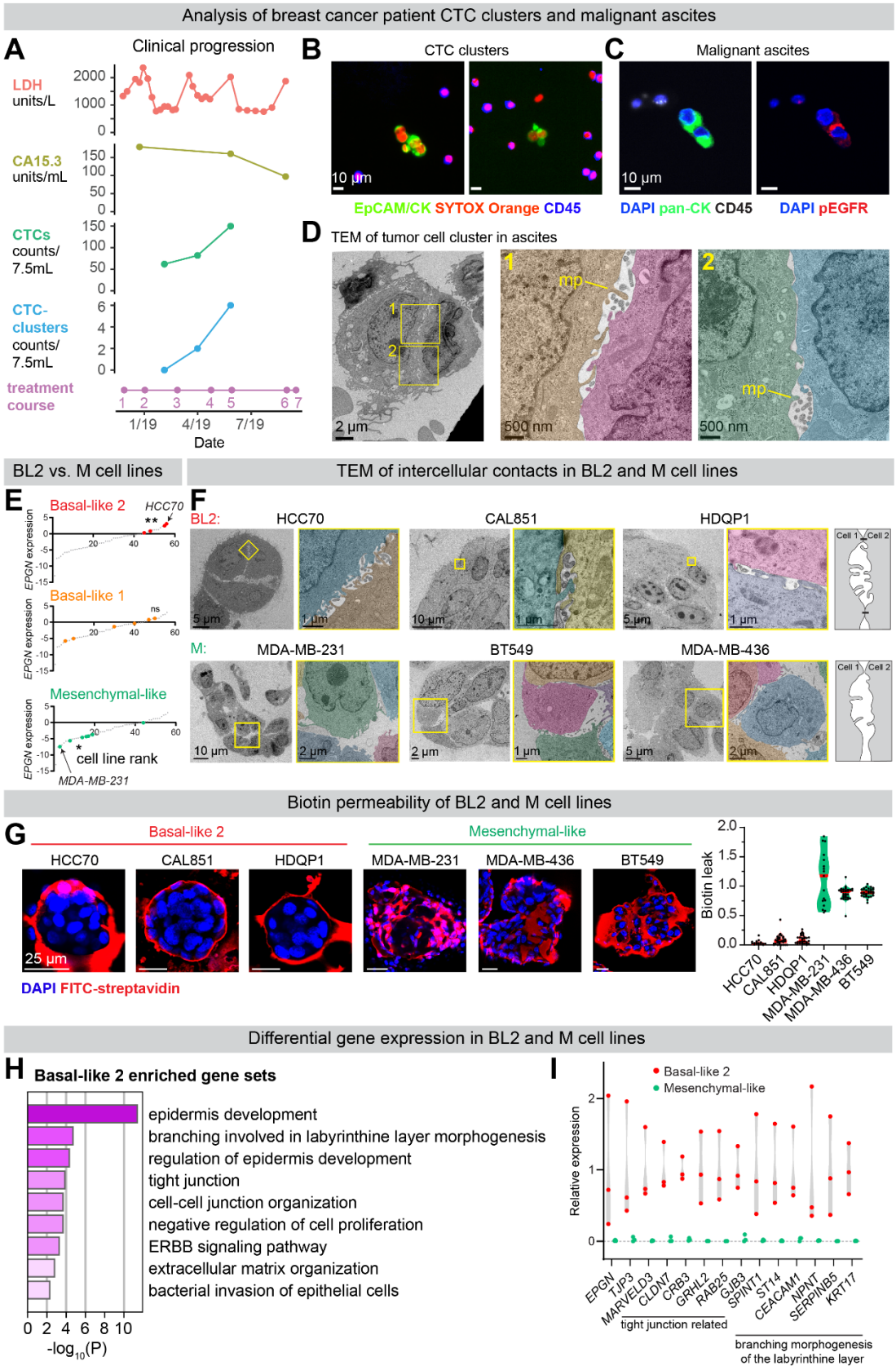
Analysis of breast cancer patient CTC clusters and malignant ascites
A
Clinical progression
LDH units/L
CA15.3 units/mL
CTCs counts/ 7.5mL
CTC-clusters counts/ 7.5mL
treatment course
1/19
4/19
7/19
Date
B
CTC clusters
EpCAM/CK SYTOX Orange CD45
C
Malignant ascites
DAPI pan-CK CD45
DAPI pEGFR
D
TEM of tumor cell cluster in ascites
mp
BL2 vs. M cell lines
TEM of intercellular contacts in BL2 and M cell lines
E
Basal-like 2
Basal-like 1
Mesenchymal-like
EPGN expression
cell line rank
MDA-MB-231
F
BL2:
HCC70
CAL851
HDQP1
M:
MDA-MB-231
BT549
MDA-MB-436
Cell 1
Cell 2
Biotin permeability of BL2 and M cell lines
G
Basal-like 2
Mesenchymal-like
HCC70
CAL851
HDQP1
MDA-MB-231
MDA-MB-436
BT549
DAPI FITC-streptavidin
Biotin leak
Differential gene expression in BL2 and M cell lines
H
Basal-like 2 enriched gene sets
epidermis development
branching involved in labyrinthine layer morphogenesis
regulation of epidermis development
tight junction
cell-cell junction organization
negative regulation of cell proliferation
ERBB signaling pathway
extracellular matrix organization
bacterial invasion of epithelial cells
-log10(P)
I
Basal-like 2
Mesenchymal-like
Relative expression
EPGN
TJP3
MARVELD3
CLDN7
CRB3
GRHL2
RAB25
GJB3
SPINT1
ST14
CEACAM1
NPNT
SERPINB5
KRT17
tight junction related
branching morphogenesis of the labyrinthine layer

Figure 3.6. Epigen expression and nanolumina formation are associated with the basal-like 2 subgroup of triple-negative breast cancer.

(A) Clinical progression of a patient with metastatic ER+/PR+/HER2- breast cancer Treatment course: (1) vinorelbine, (2) cytoxan/methotrexate, (3) drug holiday, (4) cytoxan/methotrexate, (5) irinotecan, (6) low dose doxorubicin, (7) hospice. LDH = serum lactate dehydrogenase. CA15.3 = cancer antigen 15-3. **(B)** CTC clusters in the blood. EpCAM/pan-CK = epithelial cells. CD45 = immune cells. SYTOX Orange = nucleic acid stain. **(C)** pEGFR (Y1068) IF of tumor cell clusters in malignant ascites (pan-CK+ = epithelial cells, CD45+ = immune cells). **(D)** TEM of malignant ascites from a metastatic breast cancer patient. MP = microvilli-like protrusion. **(E)** Epigen mRNA expression in human cell lines (Barretina et al., 2012) classified by triple-negative breast cancer sub-groups (Lehmann et al., 2011). P-values = Kolmogorov-Smirnov tests. **(F)** TEM of tumor cell clusters from basal-like 2 and mesenchymal-like breast cancer cell lines. Right, schematic of intercellular morphologies. **(G)** Test of cluster permeability using sulfo-NHS-biotin. Right, quantification of biotin leak (biotin signal internal to the cluster divided by biotin signal along the cell-matrix border of the cluster). n (# clusters/# biological replicates): HCC70 = 25/2, CAL851 = 30/3, HDQP1 = 30/3, MDA-MB-231 = 17/2, MDA-MB-436 = 30/3, BT549 = 30/3. **(H)** Gene sets (Metascape, FDR ≤ 0.01) enriched in BL2 (HCC70, CAL851, HDQP1) vs. M-like (MDA-MB-231, MDA-MB-436, BT549) cell lines (CCLE). **(I)** RNA expression of individual genes (CCLE) in BL2 (HCC70, CAL851, HDQP1) vs. M-like (MDA-MB-231, MDA-MB-436, BT549) cell lines.

See also **Supplemental Figure 3.7** and **Table 3.5**.

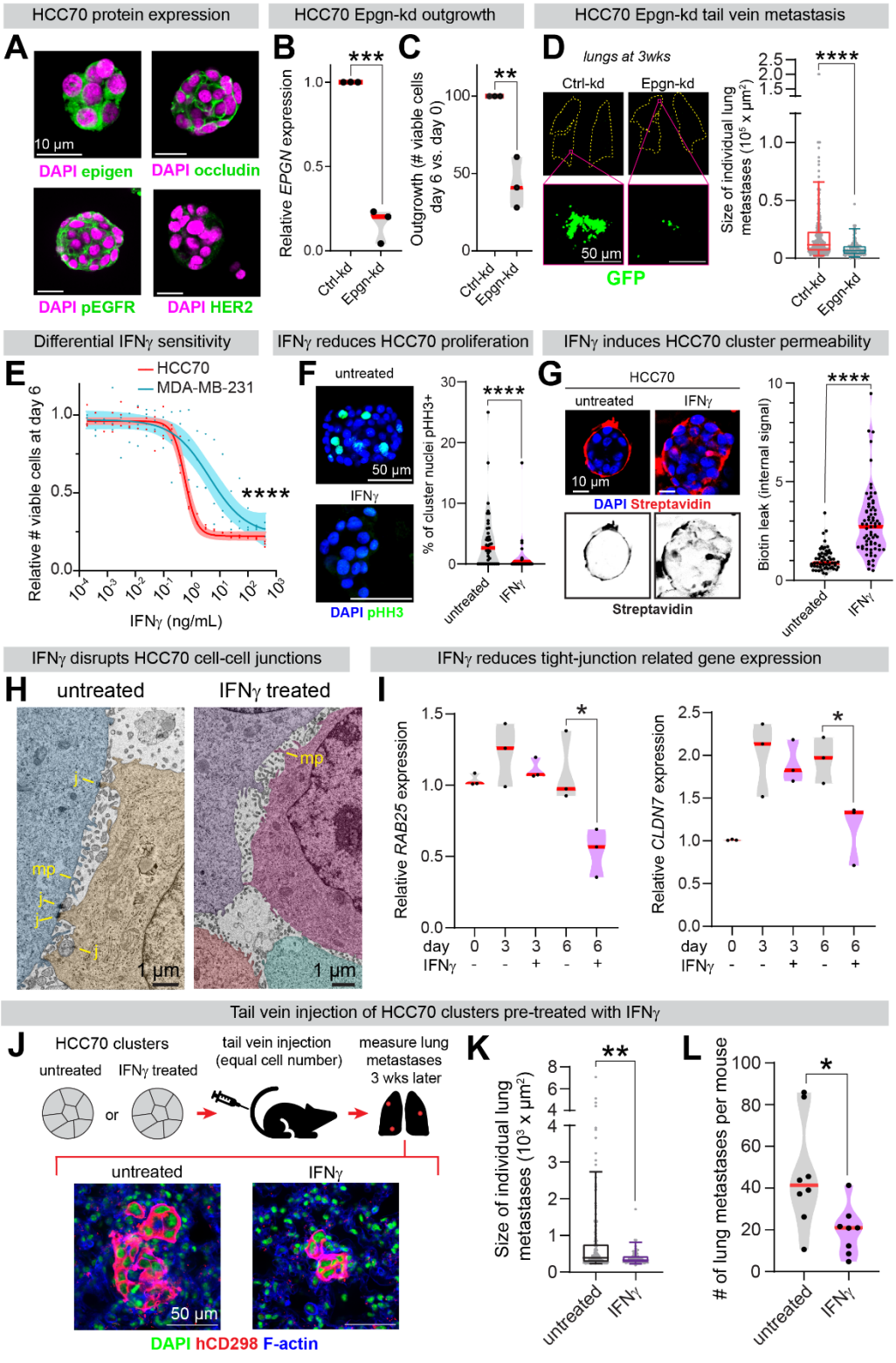
HCC70 protein expression
HCC70 Epgn-kd outgrowth
HCC70 Epgn-kd tail vein metastasis
A
10 μm
DAPI epigen
DAPI occludin
DAPI pEGFR
DAPI HER2
B
Relative EPGN expression
***
Ctrl-kd
Epgn-kd
C
Outgrowth (# viable cells day 6 vs. day 0)
**
D
lungs at 3wks
Ctrl-kd
Epgn-kd
50 μm
GFP
Size of individual lung metastases (10⁵ x μm²)
****
Differential IFNγ sensitivity
IFNγ reduces HCC70 proliferation
IFNγ induces HCC70 cluster permeability
E
HCC70
MDA-MB-231
Relative # viable cells at day 6
****
IFNγ (ng/mL)
F
untreated
50 μm
IFNγ
DAPI pHH3
% of cluster nuclei pHH3+
****
G
HCC70
untreated
IFNγ
10 μm
DAPI Streptavidin
Streptavidin
Biotin leak (internal signal)
****
IFNγ disrupts HCC70 cell-cell junctions
IFNγ reduces tight-junction related gene expression
H
untreated
IFNγ treated
mp
j
1 μm
I
Relative RAB25 expression
*
day
IFNγ
Relative CLDN7 expression
*
Tail vein injection of HCC70 clusters pre-treated with IFNγ
J
HCC70 clusters
untreated
IFNγ treated
or
tail vein injection
(equal cell number)
measure lung metastases 3 wks later
untreated
IFNγ
50 μm
DAPI hCD298 F-actin
K
Size of individual lung metastases (10³ x μm²)
**
L
# of lung metastases per mouse
*

Figure 3.7. HCC70 outgrowth depends on epigen expression and is sensitive to IFNγ which induces nanolumen permeability.

(A) Immunofluorescence of HCC70 (basal-like 2, epigen high cell line) clusters. **(B)** qPCR of *EPGN* in Ctrl-kd and Epgn-kd HCC70 clusters. n=3 biological replicates. P-values = unpaired t-tests. **(C)** Ctrl-kd and Epgn-kd HCC70 viable cell count (day 6 vs. day 0). n=3 biological replicates. P-values = unpaired t-tests. **(D)** Left, lungs 3 weeks after tail vein injection of Ctrl-kd or Epgn-kd HCC70 clusters. Right, individual metastasis areas. n (# of metastases): Ctrl-kd = 299, Epgn-kd = 87. n=7 mice/condition. Box plot = 5-95%. P-value = Mann-Whitney test. **(E)** Viable cell quantification after 6 days of IFNγ treatment. Line = non-linear regression. Band = 95% CI. n = 3 biological replicates. P-value = extra sum-of-squares F test. **(F)** pHH3 IF to mark mitotic cells in HCC70 clusters after 6 days +/- 3 ng/mL IFNγ treatment. Right, % pHH3+ nuclei in clusters from each condition. n=3 biological replicates. n = 40 untreated, 34 IFNγ treated clusters. P-value = Mann-Whitney test. **(G)** Biotin permeability of HCC70 clusters after 6 days +/- 3ng/mL IFNγ. Right, internal FITC-streptavidin intensity per cluster. n = 60 untreated, 70 IFNγ treated clusters. n = 3 biological replicates. P-value = Mann-Whitney test. **(H)** TEM of HCC70 clusters after 6 days +/- IFNγ treatment (3 ng/mL). Cells pseudo-colored. MP = microvilli-like protrusions. J = cell-cell junctions. **(I)** qPCR of (left) *RAB25* and (right) *CLDN7* in HCC70 clusters +/- 3 ng/mL IFNγ treatment. n=3 biological replicates. P-value = unpaired t-test. **(J)** HCC70 clusters (24hrs aggregation) were treated +/- 2 ng/mL IFNγ. After 6 days, clusters from each condition were injected by tail vein into NSG mice (200,000 viable clustered cells per mouse). 3 weeks later, lung metastases were scored using a human-

specific CD298 antibody. **(K)** Sizes of individual HCC70 metastases 3 weeks after cluster tail vein injection. n=8 mice/condition, 217 untreated metastases, 79 IFNγ pre-treated metastases. Box plot = 5-95%. P-value = Mann-Whitney test. **(L)** Number of lung metastases per mouse 3 weeks after HCC70 cluster tail vein injection +/- IFNγ (2ng/mL) pre-treatment. n=8 mice/condition. P-value = Mann-Whitney test.

See also **Supplemental Figure 3.7**.

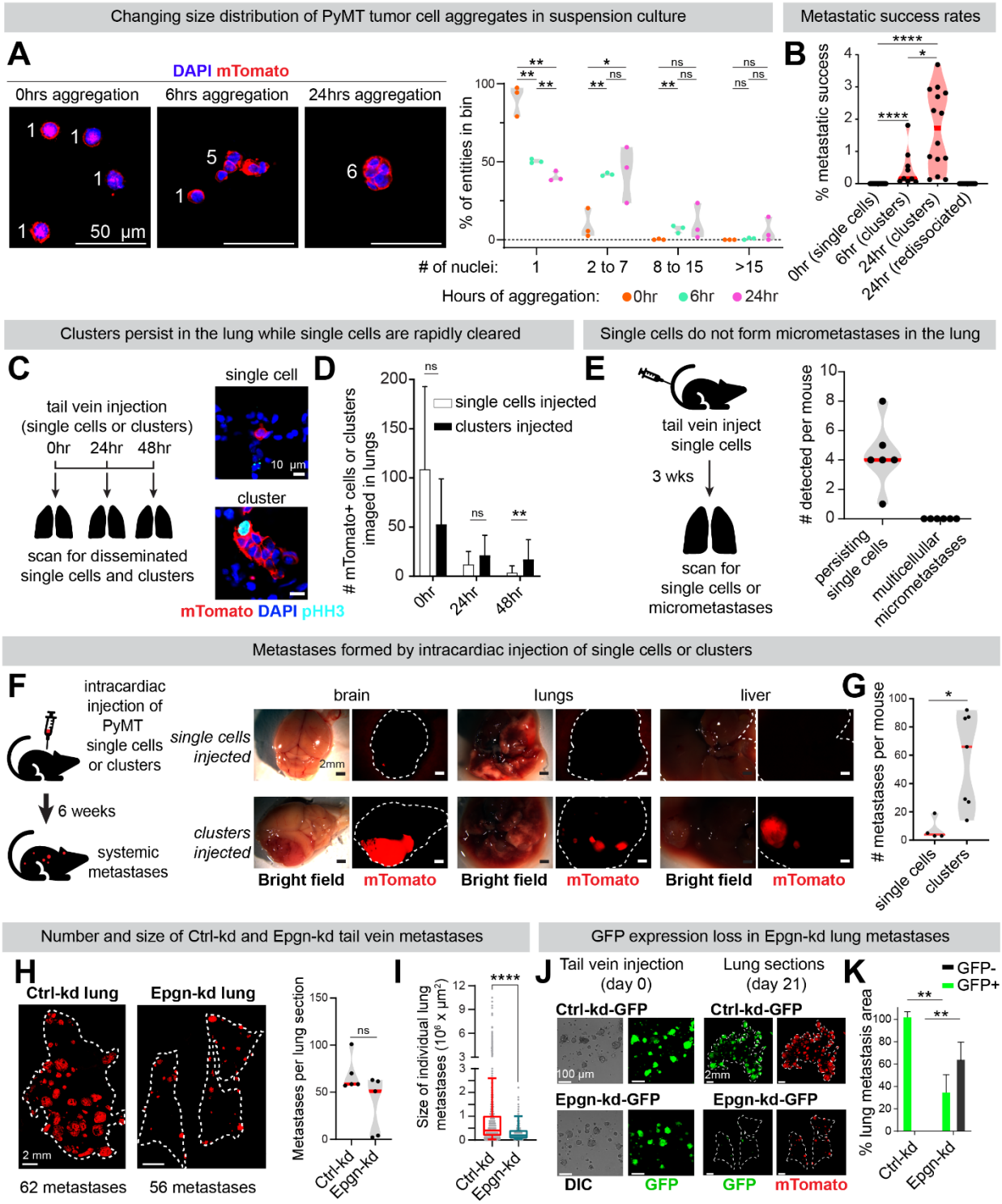
Changing size distribution of PyMT tumor cell aggregates in suspension culture
Metastatic success rates
A
DAPI mTomato
0hrs aggregation
6hrs aggregation
24hrs aggregation
50 μm
% of entities in bin
# of nuclei:
1
2 to 7
8 to 15
>15
Hours of aggregation:
0hr
6hr
24hr
B
% metastatic success
0hr (single cells)
6hr (clusters)
24hr (clusters)
24hr (redissociated)
Clusters persist in the lung while single cells are rapidly cleared
Single cells do not form micrometastases in the lung
C
tail vein injection
(single cells or clusters)
0hr 24hr 48hr
scan for disseminated
single cells and clusters
single cell
cluster
10 μm
mTomato DAPI pHH3
D
mTomato+ cells or clusters
imaged in lungs
single cells injected
clusters injected
0hr
24hr
48hr
E
tail vein inject
single cells
3 wks
scan for
single cells or
micrometastases
detected per mouse
persisting
single cells
multicellular
micrometastases
Metastases formed by intracardiac injection of single cells or clusters
F
intracardiac
injection of
PyMT
single cells
or clusters
6 weeks
systemic
metastases
brain
lungs
liver
single cells
injected
clusters
injected
2mm
Bright field
mTomato
G
metastases per mouse
single cells
clusters
Number and size of Ctrl-kd and Epgn-kd tail vein metastases
GFP expression loss in Epgn-kd lung metastases
H
Ctrl-kd lung
Epgn-kd lung
2 mm
62 metastases
56 metastases
Metastases per lung section
Ctrl-kd
Epgn-kd
I
Size of individual lung
metastases (10^6 x μm^2)
J
Tail vein injection
(day 0)
Lung sections
(day 21)
Ctrl-kd-GFP
Epgn-kd-GFP
100 μm
2mm
DIC
GFP
mTomato
K
GFP-
GFP+
% lung metastasis area

Supplemental Figure 3.1. Characterizing single cell vs. cluster metastatic potential and persistence in vivo. Related to Figure 3.1.

(A) MMTV-PyMT mTomato+ single cells were aggregated for 0, 6, or 24 hrs and stained for DAPI. Right: quantification of number of nuclei per entity (single confocal slice), with a mean number of cells per cluster of 4.4 (SD ± 4.2) and 5.4 (SD ± 5.2) at 6 and 24 hrs, respectively. n=3 biological replicates. n (# entities, single cells or clusters): 0hr=307, 6hr=359, 24hr=326. P-values = unpaired t-tests. **(B)** Number of metastases formed 3 weeks after mTomato-PyMT tail vein relative to the number of entities (single cells or clusters) injected based on measurements in Fig. S1A. % success = (100 x number of metastases)/number of entities injected. n (# mice) = 19 (0hr), 9 (6hr), 14 (24hr), 10 (re-dissociated). P-values = Mann-Whitney tests. Medians: 0hr = 0%, 6hr = 0.16%, 24hr clusters = 1.72%, 24hr redissociated = 0%. **(C)** Experimental schematic: 200,000 mTomato-PyMT cells were injected by tail vein into NSG mice either as single cells or clusters. 0, 24, and 48 hrs after injection the lungs were harvested. Non-consecutive sections were imaged and the number of mTomato+ clusters and single cells was quantified for each field of view. **(D)** Quantification of the number of mTomato+ single cells or clusters detected in lung sections at 0, 24, and 48 hrs after tail vein injection. For each mouse 3 sections were imaged (10 25x fields per section). n=4 mice per time point. **(E)** To determine whether single tumor cells form micro-metastases that are not visible at low magnification, lungs were sectioned 3 weeks after tail vein injection of single mTomato+ PyMT cells. Sections were imaged at 10x magnification and the number of mTomato+ single cells and clusters was counted. n=6 mice, 1 section per mouse. **(F)**

Schematic of intracardiac injection of mTomato-PyMT clusters or single cells into the left ventricle of immunocompromised mice to generate systemic metastases. Right, organs 6 weeks after intracardiac injection. **(G)** Quantification of systemic metastases 6 weeks after intracardiac injection of mTomato-PyMT clusters. n = 4 single cell injected mice, 7 cluster injected mice. p-values = Mann-Whitney test. **(H)** Lung sections of mice injected by tail vein with Ctrl-kd or Epgn-kd clusters. Red signal = mTomato+ metastases. Right, quantification of the number of metastases per lung section. n = 5 mice per condition, 1-2 sections per mouse. P-value = Mann-Whitney test. **(I)** Size of individual lung metastases 3 weeks after tail vein injection of Ctrl-kd or Epgn-kd clusters. Box plot = 5-95%. P-value = Mann-Whitney test. **(J)** Left: 24hr aggregated Ctrl-kd-GFP and Epgn-kd-GFP clusters shortly before tail vein injection. Right: lung sections 3 weeks after tail vein injection of mTomato-PyMT Ctrl-kd-GFP or Epgn-kd-GFP clusters. **(K)** Quantification of double positive (GFP+ and mTomato+) and shRNA escape (mTomato+ but GFP-) areas in Ctrl-kd or Epgn-kd lung metastases 3 weeks after tail vein injection. n = 3 mice per condition. P-values = unpaired t-tests.

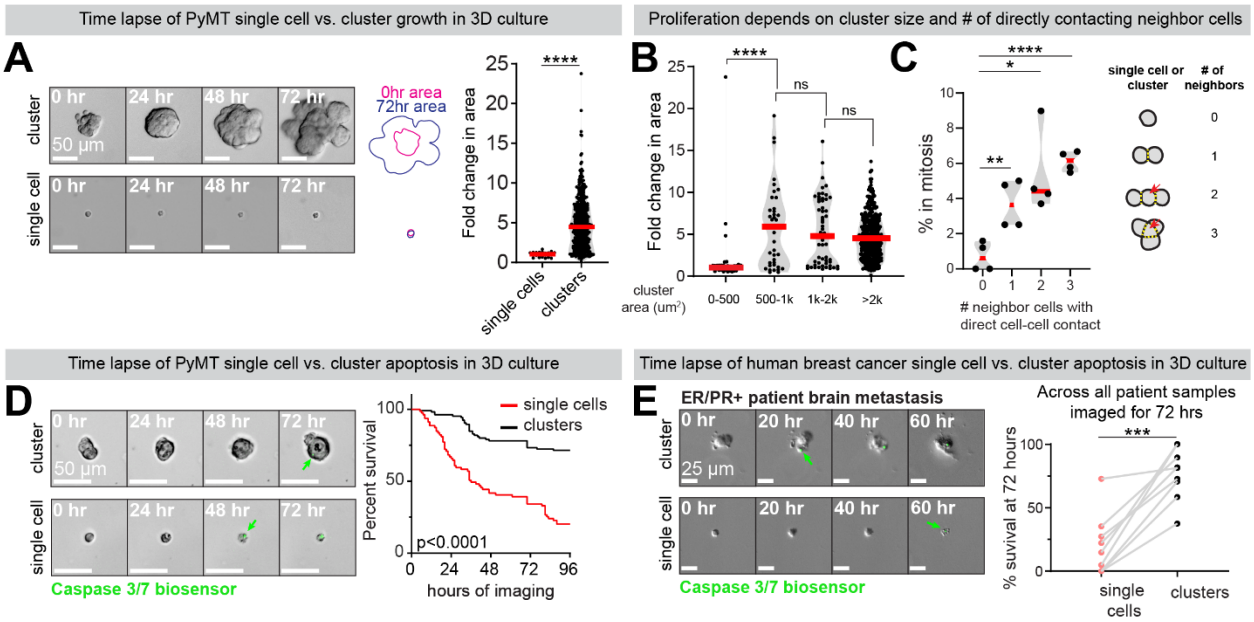

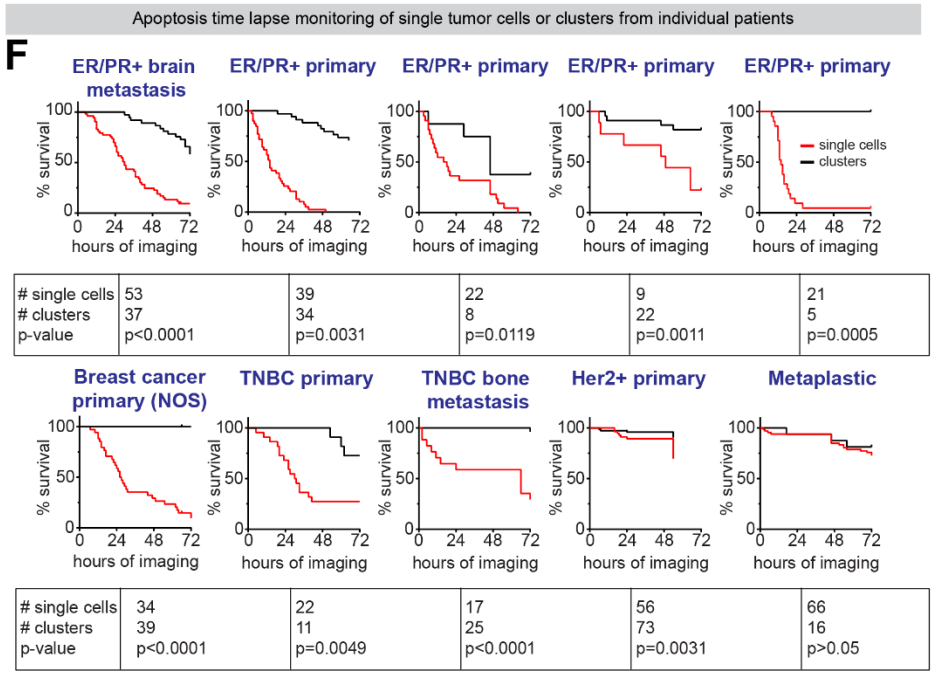

# single cells	53	39	22	9	21
# clusters	37	34	8	22	5
p-value	p<0.0001	p=0.0031	p=0.0119	p=0.0011	p=0.0005

# single cells	34	22	17	56	66
# clusters	39	11	25	73	16
p-value	p<0.0001	p=0.0049	p<0.0001	p=0.0031	p>0.05

Supplemental Figure 3.2. Clustered tumor cells show increased survival and outgrowth ex vivo compared to single cells. Related to Figure 3.1.

(A) Time lapse images of a MMTV-PyMT single cell and cluster cultured in 3D basement membrane-rich gels for 4 days. Right, outgrowth quantification as fold change in area. n = 8 mice, 23 single cells, 500 clusters. P-value = Mann-Whitney test. **(B)** Outgrowth measured by fold change in area over 4 days of time lapse imaging for MMTV-PyMT single cells and clusters of different sizes in 3D basement membrane-rich gels. P-values = Mann-Whitney tests. n (# of single cells or clusters): 0-500 μm^2 = 39, 500-1000 μm^2 = 39, 1000-2000 μm^2= 58, >2000 μm^2= 387. n = 8 biological replicates. **(C)** % of nuclei in mitosis (scored by pHH3 staining) binned by number of neighboring cells with visible direct membrane-membrane contact. n = 4 biological replicates. n (# cells): 0 contacts (single cells) = 453, 1 contact = 698, 2 contacts = 704, 3 contacts = 667. P-values = unpaired t-tests. **(D)** Time lapse DIC and GFP images of a MMTV-PyMT single cell and cluster in the presence of a caspase-3/7 activated green fluorescing DNA dye in 3D basement membrane-rich gels. Right, quantification of MMTV-PyMT single cell vs. cluster survival over time. Clusters were marked as dead once a majority of cells in the clusters apoptosed. n = 4 mice, 79 single cells and 105 clusters. P-value = Mantel-Cox. **(E)** Time lapse DIC and GFP (Caspase 3/7 biosensor) images of a single cell and cluster derived from a human breast cancer brain metastasis. Right, summary of single cell vs. cluster survival after 72hrs of time lapse in 3D basement membrane-rich gels from 9 human breast tumor specimens (HU1-8, 10). n = 283 single cells and 197 clusters. P-

value = pairwise t-test. **(F)** Survival of single cells vs. clusters from 10 individual human breast cancer patient samples (HU1-10). P-values = Mantel-Cox.

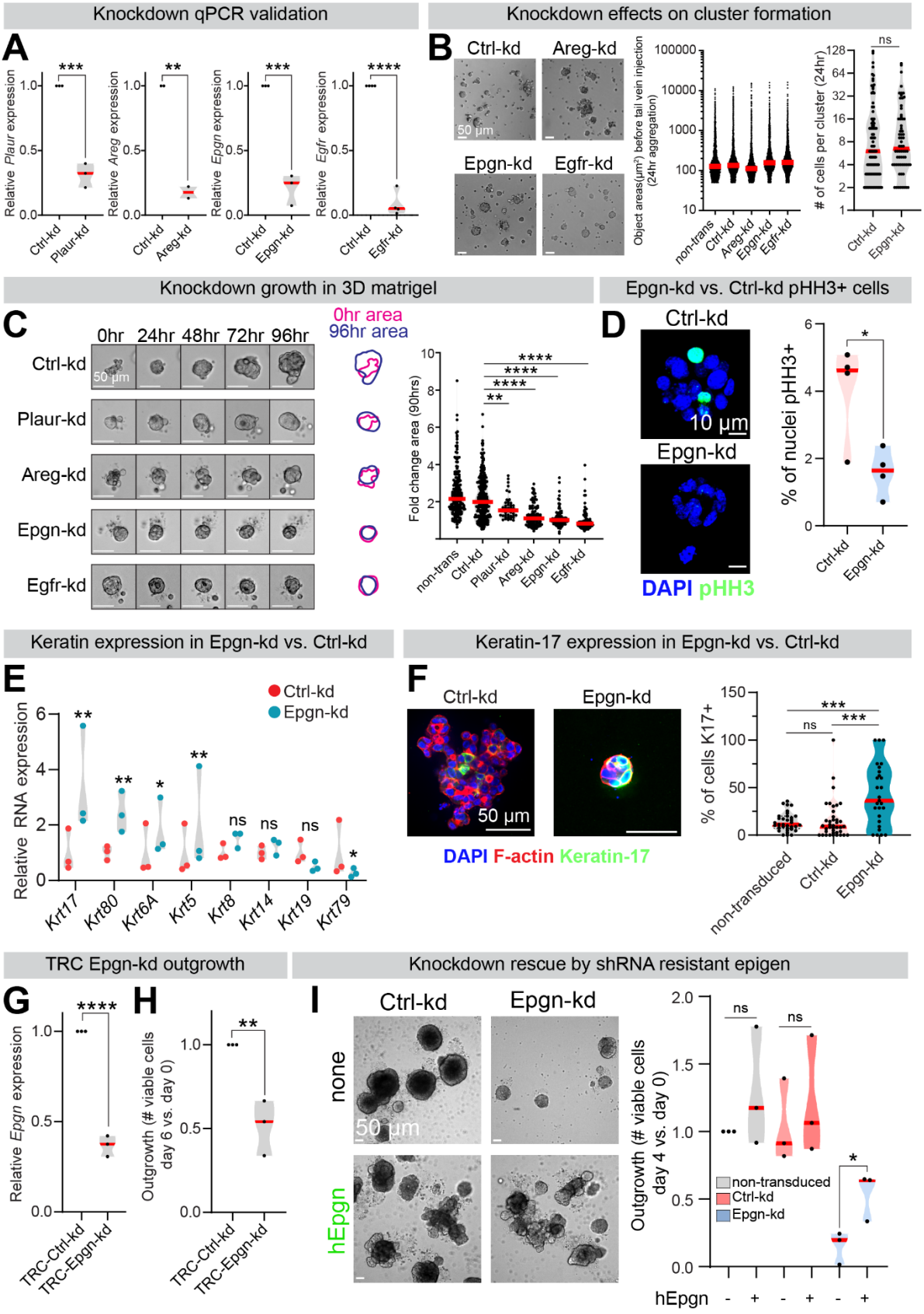
Knockdown qPCR validation
Knockdown effects on cluster formation
A
Relative Plaur expression
Relative Areg expression
Relative Epgn expression
Relative Egfr expression
Ctrl-kd
Plaur-kd
Areg-kd
Epgn-kd
Egfr-kd
B
Ctrl-kd
Areg-kd
Epgn-kd
Egfr-kd
50 μm
Object areas(μm²) before tail vein injection (24hr aggregation)
non-trans
# of cells per cluster (24hr)
ns
Knockdown growth in 3D matrigel
Epgn-kd vs. Ctrl-kd pHH3+ cells
C
0hr
24hr
48hr
72hr
96hr
0hr area
96hr area
Fold change area (90hrs)
D
10 μm
% of nuclei pHH3+
DAPI pHH3
Keratin expression in Epgn-kd vs. Ctrl-kd
Keratin-17 expression in Epgn-kd vs. Ctrl-kd
E
Relative RNA expression
Krt17
Krt80
Krt6A
Krt5
Krt8
Krt14
Krt19
Krt79
F
50 μm
DAPI F-actin Keratin-17
% of cells K17+
non-transduced
TRC Epgn-kd outgrowth
Knockdown rescue by shRNA resistant epigen
G
Relative Epgn expression
TRC-Ctrl-kd
TRC-Epgn-kd
H
Outgrowth (# viable cells day 6 vs. day 0)
I
none
hEpgn
Outgrowth (# viable cells day 4 vs. day 0)
hEpgn

Supplemental Figure 3.3. Validation and characterization of EGFR related gene knockdowns. Related to Figure 3.1 and Figure 3.2.

(A) Validation of MMTV-PyMT shRNA knockdowns by qPCR. Red line = mean. # of biological replicates; Plaur-kd n=3, Egfr-kd n=4, Areg-kd n=2, Epgn-kd n=3. **(B)** Left, images of Ctrl and knockdown cells after 24 hrs of aggregation, plated at equal cell densities. Middle, quantification of suspension object areas (MATLAB) prior to tail vein injection. n (# entities): Ctrl-kd = 6931, Egfr-kd = 3561, Areg-kd = 3158, Epgn-kd = 3367. Right, number of nuclei (by DAPI staining) of Ctrl-kd or Epgn-kd clusters aggregated for 24hrs. n=3 biological replicates. n= 100 Ctrl-kd clusters, 66 Epgn-kd clusters. P-value = unpaired t-test. **(C)** DIC time lapse images of Ctrl-kd, Plaur-kd, Egfr-kd, Epgn-kd, Areg-kd MMTV-PyMT clusters growing in 3D basement membrane-rich gels for 90 hrs. Right, quantification of fold growth by change in area over 4 days of time lapse imaging. Ctrl-kd: n=8 mice, 246 clusters. Plaur-kd: n=2 mice, n=31 clusters. Egfr-kd: n=3 mice, 84 clusters. Areg-kd: n=3 mice, 108 clusters. Epgn-kd: n=3 mice, 90 clusters. **(D)** % of Ctrl-kd and Epgn-kd nuclei in mitosis after 24 hrs of aggregation, measured as % phospho-histone H3 positive. n=4 biological replicates. n (# nuclei): Ctrl-kd = 2636, Epgn-kd = 1790. P-value = unpaired t-test. **(E)** RNA expression (RNA-seq) of cytokeratin genes in Ctrl-kd and Epgn-kd MMTV-PyMT clusters, n=3. Adjusted p-values. **(F)** Immunofluorescence of keratin-17 in Ctrl-kd and Epgn-kd clusters in 3D basement membrane-rich gels after 6 days of outgrowth. Right, quantification of % cells in each cluster keratin-17 positive by immunofluorescence. n=2 biological replicates. n (# clusters): non-transduced = 34, Ctrl-kd = 39, Epgn-kd = 27. P-values = unpaired t-tests. **(G)** Validation of MMTV-PyMT TRC-

Epgn-kd by qPCR. n=3 biological replicates. P-value = unpaired t-test. **(H)** Relative viable cell number of TRC-Ctrl-kd and TRC-Epgn-kd after 6 days of outgrowth in low basement membrane suspension culture. n=3 biological replicates. P-value = unpaired t-test. **(I)** DIC images of Ctrl-kd and Epgn-kd clusters after 4 days growth with and without transduction with an shRNA resistant human epigen construct (MOI <1). Right, quantification of viable cell number using CellTiter-Glo. n=3 biological replicates. P-value = unpaired t-test.

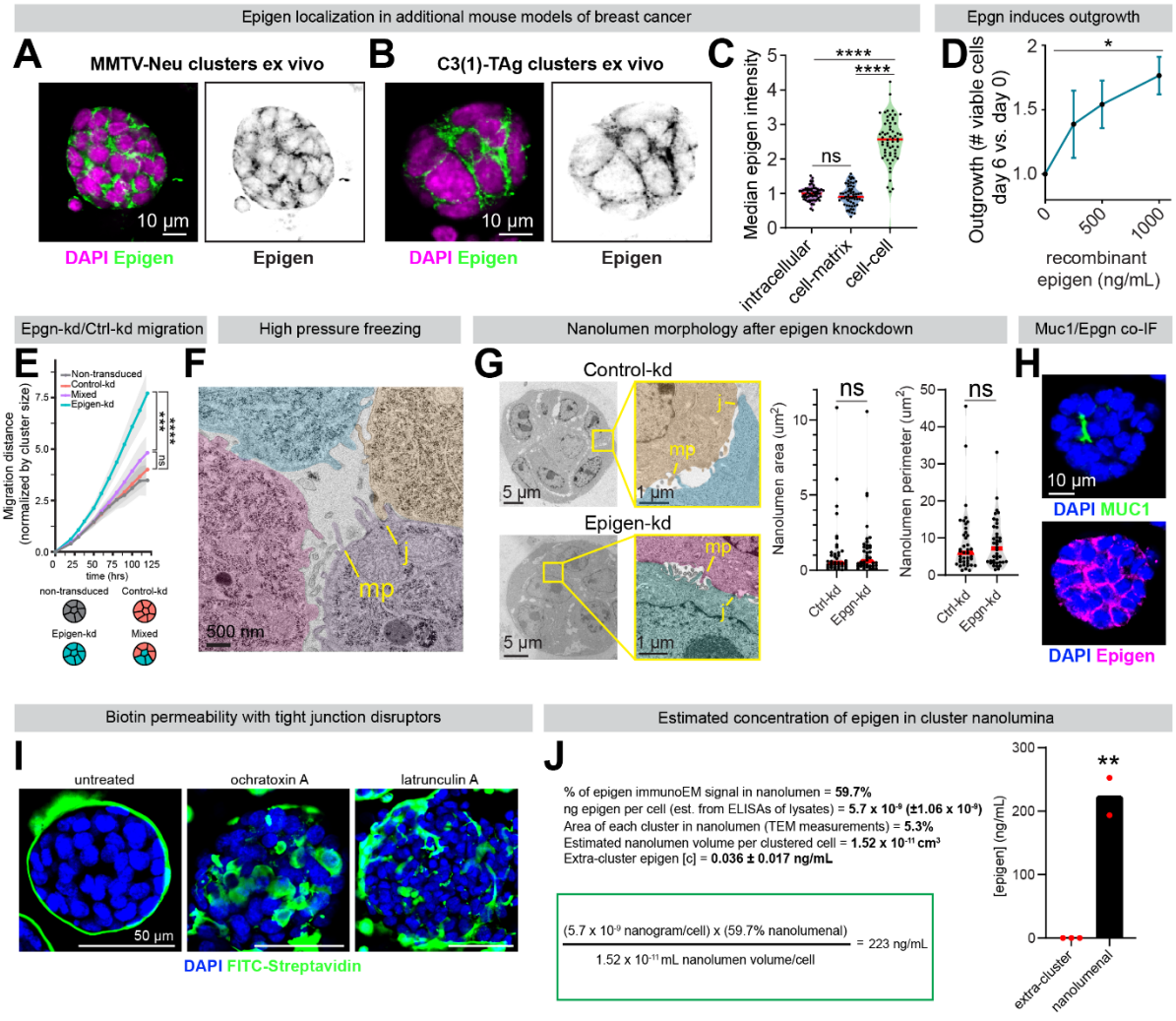

Supplemental Figure 3.4. Detailed characterization of tumor cell cluster nanolumenal structure and epigen concentration. Related to Figure 3.3 and Figure 3.4.

(A-B) Immunofluorescence of epigen in tumor cell clusters ex vivo from MMTV-Neu tumors (A) and C3(1)Tag tumors (B). **(C)** Quantification of epigen immunofluorescence signal along cytosolic, cell-cell, or cell-matrix areas in C3(1)-TAg clusters. n = 60 clusters,

3 biological replicates. P-values = Mann-Whitney test. **(D)** Relative number of viable cells after 6 days of treatment of PyMT cells in suspension with recombinant epigen. n=3 biological replicates. P-value = unpaired t-test. **(E)** Cumulative migration distance of individual clusters, normalized to initial cluster cell number, in 3D basement membrane-rich gels over 120 hrs. Mixed clusters were generated by aggregating Ctrl-kd and Epgn-kd cells at a 1:1 ratio. Data are plotted as mean with 5-95% CI. n (# of clusters): Non-transduced = 49, Ctrl-kd = 50, Epgn-kd = 47, Mixed 1:1 = 35. n (# of biological replicates) = 2. P-values = unpaired t-tests. **(F)** Ultrastructure of tumor cell cluster using high pressure freezing electron microscopy. Pseudo-color highlights different cells. MP = microvilli-like protrusions. J = cell-cell junction. **(G)** Transmission electron microscopy of Ctrl-kd and Epgn-kd PyMT clusters. Right, nanolumenal area and perimeter measurements. n = 40 nanolumina measured per condition (measured junction to junction). MP = microvilli-like protrusions. J = cell-cell junction. **(H)** Immunofluorescence of epigen and apical marker Muc-1 in a MMTV-PyMT cluster. **(I)** Biotin leak-in assay of MMTV-PyMT clusters without treatment, treated with ochratoxin A (200 μm, 1 hr) (McLaughlin et al., 2004), or treated with latrunculin A (0.2 μm, 1hr) (Shen and Turner, 2005) to disrupt cell-cell junctions. **(J)** Estimated concentration of epigen in nanolumen, based on TEM estimates of nanolumenal volume per cell and ELISA measurements of epigen protein per cell. Secreted epigen was also measured by epigen ELISA of 18 hr tumor cell cluster supernatants (extra-cluster concentration). Supernatants: n = 3 biological replicates. Cell lysates: n = 2 biological replicates. P-values = unpaired t-tests.

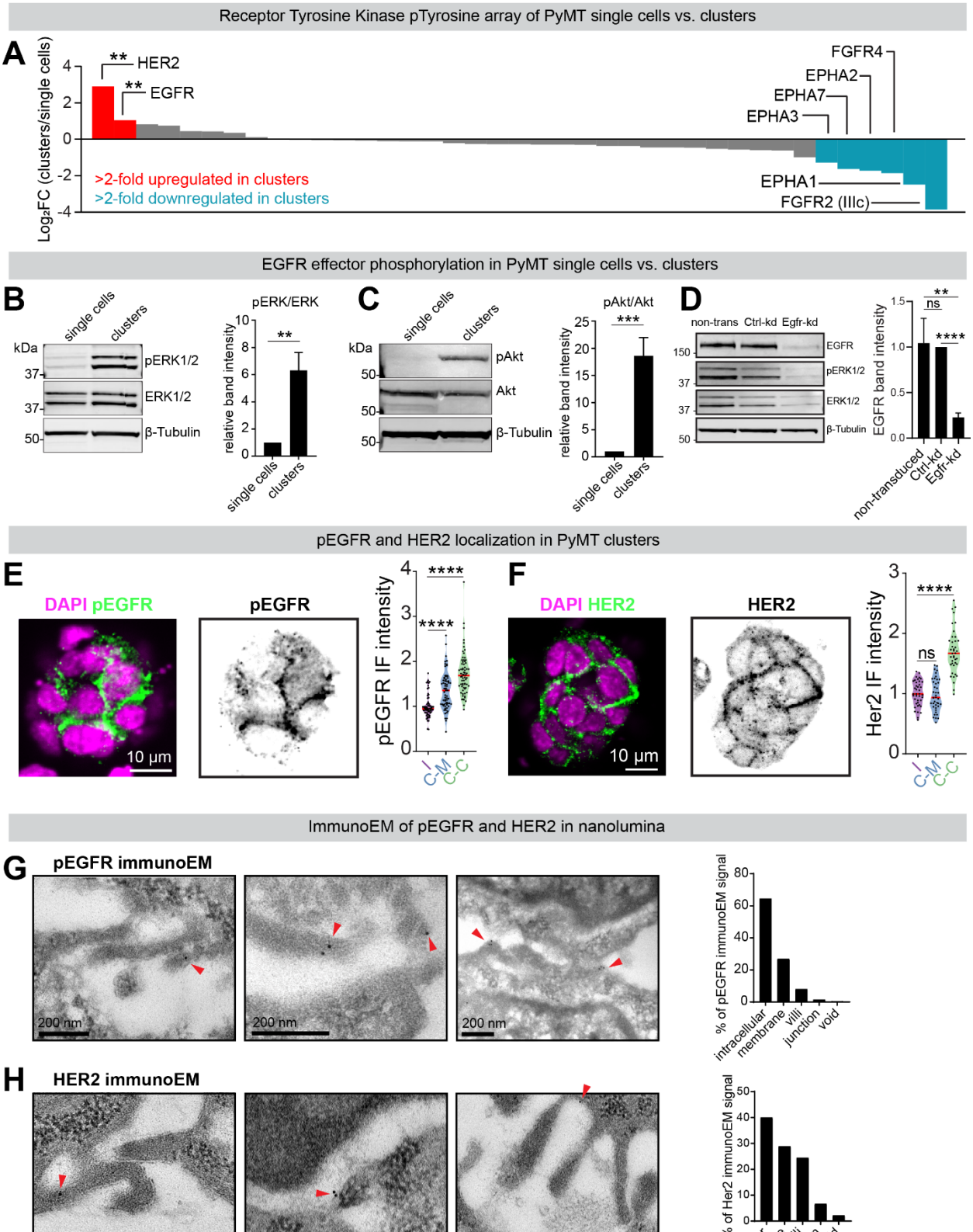
Receptor Tyrosine Kinase pTyrosine array of PyMT single cells vs. clusters
A
Log2FC (clusters/single cells)
HER2
EGFR
FGFR4
EPHA2
EPHA7
EPHA3
EPHA1
FGFR2 (IIIc)
>2-fold upregulated in clusters
>2-fold downregulated in clusters
EGFR effector phosphorylation in PyMT single cells vs. clusters
B
single cells
clusters
kDa
pERK1/2
ERK1/2
β-Tubulin
pERK/ERK
relative band intensity
C
pAkt
Akt
pAkt/Akt
D
non-trans
Ctrl-kd
Egfr-kd
EGFR
EGFR band intensity
non-transduced
pEGFR and HER2 localization in PyMT clusters
E
DAPI pEGFR
pEGFR
pEGFR IF intensity
10 µm
F
DAPI HER2
HER2
Her2 IF intensity
ImmunoEM of pEGFR and HER2 in nanolumina
G
pEGFR immunoEM
200 nm
% of pEGFR immunoEM signal
intracellular
membrane
villi
junction
void
H
HER2 immunoEM
100 nm
% of Her2 immunoEM signal

Supplemental Figure 3.5. EGFR phosphorylation and effector activation in tumor cell clusters. Related to Figure 3.4.

(A) Quantification of receptor tyrosine kinase phospho-tyrosine array signal for MMTV-PyMT cluster (6hrs aggregation) vs. PyMT single cell (0hr aggregation) lysates. n=3 biological replicates. P-values = unpaired t-tests. **(B)** Immunoblots of single cell (0 hr) vs. cluster (6hrs aggregation) MMTV-PyMT lysates for phospho (Thr 202/Tyr204) and total ERK1/2. Right: quantification of n = 3 biological replicates. P-values = unpaired t-tests. **(C)** Immunoblots of single cell (0hr) vs. cluster (6hrs aggregation) MMTV-PyMT lysates for phospho (S473) and total Akt. Right: quantification of n = 3 biological replicates. P-values = unpaired t-tests. **(D)** Immunoblot of EGFR and EGFR effectors pERK1/2 in non-transduced, Ctrl-kd, and Egfr-kd PyMT tumor cell clusters. Right: quantification of n = 3 biological replicates. P-values = unpaired t-tests. **(E)** Immunofluorescence of pEGFR (Y1068) in a MMTV-PyMT cluster ex vivo. Right, quantification of pEGFR at intracellular (I), cell-matrix (C-M), and cell-cell (C-C) spaces in MMTV-PyMT clusters. n = 68 clusters, n = 3 biological replicates. P-values = Mann-Whitney tests. **(F)** Immunofluorescence of HER2 in a MMTV-PyMT cluster ex vivo. Right, quantification of HER2 immunofluorescence at intracellular (I), cell-matrix (C-M), and cell-cell (C-C) spaces in MMTV-PyMT clusters. n = 40 clusters, n = 2 biological replicates. P-values = Mann-Whitney tests. **(G)** Immunogold labeling of pEGFR along nanolumina in MMTV-PyMT clusters. Arrows = pEGFR immunogold signal. Right, quantification of labeling in intercellular areas, along nanolumenal membranes, along nanolumenal villi, at cell-cell junctions, and within nanolumenal voids. n = 93 gold

particles. **(H)** Immunogold labeling of HER2 along nanolumina in MMTV-PyMT clusters. Arrows = HER2 immunogold signal. Right, quantification labeling in intracellular areas, along nanolumenal membranes, along nanolumenal villi, at cell-cell junctions, and within nanolumenal voids. n = 45 gold particles.

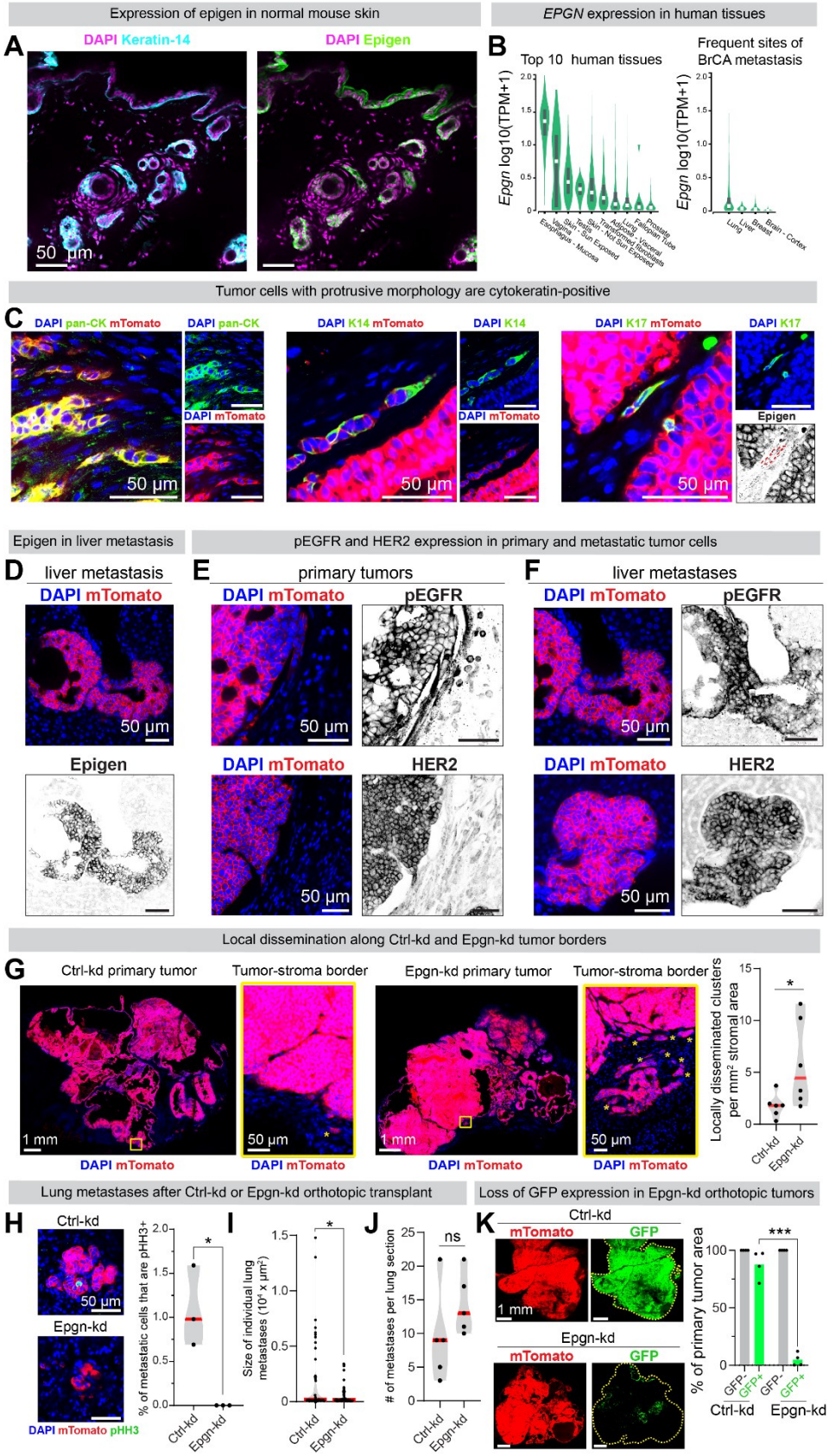
Expression of epigen in normal mouse skin
EPGN expression in human tissues
A
DAPI Keratin-14
DAPI Epigen
50 µm
B
Top 10 human tissues
Frequent sites of BrCA metastasis
Epgn log10(TPM+1)
Tumor cells with protrusive morphology are cytokeratin-positive
C
DAPI pan-CK mTomato
DAPI pan-CK
DAPI mTomato
DAPI K14 mTomato
DAPI K14
DAPI K17 mTomato
DAPI K17
Epigen
Epigen in liver metastasis
pEGFR and HER2 expression in primary and metastatic tumor cells
D
liver metastasis
E
primary tumors
F
liver metastases
DAPI mTomato
pEGFR
HER2
Local dissemination along Ctrl-kd and Epgn-kd tumor borders
G
Ctrl-kd primary tumor
Tumor-stroma border
Epgn-kd primary tumor
1 mm
Locally disseminated clusters per mm² stromal area
Ctrl-kd
Epgn-kd
Lung metastases after Ctrl-kd or Epgn-kd orthotopic transplant
Loss of GFP expression in Epgn-kd orthotopic tumors
H
DAPI mTomato pHH3
% of metastatic cells that are pHH3+
I
Size of individual lung metastases (10⁴ x µm²)
J
# of metastases per lung section
ns
K
mTomato
GFP
% of primary tumor area
GFP-
GFP+

Supplemental Figure 3.6. Epigen expression and function during metastatic progression vivo. Related to Figure 3.5.

(A) Immunofluorescence of epigen and keratin-14 in normal FVB mouse back skin as an antibody positive control, as epigen is known to be expressed in hair follicles (Kochupurakkal et al., 2005). **(B)** Genotype-Tissue Expression (GTEx) RNA sequencing data of *EPGN* in normal human tissues including (left) the top 10 *EPGN* expressing tissues by median expression and (right) frequent sites of breast cancer metastasis. **(C)** Pan-cytokeratin, Keratin-14, Keratin-17, and epigen immunofluorescence of protrusive tumor strands on the border of mTomato-PyMT orthotopic tumors 10 weeks after transplant of non-transduced (pan-CK, K17) or Ctrl-kd clusters (K14). **(D)** Immunofluorescence of epigen in a liver metastasis 6 weeks after intracardiac injection of mTomato-PyMT clusters. **(E)** pEGFR (Y1068) immunofluorescence of a primary tumor 10 weeks after mTomato-PyMT organoid orthotopic transplant into the mammary fat pad and of a liver metastasis 6 weeks after intracardiac injection of mTomato-PyMT clusters. **(F)** HER2 immunofluorescence of a primary tumor 10 weeks after mTomato-PyMT organoid orthotopic transplant into the mammary fat pad and of a liver metastasis 6 weeks after intracardiac injection of mTomato-PyMT clusters. **(G)** 20X tiled images were taken of sections from Ctrl-kd and Epgn-kd orthotopic transplant tumors. Right, quantification of the number of locally disseminated clusters (mTomato+) per mm^2 stromal area (DAPI+/mTomato-). n=6 Ctrl-kd tumors (148 clusters), 6 Epgn-kd tumors (218 clusters). P-values = unpaired t-tests. **(H)** Left, images of lung metastases 6 weeks after orthotopic transplant of Ctrl-kd or Epgn-kd organoids, stained for mitotic marker pHH3. Right, quantification of % of lung metastasis cells pHH3+. n=3 Ctrl-kd mice (925 cells), n=3

Epgn-kd mice (157 cells). P-value = unpaired t-test. **(I)** Area measurements of individual metastases (including disseminated single cells) in lungs 6 weeks after orthotopic transplant of Ctrl-kd or Epgn-kd organoids. n=5 mice per condition. n=47 Ctrl-kd metastases, 72 Epgn-kd metastases. P-value = Mann-Whitney test. **(J)** Number of metastases detected in each lung section from mice 6 weeks after orthotopic transplant of Ctrl-kd or Epgn-kd organoids. n=5 mice per condition. P-value = unpaired t-test. **(K)** mTomato+ and GFP+ areas were measured in Ctrl-kd and Epgn-kd orthotopic tumor sections using 20X tiled images. Right, quantification of the GFP+ area as a percent of the mTomato+ area. n=4 Ctrl-kd tumors, 4 Epgn-kd tumors. P-value = unpaired t-test.

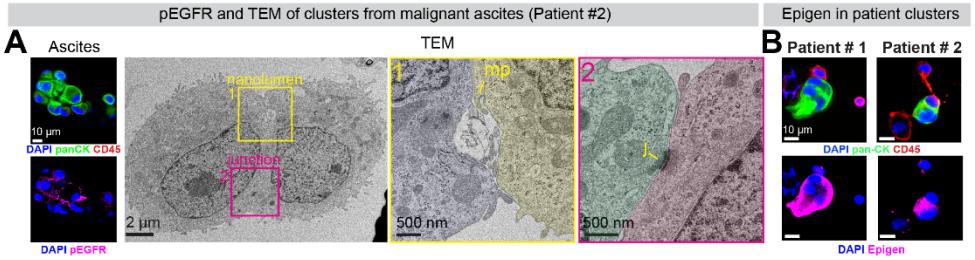

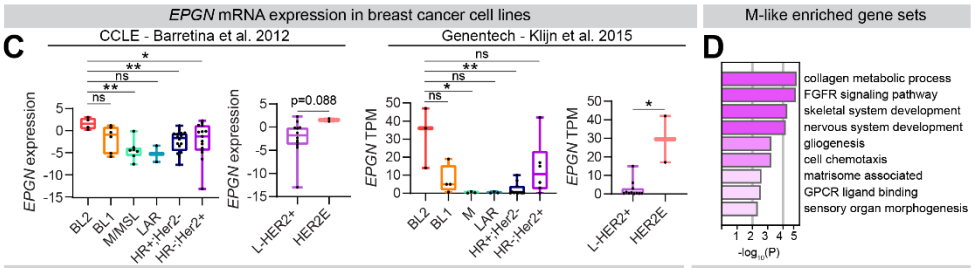

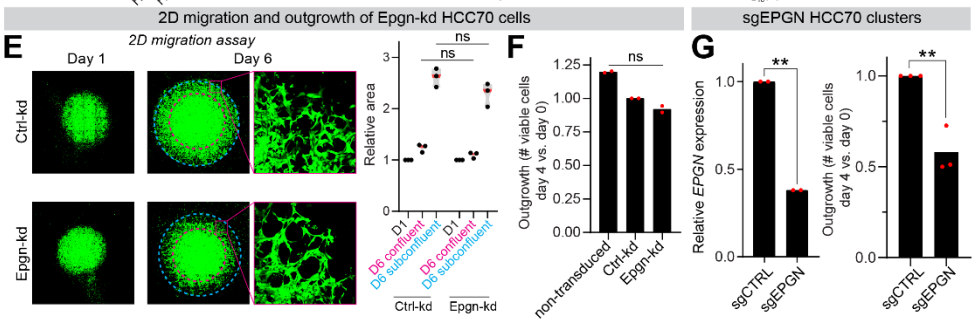

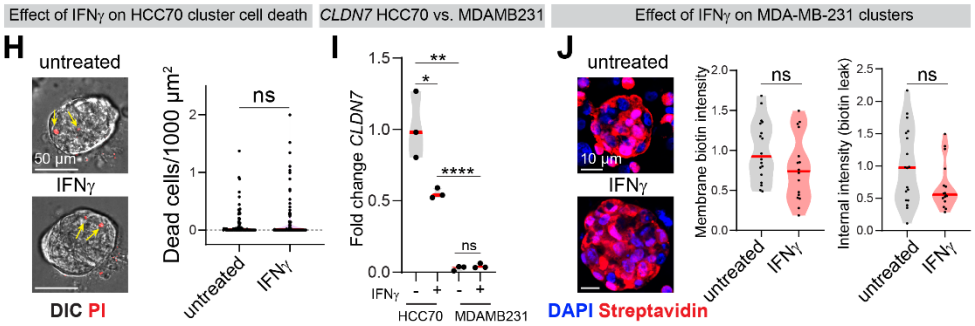

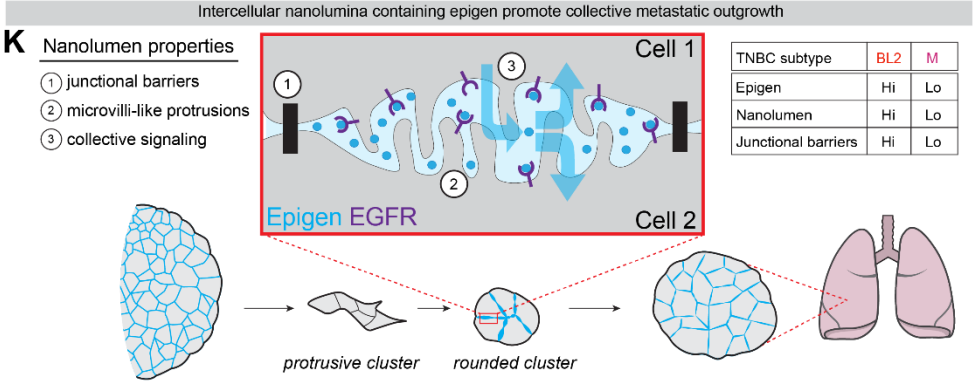

TNBC subtype	BL2	M
Epigen	Hi	Lo
Nanolumen	Hi	Lo
Junctional barriers	Hi	Lo

Supplemental Figure 3.7. Assessment of nanolumina, gene expression, and epigen-induced growth in human tumor cell clusters. Related to Figure 3.6 and Figure 3.7.

(A) Shown are representative tumor cell clusters obtained directly from the ascites fluid of a metastatic ER+/PR+/HER2- breast cancer patient with disease to bone, liver, chest wall, stomach and peritoneum. Left: image of ascites cluster stained for pan-cytokeratin, CD45, and pEGFR. Right: TEM images of ascites clusters. MP = microvilli-like protrusions. J = cell-cell junction. **(B)** Epigen immunofluorescence of tumor cell clusters in malignant ascites from patients #1 and #2 using a pan-cytokeratin antibody to identify tumor cell clusters and CD45 to identify immune cells. **(C)** Epigen mRNA expression in two panels of breast cancer cell lines (Barretina et al., 2012; Klijn et al., 2015). Triple-negative sub-groups: BL2 = basal-like 2, BL1 = basal-like 1, M = mesenchymal, LAR = luminal androgen receptor. L-HER2+ = luminal like HER2+ cell lines. HER2E = basal like HER2+ cell lines (TCGA, 2012; Watson et al., 2018). **(D)** Gene sets (Metascape, FDR ≤ 0.05) enriched in M-like (MDA-MB-231, MDA-MB-436, and BT549) vs. BL2 (HCC70, CAL851, HDQP1) cell lines (CCLE). **(E)** GFP images of Ctrl-kd and Epgn-kd cells grown on collagen I coated plates to assess 2D migration. Right, quantification of the colony area one day after plating (D1) and of the dense monolayer (“confluent”) and invasive outer layer (“subconfluent”) formed 6 days after plating (D6). n=3 biological replicates. P-values = unpaired t-tests. **(F)** Relative number of viable cells of non-transduced, Ctrl-kd, and Epgn-kd HCC70 cells after 4 days of growth (seeded at equal cell number) in 2D on tissue culture treated plates. n=3 biological replicates. P-value = unpaired t-test. **(G)** Left: qPCR validation of HCC70 clusters transduced with non-targeting or epigen-targeting

CRISPR sgRNAs. Cells were not clonally selected i.e. these represent mixed populations of cells with <100% knockout. n=2 biological replicates. Right, relative number of viable cells after 4 days of growth as clusters in low-basement membrane suspension. n=3 biological replicates. P-values = unpaired t-tests. **(H)** Number of non-viable nuclei per 1000 μm^2 area in HCC70 clusters ex vivo, measured by confocal imaging of propidium iodide staining after 6 days with or without 3 ng/mL IFNγ treatment. n=3 biological replicates. n = 76 untreated clusters, 72 IFNγ treated clusters. **(I)** Fold change of *CLDN7* mRNA (relative to *RPL32* housekeeping control) for MDA-MB-231 and HCC70 clusters after 6 days with or without 3ng/mL IFNγ. n=3 biological replicates. P-values = unpaired t-tests. *RAB25* was not detected by qPCR in MDA-MB-231 cells at any time point. **(J)** Representative images of biotin leak-in assay of MDA-MB-231 clusters after 6 days of treatment with or without 3ng/mL IFNγ. Right, quantification of biotin leak-in (internal FITC-streptavidin intensity). n = 18 untreated clusters, 16 IFNγ treated clusters. n = 2 biological replicates. P-value = Mann-Whitney test. **(K)** Here, we find that tumor cell clusters generate sealed, intercellular nanolumina. These nanolumina contain high concentrations of the growth factor epigen. Collective signaling by epigen within nanolumina promotes primary and metastatic tumor outgrowth. High epigen expression and nanolumenal impermeability were found in basal-like 2 human breast cancer cells, whereas mesenchymal-like cells were highly permeable and lowly expressed epigen. Suppression of epigen signaling in basal-like 2 breast cancer cells reduced collective metastatic outgrowth.

3.6 TABLES AND SUPPLEMENTAL ITEMS

Table 3.1. Related to Supplemental Figure 3.2, summary of breast cancer patient samples. Summary of human breast cancer patient tumor samples used for ex vivo experiments.

Table 3.2. Related to Figure 3.1, gene sets differentially expressed throughout PyMT cell aggregation. Genes and gene sets (Metascape) enriched at different time points during aggregation. Genes were sequentially ordered in the dataset by their time-point of maximum expression (5 time points: 0hrs, 6hrs, 12hrs, 24hrs, 48hrs of aggregation), mean-variance normalized, and clustered together.

Table 3.3. Related to Figure 3.1, genes differentially expressed throughout PyMT cell aggregation. Gene expression of MMTV-PyMT cells at 0, 6, 12, 24, and 48hrs of aggregation after dissociation to single cells.

Table 3.4. Related to Figure 3.2, genes differentially expressed upon *Epgn* knockdown. Differentially expressed genes and gene sets (Metascape) between MMTV-PyMT Ctrl-kd clusters and Epgn-kd clusters (after 24 hrs of aggregation).

Table 3.5. Related to Figure 3.6, basal-like 2 vs. mesenchymal-like triple negative breast cancer cell line gene expression. Genes (Barretina et al., 2012) and gene sets (Metascape) enriched in basal-like 2 (HCC70, CAL851, HDQP1) vs. mesenchymal-like (MDA-MB-231, MDA-MB-436, BT549) breast cancer cell lines.

Video 3.1. Related to Figure 3.1, PyMT cell aggregation in non-adherent suspension culture. DIC time-lapse of MMTV-PyMT single cells self-assembling into clusters in low-basement membrane suspension culture.

Video 3.2. Related to Figure 3.2, migration and outgrowth of Ctrl-kd and Epgn-kd clusters in 3D basement membrane-rich gels. DIC time-lapse of Epgn-kd and Ctrl-kd MMTV-PyMT tumor cell clusters cultured in 3D basement membrane-rich gels for 120 hrs. (Bottom) migration tracks of all Ctrl-kd and Epgn-kd clusters, with the examples from this movie highlighted in red and blue lines, respectively.

3.7 METHODS

DATA AND CODE AVAILABILITY

RNA sequencing data sets have been deposited to the NCBI Sequence Read Archive (PRJNA648151, PRJNA648435).

EXPERIMENTAL MODEL AND SUBJECT DETAILS

Animal models

All mice were maintained under specific-pathogen-free conditions, and experiments conformed to the guidelines as approved by the Institutional Animal Care and Use Committee of Fred Hutchinson Cancer Research Center (FHCRC). FVB/N-Tg(MMTV-PyVT)634Mul/J (MMTV-PyMT) were maintained and tumor growth was monitored every 2 days. MMTV-PyMT mice were crossed with ROSA mTomato/mGFP mice (Gt(ROSA)26Sor$^{tm4(ACTB-tdTomato,-EGFP)Luo}$/J) to generate mTmG-PyMT mice with mTomato+ cell membranes. For injection experiments, immunocompromised NSG mice (NOD.Cg-Prkdc^{scid} Il2rg^{tm1Wjl}/SzJ) were used. Adult female mice were used for all experiments.

Human breast cancer patient samples

Deidentified human breast cancer primary or metastatic samples were received from (1) the Cooperative Human Tissues Network, a program funded by the National Cancer Institute, shipped overnight on wet ice or (2) received same day from the University of Washington/Seattle Cancer Care Alliance, with patients consented and samples obtained under a Fred Hutch IRB approved study (FH5306). Tumor samples were processed as previously described to generate organoids (Nguyen-Ngoc et al., 2012), detailed below. Blood and ascites fluid were collected from patients consented and samples obtained

under a Fred Hutch IRB approved study (FH8649) for longitudinal monitoring of circulating tumor cells in metastatic breast cancer patients. CTCs and CTC-clusters were enumerated in these fluid samples using a Rarecyte assay (Kaldjian et al., 2018). For details on the receptor status and pathology of each deidentified human sample used, see **Table 3.1**.

Cell lines

293FT (ThermoFisher Scientific R70007), MDA-MB-231-YFP (generated from ATCC HTB-26), CAL-85-1 (DSMZ ACC 440), HDQ-P1 (DSMZ ACC 494), and MDA-MB-436 (ATCC HTB-130) cell lines were grown at 37ºC, 5% CO_2 in DMEM high glucose (Gibco 10569-010) supplemented with 10% fetal bovine serum (Sigma-Aldrich F0926-500ML) and 1X penicillin/streptomycin (Sigma-Aldrich P4333). BT549 (ATCC HTB-122) and HCC70 (ATCC CRL2315) cell lines were grown at 37ºC, 5% CO_2 in RPMI (Gibco 61870-127) supplemented with 10% fetal bovine serum (Sigma-Aldrich F0926-500ML) and 1X penicillin/streptomycin (Sigma-Aldrich P4333). MDA-MB-231 cells were a gift from Cyrus Ghajar. All cell lines used were from human females.

METHOD DETAILS

Tail vein and intracardiac injection of NSG mice

For single cell vs. cluster experiments, mTomato-PyMT organoids were dissociated to single cells at day 0 using Accumax (20 minutes at 37ºC). 200,000 cells in 200 μL DPBS were injected per mouse in the tail vein. To generate clusters, single cells were plated in non-adherent dishes at 150,000 cells/mL in media +2% basement membrane-rich gel (v/v) and then injected as above 6hr or 24 hrs later into Nod *scid* gamma (NSG)

immunocompromised mice. shRNA knockdown injections were all carried out with 24hr aggregated clusters. DIC images were taken before injection and assessed to ensure similar number and size of clusters injected between conditions. 3 weeks after tail vein injection mice were euthanized and both sides of the lungs were imaged under a dissecting microscope for quantification of fluorescent (metastatic) area. For intracardiac injections, 100,000 mTomato-PyMT clustered cells were injected into the left ventricle in 100 µL of PBS using a 26g needle with ultrasound guidance with 2.5% isoflurane anesthesia. 6 weeks later the brain, liver, lung, femur, kidneys, and ovaries were collected. Collected organs were fixed in 4% PFA for 4 hrs, then transferred to 25% sucrose in DPBS overnight at 4^{o}C before embedding in OCT and storing at -80^{o}C.

Mouse mammary tumor organoid culture

Organoids were isolated from MMTV-PyMT, C3(1)TAg, or MMTV-Neu mouse mammary tumors as previously described (Nguyen-Ngoc et al., 2015). Mice were harvested as the largest tumor neared 1.5 cm in diameter. MMTV-PyMT mammary tumors were dissected, mechanically disrupted with a scalpel, and then digested in a collagenase-trypsin solution for 30-60 minutes shaking at an angle at 100-150 rpm at 37^{o}C. The digestion solution (in 20 mL of DMEM/F12) contained 2 mg/mL collagenase (Sigma C2139), 2mg/mL trypsin (Gibco 27250–018), 5% fetal bovine serum, 5 µg/mL human insulin (Sigma-Aldrich I9278), 50 µg/mL gentamicin (Gibco 15750-060). Tumor fragments were centrifuged for 10 minutes at 1500 rpm, resuspended in 4 mL DMEM/F12 and treated with 40 µL (2000 U/mL) of DNAse (Sigma D4263) for 3 minutes then resuspended in 10mL DMEM/F12. The solution was centrifuged for 4 seconds at 1500 rpm (453g) to isolate multicellular organoids, then resuspended in 10 mL DMEM/F12.

This was repeated for a total of 4 washes. For 3D culture, 100-200 clusters were embedded in 100 μL of growth-factor reduced Matrigel (Corning), the Matrigel was allowed to polymerize for 30-60 minutes at 37°C, then 1 mL of organoid media (DMEM-F12, FGF2, insulin-transferrin selenium, & penicillin/streptomycin) was added. For suspension culture, clusters were cultured in non-adherent dishes in organoid media + 2% (v/v) Matrigel. Tips and tubes used to handle organoids were first coated in 2.5% BSA in DPBS to prevent loss of material. To create single cell suspensions, organoids were centrifuged, resuspended in Accumax (Innovative Cell Technologies) for 20 minutes at 37°C, and counted on a hemocytometer to ensure a low number of residual clusters.

Human cell line and patient tumor organoid culture

Human cell lines were cultured in complete media (DMEM high glucose or RPMI with penicillin/streptomycin + 10% FBS) on tissue-culture treated plates, or in non-adherent plates supplemented with 2% Matrigel (v/v). To assess migration in 2D, 100,000 viable cells in 10 μL media were seeded as a droplet at the center of a Collagen I coated 24 well plate. After 30 minutes at 37°C, 1 mL of complete media was added. Tiled DIC and GFP images were taken 1 day and 6 days after plating. Deidentified human breast cancer primary or metastatic samples were received from the Cooperative Human Tissues Network and the Seattle Cancer Care Alliance. Tumor samples were processed as previously described to generate organoids (Nguyen-Ngoc et al., 2012). Samples were washed with DPBS containing 200 U/mL penicillin/200 μg/mL streptomycin (Sigma-Aldrich P4333) and 5 μg/mL Amphotericin B (ThermoFisher Scientific 15290-018). They were then minced with a scalpel and resuspended in digestion solution. The digestion solution (in 40 mL of DMEM/F12) contained 2 mg/mL collagenase (Sigma C2139), 5%

fetal bovine serum, 1X penicillin/streptomycin (Sigma-Aldrich P4333), and 5 µg/mL human insulin (Sigma-Aldrich I9278). Samples were incubated at 37°C shaking at 200 rpm for 2-5 hours. Tumor fragments were centrifuged for 10 minutes at 1500 rpm, resuspended in 4 mL DMEM/F12 and treated with 40 µL (2000 U/mL) of DNAse (Sigma D4263) for 3 minutes then resuspended in fresh 10mL DMEM/F12. The solution was centrifuged for 4 seconds at 1500 rpm (453g) to isolate multicellular organoids. Human organoids were cultured with 2% (v/v) or 100% growth factor reduced Matrigel (Corning) with complete HuMEC Ready media (Fisher 12752010).

Scoring metastatic foci and outgrowth after tail vein injection

3 weeks after tail vein injection, lungs were removed and imaged under a dissecting microscope. Bright field and DsRed images were taken for all experiments using mTomato-PyMT cells, GFP images were collected for cells expressing GFP-shRNAs. To measure outgrowth in whole lungs or lung sections, fluorescence images were thresholded equally in FIJI software (Schindelin et al., 2012) and total fluorescent area was measured. For each tail vein injected mouse, the total area of lung metastases was measured as the cm^2 GFP+ area in the lungs using FIJI software. For each animal, the total area of lung metastases was normalized by the mean total metastatic area of Ctrl-kd mice within each cohort of tail vein injections. This allowed the effect size of control vs. gene knockdowns to be compared, accounting for intrinsic differences in organoid line growth rates between injections. Statistical analysis was performed using one-way ANOVA followed by Dunnett's Test for multiple comparisons. To measure individual metastasis areas, the area of each visible metastasis was measured manually using FIJI software. To identify and measure micrometastases, 50 µm thick lung sections were

imaged at 10X magnification, tiled, and assembled. Metastasis counts from lung sections were normalized to the area of the lung imaged.

Immunofluorescence

Cells were fixed with 4% paraformaldehyde (10 min), permeabilized 30 minutes with 0.5% Triton-X, and blocked 1-2 hrs at room temperature with 10% FBS/1% BSA/0.1% Triton-X in DPBS. For cells in suspension culture or in malignant ascites, cells were centrifuged onto tissue pathology slides using a Cytospin 4 (A78300003), 800 rpm for 5 minutes and then treated as above. Primary antibodies were added in block solution and incubated at 4ºC overnight. Secondary antibodies (1:200) were incubated for 2-3 hrs at room temperature with 5% host serum. Confocal mages were acquired using an Andor CSU-W confocal spinning disk on a Leica DMi8 inverted microscope. For Leica 3X STED imaging, cells were stained with Alexa Fluor 594 Phalloidin (ThermoFisher Scientific A12381) and imaged using a Leica TCS SP8. DAPI was not included for STED imaging due to high background.

Time-lapse imaging for apoptosis, migration, and outgrowth analysis

Single or clustered cells were plated in growth factor reduced basement membrane-rich gels. Differential interference contrast (DIC) and fluorescent images were captured hourly using a Leica SPE at 10X or 20X magnification. For growth assays, DIC images were acquired. For survival assays, 30 minutes before imaging NucView 488 (Biotium) in PBS was added to the media at 1:1000 to mark nuclei in cells with active executioner caspases. Exposure times were <30ms for BF/DIC, and ~150ms for fluorescence. Temperature was maintained at 37ºC and CO_2 at 5%. Motility and NucView positivity were used to score apoptosis in single cells and clusters. Clusters were marked as dead

when the large majority of cells had died i.e. if a few cells were still alive in the apoptotic debris after most the cluster died, the cluster was not scored as alive. FIJI software was used to score the area of cells or clusters to measure outgrowth (as final area/initial area). Objects smaller than 250 μm^2 were scored as single cells (this cutoff may have occasionally included small MMTV-PyMT doublets). Images were acquired using a Leica DMi8 TCS SPE. For migration analysis, the centroid position of each individual organoid was tracked over time relative to static objects in the gel (e.g. debris). Each migration track was then normalized by the number of cells per organoid, determined by dividing the area of the organoid at time = 0 hr by the mean μm^2 area per cell, which here we determined to be ~76 μm^2 (n=71 organoids, 8613 cells). Cumulative path was determined by summing over the path length of each migration track.

Mixed culture experiments measuring Epgn-kd outgrowth with non-transduced neighbors

On day zero, 22,500 cells were plated in wells of a non-adherent 96 well plate at 100% knockdown, 90% knockdown/10% non-transduced (e.g. 20250 knockdown cells, 2250 non-transduced cells), 50% knockdown/50% non-transduced, or 10% knockdown/90% non-transduced. On day 6, each well was centrifuged and resuspended in Accumax for 20 minutes at 37^{o}C. Dissociated single cells were resuspended in organoid media and plated in glass-bottomed 8-well plates, allowed to settle, then imaged at 40X magnification (at least 10 fields per well). GFP positive and negative cells were manually counted in each field. For GFP+ cell growth calculations, this measurement was normalized to the starting number of GFP+ knockdown cells plated.

Transmission electron microscopy

Tumor cell clusters from cell lines, organoids, patient samples, or primary tumors (minced with a scalpel to <1mm^3) were centrifuged, washed in DPBS, then fixed in 1/2 strength Karnovsky's fixative (2% PFA/2.5% glutaraldehyde in 0.1M cacodylate buffer) at 4^{o}C for at least 16 hrs. Samples were then processed by the Fred Hutchinson Cellular Imaging core. Samples were visualized using a JEOL-1400 transmission electron microscope operated at 120 kV. For ascites-derived samples, tumor cells were identified based on gross morphological differences from stromal and blood cells in the same sample, as well as by the presence of electron dense cell-cell junctions.

Immunoelectron microscopy

For pEGFR and epigen immunogold staining, MMTV-PyMT clusters were collected and fixed in 4% PFA. For HER2 immunogold staining, MMTV-PyMT clusters were collected in 4% PFA + 0.1% glutaraldehyde. Approximately 70nm ultra thin sections were picked up on nickel grids (from Ted Pella, Inc., performed by Fred Hutchinson Cellular Imaging core). Grids were blocked with 50 mM glycine for 20 minutes, washed in PBS 3 times, blocked in 5% BSA for 30 minutes, washed with incubation buffer (1% BSA-C, 0.16% Tween-20 in PBS) 6 x 4 minutes, incubated with primary antibody (R&D MAB11271, Abcam ab40815, or CST 2165) for 2 hrs in incubation buffer, washed in PBS 4 times, washed in incubation buffer 6 x 4 minutes, incubated with secondary antibody (10nm gold goat-anti-rabbit or goat-anti-rat), washed in incubation buffer 10 x 4 minutes, post-fixed in 2% glutaraldehyde for 10 minutes, and washed in warm DI water. Samples were visualized using a JEOL-1400 transmission electron microscope with a Gatan Rio

4K camera. Images were compared against a negative control not incubated with primary antibody to ensure secondary specificity.

Biotin permeability testing and immunofluorescence

To test the permeability of tumor cell clusters, sulfo-NHS-biotin (Thermo Fisher Scientific A39256) was added to a final concentration of 0.8 mM in PBS for 30 minutes at 37^{o}C. Treatment with 1mM EGTA, Latrunculin A, or Ochratoxin A was for 1hr, prior to biotin incubation. Treatment with interferon gamma was for 6 days prior to biotin permeability experiments. Cells were washed three times with cold PBS then centrifuged onto tissue pathology slides using a Cytospin 4 (800 rpm for 5 minutes) and fixed with 4% PFA for 10 minutes. Freshly dissected primary tumors or lungs were immersed in 0.8 mM sulfo-NHS-biotin in PBS for 30 minutes then washed 3 times with PBS prior to fixation and embedding in OCT. Immunofluorescence was conducted (as above) with FITC-conjugated streptavidin to localize biotin. Human breast cancer cell lines were cultured for 6 days as clusters in suspension before assessing biotin permeability.

Immunofluorescence quantification

Phalloidin staining and DAPI were used to define membrane and nuclear areas, respectively. Using the freehand line tool in FIJI software, lines along cell-matrix (outer membrane), cell-cell (intercellular) membranes, and intracellular (cytosolic) areas were drawn and median fluorescence intensity was measured for each channel. Values were normalized to cytosolic signal. For biotin leak-in assays, the freehand line tool was used to draw along the cell-matrix membranes of the cluster and measure FITC-streptavidin intensity. Then the polygon selection tool was used to measure FITC-streptavidin intensity in the cluster core (excluding the cell-matrix contacts) and in adjacent stromal regions. To

assess biotin permeability in tumor vs. stroma areas, mean FITC-streptavidin signal was measured in FIJI in equally sized squares in adjacent pure tumor or pure stroma areas. To score protrusive vs. non-protrusive epigen immunofluorescence intensity, the polygon tool in FIJI software was used to measure epigen signal in locally disseminated mTomato+ PyMT clusters. Only protrusive and non-protrusive clusters in the same field of view were compared to one another, to account for differences in staining intensity between different regions of the tumor and different biological replicates. Protrusive clusters were identified based on the presence of strand-like organization and membrane protrusions. Non-protrusive clusters had more rounded organization and smooth borders. Clusters with intermediate or unclear morphology were not scored. Clusters with one type of morphology in one region, and another in a different region, were not scored. To count DAPI+ nuclei in clusters, a single confocal slice from the thickest part of the cluster was used. To assess cell death in clusters, propidium iodide (a fluorescent dye excluded from viable cells) was added to cell media at 0.5 ug/mL for 10 minutes prior to imaging.

Lentivirus production and transduction

Lentivirus was produced in HEK293FT cells using PsPax and MD2.G packaging plasmids for pLKO.1 (Moffat et al., 2006), LentiCRISPRv2 (Sanjana et al., 2014), or lentiviral shRNA vectors (transOMIC). Supernatants were concentrated using Lenti-X (Clontech), resuspended in 1/100th the supernatant volume of PBS, and frozen at -80^{o}C. Viruses were titered using a p24 ELISA (Retrotek). Tumor organoids were dissociated to single cells in Accumax and resuspended at 150,000 viable cells/mL in organoid media + 2% (v/v) Matrigel. Protamine sulfate was added at 8ug/mL to enhance transduction efficiency. For plasmids with PuroR, 2 days after transduction puromycin was included in

the media at 1-2 ug/mL for selection. Cells were maintained in puromycin for at least 5 days before experiments and puromycin was included in the media throughout ex vivo culture. CRISPR sgRNA transduced cells were kept in puromycin at least 10 days before conducting experiments.

RTK array and quantification

The R&D Proteome Profiler Mouse Phospho-RTK Array Kit (R&D ARY014) was performed according to manufacturer instructions using 125 ug of dissociated single cell or clustered (6 hrs aggregation) MMTV-PyMT lysates. X-ray film was exposed to membranes for 1 to 10 minutes. To quantify signal, the pixel intensity of each coordinate was measured using FIJI software for film scans in which the signal was not over or under exposed. The signal of the negative control (PBS) was then subtracted from each measurement.

Western Blotting

Clusters were lysed in RIPA buffer with protease and phosphatase inhibitors for 30 minutes at 4^{o}C and then centrifuged (15 minutes at 12000g). Clusters were cultured in 2% basement membrane suspension prior to lysate collection. Protein concentration was quantified using a BCA assay (Pierce), lysates were loaded onto a 4-12% Bis-Tris NuPage protein gel. Semi-dry transfers (iBlot2, P3 5-8min) were performed using PVDF membranes which were then blocked with 5% BSA in TBST for 1 hr. Primary antibodies were incubated overnight at 4^{o}C in 1% BSA in TBST, diluted 1:1000. Species specific LI-COR 680 and 800 secondary antibodies were used in TBST plus 1% BSA. Primary antibodies used: ERK1/2 (CST 4695), pERK1/2 (CST 4370), pAkt (CST 4060), Akt (CST 4691), beta-tubulin (Abcam ab40815), EGFR (Millipore 06-847). Band intensity was

measured using the “Analyze Gels” tool in FIJI software, relative to beta-tubulin as a loading control.

Mammary fat pad orthotopic transplantation

MMTV-PyMT-mTomato organoids were resuspended in 50% basement membrane-rich gel in DMEM/F12 (vol/vol) on ice. 3-4 week old NSG mice were anesthetized with 2.5% isoflurane and the surgical site was sterilized with ethanol and chlorhexidine. A 1 cm midline incision was made, allowing the #4 mammary fat pad to be exposed. 50,000 clustered cells per gland (aggregated at 250,000 viable cells/mL overnight) were injected into the left and right #4 mammary gland. The surgical area was locally infiltrated with 0.25% bupivacaine for pain relief. Surgical wounds were closed with 9mm autoclips and tissue glue. Triple antibiotic ointment was applied to the incision. Mice were monitored closely with autoclip removal two weeks after surgery. Tumor volume was estimated based on caliper measurements as: (4/3) x (π) x (width/2) x (width/2) x (length/2). At endpoint weeks, mice were euthanized, and primary tumors and lungs were fixed in 4% PFA for 4 hrs, then transferred to 25% sucrose in DPBS overnight at 4^{o}C before embedding in OCT and storing at -80^{o}C. Lung metastases were quantified using a fluorescence dissecting microscope at endpoint. Ctrl-kd and Epgn-kd tumors were harvested at the same time, when the first Ctrl-kd tumors reached the maximum allowable size (15 mm diameter).

RNA sequencing and bioinformatic analysis

MMTV-PyMT cells or clusters in suspension culture (non-adherent plates in media +2% Corning Matrigel) were collected for RNA extraction. Cells were pelleted 5 min. at 300g then resuspended in 1mL of Trizol. Samples were incubated at room temperature

for 5 min. to ensure lysis, and then stored at -20^{o}C. RNA samples were quantified using Qubit 2.0 Fluorometer and RNA integrity was checked with Agilent TapeStation (Agilent, RIN range 8.7 to 9.3). RNA sequencing libraries were prepared by GENEWIZ using the NEBNext Ultra RNA Library Prep Kit for Illumina following manufacturer's instructions. The sequencing libraries were validated on the Agilent TapeStation and quantified by using Qubit 2.0 Fluorometer as well as by quantitative PCR (KAPA Biosystems, Wilmington, MA, USA). The sequencing libraries were clustered on 1 lane of a flowcell. After clustering, the flowcell was loaded on the Illumina HiSeq instrument (4000 or equivalent) according to manufacturer's instructions. The samples were sequenced using a 2x150bp Paired End (PE) configuration. Image analysis and base calling were conducted by the HiSeq Control Software (HCS).

Raw sequence data (.bcl files) generated from Illumina HiSeq were converted into fastq files and de-multiplexed using Illumina's bcl2fastq 2.17 software. One mismatch was allowed for index sequence identification. Raw sequencing data was demultiplexed to generate two fastq files per sample with between 24.1 to 32.7 million reads per sample. Kallisto pseudoalignment v0.46.0 (Bray et al., 2016) was used for transcript abundance estimation, and differential transcript expression analysis was performed using Sleuth v0.30.0 (Pimentel et al., 2017). Kallisto was run with bootstrap-samples=100, and the transcript target was Ensembl (release 97) Mus musculus transcriptome (Mus_musculus.GRCm38.cdna.all.fa). For gene-level analyses, aggregated transcripts per million (TPM) scaled using the average transcript length and averaged over samples and to library size were generated with tximport and were used in further downstream differential gene expression analysis using limma-voom.

To visualize expression dynamics, genes were sequentially ordered in the dataset by their time-point of maximum expression, mean-variance normalized, and clustered together by time-point of maximum expression. Gene cluster enriched biological processes and signaling pathways were identified using Metascape (Zhou et al., 2019).

RNA sequencing data sets

Human RNA sequencing data from the Genotype-Tissue Expression (GTEx) Project were accessed using the GTEx portal (https://www.gtexportal.org/home/gene/EPGN). Breast cancer cell line RNA sequencing data sets were accessed from the Broad Institute CCLE portal (https://portals.broadinstitute.org/ccle) (Barretina et al., 2012) or EMBL-EBI (https://www.ebi.ac.uk/arrayexpress/experiments/E-MTAB-2706/) (Klijn et al., 2015).

Epigen ELISA

Epigen ELISAs were performed according to manufacturer instructions (R&D DuoSet) using MMTV-PyMT single cell or day 1 cluster (18hrs aggregation) lysates in RIPA buffer diluted at least 5-fold in ELISA reagent diluent. At least 30 ug of total protein was loaded. Recombinant epigen (R&D 1127-EP) was used as a standard. Antibodies MAB11271 (R&D) and AF1127 (R&D) were used for coating and detection, respectively.

Real-time qPCR

Human or mouse tumor cell clusters were pelleted and snap frozen in liquid nitrogen. RNA was extracted using an RNEasy mini kit (Qiagen). 250ng-1ug of RNA was used to generate cDNA with a SuperScript III First-Strand Synthesis kit (ThermoFisher) with oligo(dT) primers. RT-qPCR was performed using PowerUp SYBR Green master mix in 10-20 μL reactions on a QuantStudio 5 real-time PCR instrument. Pre-designed

Millipore Sigma KiCqStart™ primers were used (https://www.kicqstart-primers-sigmaaldrich.com/KiCqStartPrimers.php), primer pair IDs can be found in the Key Resources Table. Data were analyzed using the ΔΔCt method.

QUANTIFICATION AND STATISTICAL ANALYSIS

Bars are presented as mean ± standard deviation. Red lines denote medians, unless otherwise noted. Graphs were created and statistical tests conducted in GraphPad Prism 8. Non-parametric tests were used when data were not normally distributed or when the median was a better representation of the sample than the mean. Experiments using cell lines on different days or using organoids generated from different mice were considered biological replicates. All statistical tests are two-sided. $p \leq 0.05$ was considered significant. P-values: "ns" $p > 0.05$, *$p \leq 0.05$, **$p \leq 0.01$, ***$p \leq 0.001$, ****$p \leq 0.0001$.

KEY RESOURCES TABLE

REAGENT or RESOURCE	SOURCE	IDENTIFIER
Antibodies		
Rat-anti-Epigen (for mouse cells)	R&D	MAB11271
Goat-anti-Epigen (for ELISAs)	R&D	AF1127
Rabbit-anti-Epigen (for human cells)	Bioss	bs-5767R
Rabbit-anti-Her2	Cell Signaling Technology	2165
Rabbit-anti-pEGFR (Tyr1068/1092)	Abcam	ab40815
Rabbit-anti-Keratin 17 (D73C7)	Cell Signaling Technology	4543
Rat-anti-E-Cadherin (DECMA-1)	EMD Millipore	MABT26
Mouse-anti-human-CD298	BioLegend	341704
Rabbit-anti-phospho-Histone H3 (Ser10)	Cell Signaling Technology	9701
Rat-anti-Keratin 8	DSHB	TROMA-I
Alexa Fluor 647 anti-human CD45	BioRad	MCA87A647T

Alexa Fluor 488 pan-cytokeratin	Cell Signaling Technology	4523
Rabbit-anti-Keratin 14	BioLegend	905301
Rat-anti-PyMT	Abcam	ab15085
Rabbit-anti-EGFR	EMD Millipore	06-847
Rabbit-anti-pERK1/2 (Thr202/Tyr204)	Cell Signaling Technology	4370
Rabbit-anti-ERK1/2	Cell Signaling Technology	4695
Rabbit-anti-pAkt (Ser473)	Cell Signaling Technology	4060
Rabbit-anti-Akt	Cell Signaling Technology	4691
Rabbit-anti-Beta tubulin	Abcam	ab6046
Rabbit-anti-Muc1	Abcam	ab45167
Rabbit-anti-Occludin	Thermo Fisher Scientific	71-1500
Goat-anti-Rat IgG (H&L) EM grade 10nm	Electron Microscopy Sciences	25189
Aurion F(ab')2 Fragment Goat-anti-Rabbit IgG (H&L)	Electron Microscopy Sciences	25365
Biological Samples		
Human breast cancer, tumor samples	Cooperative Human Tissues Network	See Table S1
Human breast cancer, tumor samples	Seattle Cancer Care Alliance	See Table S1
Human breast cancer, blood samples	Seattle Cancer Care Alliance	See Table S1
Human breast cancer, ascites samples	Seattle Cancer Care Alliance	See Table S1
Chemicals, Peptides, and Recombinant Proteins		
NucView 488	Biotium	10403
EZ-Link Sulfo-NHS-Biotin No Weigh Format	Thermo Fisher Scientific	A39256
Streptavidin-FITC	Thermo Fisher Scientific	SA10002
Recombinant human IFN-γ Carrier Free	Biolegend	570204
Latrunculin A	Tocris	3973
Ochratoxin A	Fisher Scientific	12-911
Recombinant epigen	GenScript	Z03107-50
Critical Commercial Assays		
Proteome Profiler Mouse phospho-RTK Array	R&D	ARY014

Collagen I, Coated Plate, 24 well	ThermoFisher Scientific	A1142802
Deposited Data		
RNA sequencing of MMTV-PyMT cells during aggregation	This paper	NCBI PRJNA648151
RNA sequencing of Ctrl-kd vs. Epgn-kd MMTV-PyMT organoids	This paper	NCBI PRJNA648435
Broad Institute Cancer Cell Line Encyclopedia	Barretina et al. 2012	NCBI PRJNA155793
RNA-seq of 675 commonly used human cancer cell lines	Klijn et al. 2015	E-MTAB-2706
GTEx Analysis Release V8	The Genotype-Tissue Expression project	dbGaP Accession phs000424.v8.p2
Experimental Models: Cell Lines		
Human: 293FT	ThermoFisher Scientific	R70007
Human: HCC70	ATCC	CRL-2315
Human: CAL-85-1	DSMZ	ACC 440
Human: HDQ-P1	DSMZ	ACC 494
Human: BT549	ATCC	HTB-122
Human: MDA-MB-436	ATCC	HTB-130
Human: YFP-MDA-MB-231	Cyrus Ghajar	NA
Experimental Models: Organisms/Strains		
Mouse: FVB/NTg(MMTV-PyVT)634Mul/J (MMTV-PyMT)	The Jackson Laboratory	002374
Mouse: ROSA mTomato/mGFP	The Jackson Laboratory	007576
Mouse: NOD.Cg-Prkdc^{scid} Il2rg^{tm1Wjl}/SzJ	The Jackson Laboratory	005557
Mouse: FVB-Tg(C3-1-TAg)cJeg/JegJ	Andrew Ewald	NA
Mouse: FVB/N-Tg(MMTVneu)202Mul/J	Sasha Stanton	NA
Oligonucleotides		
Mouse beta actin qPCR primer	Millipore Sigma	KiCqStart M_ActB_1
Mouse *Areg* qPCR primer	Millipore Sigma	KiCqStart M_Areg_1
Mouse *Epgn* qPCR primer	Millipore Sigma	KiCqStart M_Epgn_1
Mouse *Egfr* qPCR primer	Millipore Sigma	KiCqStart M_Egfr_2
Mouse *Plaur* qPCR primer	Millipore Sigma	KiCqStart M_Plaur_1
Human beta actin qPCR primer	Millipore Sigma	KiCqStart M_ActB_1

Human *RPL32* qPCR primer	Millipore Sigma	KiCqStart M_RPL32_1
Human *EPGN* qPCR primer	Millipore Sigma	KiCqStart M_EPGN_1
Human *RAB25* qPCR primer	Millipore Sigma	KiCqStart M_RAB25_1
Human *CLDN7* qPCR primer	Millipore Sigma	KiCqStart M_CLDN7_1
CRISPR non-targeting control GTAGCGAACGTGTCCGGCGT	Patrick Paddison	NA
EPGN CRISPR sgRNA #2 GAAGTTCTCACACCTTTGCC	GenScript	NA
Recombinant DNA		
PsPax2	A gift from Didier Trono	Addgene #12260
MD2.G	A gift from Didier Trono	Addgene #12259
shCtrl Non-targeting #4 (Ctrl-kd)	transOMIC	TLMSU1400-NT4
pZIP-mCMV-ZsGreen-Mouse-shEGFR	transOMIC	ULTRA-3213354
pZIP-mCMV-ZsGreen-Mouse-Plaur	transOMIC	ULTRA-3232040
pZIP-mCMV-ZsGreen-Mouse-shAreg	transOMIC	ULTRA-3205528
pZIP-mCMV-ZsGreen-Mouse-shEpgn	transOMIC	ULTRA-3383713
pLenti-C-mGFP-hEpgn	OriGene Technologies	RC214501L4
pLenti-C-mGFP-mEpgn	OriGene Technologies	MR219218L4
pLKO.1 TRC control	Moffat et al. 2006	Addgene #10879
pLKO.1 TRC shEpgn #175159	Sigma Aldrich	SHCLNG-NM_053087
LentiCRISPRv2	Sanjana et al. 2014	Addgene #52961
Software and algorithms		
GraphPad Prism 8	Graphpad Software	https://www.graphpad.com/scientific-software/prism/
FIJI v2.0.0-rc-69/1.52p	Schindelin et al. 2012	https://fiji.sc/
R v3.6.1	R Core Team	https://www.r-project.org/
Metascape	Zhou et al. 2019	https://metascape.org/
bcl2fastq v2.17	Illumina, Inc.	https://support.illumina.com/sequ

		encing/sequencing_software/bcl2fastq-conversion-software.html
Kallisto v0.46.0	Bray et al. 2016	http://pachterlab.github.io/kallisto/download
Sleuth v0.30.0	Pimental et al. 2017	https://www.rdocumentation.org/packages/sleuth/versions/0.30.0
Tximport v1.12.3	Bioconductor	https://bioconductor.org/packages/release/bioc/html/tximport.html
Limma v3.40.6	Bioconductor	https://bioconductor.org/packages/release/bioc/html/limma.html

Chapter 4. CONCLUSIONS AND FUTURE DIRECTIONS

4.1 SUMMARY OF PRIMARY FINDINGS

Despite repeated studies since the early 1950s demonstrating that tumor cell clusters can have higher rates of successful metastasis than single tumor cells, our understanding of the molecular processes generating high metastatic potential in cell clusters has remained rudimentary. Throughout my doctoral research, I utilized novel ex vivo 3D culture methods, transcriptomic analyses, live-imaging, genetic perturbation, super-resolution and electron microscopy, and in vivo metastasis assays, among others, to disentangle some of the molecular components underlying this phenotype.

Specifically, I was able to identify and characterize a site generating collective growth signaling in tumor cell clusters, which we refer to as nanolumina. These interstitial structures, lined by microvillous protrusions and bounded by cell-cell junctions, form between clustered tumor cells. Nanolumina can accumulate high concentrations of the growth factor epigen, which we found to be required for efficient metastatic outgrowth in the MMTV-PyMT breast cancer model. Though previous electron microscopy studies in breast cancer have briefly commented on the presence of these structures, to my knowledge our findings are the first to term them nanolumina and to show that they are a site of intercellular signaling which promotes outgrowth.

The molecular properties of tumor cell clusters we have identified have some useful implications for our understanding of cluster-based metastasis. Still, additional studies will be needed to expand on these mechanistic insights and to rigorously assess their relevance to specific subgroups of patients. Below, I highlight some of the properties of collective metastasis elucidated by my doctoral research:

The failure of MMTV-PyMT single cells to metastasize arises partly from early clearance of metastatic cells, not failure to seed metastatic sites. After tail vein injection of fluorescently labeled single or clustered MMTV-PyMT tumor cells, we collected mouse lungs at both early (0hr, 24hr, 48hr) and late (3wk) time points. I found that tumor cell clusters were 10-times more persistent during early lung seeding (30% of initial seeded clusters remaining 48 hours after tail vein injection vs. 3% of initial seeded single cells). These results corroborate prior findings in other models that large amounts of cell attrition occur during early colonization (Chambers et al., 2002; Luzzi et al., 1998; Wong et al., 2001; Yoshida et al., 1993).

One caveat to this study is that metastatic clearance was assessed after experimental injection of tumor cells, instead of via spontaneous metastasis. It is plausible that cells which have successfully intravasated and circulated endogenously have different sensitivity to apoptosis than manually injected cells. An additional caveat is the use of immunocompromised NSG mice, which do not possess functional B, T, or NK cells (Kenney et al., 2016). Repeating these experiments in immunocompetent models could give us useful information about the role of the immune system in regulating tumor cell death or dormancy at this early stage of metastatic colonization, especially given recent findings that clusters are not effectively targeted by natural killer cells (Lo et al., 2020).

But, usefully, this experimental model allowed me to synchronize the circulation and seeding of tumor cells, facilitating a more detailed understanding of cluster vs. single cell phenotypes over the first 72 hours of lung seeding. My findings indicate that, at least in the MMTV-PyMT model, relatively few single or clustered cells remain in the lungs just a few days after initial seeding. However, organization in multicellular clusters appears to

substantially enhance persistence of MMTV-PyMT cells during this critical early period of metastatic colonization.

Apoptosis in mouse and human tumor cells is inhibited by cell-cell adhesion ex vivo. The fragmented nuclei and disrupted morphology of single cells a few days after seeding in the lungs were consistent with induction of apoptosis. This led us to hypothesize that clustering induced pro-survival signaling to enhance early metastatic persistence. However, it was unclear whether cell death was induced by the lung metastatic microenvironment, possibly by pro-apoptotic signals generated by non-tumor cells, or by a lack of intrinsic pro-survival signaling in single tumor cells.

I set out to assess intrinsic differences in induction of apoptosis in single cells vs. clusters in a 3D ex vivo culture system. Using hourly time lapse imaging in the presence of an apoptosis biosensor, I was able to monitor the induction of apoptosis in hundreds of MMTV-PyMT single cells and clusters hourly across several days of culture. I found that even small (less than 10 cell) clusters had greatly increased survival in basement membrane-rich 3D culture compared to single cells from the same tumors and cultured in the same wells. Surviving clusters over a certain size threshold (roughly 10 cells) frequently underwent rapid outgrowth in addition to having high viability. Moreover, 8 of 10 human breast cancer tumors processed shortly after surgical resection had significantly increased survival as clusters in this 3D culture system. Notably, apoptosis induction in the presence of basement-membrane rich extract indicated that these differences in survival between single cells and clusters are not likely to be due to anoikis, i.e. a loss of cell-matrix adhesion. Still, further experiments are needed to identify the

molecular pathways generating this phenotype, and to assess their activation and relevance to metastasis in vivo.

A recent study, also using the MMTV-PyMT model, found that cell-cell adhesion through E-cadherin promotes tumor cell survival via TGFβ signaling and mitigation of oxidative stress (Padmanaban et al., 2019). Future experiments could clarify whether the induction of apoptosis during early seeding I observed is likewise oxidative stress dependent. Additionally, my finding that 2 of 10 human breast cancer samples, a HER2+ tumor and a metaplastic tumor, were able to survive equally well as single cells or clusters suggests inter-tumor heterogeneity exists in apoptosis induction of single cells. Molecular analyses of different mouse and human samples that are sensitive or insensitive to dissociation-induced apoptosis could provide more mechanistic insight into the pro-survival cues generated by aggregation, and their necessity during metastasis.

Aggregation of tumor cells results in sequential transcriptional changes, including early induction of EGFR-related genes which support metastatic outgrowth. Using aggregation of MMTV-PyMT single cells in non-adherent suspension culture I was able to utilize RNA-sequencing to identify sequential expression of genes and pathways throughout the process of tumor cell cluster formation. These transcriptomic analyses demonstrated a rapid induction of EGFR signaling and EGFR ligand expression upon aggregation. I was initially unsure if this method would adequately model tumor cell clusters in vivo; existence in suspension, enzymatic dissociation and reaggregation, and exogeneous growth factor supplementation each represent deviations from in vivo tumor biology. Despite these limitations, this system allowed me to successfully generate hypotheses and identify

genes which later proved to be relevant in vivo. Most importantly, we identified *Epgn* as the most cluster-upregulated gene (comparing 6hr aggregates to single cells), and knockdown of *Epgn* greatly reduced lung metastatic burden relative to control 3 weeks after injection of tumor cell clusters.

However, epigen was just one of many genes and pathways with interesting patterns of expression dependent upon clustering. I additionally identified the EGFR ligand amphiregulin (*Areg*) as a cluster-upregulated gene required for efficient metastatic outgrowth, though the specific mechanism of *Areg*-dependent growth remains to be elucidated. Notably, amphiregulin was recently implicated in cooperative paracrine interactions promoting peritoneal metastasis of cell clusters in ovarian cancer (Naffar-Abu Amara et al., 2020).

Transcriptomic analyses of clusters later during aggregation (12-48 hours of clustering) also indicate that clustering can cause global changes to ribosome biogenesis, epigenetic regulation, and fatty acid synthesis related gene expression, which are each known to alter metastatic potential (Ebright et al., 2020; Feinberg et al., 2016; Hsieh et al., 2011; Röhrig and Schulze, 2016). Further analysis of genes induced or repressed by clustering could generate additional hypotheses on the molecular distinctions between single and clustered tumor cells that lead to their metastatic failure and success, respectively.

Epigen acts as a short-range paracrine growth factor through sequestration in intercellular nanolumina. I found that tumor cell clusters from mouse and human tumors form intercellular nanolumina, often lined by microvilli-like protrusions which can interdigitate

between neighboring cells and provide high surface area for intercellular interactions. We found that epigen is trafficked into nanolumina where it achieves concentrations much higher than those outside the cell cluster. Suppressing epigen expression profoundly reduces both primary tumor growth and metastatic outgrowth in the MMTV-PyMT model.

Overall, my findings indicate that the physical architecture created by multicellularity can generate non-cell-autonomous signaling through the formation of a shared intercellular compartment. By secreting a growth signal into this space, clusters promote proliferation during metastasis. Nanolumenal signaling is an emergent feature of clusters, as these structures cannot form in single cells lacking cell-cell adhesions to generate interstitial spaces with other tumor cells. However, an interesting future direction of this study would be to determine if single tumor cells are ever able to form heterotypic nanolumina. It is possible that single tumor cells form these compartments by adhering to non-tumor cells in their microenvironment such as normal epithelia, or through heterotypic cell-cell adhesion as has been observed with N-cadherin expressing fibroblasts (Labernadie et al., 2017). Future ex vivo co-culture and in vivo experiments could clarify if nanolumina form via adhesion to other cell types in the tumor microenvironment, and whether this promotes tumor cell growth or survival.

Epigen suppression is associated with migratory states. We observed that epigen expression is not universally high throughout metastasis. Proliferative tumors and disseminated clusters with rounded, epithelial morphology were predominantly epigen high. But we also identified a population of tumor cell clusters in the peritumoral area with extensive membrane protrusions and a strand-like morphology that lowly expressed

intercellular epigen. I am curious if these represent more motile clusters, since protrusive morphology is often associated with invasion (Friedl et al., 2012). But, fixed tumor sections do not allow me to functionally assess the migration of these clusters in vivo. Intravital imaging of peritumoral areas could provide a means of directly visualizing local epigen-high and epigen-low cluster motility (Ilina et al., 2018). These experiments were out of the scope of my doctoral research but could represent an exciting future direction of this project.

That being said, the fact that epigen knockdown in orthotopic tumor transplants results in a modest increase in the presence of peritumoral clusters in vivo, and notably enhanced collective migration of clusters ex vivo, suggests there may be an interesting anti-correlation between *Epgn* expression and migratory state. Further study could reveal the mechanistic connections between epigen and collective migration, if any.

Nanolumina and epigen signaling are enriched in specific subtypes of breast cancer. Naturally, a caveat to any study in mouse models of cancer is the possibility that one has discovered a species-specific mechanism present in mice but not humans. To address this possibility, I analyzed several different kinds of human breast cancer tissues. I directly observed nanolumenal structures in freshly isolated tumor cell clusters collected from malignant ascites. Further, I identified a subset of *EPGN*-high cell lines derived from aggressive triple negative breast cancers, specifically of the basal-like 2 (BL2) subtype. Three of three tested BL2 cell lines contained intercellular nanolumina. *EPGN* knockdown in the HCC70 BL2 cell line, whose transcription has relatively high concordance with patient tumors (Liu et al., 2019b), suppressed cluster growth ex vivo and in the lungs.

These data support the functional relevance of this pathway to metastatic outgrowth in human cancer.

Conversely, when I assessed epigen-low triple negative cell lines from the mesenchymal-like (M-like) phenotype I found that intercellular spaces in these clusters were poorly organized, with reduced microvillous protrusions and cell-cell adhesion compared to BL2 clusters. Based on this heterogeneity between these cell lines, I anticipate that only certain subsets of patients may benefit from therapies that inhibit nanolumenal epigen signaling. Regardless, additional pre-clinical studies will be needed first to understand nanolumenal signaling in greater detail across all subtypes of breast cancer, and perhaps other epithelial cancers.

4.2 REMAINING RESEARCH QUESTIONS AND FUTURE DIRECTIONS

Like most scientific undertakings, my research has created far more questions than it has answered. Some of these may represent fruitful areas for further inquiry into the mechanisms of collective metastasis. Below, I list some intriguing questions left largely unanswered by my doctoral dissertation.

What other components are enriched in or signal through nanolumina? The presence and accumulation of epigen in nanolumina is an interesting finding given its apparent requirement for efficient MMTV-PyMT cluster outgrowth. However, there may be a number of other growth factors, proteins, metabolites, or signaling molecules likewise enriched in the nanolumina. Collection and purification of the nanolumenal fraction within

mouse and human tumor cell clusters, followed by analyses using mass spectrometry or reverse phase protein arrays, could help reveal other pathways with nanolumina-dependent functions. Once identified, an interesting future direction would be to assess these components in nanolumina across different metastatic phenotypes such as invasion, circulation, immune evasion, and outgrowth. It may be that nanolumenal signaling shifts throughout metastasis, and such shifts could contribute to the plasticity needed to accomplish the entire metastatic cascade. These hypotheses remain untested at this time, but the development of tools to isolate and assess nanolumenal signaling factors could lead to interesting discoveries about this compartment's role during metastasis.

How is epigen expression regulated dynamically in tumor cells? We identified subsets of high and low epigen expressing tumor cell clusters in vivo. The increased migratory behavior of *Epgn* knockdown clusters ex vivo suggests that epigen-low clusters may represent a low proliferation but high motility subpopulation of tumor cell clusters. However, the mechanisms regulating transitions between epigen-high and epigen-low states remain unknown. Does epigen downregulation specifically promote migratory gene expression, as indicated by our ex vivo RNA-sequencing data? Alternatively, do environmental factors promote a migratory phenotype, which then results in epigen downregulation? Perhaps both are true through the creation of positive feedback loops. Reverse chromatin immunoprecipitation and gene locus proximity labeling-based techniques could be useful for identification of specific regulators of *Epgn* transcription, though these techniques may require optimization for use in breast cancer organoids

(Gauchier et al., 2020). Understanding this transcriptional regulation in greater detail might provide insight into genes regulating important transitions between migratory and proliferative states in tumor cell clusters in vivo.

What junctions gate the nanolumina? Can they be targeted to reduce intercellular communication? An important feature of nanolumenal signaling that we identified is the ability for cell-cell junctions to regulate permeability, preventing molecules like sulfo-NHS-biotin from leaking into intercellular spaces, and largely preventing the escape of epigen into the microenvironment. Using transmission electron microscopy, we identify frequent electron-dense cell-cell junctions sealing nanolumina and establishing their 3D structure. However, the components making up these junctions, and their specific contributions to nanolumenal signaling or junctional permeability, are still unknown. Immunofluorescence and immunoelectron microscopy studies could be used to assess the presence of tight junctions, homophilic or heterophilic cadherin junctions, desmosomes, gap junctions, or other cell-cell adhesions. CRISPR knockout strategies could then be used to

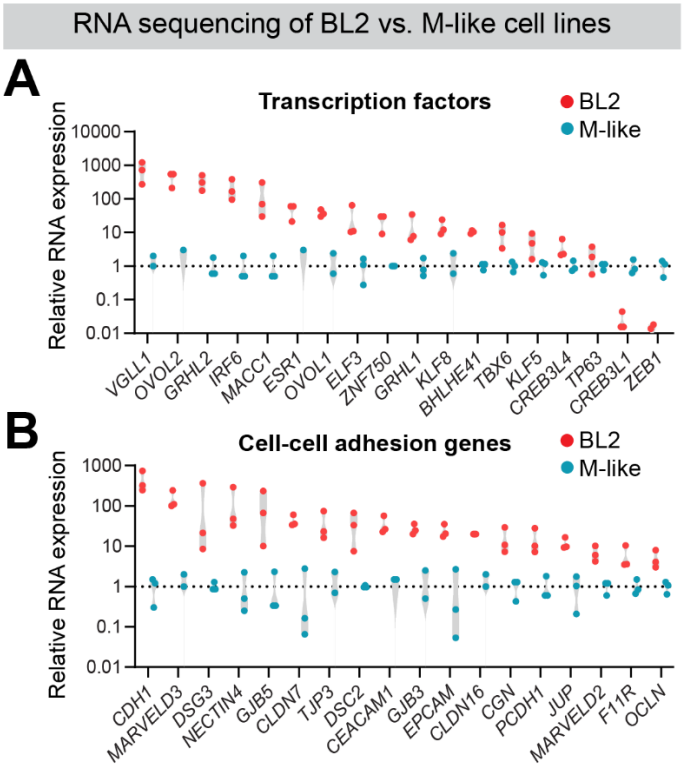

Figure 4.1. BL2 vs M transcription.
Differentially expressed **(A)** transcription factors and **(B)** cell-cell adhesion genes between basal-like 2/epigen-high (HCC70, CAL851, HDQP1) and mesenchymal-like/epigen-low (MDA-MB-231, MDA-MB-436, BT549) cell lines (adjusted p-value ≤ 0.05; CCLE, Barretina et al. 2012).

determine if ablation of these genes prevents the formation of nanolumina, or increases their permeability to molecules present in the local microenvironment.

Analyzing differentially expressed genes between nanolumen/epigen-high (BL2) and nanolumen/epigen-low (M-like) cell lines points to some interesting candidates regulators of nanolumen formation **(Figure 4.1A)**, such as the transcription factor GRHL2 which is known to regulate lumen formation, tight junction expression, and epithelial morphogenesis (Senga et al., 2012; Xiang et al., 2012). Likewise evaluating the expression of BL2 enriched cell-cell adhesion molecules **(Figure 4.1B)** could help us identify the junctional complexes organizing nanolumenal spaces. Together these studies would give us a better understanding of the generation and maintenance of nanolumina, which may in turn reveal therapeutic vulnerabilities of these structures.

Do other tissues contain nanolumina? Do they play an important role in normal signaling or development? Intercellular cavities similar to those described here have been previously observed in normal mammary epithelia and breast cancer (Ewald et al., 2012; Mazzucchelli et al., 2019; Tarin, 1969). Additionally, further review of published electron microscopy micrographs reveals the presence of intercellular structures with similar morphology in other tissues including liver ductal plate cells (Benhamouche-Trouillet et al., 2018), podocyte organoids (Kim et al., 2017b; Przepiorski et al., 2018), hair follicles (Behrendt et al., 2012), airway organoids (Sachs et al., 2019), meningiomas (Georgescu et al., 2018), lung cancer (Albero-González et al., 2019; Obiditsch-Mayer and Breitfellner, 1968), and ovarian cancer (Blaustein, 1976; Le et al., 2010). In some developmental tissues, these intercellular lumina are thought to fuse into larger macrolumina later in

development (Dumortier et al., 2019; Marty-Santos and Cleaver, 2016; Villasenor et al., 2010).

It may be that these structures are dispensable for intercellular signaling in other tissues. But, given the important function they serve in breast cancer cell clusters reported here, it seems plausible that nanolumina might facilitate similar collective signaling mechanisms in other tissues. Examining these compartments and their contents in a broad range of tissue types and conditions might lead to more general insights into intercellular interactions during epithelial development, homeostasis, wound healing, or cancer.

4.3 GRAPHICAL RESEARCH SUMMARY

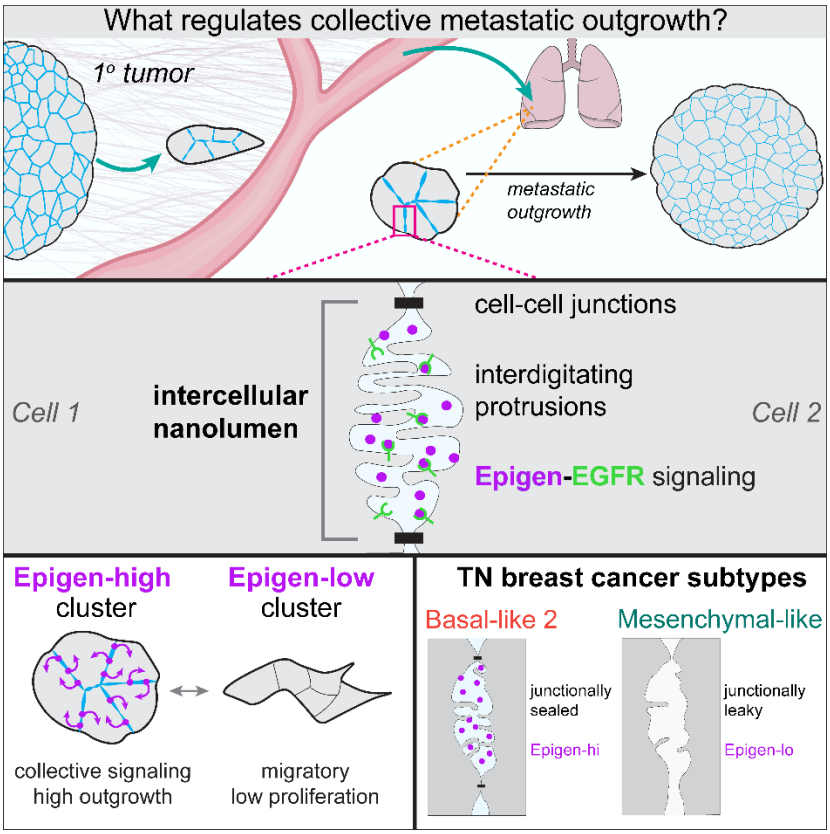

Figure 4.2. Graphical Research Summary.

My doctoral dissertation research has revealed that tumor cell clusters can form intercellular nanolumina which accumulate high concentrations of the growth factor epigen. Nanolumina and high epigen expression were observed in basal-like 2 human breast cancer cells, but not mesenchymal-like triple negative breast cancer cells. Interruption of this signaling through *Epgn* knockdown strongly reduces primary and metastatic outgrowth. These findings present a specific and potentially targetable molecular mechanism underlying the rapid metastatic outgrowth of tumor cell clusters.

BIBLIOGRAPHY

Aasen, T., Mesnil, M., Naus, C.C., Lampe, P.D., and Laird, D.W. (2016). Gap junctions and cancer: communicating for 50 years. Nature Reviews Cancer *16*, 775-788.

Aceto, N. (2020). Bring along your friends: Homotypic and heterotypic circulating tumor cell clustering to accelerate metastasis. Biomedical Journal *43*, 18-23.

Aceto, N., Bardia, A., Miyamoto, D.T., Donaldson, M.C., Wittner, B.S., Spencer, J.A., Yu, M., Pely, A., Engstrom, A., Zhu, H.*, et al.* (2014). Circulating tumor cell clusters are oligoclonal precursors of breast cancer metastasis. Cell *158*, 1110-1122.

Aceto, N., Toner, M., Maheswaran, S., and Haber, D.A. (2015). En Route to Metastasis: Circulating Tumor Cell Clusters and Epithelial-to-Mesenchymal Transition. Trends Cancer *1*, 44-52.

Aisenbrey, E.A., and Murphy, W.L. (2020). Synthetic alternatives to Matrigel. Nature Reviews Materials.

Al-Mehdi, A.B., Tozawa, K., Fisher, A.B., Shientag, L., Lee, A., and Muschel, R.J. (2000). Intravascular origin of metastasis from the proliferation of endothelium-attached tumor cells: a new model for metastasis. Nature Medicine *6*, 100-102.

Al Habyan, S., Kalos, C., Szymborski, J., and McCaffrey, L. (2018). Multicellular detachment generates metastatic spheroids during intra-abdominal dissemination in epithelial ovarian cancer. Oncogene *37*, 5127-5135.

Albero-González, R., Munné-Collado, J., Pijuan, L., Simón, M., Gimeno-Beltrán, J., Mojal, S., Salido, M., Clavé, S., Juanpere, N., Dalmases, A.*, et al.* (2019). Complementary value of electron microscopy and immunohistochemistry in the diagnosis of non-small cell lung cancer: A potential role for electron microscopy in the era of targeted therapy. Ultrastructural Pathology *43*, 237-247.

Aleskandarany, M.A., Sonbul, S.N., Mukherjee, A., and Rakha, E.A. (2015). Molecular Mechanisms Underlying Lymphovascular Invasion in Invasive Breast Cancer. Pathobiology *82*, 113-123.

Allard, W.J., Matera, J., Miller, M.C., Repollet, M., Connelly, M.C., Rao, C., Tibbe, A.G.J., Uhr, J.W., and Terstappen, L.W.M.M. (2004). Tumor Cells Circulate in the Peripheral Blood of All Major Carcinomas but not in Healthy Subjects or Patients With Nonmalignant Diseases. Clinical Cancer Research *10*, 6897-6904.

Allen, T.A., Asad, D., Amu, E., Hensley, M.T., Cores, J., Vandergriff, A., Tang, J., Dinh, P.-U., Shen, D., and Qiao, L. (2019). Circulating tumor cells exit circulation while maintaining multicellularity, augmenting metastatic potential. Journal of Cell Science *132*, jcs231563.

Allen, T.A., Gracieux, D., Talib, M., Tokarz, D.A., Hensley, M.T., Cores, J., Vandergriff, A., Tang, J., de Andrade, J.B., and Dinh, P.U. (2017). Angiopellosis as an alternative mechanism of cell extravasation. Stem Cells *35*, 170-180.

Aman, A., and Piotrowski, T. (2008). Wnt/beta-catenin and Fgf signaling control collective cell migration by restricting chemokine receptor expression. Developmental cell *15*, 749-761.

Amantini, C., Morelli, M.B., Nabissi, M., Piva, F., Marinelli, O., Maggi, F., Bianchi, F., Bittoni, A., Berardi, R., Giampieri, R.*, et al.* (2019). Expression Profiling of Circulating Tumor Cells in Pancreatic Ductal Adenocarcinoma Patients: Biomarkers Predicting Overall Survival. Front Oncol *9*, 874.

Amintas, S., Bedel, A., Moreau-Gaudry, F., Boutin, J., Buscail, L., Merlio, J.P., Vendrely, V., Dabernat, S., and Buscail, E. (2020). Circulating Tumor Cell Clusters: United We Stand Divided We Fall. Int J Mol Sci *21*.

Anderberg, C., Cunha, S.I., Zhai, Z., Cortez, E., Pardali, E., Johnson, J.R., Franco, M., Páez-Ribes, M., Cordiner, R., and Fuxe, J. (2013). Deficiency for endoglin in tumor vasculature weakens the endothelial barrier to metastatic dissemination. Journal of Experimental Medicine *210*, 563-579.

Antonioli, L., Blandizzi, C., Pacher, P., Guilliams, M., and Hasko, G. (2019). Rethinking Communication in the Immune System: The Quorum Sensing Concept. Trends in immunology *40*, 88-97.

Archetti, M., and Pienta, K.J. (2019). Cooperation among cancer cells: applying game theory to cancer. Nature Reviews Cancer *19*, 110-117.

Ashworth, T. (1869). A case of cancer in which cells similar to those in the tumours were seen in the blood after death. Aust Med J *14*, 146-149.

Au, S.H., Edd, J., Haber, D.A., Maheswaran, S., Stott, S.L., and Toner, M. (2017). Clusters of Circulating Tumor Cells: a Biophysical and Technological Perspective. Curr Opin Biomed Eng *3*, 13-19.

Au, S.H., Storey, B.D., Moore, J.C., Tang, Q., Chen, Y.L., Javaid, S., Sarioglu, A.F., Sullivan, R., Madden, M.W., O'Keefe, R.*, et al.* (2016). Clusters of circulating tumor cells traverse capillary-sized vessels. Proc Natl Acad Sci U S A *113*, 4947-4952.

Avagliano, A., Fiume, G., Ruocco, M.R., Martucci, N., Vecchio, E., Insabato, L., Russo, D., Accurso, A., Masone, S., and Montagnani, S. (2020). Influence of fibroblasts on mammary gland development, breast cancer microenvironment remodeling, and cancer cell dissemination. Cancers *12*, 1697.

Azzam, E.I., de Toledo, S.M., and Little, J.B. (2003). Oxidative metabolism, gap junctions and the ionizing radiation-induced bystander effect. Oncogene *22*, 7050-7057.

Balak, J.R.A., de Graaf, N., Zaldumbide, A., Rabelink, T.J., Hoeben, R.C., de Koning, E.J.P., and Carlotti, F. (2019). Highly efficient ex vivo lentiviral transduction of primary human pancreatic exocrine cells. Scientific Reports *9*, 15870.

Baluk, P., Morikawa, S., Haskell, A., Mancuso, M., and McDonald, D.M. (2003). Abnormalities of basement membrane on blood vessels and endothelial sprouts in tumors. The American journal of pathology *163*, 1801-1815.

Barretina, J., Caponigro, G., Stransky, N., Venkatesan, K., Margolin, A.A., Kim, S., Wilson, C.J., Lehar, J., Kryukov, G.V., Sonkin, D.*, et al.* (2012). The Cancer Cell Line

Encyclopedia enables predictive modelling of anticancer drug sensitivity. Nature *483*, 603-607.

Behrendt, K., Klatte, J., Pofahl, R., Bloch, W., Smyth, N., Tscharntke, M., Krieg, T., Paus, R., Niessen, C., Niemann, C.*, et al.* (2012). A function for Rac1 in the terminal differentiation and pigmentation of hair. Journal of Cell Science *125*, 896-905.

Ben-Jacob, E., Coffey, D.S., and Levine, H. (2012). Bacterial survival strategies suggest rethinking cancer cooperativity. Trends in microbiology *20*, 403-410.

Benham-Pyle, B.W., Pruitt, B.L., and Nelson, W.J. (2015). Mechanical strain induces E-cadherin–dependent Yap1 and β-catenin activation to drive cell cycle entry. Science (New York, NY) *348*, 1024-1027.

Benhamouche-Trouillet, S., O'Loughlin, E., Liu, C.H., Polacheck, W., Fitamant, J., McKee, M., El-Bardeesy, N., Chen, C.S., and McClatchey, A.I. (2018). Proliferation-independent role of NF2 (merlin) in limiting biliary morphogenesis. Development *145*.

Bilandzic, M., Rainczuk, A., Green, E., Fairweather, N., Jobling, T.W., Plebanski, M., and Stephens, A.N. (2019). Keratin-14 (KRT14) positive leader cells mediate mesothelial clearance and invasion by ovarian cancer cells. Cancers *11*, 1228.

Binnewies, M., Roberts, E.W., Kersten, K., Chan, V., Fearon, D.F., Merad, M., Coussens, L.M., Gabrilovich, D.I., Ostrand-Rosenberg, S., Hedrick, C.C.*, et al.* (2018). Understanding the tumor immune microenvironment (TIME) for effective therapy. Nature Medicine *24*, 541-550.

Birkbak, N.J., and McGranahan, N. (2020). Cancer Genome Evolutionary Trajectories in Metastasis. Cancer cell *37*, 8-19.

Blaustein, A. (1976). Papillary serous tumors of the ovary: An electron microscopic study. Gynecologic Oncology *4*, 314-323.

Boareto, M., Jolly, M.K., Goldman, A., Pietilä, M., Mani, S.A., Sengupta, S., Ben-Jacob, E., Levine, H., and Onuchic, J.N. (2016). Notch-Jagged signalling can give rise to clusters of cells exhibiting a hybrid epithelial/mesenchymal phenotype. J R Soc Interface *13*.

Bockhorn, M., Jain, R.K., and Munn, L.L. (2007). Active versus passive mechanisms in metastasis: do cancer cells crawl into vessels, or are they pushed? Lancet Oncol *8*, 444-448.

Bray, N.L., Pimentel, H., Melsted, P., and Pachter, L. (2016). Near-optimal probabilistic RNA-seq quantification. Nature biotechnology *34*, 525-527.

Bronsert, P., Enderle-Ammour, K., Bader, M., Timme, S., Kuehs, M., Csanadi, A., Kayser, G., Kohler, I., Bausch, D., Hoeppner, J.*, et al.* (2014). Cancer cell invasion and EMT marker expression: a three-dimensional study of the human cancer-host interface. J Pathol *234*, 410-422.

Brown, C.W., Amante, J.J., and Mercurio, A.M. (2018). Cell clustering mediated by the adhesion protein PVRL4 is necessary for alpha6beta4 integrin-promoted ferroptosis resistance in matrix-detached cells. The Journal of biological chemistry *293*, 12741-12748.

Brücher, B.L., and Jamall, I.S. (2014). Cell-cell communication in the tumor microenvironment, carcinogenesis, and anticancer treatment. Cell Physiol Biochem *34*, 213-243.

Bruewer, M., Luegering, A., Kucharzik, T., Parkos, C.A., Madara, J.L., Hopkins, A.M., and Nusrat, A. (2003). Proinflammatory Cytokines Disrupt Epithelial Barrier Function by Apoptosis-Independent Mechanisms. The Journal of Immunology *171*, 6164-6172.

Bruner, H.C., and Derksen, P.W.B. (2018). Loss of E-Cadherin-Dependent Cell-Cell Adhesion and the Development and Progression of Cancer. Cold Spring Harb Perspect Biol *10*.

Bruno, R.D., Fleming, J.M., George, A.L., Boulanger, C.A., Schedin, P., and Smith, G.H. (2017). Mammary extracellular matrix directs differentiation of testicular and embryonic stem cells to form functional mammary glands in vivo. Sci Rep *7*, 40196.

Buscail, E., Alix-Panabières, C., Quincy, P., Cauvin, T., Chauvet, A., Degrandi, O., Caumont, C., Verdon, S., Lamrissi, I., Moranvillier, I.*, et al.* (2019). High Clinical Value of Liquid Biopsy to Detect Circulating Tumor Cells and Tumor Exosomes in Pancreatic Ductal Adenocarcinoma Patients Eligible for Up-Front Surgery. Cancers (Basel) *11*.

Cai, D., Chen, S.C., Prasad, M., He, L., Wang, X., Choesmel-Cadamuro, V., Sawyer, J.K., Danuser, G., and Montell, D.J. (2014). Mechanical feedback through E-cadherin promotes direction sensing during collective cell migration. Cell *157*, 1146-1159.

Camerer, E., Qazi, A.A., Duong, D.N., Cornelissen, I., Advincula, R., and Coughlin, S.R. (2004). Platelets, protease-activated receptors, and fibrinogen in hematogenous metastasis. Blood *104*, 397-401.

Carlson, P., Dasgupta, A., Grzelak, C.A., Kim, J., Barrett, A., Coleman, I.M., Shor, R.E., Goddard, E.T., Dai, J., Schweitzer, E.M.*, et al.* (2019). Targeting the perivascular niche sensitizes disseminated tumour cells to chemotherapy. Nature cell biology *21*, 238-250.

Casasent, A.K., Schalck, A., Gao, R., Sei, E., Long, A., Pangburn, W., Casasent, T., Meric-Bernstam, F., Edgerton, M.E., and Navin, N.E. (2018). Multiclonal Invasion in Breast Tumors Identified by Topographic Single Cell Sequencing. Cell *172*, 205-217.e212.

Catenacci, D.V., Chapman, C.G., Xu, P., Koons, A., Konda, V.J., Siddiqui, U.D., and Waxman, I. (2015). Acquisition of Portal Venous Circulating Tumor Cells From Patients With Pancreaticobiliary Cancers by Endoscopic Ultrasound. Gastroenterology *149*, 1794-1803.e1794.

Cattaneo, C.M., Dijkstra, K.K., Fanchi, L.F., Kelderman, S., Kaing, S., van Rooij, N., van den Brink, S., Schumacher, T.N., and Voest, E.E. (2020). Tumor organoid–T-cell coculture systems. Nature Protocols *15*, 15-39.

Celià-Terrassa, T., and Kang, Y. (2016). Distinctive properties of metastasis-initiating cells. Genes Dev *30*, 892-908.

Chabottaux, V., Ricaud, S., Host, L., Blacher, S., Paye, A., Thiry, M., Garofalakis, A., Pestourie, C., Gombert, K., and Bruyere, F. (2009). Membrane-type 4 matrix

metalloproteinase (MT4-MMP) induces lung metastasis by alteration of primary breast tumour vascular architecture. Journal of cellular and molecular medicine *13*, 4002-4013.

Chambers, A.F., Groom, A.C., and MacDonald, I.C. (2002). Dissemination and growth of cancer cells in metastatic sites. Nature Reviews Cancer *2*, 563-572.

Chan, I.S., Knútsdóttir, H., Ramakrishnan, G., Padmanaban, V., Warrier, M., Ramirez, J.C., Dunworth, M., Zhang, H., Jaffee, E.M., Bader, J.S.*, et al.* (2020). Cancer cells educate natural killer cells to a metastasis-promoting cell state. The Journal of cell biology *219*.

Chang, M.C., Chang, Y.T., Chen, J.Y., Jeng, Y.M., Yang, C.Y., Tien, Y.W., Yang, S.H., Chen, H.L., Liang, T.Y., Wang, C.F.*, et al.* (2016). Clinical Significance of Circulating Tumor Microemboli as a Prognostic Marker in Patients with Pancreatic Ductal Adenocarcinoma. Clin Chem *62*, 505-513.

Chang, Y.S., di Tomaso, E., McDonald, D.M., Jones, R., Jain, R.K., and Munn, L.L. (2000). Mosaic blood vessels in tumors: Frequency of cancer cells in contact with flowing blood. Proceedings of the National Academy of Sciences *97*, 14608-14613.

Chen, C.C., Plikus, M.V., Tang, P.C., Widelitz, R.B., and Chuong, C.M. (2016). The Modulatable Stem Cell Niche: Tissue Interactions during Hair and Feather Follicle Regeneration. J Mol Biol *428*, 1423-1440.

Chen, C.C., Wang, L., Plikus, M.V., Jiang, T.X., Murray, P.J., Ramos, R., Guerrero-Juarez, C.F., Hughes, M.W., Lee, O.K., Shi, S.*, et al.* (2015). Organ-level quorum sensing directs regeneration in hair stem cell populations. Cell *161*, 277-290.

Chen, M.B., Hajal, C., Benjamin, D.C., Yu, C., Azizgolshani, H., Hynes, R.O., and Kamm, R.D. (2018). Inflamed neutrophils sequestered at entrapped tumor cells via chemotactic confinement promote tumor cell extravasation. Proceedings of the National Academy of Sciences *115*, 7022-7027.

Cheng, L., Montironi, R., Davidson, D.D., and Lopez-Beltran, A. (2009). Staging and reporting of urothelial carcinoma of the urinary bladder. Modern Pathology *22*, S70-S95.

Cheung, K.J., and Ewald, A.J. (2016). A collective route to metastasis: Seeding by tumor cell clusters. Science (New York, NY) *352*, 167-169.

Cheung, K.J., Gabrielson, E., Werb, Z., and Ewald, A.J. (2013). Collective invasion in breast cancer requires a conserved basal epithelial program. Cell *155*, 1639-1651.

Cheung, K.J., Padmanaban, V., Silvestri, V., Schipper, K., Cohen, J.D., Fairchild, A.N., Gorin, M.A., Verdone, J.E., Pienta, K.J., Bader, J.S.*, et al.* (2016). Polyclonal breast cancer metastases arise from collective dissemination of keratin 14-expressing tumor cell clusters. Proceedings of the National Academy of Sciences of the United States of America *113*, E854-863.

Chiossone, L., Dumas, P.-Y., Vienne, M., and Vivier, E. (2018). Natural killer cells and other innate lymphoid cells in cancer. Nature Reviews Immunology *18*, 671-688.

Cho, E.H., Wendel, M., Luttgen, M., Yoshioka, C., Marrinucci, D., Lazar, D., Schram, E., Nieva, J., Bazhenova, L., Morgan, A.*, et al.* (2012). Characterization of circulating tumor cell aggregates identified in patients with epithelial tumors. Phys Biol *9*, 016001.

Choi, J.-H., Park, J.T., Davidson, B., Morin, P.J., Shih, I.-M., and Wang, T.-L. (2008). Jagged-1 and Notch3 Juxtacrine Loop Regulates Ovarian Tumor Growth and Adhesion. Cancer research *68*, 5716-5723.

Choi, J.W., Kim, J.K., Yang, Y.J., Kim, P., Yoon, K.-H., and Yun, S.H. (2015). Urokinase Exerts Antimetastatic Effects by Dissociating Clusters of Circulating Tumor Cells. Cancer research *75*, 4474-4482.

Cichon, M.A., Degnim, A.C., Visscher, D.W., and Radisky, D.C. (2010). Microenvironmental Influences that Drive Progression from Benign Breast Disease to Invasive Breast Cancer. Journal of Mammary Gland Biology and Neoplasia *15*, 389-397.

Ciriello, G., Gatza, Michael L., Beck, Andrew H., Wilkerson, Matthew D., Rhie, Suhn K., Pastore, A., Zhang, H., McLellan, M., Yau, C., Kandoth, C.*, et al.* (2015). Comprehensive Molecular Portraits of Invasive Lobular Breast Cancer. Cell *163*, 506-519.

Clark, A.G., and Vignjevic, D.M. (2015). Modes of cancer cell invasion and the role of the microenvironment. Current Opinion in Cell Biology *36*, 13-22.

Cleary, A.S., Leonard, T.L., Gestl, S.A., and Gunther, E.J. (2014). Tumour cell heterogeneity maintained by cooperating subclones in Wnt-driven mammary cancers. Nature *508*, 113-117.

Commander, R., Wei, C., Sharma, A., Mouw, J.K., Burton, L.J., Summerbell, E., Mahboubi, D., Peterson, R.J., Konen, J., Zhou, W.*, et al.* (2020). Subpopulation targeting of pyruvate dehydrogenase and GLUT1 decouples metabolic heterogeneity during collective cancer cell invasion. Nature communications *11*, 1533.

Cornetta, K., and Anderson, W.F. (1989). Protamine sulfate as an effective alternative to polybrene in retroviral-mediated gene-transfer: implications for human gene therapy. Journal of Virological Methods *23*, 187-194.

Costa, C., Muinelo-Romay, L., Cebey-López, V., Pereira-Veiga, T., Martínez-Pena, I., Abreu, M., Abalo, A., Lago-Lestón, R.M., Abuín, C., Palacios, P.*, et al.* (2020). Analysis of a Real-World Cohort of Metastatic Breast Cancer Patients Shows Circulating Tumor Cell Clusters (CTC-clusters) as Predictors of Patient Outcomes. Cancers *12*.

Cristofanilli, M., Budd, G.T., Ellis, M.J., Stopeck, A., Matera, J., Miller, M.C., Reuben, J.M., Doyle, G.V., Allard, W.J., Terstappen, L.W.M.M.*, et al.* (2004). Circulating Tumor Cells, Disease Progression, and Survival in Metastatic Breast Cancer. New England Journal of Medicine *351*, 781-791.

Cristofanilli, M., Pierga, J.-Y., Reuben, J., Rademaker, A., Davis, A.A., Peeters, D.J., Fehm, T., Nolé, F., Gisbert-Criado, R., Mavroudis, D.*, et al.* (2019). The clinical use of circulating tumor cells (CTCs) enumeration for staging of metastatic breast cancer (MBC): International expert consensus paper. Critical Reviews in Oncology/Hematology *134*, 39-45.

Daher, M., and Rezvani, K. (2018). Next generation natural killer cells for cancer immunotherapy: the promise of genetic engineering. Curr Opin Immunol *51*, 146-153.

Dang, H.X., Krasnick, B.A., White, B.S., Grossman, J.G., Strand, M.S., Zhang, J., Cabanski, C.R., Miller, C.A., Fulton, R.S., Goedegebuure, S.P.*, et al.* (2020). The clonal evolution of metastatic colorectal cancer. Science Advances *6*, eaay9691.

Das, T., Safferling, K., Rausch, S., Grabe, N., Boehm, H., and Spatz, J.P. (2015). A molecular mechanotransduction pathway regulates collective migration of epithelial cells. Nature cell biology *17*, 276-287.

Dasgupta, A., Lim, A.R., and Ghajar, C.M. (2017). Circulating and disseminated tumor cells: harbingers or initiators of metastasis? Molecular oncology *11*, 40-61.

Davis, R.T., Blake, K., Ma, D., Gabra, M.B.I., Hernandez, G.A., Phung, A.T., Yang, Y., Maurer, D., Lefebvre, A., Alshetaiwi, H.*, et al.* (2020). Transcriptional diversity and bioenergetic shift in human breast cancer metastasis revealed by single-cell RNA sequencing. Nature cell biology *22*, 310-320.

de Witte, C.J., Espejo Valle-Inclan, J., Hami, N., Lõhmussaar, K., Kopper, O., Vreuls, C.P.H., Jonges, G.N., van Diest, P., Nguyen, L., Clevers, H.*, et al.* (2020). Patient-Derived Ovarian Cancer Organoids Mimic Clinical Response and Exhibit Heterogeneous Inter- and Intrapatient Drug Responses. Cell reports *31*, 107762.

Debnath, J., and Brugge, J.S. (2005). Modelling glandular epithelial cancers in three-dimensional cultures. Nature reviews Cancer *5*, 675-688.

Debnath, J., Muthuswamy, S.K., and Brugge, J.S. (2003). Morphogenesis and oncogenesis of MCF-10A mammary epithelial acini grown in three-dimensional basement membrane cultures. Methods *30*, 256-268.

Deisboeck, T.S., and Couzin, I.D. (2009). Collective behavior in cancer cell populations. Bioessays *31*, 190-197.

Delattre, J.Y., Krol, G., Thaler, H.T., and Posner, J.B. (1988). Distribution of brain metastases. Arch Neurol *45*, 741-744.

Derynck, R., and Weinberg, R.A. (2019). EMT and Cancer: More Than Meets the Eye. Dev Cell *49*, 313-316.

Diermeier, S.D., Chang, K.C., Freier, S.M., Song, J., El Demerdash, O., Krasnitz, A., Rigo, F., Bennett, C.F., and Spector, D.L. (2016). Mammary Tumor-Associated RNAs Impact Tumor Cell Proliferation, Invasion, and Migration. Cell reports *17*, 261-274.

Doganer, B.A., Yan, L.K.Q., and Youk, H. (2016). Autocrine Signaling and Quorum Sensing: Extreme Ends of a Common Spectrum. Trends in cell biology *26*, 262-271.

Dominguez, A.A., Lim, W.A., and Qi, L.S. (2016). Beyond editing: repurposing CRISPR-Cas9 for precision genome regulation and interrogation. Nature reviews Molecular cell biology *17*, 5-15.

Donà, E., Barry, J.D., Valentin, G., Quirin, C., Khmelinskii, A., Kunze, A., Durdu, S., Newton, L.R., Fernandez-Minan, A., Huber, W.*, et al.* (2013). Directional tissue migration through a self-generated chemokine gradient. Nature *503*, 285-289.

Dong, L.Q., Shi, Y., Ma, L.J., Yang, L.X., Wang, X.Y., Zhang, S., Wang, Z.C., Duan, M., Zhang, Z., Liu, L.Z.*, et al.* (2018). Spatial and temporal clonal evolution of intrahepatic cholangiocarcinoma. J Hepatol *69*, 89-98.

Dongre, A., and Weinberg, R.A. (2019). New insights into the mechanisms of epithelial-mesenchymal transition and implications for cancer. Nature reviews Molecular cell biology *20*, 69-84.

Drost, J., and Clevers, H. (2018). Organoids in cancer research. Nature reviews Cancer *18*, 407-418.

Drost, J., Karthaus, W.R., Gao, D., Driehuis, E., Sawyers, C.L., Chen, Y., and Clevers, H. (2016). Organoid culture systems for prostate epithelial and cancer tissue. Nature Protocols *11*, 347-358.

Duda, D.G., Duyverman, A.M.M.J., Kohno, M., Snuderl, M., Steller, E.J.A., Fukumura, D., and Jain, R.K. (2010). Malignant cells facilitate lung metastasis by bringing their own soil. Proceedings of the National Academy of Sciences *107*, 21677-21682.

Dumortier, J.G., Le Verge-Serandour, M., Tortorelli, A.F., Mielke, A., de Plater, L., Turlier, H., and Maître, J.L. (2019). Hydraulic fracturing and active coarsening position the lumen of the mouse blastocyst. Science (New York, NY) *365*, 465-468.

Durdu, S., Iskar, M., Revenu, C., Schieber, N., Kunze, A., Bork, P., Schwab, Y., and Gilmour, D. (2014). Luminal signalling links cell communication to tissue architecture during organogenesis. Nature *515*, 120-124.

Ebright, R.Y., Lee, S., Wittner, B.S., Niederhoffer, K.L., Nicholson, B.T., Bardia, A., Truesdell, S., Wiley, D.F., Wesley, B., Li, S.*, et al.* (2020). Deregulation of ribosomal protein expression and translation promotes breast cancer metastasis. Science (New York, NY) *367*, 1468-1473.

Echeverria, G.V., Powell, E., Seth, S., Ge, Z., Carugo, A., Bristow, C., Peoples, M., Robinson, F., Qiu, H., Shao, J.*, et al.* (2018). High-resolution clonal mapping of multi-organ metastasis in triple negative breast cancer. Nature communications *9*, 5079.

Egan, K., Cooke, N., and Kenny, D. (2014). Living in shear: platelets protect cancer cells from shear induced damage. Clinical & experimental metastasis *31*, 697-704.

Egeblad, M., Nakasone, E.S., and Werb, Z. (2010). Tumors as organs: complex tissues that interface with the entire organism. Dev Cell *18*, 884-901.

Ellison, D., Mugler, A., Brennan, M.D., Lee, S.H., Huebner, R.J., Shamir, E.R., Woo, L.A., Kim, J., Amar, P., Nemenman, I.*, et al.* (2016). Cell–cell communication enhances the capacity of cell ensembles to sense shallow gradients during morphogenesis. Proceedings of the National Academy of Sciences *113*, E679-E688.

Enderle-Ammour, K., Bader, M., Ahrens, T.D., Franke, K., Timme, S., Csanadi, A., Hoeppner, J., Kulemann, B., Maurer, J., Reiss, P.*, et al.* (2017). Form follows function: Morphological and immunohistological insights into epithelial-mesenchymal transition characteristics of tumor buds. Tumour Biol *39*, 1010428317705501.

Ewald, A.J., Huebner, R.J., Palsdottir, H., Lee, J.K., Perez, M.J., Jorgens, D.M., Tauscher, A.N., Cheung, K.J., Werb, Z., and Auer, M. (2012). Mammary collective cell

migration involves transient loss of epithelial features and individual cell migration within the epithelium. J Cell Sci *125*, 2638-2654.

Fattet, L., Jung, H.-Y., Matsumoto, M.W., Aubol, B.E., Kumar, A., Adams, J.A., Chen, A.C., Sah, R.L., Engler, A.J., Pasquale, E.B.*, et al.* (2020). Matrix Rigidity Controls Epithelial-Mesenchymal Plasticity and Tumor Metastasis via a Mechanoresponsive EPHA2/LYN Complex. Developmental cell.

Feinberg, A.P., Koldobskiy, M.A., and Göndör, A. (2016). Epigenetic modulators, modifiers and mediators in cancer aetiology and progression. Nat Rev Genet *17*, 284-299.

Ferreira, M.M., Ramani, V.C., and Jeffrey, S.S. (2016). Circulating tumor cell technologies. Molecular oncology *10*, 374-394.

Fidler, I.J. (1973). The relationship of embolic homogeneity, number, size and viability to the incidence of experimental metastasis. Eur J Cancer *9*, 223-227.

Fidler, I.J., and Kripke, M.L. (2015). The challenge of targeting metastasis. Cancer Metastasis Rev *34*, 635-641.

Follain, G., Herrmann, D., Harlepp, S., Hyenne, V., Osmani, N., Warren, S.C., Timpson, P., and Goetz, J.G. (2020). Fluids and their mechanics in tumour transit: shaping metastasis. Nature Reviews Cancer *20*, 107-124.

Follain, G., Osmani, N., Azevedo, A.S., Allio, G., Mercier, L., Karreman, M.A., Solecki, G., Garcia Leòn, M.J., Lefebvre, O., Fekonja, N.*, et al.* (2018). Hemodynamic Forces Tune the Arrest, Adhesion, and Extravasation of Circulating Tumor Cells. Developmental cell *45*, 33-52.e12.

Freed, D.M., Bessman, N.J., Kiyatkin, A., Salazar-Cavazos, E., Byrne, P.O., Moore, J.O., Valley, C.C., Ferguson, K.M., Leahy, D.J., Lidke, D.S.*, et al.* (2017). EGFR Ligands Differentially Stabilize Receptor Dimers to Specify Signaling Kinetics. Cell *171*, 683-695.e618.

Friedl, P., and Alexander, S. (2011). Cancer invasion and the microenvironment: plasticity and reciprocity. Cell *147*, 992-1009.

Friedl, P., and Gilmour, D. (2009). Collective cell migration in morphogenesis, regeneration and cancer. Nature reviews Molecular cell biology *10*, 445-457.

Friedl, P., Locker, J., Sahai, E., and Segall, J.E. (2012). Classifying collective cancer cell invasion. Nature cell biology *14*, 777-783.

Friedl, P., and Mayor, R. (2017). Tuning Collective Cell Migration by Cell-Cell Junction Regulation. Cold Spring Harb Perspect Biol *9*.

Friedl, P., Noble, P.B., Walton, P.A., Laird, D.W., Chauvin, P.J., Tabah, R.J., Black, M., and Zänker, K.S. (1995). Migration of coordinated cell clusters in mesenchymal and epithelial cancer explants in vitro. Cancer research *55*, 4557-4560.

Friedl, P., and Wolf, K. (2003). Tumour-cell invasion and migration: diversity and escape mechanisms. Nature Reviews Cancer *3*, 362-374.

Fujita, Y., Yoshioka, Y., and Ochiya, T. (2016). Extracellular vesicle transfer of cancer pathogenic components. Cancer Sci *107*, 385-390.

Gaggioli, C., Hooper, S., Hidalgo-Carcedo, C., Grosse, R., Marshall, J.F., Harrington, K., and Sahai, E. (2007). Fibroblast-led collective invasion of carcinoma cells with differing roles for RhoGTPases in leading and following cells. Nature cell biology *9*, 1392-1400.

Gao, X.L., Wu, J.S., Cao, M.X., Gao, S.Y., Cen, X., Jiang, Y.P., Wang, S.S., Tang, Y.J., Chen, Q.M., Liang, X.H.*, et al.* (2017). Cytokeratin-14 contributes to collective invasion of salivary adenoid cystic carcinoma. PLoS One *12*, e0171341.

Garcia, M.A., Nelson, W.J., and Chavez, N. (2018). Cell-Cell Junctions Organize Structural and Signaling Networks. Cold Spring Harbor perspectives in biology *10*, a029181.

Gauchier, M., van Mierlo, G., Vermeulen, M., and Déjardin, J. (2020). Purification and enrichment of specific chromatin loci. Nature Methods *17*, 380-389.

Gava, F., Rigal, L., Mondesert, O., Pesce, E., Ducommun, B., and Lobjois, V. (2018). Gap junctions contribute to anchorage-independent clustering of breast cancer cells. BMC Cancer *18*, 221.

Gensbittel, V., Kräter, M., Harlepp, S., Busnelli, I., Guck, J., and Goetz, J.G. (2021). Mechanical Adaptability of Tumor Cells in Metastasis. Developmental cell *56*, 164-179.

Georgescu, M.-M., Olar, A., Mobley, B.C., Faust, P.L., and Raisanen, J.M. (2018). Epithelial differentiation with microlumen formation in meningioma: diagnostic utility of NHERF1/EBP50 immunohistochemistry. Oncotarget *9*, 28652-28665.

Gerhardt, H., Golding, M., Fruttiger, M., Ruhrberg, C., Lundkvist, A., Abramsson, A., Jeltsch, M., Mitchell, C., Alitalo, K., and Shima, D. (2003). VEGF guides angiogenic sprouting utilizing endothelial tip cell filopodia. The Journal of cell biology *161*, 1163-1177.

Ghajar, C.M. (2015). Metastasis prevention by targeting the dormant niche. Nature reviews Cancer *15*, 238-247.

Ghajar, C.M., Peinado, H., Mori, H., Matei, I.R., Evason, K.J., Brazier, H., Almeida, D., Koller, A., Hajjar, K.A., Stainier, D.Y.R.*, et al.* (2013). The perivascular niche regulates breast tumour dormancy. Nature cell biology *15*, 807-817.

Ghatak, S., Dolatabadi, N., Trudler, D., Zhang, X., Wu, Y., Mohata, M., Ambasudhan, R., Talantova, M., and Lipton, S.A. (2019). Mechanisms of hyperexcitability in Alzheimer's disease hiPSC-derived neurons and cerebral organoids vs isogenic controls. eLife *8*, e50333.

Giandomenico, S.L., Mierau, S.B., Gibbons, G.M., Wenger, L.M.D., Masullo, L., Sit, T., Sutcliffe, M., Boulanger, J., Tripodi, M., Derivery, E.*, et al.* (2019). Cerebral organoids at the air–liquid interface generate diverse nerve tracts with functional output. Nature Neuroscience *22*, 669-679.

Gilmour, D., Rembold, M., and Leptin, M. (2017). From morphogen to morphogenesis and back. Nature *541*, 311-320.

Giuliano, M., Shaikh, A., Lo, H.C., Arpino, G., De Placido, S., Zhang, X.H., Cristofanilli, M., Schiff, R., and Trivedi, M.V. (2018). Perspective on Circulating Tumor Cell Clusters: Why It Takes a Village to Metastasize. Cancer Res *78*, 845-852.

Gkountela, S., Castro-Giner, F., Szczerba, B.M., Vetter, M., Landin, J., Scherrer, R., Krol, I., Scheidmann, M.C., Beisel, C., Stirnimann, C.U.*, et al.* (2019). Circulating Tumor Cell Clustering Shapes DNA Methylation to Enable Metastasis Seeding. Cell *176*, 98-112.e114.

Glaves, D., Huben, R.P., and Weiss, L. (1988). Haematogenous dissemination of cells from human renal adenocarcinomas. Br J Cancer *57*, 32-35.

Gorvel, L., and Olive, D. (2020). Targeting the "PVR-TIGIT axis" with immune checkpoint therapies. F1000Research *9*.

Granit, R.Z., Masury, H., Condiotti, R., Fixler, Y., Gabai, Y., Glikman, T., Dalin, S., Winter, E., Nevo, Y., Carmon, E.*, et al.* (2018). Regulation of Cellular Heterogeneity and Rates of Symmetric and Asymmetric Divisions in Triple-Negative Breast Cancer. Cell reports *24*, 3237-3250.

Gritsenko, P.G., Atlasy, N., Dieteren, C.E.J., Navis, A.C., Venhuizen, J.H., Veelken, C., Schubert, D., Acker-Palmer, A., Westerman, B.A., Wurdinger, T.*, et al.* (2020). p120-catenin-dependent collective brain infiltration by glioma cell networks. Nat Cell Biol *22*, 97-107.

Gundem, G., Van Loo, P., Kremeyer, B., Alexandrov, L.B., Tubio, J.M.C., Papaemmanuil, E., Brewer, D.S., Kallio, H.M.L., Högnäs, G., Annala, M.*, et al.* (2015). The evolutionary history of lethal metastatic prostate cancer. Nature *520*, 353-357.

Gupta, P.B., Pastushenko, I., Skibinski, A., Blanpain, C., and Kuperwasser, C. (2019). Phenotypic Plasticity: Driver of Cancer Initiation, Progression, and Therapy Resistance. Cell Stem Cell *24*, 65-78.

Gurdon, J., Lemaire, P., and Kato, K. (1993). Community effects and related phenomena in development. Cell *75*, 831-834.

Gurdon, J.B. (1988). A community effect in animal development. Nature *336*, 772-774.

Guy, C.T., Cardiff, R.D., and Muller, W.J. (1992). Induction of mammary tumors by expression of polyomavirus middle T oncogene: a transgenic mouse model for metastatic disease. Molecular and cellular biology *12*, 954-961.

Haeger, A., Alexander, S., Vullings, M., Kaiser, F.M.P., Veelken, C., Flucke, U., Koehl, G.E., Hirschberg, M., Flentje, M., Hoffman, R.M.*, et al.* (2020). Collective cancer invasion forms an integrin-dependent radioresistant niche. J Exp Med *217*.

Hamy, A.S., Lam, G.T., Laas, E., Darrigues, L., Balezeau, T., Guerin, J., Livartowski, A., Sadacca, B., Pierga, J.Y., Vincent-Salomon, A.*, et al.* (2018). Lymphovascular invasion after neoadjuvant chemotherapy is strongly associated with poor prognosis in breast carcinoma. Breast Cancer Res Treat *169*, 295-304.

Hanley, C.J., Henriet, E., Sirka, O.K., Thomas, G.J., and Ewald, A.J. (2020). Tumor-Resident Stromal Cells Promote Breast Cancer Invasion through Regulation of the Basal Phenotype. Molecular Cancer Research *18*, 1615-1622.

Hanna, S.J., McCoy-Simandle, K., Leung, E., Genna, A., Condeelis, J., and Cox, D. (2019). Tunneling nanotubes, a novel mode of tumor cell–macrophage communication in tumor cell invasion. Journal of cell science *132*.

Heeke, S., Mograbi, B., Alix-Panabières, C., and Hofman, P. (2019). Never Travel Alone: The Crosstalk of Circulating Tumor Cells and the Blood Microenvironment. Cells *8*.

Hennessy, B.T., Gonzalez-Angulo, A.-M., Stemke-Hale, K., Gilcrease, M.Z., Krishnamurthy, S., Lee, J.-S., Fridlyand, J., Sahin, A., Agarwal, R., and Joy, C. (2009). Characterization of a naturally occurring breast cancer subset enriched in epithelial-to-mesenchymal transition and stem cell characteristics. Cancer research *69*, 4116-4124.

Hickson, J., Diane Yamada, S., Berger, J., Alverdy, J., O'Keefe, J., Bassler, B., and Rinker-Schaeffer, C. (2009). Societal interactions in ovarian cancer metastasis: a quorum-sensing hypothesis. Clinical & experimental metastasis *26*, 67-76.

Hirata, E., and Sahai, E. (2017). Tumor Microenvironment and Differential Responses to Therapy. Cold Spring Harb Perspect Med *7*.

Hirotsu, Y., Hada, M., Amemiya, K., Oyama, T., Mochizuki, H., and Omata, M. (2020). Multi-regional sequencing reveals clonal and polyclonal seeding from primary tumor to metastases in advanced gastric cancer. J Gastroenterol *55*, 553-564.

Hitomi, M., Deleyrolle, Loic P., Mulkearns-Hubert, Erin E., Jarrar, A., Li, M., Sinyuk, M., Otvos, B., Brunet, S., Flavahan, William A., Hubert, Christopher G.*, et al.* (2015). Differential Connexin Function Enhances Self-Renewal in Glioblastoma. Cell reports *11*, 1031-1042.

Hobor, S., Van Emburgh, B.O., Crowley, E., Misale, S., Di Nicolantonio, F., and Bardelli, A. (2014). TGFα and amphiregulin paracrine network promotes resistance to EGFR blockade in colorectal cancer cells. Clin Cancer Res *20*, 6429-6438.

Hou, J.M., Krebs, M.G., Lancashire, L., Sloane, R., Backen, A., Swain, R.K., Priest, L.J., Greystoke, A., Zhou, C., Morris, K.*, et al.* (2012). Clinical significance and molecular characteristics of circulating tumor cells and circulating tumor microemboli in patients with small-cell lung cancer. J Clin Oncol *30*, 525-532.

Hsieh, A.C., Truitt, M.L., and Ruggero, D. (2011). Oncogenic AKTivation of translation as a therapeutic target. British Journal of Cancer *105*, 329-336.

Hu, M., Yao, J., Carroll, D.K., Weremowicz, S., Chen, H., Carrasco, D., Richardson, A., Violette, S., Nikolskaya, T., and Nikolsky, Y. (2008). Regulation of in situ to invasive breast carcinoma transition. Cancer cell *13*, 394-406.

Hu, Z., Li, Z., Ma, Z., and Curtis, C. (2020). Multi-cancer analysis of clonality and the timing of systemic spread in paired primary tumors and metastases. Nat Genet.

Hubert, C.G., Rivera, M., Spangler, L.C., Wu, Q., Mack, S.C., Prager, B.C., Couce, M., McLendon, R.E., Sloan, A.E., and Rich, J.N. (2016). A Three-Dimensional Organoid Culture System Derived from Human Glioblastomas Recapitulates the Hypoxic Gradients and Cancer Stem Cell Heterogeneity of Tumors Found In Vivo. Cancer research *76*, 2465-2477.

Hudson, L.G., Zeineldin, R., and Stack, M.S. (2008). Phenotypic plasticity of neoplastic ovarian epithelium: unique cadherin profiles in tumor progression. Clinical & experimental metastasis *25*, 643-655.

Hunter, K.W., Amin, R., Deasy, S., Ha, N.-H., and Wakefield, L. (2018). Genetic insights into the morass of metastatic heterogeneity. Nature Reviews Cancer *18*, 211-223.

Hwang, H.J., Oh, M.-S., Lee, D.W., and Kuh, H.-J. (2019a). Multiplex quantitative analysis of stroma-mediated cancer cell invasion, matrix remodeling, and drug response in a 3D co-culture model of pancreatic tumor spheroids and stellate cells. Journal of Experimental & Clinical Cancer Research *38*, 258.

Hwang, P.Y., Brenot, A., King, A.C., Longmore, G.D., and George, S.C. (2019b). Randomly Distributed K14(+) Breast Tumor Cells Polarize to the Leading Edge and Guide Collective Migration in Response to Chemical and Mechanical Environmental Cues. Cancer research *79*, 1899-1912.

Hwang, T.L., Close, T.P., Grego, J.M., Brannon, W.L., and Gonzales, F. (1996). Predilection of brain metastasis in gray and white matter junction and vascular border zones. Cancer *77*, 1551-1555.

Ilina, O., Campanello, L., Gritsenko, P.G., Vullings, M., Wang, C., Bult, P., Losert, W., and Friedl, P. (2018). Intravital microscopy of collective invasion plasticity in breast cancer. Dis Model Mech *11*.

Ilina, O., Gritsenko, P.G., Syga, S., Lippoldt, J., La Porta, C.A.M., Chepizhko, O., Grosser, S., Vullings, M., Bakker, G.-J., Starruß, J.*, et al.* (2020). Cell–cell adhesion and 3D matrix confinement determine jamming transitions in breast cancer invasion. Nature cell biology *22*, 1103-1115.

Inman, J.L., Robertson, C., Mott, J.D., and Bissell, M.J. (2015). Mammary gland development: cell fate specification, stem cells and the microenvironment. Development *142*, 1028-1042.

Jackstadt, R., van Hooff, S.R., Leach, J.D., Cortes-Lavaud, X., Lohuis, J.O., Ridgway, R.A., Wouters, V.M., Roper, J., Kendall, T.J., Roxburgh, C.S.*, et al.* (2019). Epithelial NOTCH Signaling Rewires the Tumor Microenvironment of Colorectal Cancer to Drive Poor-Prognosis Subtypes and Metastasis. Cancer cell *36*, 319-336.e317.

Jamieson, P.R., Dekkers, J.F., Rios, A.C., Fu, N.Y., Lindeman, G.J., and Visvader, J.E. (2017). Derivation of a robust mouse mammary organoid system for studying tissue dynamics. Development *144*, 1065-1071.

Janiszewska, M., Tabassum, D.P., Castaño, Z., Cristea, S., Yamamoto, K.N., Kingston, N.L., Murphy, K.C., Shu, S., Harper, N.W., Del Alcazar, C.G.*, et al.* (2019). Subclonal cooperation drives metastasis by modulating local and systemic immune microenvironments. Nature Cell Biology *21*, 879-888.

Jansson, S., Bendahl, P.-O., Larsson, A.-M., Aaltonen, K.E., and Rydén, L. (2016). Prognostic impact of circulating tumor cell apoptosis and clusters in serial blood samples from patients with metastatic breast cancer in a prospective observational cohort. BMC Cancer *16*, 433.

Jardé, T., Lloyd-Lewis, B., Thomas, M., Kendrick, H., Melchor, L., Bougaret, L., Watson, P.D., Ewan, K., Smalley, M.J., and Dale, T.C. (2016). Wnt and Neuregulin1/ErbB signalling extends 3D culture of hormone responsive mammary organoids. Nature communications *7*, 13207.

Jensen, D.H., Reibel, J., Mackenzie, I.C., and Dabelsteen, E. (2015). Single cell migration in oral squamous cell carcinoma - possible evidence of epithelial-mesenchymal transition in vivo. J Oral Pathol Med *44*, 674-679.

Jiang, X., Wong, K.H.K., Khankhel, A.H., Zeinali, M., Reategui, E., Phillips, M.J., Luo, X., Aceto, N., Fachin, F., Hoang, A.N.*, et al.* (2017). Microfluidic isolation of platelet-covered circulating tumor cells. Lab Chip *17*, 3498-3503.

Jolly, M.K., Boareto, M., Debeb, B.G., Aceto, N., Farach-Carson, M.C., Woodward, W.A., and Levine, H. (2017). Inflammatory breast cancer: a model for investigating cluster-based dissemination. NPJ breast cancer *3*, 21.

Jolly, M.K., Kulkarni, P., Weninger, K., Orban, J., and Levine, H. (2018). Phenotypic Plasticity, Bet-Hedging, and Androgen Independence in Prostate Cancer: Role of Non-Genetic Heterogeneity. Frontiers in Oncology *8*.

Joung, J., Konermann, S., Gootenberg, J.S., Abudayyeh, O.O., Platt, R.J., Brigham, M.D., Sanjana, N.E., and Zhang, F. (2017). Genome-scale CRISPR-Cas9 knockout and transcriptional activation screening. Nature Protocols *12*, 828-863.

Kai, F., Drain, A.P., and Weaver, V.M. (2019). The Extracellular Matrix Modulates the Metastatic Journey. Developmental cell *49*, 332-346.

Kai, K., Iwamoto, T., Zhang, D., Shen, L., Takahashi, Y., Rao, A., Thompson, A., Sen, S., and Ueno, N.T. (2018). CSF-1/CSF-1R axis is associated with epithelial/mesenchymal hybrid phenotype in epithelial-like inflammatory breast cancer. Scientific Reports *8*, 9427.

Kaldjian, E.P., Ramirez, A.B., Sun, Y., Campton, D.E., Werbin, J.L., Varshavskaya, P., Quarre, S., George, T., Madan, A., Blau, C.A.*, et al.* (2018). The RareCyte® platform for next-generation analysis of circulating tumor cells. Cytometry Part A *93*, 1220-1225.

Kantak, S.S., and Kramer, R.H. (1998). E-cadherin regulates anchorage-independent growth and survival in oral squamous cell carcinoma cells. The Journal of biological chemistry *273*, 16953-16961.

Karagiannis, G.S., Pastoriza, J.M., Wang, Y., Harney, A.S., Entenberg, D., Pignatelli, J., Sharma, V.P., Xue, E.A., Cheng, E., D'Alfonso, T.M.*, et al.* (2017). Neoadjuvant chemotherapy induces breast cancer metastasis through a TMEM-mediated mechanism. Sci Transl Med *9*.

Katt, M.E., Wong, A.D., and Searson, P.C. (2018). Dissemination from a Solid Tumor: Examining the Multiple Parallel Pathways. Trends Cancer *4*, 20-37.

Kawai, S., Yamazaki, M., Shibuya, K., Yamazaki, M., Fujii, E., Nakano, K., and Suzuki, M. (2020). Three-dimensional culture models mimic colon cancer heterogeneity induced by different microenvironments. Scientific Reports *10*, 3156.

Kenney, L.L., Shultz, L.D., Greiner, D.L., and Brehm, M.A. (2016). Humanized Mouse Models for Transplant Immunology. American Journal of Transplantation *16*, 389-397.

Kessenbrock, K., Plaks, V., and Werb, Z. (2010). Matrix Metalloproteinases: Regulators of the Tumor Microenvironment. Cell *141*, 52-67.

Khalil, A.A., Ilina, O., Gritsenko, P.G., Bult, P., Span, P.N., and Friedl, P. (2017). Collective invasion in ductal and lobular breast cancer associates with distant metastasis. Clinical & experimental metastasis *34*, 421-429.

Khalil, A.A., Ilina, O., Vasaturo, A., Venhuizen, J.H., Vullings, M., Venhuizen, V., Bilos, A., Figdor, C.G., Span, P.N., and Friedl, P. (2020). Collective invasion induced by an autocrine purinergic loop through connexin-43 hemichannels. The Journal of cell biology *219*.

Kim, M.Y., Oskarsson, T., Acharyya, S., Nguyen, D.X., Zhang, X.H., Norton, L., and Massagué, J. (2009). Tumor self-seeding by circulating cancer cells. Cell *139*, 1315-1326.

Kim, T.H., Wang, Y., Oliver, C.R., Thamm, D.H., Cooling, L., Paoletti, C., Smith, K.J., Nagrath, S., and Hayes, D.F. (2019). A temporary indwelling intravascular aphaeretic system for in vivo enrichment of circulating tumor cells. Nature communications *10*, 1478.

Kim, Y.H., Choi, Y.W., Lee, J., Soh, E.Y., Kim, J.-H., and Park, T.J. (2017a). Senescent tumor cells lead the collective invasion in thyroid cancer. Nature communications *8*, 1-14.

Kim, Y.K., Refaeli, I., Brooks, C.R., Jing, P., Gulieva, R.E., Hughes, M.R., Cruz, N.M., Liu, Y., Churchill, A.J., Wang, Y.*, et al.* (2017b). Gene-Edited Human Kidney Organoids Reveal Mechanisms of Disease in Podocyte Development. Stem Cells *35*, 2366-2378.

Kitamura, T., Qian, B.-Z., and Pollard, J.W. (2015). Immune cell promotion of metastasis. Nature Reviews Immunology *15*, 73-86.

Kleer, C.G., van Golen, K.L., and Merajver, S.D. (2000). Molecular biology of breast cancer metastasis Inflammatory breast cancer: clinical syndrome and molecular determinants. Breast Cancer Research *2*, 423.

Klijn, C., Durinck, S., Stawiski, E.W., Haverty, P.M., Jiang, Z., Liu, H., Degenhardt, J., Mayba, O., Gnad, F., Liu, J.*, et al.* (2015). A comprehensive transcriptional portrait of human cancer cell lines. Nature biotechnology *33*, 306-312.

Klimek, M. (2019). Pulmonary lymphangitis carcinomatosis: systematic review and meta-analysis of case reports, 1970-2018. Postgrad Med *131*, 309-318.

Klymenko, Y., Johnson, J., Bos, B., Lombard, R., Campbell, L., Loughran, E., and Stack, M.S. (2017). Heterogeneous Cadherin Expression and Multicellular Aggregate Dynamics in Ovarian Cancer Dissemination. Neoplasia *19*, 549-563.

Kochupurakkal, B.S., Harari, D., Di-Segni, A., Maik-Rachline, G., Lyass, L., Gur, G., Kerber, G., Citri, A., Lavi, S., Eilam, R.*, et al.* (2005). Epigen, the last ligand of ErbB receptors, reveals intricate relationships between affinity and mitogenicity. J Biol Chem *280*, 8503-8512.

Kok, S.Y., Oshima, H., Takahashi, K., Nakayama, M., Murakami, K., Ueda, H.R., Miyazono, K., and Oshima, M. (2021). Malignant subclone drives metastasis of genetically and phenotypically heterogenous cell clusters through fibrotic niche generation. Nature communications *12*, 863.

Konen, J., Summerbell, E., Dwivedi, B., Galior, K., Hou, Y., Rusnak, L., Chen, A., Saltz, J., Zhou, W., Boise, L.H.*, et al.* (2017). Image-guided genomics of phenotypically heterogeneous populations reveals vascular signalling during symbiotic collective cancer invasion. Nature communications *8*, 15078.

Kong, T., Ahn, R., Yang, K., Zhu, X., Fu, Z., Morin, G., Bramley, R., Cliffe, N.C., Xue, Y., Kuasne, H.*, et al.* (2020). CD44 Promotes PD-L1 Expression and Its Tumor-Intrinsic Function in Breast and Lung Cancers. Cancer research *80*, 444-457.

Korolev, K.S., Xavier, J.B., and Gore, J. (2014). Turning ecology and evolution against cancer. Nature reviews Cancer *14*, 371-380.

Krebs, M.G., Sloane, R., Priest, L., Lancashire, L., Hou, J.M., Greystoke, A., Ward, T.H., Ferraldeschi, R., Hughes, A., Clack, G.*, et al.* (2011). Evaluation and prognostic significance of circulating tumor cells in patients with non-small-cell lung cancer. Journal of clinical oncology : official journal of the American Society of Clinical Oncology *29*, 1556-1563.

Kudo, T., Shimazu, Y., Yagishita, H., Izumo, T., Soeno, Y., Sato, K., Taya, Y., and Aoba, T. (2013). Three-dimensional reconstruction of oral tongue squamous cell carcinoma at invasion front. Int J Dent *2013*, 482765.

Kurley, S.J., Tischler, V., Bierie, B., Novitskiy, S.V., Noske, A., Varga, Z., Zürrer-Härdi, U., Brandt, S., Carnahan, R.H., Cook, R.S.*, et al.* (2020). A Requirement for p120-catenin in the metastasis of invasive ductal breast cancer. J Cell Sci.

Labelle, M., Begum, S., and Hynes, R.O. (2011). Direct signaling between platelets and cancer cells induces an epithelial-mesenchymal-like transition and promotes metastasis. Cancer cell *20*, 576-590.

Labelle, M., and Hynes, R.O. (2012). The initial hours of metastasis: the importance of cooperative host–tumor cell interactions during hematogenous dissemination. Cancer discovery *2*, 1091-1099.

Labernadie, A., Kato, T., Brugues, A., Serra-Picamal, X., Derzsi, S., Arwert, E., Weston, A., Gonzalez-Tarrago, V., Elosegui-Artola, A., Albertazzi, L.*, et al.* (2017). A mechanically active heterotypic E-cadherin/N-cadherin adhesion enables fibroblasts to drive cancer cell invasion. Nat Cell Biol *19*, 224-237.

Labuschagne, C.F., Cheung, E.C., Blagih, J., Domart, M.C., and Vousden, K.H. (2019). Cell Clustering Promotes a Metabolic Switch that Supports Metastatic Colonization. Cell Metab *30*, 720-734.e725.

Lambert, A.W., Pattabiraman, D.R., and Weinberg, R.A. (2017). Emerging Biological Principles of Metastasis. Cell *168*, 670-691.

Lambert, G., Estévez-Salmeron, L., Oh, S., Liao, D., Emerson, B.M., Tlsty, T.D., and Austin, R.H. (2011). An analogy between the evolution of drug resistance in bacterial communities and malignant tissues. Nature reviews Cancer *11*, 375-382.

Lancaster, M.A., and Knoblich, J.A. (2014). Organogenesis in a dish: Modeling development and disease using organoid technologies. Science (New York, NY) *345*, 1247125.

Lapis, K., Paku, S., and Liotta, L.A. (1988). Endothelialization of embolized tumor cells during metastasis formation. Clinical & experimental metastasis *6*, 73-89.

Larsson, A.-M., Jansson, S., Bendahl, P.-O., Levin Tykjaer Jörgensen, C., Loman, N., Graffman, C., Lundgren, L., Aaltonen, K., and Rydén, L. (2018). Longitudinal enumeration and cluster evaluation of circulating tumor cells improve prognostication for patients with newly diagnosed metastatic breast cancer in a prospective observational trial. Breast Cancer Research *20*, 48.

Lawson, D.A., Bhakta, N.R., Kessenbrock, K., Prummel, K.D., Yu, Y., Takai, K., Zhou, A., Eyob, H., Balakrishnan, S., Wang, C.-Y.*, et al.* (2015). Single-cell analysis reveals a stem-cell program in human metastatic breast cancer cells. Nature *526*, 131-135.

Le, X.-F., Mao, W., Lu, Z., Carter, B.Z., and Bast Jr, R.C. (2010). Dasatinib induces autophagic cell death in human ovarian cancer. Cancer *116*, 4980-4990.

Lee, C.H., Yu, C.C., Wang, B.Y., and Chang, W.W. (2016). Tumorsphere as an effective in vitro platform for screening anti-cancer stem cell drugs. Oncotarget *7*, 1215-1226.

Lee, G.Y., Kenny, P.A., Lee, E.H., and Bissell, M.J. (2007). Three-dimensional culture models of normal and malignant breast epithelial cells. Nat Methods *4*, 359-365.

Lee, M., Kim, E.J., Cho, Y., Kim, S., Chung, H.H., Park, N.H., and Song, Y.S. (2017). Predictive value of circulating tumor cells (CTCs) captured by microfluidic device in patients with epithelial ovarian cancer. Gynecol Oncol *145*, 361-365.

Lee, M., and Vasioukhin, V. (2008). Cell polarity and cancer–cell and tissue polarity as a non-canonical tumor suppressor. Journal of cell science *121*, 1141-1150.

Lehmann, B.D., Bauer, J.A., Chen, X., Sanders, M.E., Chakravarthy, A.B., Shyr, Y., and Pietenpol, J.A. (2011). Identification of human triple-negative breast cancer subtypes and preclinical models for selection of targeted therapies. The Journal of clinical investigation *121*, 2750-2767.

Lehmann, B.D., Jovanović, B., Chen, X., Estrada, M.V., Johnson, K.N., Shyr, Y., Moses, H.L., Sanders, M.E., and Pietenpol, J.A. (2016). Refinement of Triple-Negative Breast Cancer Molecular Subtypes: Implications for Neoadjuvant Chemotherapy Selection. PLOS ONE *11*, e0157368.

Leighton, J., Kalla, R.L., Turner, J.M., Jr., and Fennell, R.H., Jr. (1960). Pathogenesis of tumor invasion. II. Aggregate replication. Cancer research *20*, 575-586.

Leone, K., Poggiana, C., and Zamarchi, R. (2018). The Interplay between Circulating Tumor Cells and the Immune System: From Immune Escape to Cancer Immunotherapy. Diagnostics (Basel) *8*.

Leung, M.L., Davis, A., Gao, R., Casasent, A., Wang, Y., Sei, E., Vilar, E., Maru, D., Kopetz, S., and Navin, N.E. (2017). Single-cell DNA sequencing reveals a late-dissemination model in metastatic colorectal cancer. Genome Res *27*, 1287-1299.

Li, C.-F., Chen, J.-Y., Ho, Y.-H., Hsu, W.-H., Wu, L.-C., Lan, H.-Y., Hsu, D.S.-S., Tai, S.-K., Chang, Y.-C., and Yang, M.-H. (2019). Snail-induced claudin-11 prompts collective migration for tumour progression. Nature cell biology *21*, 251-262.

Li, H., and Durbin, R. (2010). Fast and accurate long-read alignment with Burrows–Wheeler transform. Bioinformatics *26*, 589-595.

Li, L., Tang, P., Li, S., Qin, X., Yang, H., Wu, C., and Liu, Y. (2017). Notch signaling pathway networks in cancer metastasis: a new target for cancer therapy. Medical Oncology *34*, 180.

Li, Y., Hofmann, M., Wang, Q., Teng, L., Chlewicki, L.K., Pircher, H., and Mariuzza, R.A. (2009). Structure of natural killer cell receptor KLRG1 bound to E-cadherin reveals basis for MHC-independent missing self recognition. Immunity *31*, 35-46.

Lim, S.B., Yu, C.S., Jang, S.J., Kim, T.W., Kim, J.H., and Kim, J.C. (2010). Prognostic significance of lymphovascular invasion in sporadic colorectal cancer. Dis Colon Rectum *53*, 377-384.

Lin, E.Y., Jones, J.G., Li, P., Zhu, L., Whitney, K.D., Muller, W.J., and Pollard, J.W. (2003). Progression to malignancy in the polyoma middle T oncoprotein mouse breast cancer model provides a reliable model for human diseases. The American journal of pathology *163*, 2113-2126.

Liotta, L., Tryggvason, K., Garbisa, S., Hart, I., Foltz, C., and Shafie, S. (1980). Metastatic potential correlates with enzymatic degradation of basement membrane collagen. Nature *284*, 67-68.

Liotta, L.A., and Kohn, E.C. (2001). The microenvironment of the tumour–host interface. Nature *411*, 375-379.

Liotta, L.A., Rao, C.N.N., and Wewer, U.M. (1986). BIOCHEMICAL INTERACTIONS OF TUMOR CELLS WITH THE BASEMENT MEMBRANE. Annual Review of Biochemistry *55*, 1037-1057.

Liotta, L.A., Saidel, M.G., and Kleinerman, J. (1976). The significance of hematogenous tumor cell clumps in the metastatic process. Cancer Res *36*, 889-894.

Liu, D., Aguirre Ghiso, J., Estrada, Y., and Ossowski, L. (2002). EGFR is a transducer of the urokinase receptor initiated signal that is required for in vivo growth of a human carcinoma. Cancer cell *1*, 445-457.

Liu, K., Newbury, P.A., Glicksberg, B.S., Zeng, W.Z.D., Paithankar, S., Andrechek, E.R., and Chen, B. (2019a). Evaluating cell lines as models for metastatic breast cancer through integrative analysis of genomic data. Nature communications *10*, 2138.

Liu, K., Newbury, P.A., Glicksberg, B.S., Zeng, W.Z.D., Paithankar, S., Andrechek, E.R., and Chen, B. (2019b). Evaluating cell lines as models for metastatic breast cancer through integrative analysis of genomic data. Nature communications *10*, 2138.

Liu, X., Taftaf, R., Kawaguchi, M., Chang, Y.F., Chen, W., Entenberg, D., Zhang, Y., Gerratana, L., Huang, S., Patel, D.B.*, et al.* (2019c). Homophilic CD44 Interactions Mediate Tumor Cell Aggregation and Polyclonal Metastasis in Patient-Derived Breast Cancer Models. Cancer Discov *9*, 96-113.

Liu, Y., Mi, Y., Mueller, T., Kreibich, S., Williams, E.G., Van Drogen, A., Borel, C., Frank, M., Germain, P.L., Bludau, I.*, et al.* (2019d). Multi-omic measurements of heterogeneity in HeLa cells across laboratories. Nature biotechnology *37*, 314-322.

Livshits, G., Kobielak, A., and Fuchs, E. (2012). Governing epidermal homeostasis by coupling cell-cell adhesion to integrin and growth factor signaling, proliferation, and apoptosis. Proceedings of the National Academy of Sciences of the United States of America *109*, 4886-4891.

Lo, H.C., Xu, Z., Kim, I.S., Pingel, B., Aguirre, S., Kodali, S., Liu, J., Zhang, W., Muscarella, A.M., Hein, S.M.*, et al.* (2020). Resistance to natural killer cell immunosurveillance confers a selective advantage to polyclonal metastasis. Nature Cancer *1*, 709-722.

Loberg, R.D., Bradley, D.A., Tomlins, S.A., Chinnaiyan, A.M., and Pienta, K.J. (2007). The lethal phenotype of cancer: the molecular basis of death due to malignancy. CA: a cancer journal for clinicians *57*, 225-241.

Long, E., Ilie, M., Bence, C., Butori, C., Selva, E., Lalvée, S., Bonnetaud, C., Poissonnet, G., Lacour, J.P., Bahadoran, P.*, et al.* (2016). High expression of TRF2, SOX10, and CD10 in circulating tumor microemboli detected in metastatic melanoma patients. A potential impact for the assessment of disease aggressiveness. Cancer Med *5*, 1022-1030.

López-Soto, A., Gonzalez, S., Smyth, M.J., and Galluzzi, L. (2017). Control of Metastasis by NK Cells. Cancer cell *32*, 135-154.

López-Soto, A., Huergo-Zapico, L., Galván, J.A., Rodrigo, L., de Herreros, A.G., Astudillo, A., and Gonzalez, S. (2013). Epithelial–Mesenchymal Transition Induces an Antitumor Immune Response Mediated by NKG2D Receptor. The Journal of Immunology *190*, 4408-4419.

Lu, H., Clauser, K.R., Tam, W.L., Fröse, J., Ye, X., Eaton, E.N., Reinhardt, F., Donnenberg, V.S., Bhargava, R., Carr, S.A.*, et al.* (2014). A breast cancer stem cell niche supported by juxtacrine signalling from monocytes and macrophages. Nature cell biology *16*, 1105-1117.

Luzzi, K.J., MacDonald, I.C., Schmidt, E.E., Kerkvliet, N., Morris, V.L., Chambers, A.F., and Groom, A.C. (1998). Multistep nature of metastatic inefficiency: dormancy of solitary cells after successful extravasation and limited survival of early micrometastases. The American journal of pathology *153*, 865-873.

Lyssiotis, C.A., and Kimmelman, A.C. (2017). Metabolic Interactions in the Tumor Microenvironment. Trends in cell biology *27*, 863-875.

Madara, J.L., and Stafford, J. (1989). Interferon-gamma directly affects barrier function of cultured intestinal epithelial monolayers. The Journal of clinical investigation *83*, 724-727.

Maddipati, R., and Stanger, B.Z. (2015). Pancreatic Cancer Metastases Harbor Evidence of Polyclonality. Cancer Discov *5*, 1086-1097.

Madsen, C.D., and Sahai, E. (2010). Cancer dissemination--lessons from leukocytes. Developmental cell *19*, 13-26.

Mak, M., Reinhart-King, C.A., and Erickson, D. (2013). Elucidating mechanical transition effects of invading cancer cells with a subnucleus-scaled microfluidic serial dimensional modulation device. Lab Chip *13*, 340-348.

Malet-Engra, G., Yu, W., Oldani, A., Rey-Barroso, J., Gov, Nir S., Scita, G., and Dupré, L. (2015). Collective Cell Motility Promotes Chemotactic Prowess and Resistance to Chemorepulsion. Current Biology *25*, 242-250.

Malladi, S., Macalinao, D.G., Jin, X., He, L., Basnet, H., Zou, Y., de Stanchina, E., and Massagué, J. (2016). Metastatic Latency and Immune Evasion through Autocrine Inhibition of WNT. Cell *165*, 45-60.

Manjunath, Y., Upparahalli, S.V., Suvilesh, K.N., Avella, D.M., Kimchi, E.T., Staveley-O'Carroll, K.F., Li, G., and Kaifi, J.T. (2019). Circulating tumor cell clusters are a potential biomarker for detection of non-small cell lung cancer. Lung Cancer *134*, 147-150.

Martín-Pardillos, A., Valls Chiva, Á., Bande Vargas, G., Hurtado Blanco, P., Piñeiro Cid, R., Guijarro, P.J., Hümmer, S., Bejar Serrano, E., Rodriguez-Casanova, A., Diaz-Lagares, Á*., et al.* (2019). The role of clonal communication and heterogeneity in breast cancer. BMC Cancer *19*, 666.

Martino, F., Perestrelo, A.R., Vinarský, V., Pagliari, S., and Forte, G. (2018). Cellular Mechanotransduction: From Tension to Function. Frontiers in Physiology *9*.

Marty-Santos, L., and Cleaver, O. (2016). Pdx1 regulates pancreas tubulogenesis and E-cadherin expression. Development *143*, 101-112.

Maru, Y., Orihashi, K., and Hippo, Y. (2016). Lentivirus-Based Stable Gene Delivery into Intestinal Organoids. Methods in molecular biology (Clifton, NJ) *1422*, 13-21.

Marusyk, A., Tabassum, D.P., Altrock, P.M., Almendro, V., Michor, F., and Polyak, K. (2014). Non-cell-autonomous driving of tumour growth supports sub-clonal heterogeneity. Nature *514*, 54-58.

Massague, J., and Obenauf, A.C. (2016). Metastatic colonization by circulating tumour cells. Nature *529*, 298-306.

Masuda, H., Baggerly, K.A., Wang, Y., Zhang, Y., Gonzalez-Angulo, A.M., Meric-Bernstam, F., Valero, V., Lehmann, B.D., Pietenpol, J.A., Hortobagyi, G.N*., et al.* (2013). Differential response to neoadjuvant chemotherapy among 7 triple-negative breast cancer molecular subtypes. Clinical cancer research : an official journal of the American Association for Cancer Research *19*, 5533-5540.

Matsumura, Y., Ito, Y., Mezawa, Y., Sulidan, K., Daigo, Y., Hiraga, T., Mogushi, K., Wali, N., Suzuki, H., Itoh, T*., et al.* (2019). Stromal fibroblasts induce metastatic tumor cell clusters via epithelial-mesenchymal plasticity. Life Sci Alliance *2*.

Mayor, R., and Etienne-Manneville, S. (2016). The front and rear of collective cell migration. Nature reviews Molecular cell biology *17*, 97-109.

Mazzucchelli, S., Piccotti, F., Allevi, R., Truffi, M., Sorrentino, L., Russo, L., Agozzino, M., Signati, L., Bonizzi, A., Villani, L.*, et al.* (2019). Establishment and Morphological Characterization of Patient-Derived Organoids from Breast Cancer. Biological Procedures Online *21*, 12.

McCart Reed, A.E., Kalaw, E., Nones, K., Bettington, M., Lim, M., Bennett, J., Johnstone, K., Kutasovic, J.R., Saunus, J.M., and Kazakoff, S. (2019). Phenotypic and molecular dissection of metaplastic breast cancer and the prognostic implications. The Journal of pathology *247*, 214-227.

McGregor, A.L., Hsia, C.-R., and Lammerding, J. (2016). Squish and squeeze—the nucleus as a physical barrier during migration in confined environments. Current Opinion in Cell Biology *40*, 32-40.

McLaughlin, J., Padfield, P.J., Burt, J.P., and O'Neill, C.A. (2004). Ochratoxin A increases permeability through tight junctions by removal of specific claudin isoforms. Am J Physiol Cell Physiol *287*, C1412-1417.

McPherson, A., Roth, A., Laks, E., Masud, T., Bashashati, A., Zhang, A.W., Ha, G., Biele, J., Yap, D., Wan, A.*, et al.* (2016). Divergent modes of clonal spread and intraperitoneal mixing in high-grade serous ovarian cancer. Nature Genetics *48*, 758-767.

Meng, S., Tripathy, D., Frenkel, E.P., Shete, S., Naftalis, E.Z., Huth, J.F., Beitsch, P.D., Leitch, M., Hoover, S., Euhus, D.*, et al.* (2004). Circulating tumor cells in patients with breast cancer dormancy. Clin Cancer Res *10*, 8152-8162.

Mesa, Kailin R., Rompolas, P., and Greco, V. (2015). The Dynamic Duo: Niche/Stem Cell Interdependency. Stem Cell Reports *4*, 961-966.

Meurette, O., and Mehlen, P. (2018). Notch Signaling in the Tumor Microenvironment. Cancer cell *34*, 536-548.

Micalizzi, D.S., Maheswaran, S., and Haber, D.A. (2017). A conduit to metastasis: circulating tumor cell biology. Genes Dev *31*, 1827-1840.

Mina, L.A., and Sledge, G.W., Jr. (2011). Rethinking the metastatic cascade as a therapeutic target. Nat Rev Clin Oncol *8*, 325-332.

Miranti, C.K., and Brugge, J.S. (2002). Sensing the environment: a historical perspective on integrin signal transduction. Nature cell biology *4*, E83-E90.

Mishra, A.K., Campanale, J.P., Mondo, J.A., and Montell, D.J. (2019). Cell interactions in collective cell migration. Development (Cambridge, England) *146*, dev172056.

Misra, S., Moro, C.F., Del Chiaro, M., Pouso, S., Sebestyén, A., Löhr, M., Björnstedt, M., and Verbeke, C.S. (2019). Ex vivo organotypic culture system of precision-cut slices of human pancreatic ductal adenocarcinoma. Scientific Reports *9*, 2133.

Mizukoshi, K., Okazawa, Y., Haeno, H., Koyama, Y., Sulidan, K., Komiyama, H., Saeki, H., Ohtsuji, N., Ito, Y., Kojima, Y.*, et al.* (2020). Metastatic seeding of human colon

cancer cell clusters expressing the hybrid epithelial/mesenchymal state. Int J Cancer *146*, 2547-2562.

Moffat, J., Grueneberg, D.A., Yang, X., Kim, S.Y., Kloepfer, A.M., Hinkle, G., Piqani, B., Eisenhaure, T.M., Luo, B., Grenier, J.K.*, et al.* (2006). A lentiviral RNAi library for human and mouse genes applied to an arrayed viral high-content screen. Cell *124*, 1283-1298.

Moffitt, L., Karimnia, N., Stephens, A., and Bilandzic, M. (2019). Therapeutic Targeting of Collective Invasion in Ovarian Cancer. Int J Mol Sci *20*.

Mohammed, R.A.A., Martin, S.G., Mahmmod, A.M., Macmillan, R.D., Green, A.R., Paish, E.C., and Ellis, I.O. (2011). Objective assessment of lymphatic and blood vascular invasion in lymph node-negative breast carcinoma: findings from a large case series with long-term follow-up. The Journal of Pathology *223*, 358-365.

Mohme, M., Riethdorf, S., and Pantel, K. (2017). Circulating and disseminated tumour cells — mechanisms of immune surveillance and escape. Nature Reviews Clinical Oncology *14*, 155-167.

Molnar, B., Ladanyi, A., Tanko, L., Sréter, L., and Tulassay, Z. (2001). Circulating tumor cell clusters in the peripheral blood of colorectal cancer patients. Clin Cancer Res *7*, 4080-4085.

Mu, Z., Wang, C., Ye, Z., Austin, L., Civan, J., Hyslop, T., Palazzo, J.P., Jaslow, R., Li, B., Myers, R.E.*, et al.* (2015). Prospective assessment of the prognostic value of circulating tumor cells and their clusters in patients with advanced-stage breast cancer. Breast Cancer Res Treat *154*, 563-571.

Muinonen-Martin, A.J., Susanto, O., Zhang, Q., Smethurst, E., Faller, W.J., Veltman, D.M., Kalna, G., Lindsay, C., Bennett, D.C., and Sansom, O.J. (2014). Melanoma cells break down LPA to establish local gradients that drive chemotactic dispersal. PLoS biol *12*, e1001966.

Müller, P., and Schier, A.F. (2011). Extracellular movement of signaling molecules. Dev Cell *21*, 145-158.

Murlidhar, V., Reddy, R.M., Fouladdel, S., Zhao, L., Ishikawa, M.K., Grabauskiene, S., Zhang, Z., Lin, J., Chang, A.C., Carrott, P.*, et al.* (2017). Poor Prognosis Indicated by Venous Circulating Tumor Cell Clusters in Early-Stage Lung Cancers. Cancer research *77*, 5194-5206.

Na, T.Y., Schecterson, L., Mendonsa, A.M., and Gumbiner, B.M. (2020). The functional activity of E-cadherin controls tumor cell metastasis at multiple steps. Proceedings of the National Academy of Sciences of the United States of America *117*, 5931-5937.

Naffar-Abu Amara, S., Kuiken, H.J., Selfors, L.M., Butler, T., Leung, M.L., Leung, C.T., Kuhn, E.P., Kolarova, T., Hage, C., Ganesh, K.*, et al.* (2020). Transient commensal clonal interactions can drive tumor metastasis. Nature communications *11*, 5799.

Nagai, T., Ishikawa, T., Minami, Y., and Nishita, M. (2020). Tactics of cancer invasion: solitary and collective invasion. The Journal of Biochemistry *167*, 347-355.

Nakamura, K., Iwamoto, R., and Mekada, E. (1995). Membrane-anchored heparin-binding EGF-like growth factor (HB-EGF) and diphtheria toxin receptor-associated

protein (DRAP27)/CD9 form a complex with integrin alpha 3 beta 1 at cell-cell contact sites. Journal of Cell Biology *129*, 1691-1705.

Neal, J.T., Li, X., Zhu, J., Giangarra, V., Grzeskowiak, C.L., Ju, J., Liu, I.H., Chiou, S.-H., Salahudeen, A.A., Smith, A.R.*, et al.* (2018). Organoid Modeling of the Tumor Immune Microenvironment. Cell *175*, 1972-1988.e1916.

Neelakantan, D., Zhou, H., Oliphant, M.U.J., Zhang, X., Simon, L.M., Henke, D.M., Shaw, C.A., Wu, M.-F., Hilsenbeck, S.G., White, L.D.*, et al.* (2017). EMT cells increase breast cancer metastasis via paracrine GLI activation in neighbouring tumour cells. Nature communications *8*, 15773.

Nguyen-Ngoc, K.V., Cheung, K.J., Brenot, A., Shamir, E.R., Gray, R.S., Hines, W.C., Yaswen, P., Werb, Z., and Ewald, A.J. (2012). ECM microenvironment regulates collective migration and local dissemination in normal and malignant mammary epithelium. Proceedings of the National Academy of Sciences of the United States of America *109*, E2595-2604.

Nguyen-Ngoc, K.V., Shamir, E.R., Huebner, R.J., Beck, J.N., Cheung, K.J., and Ewald, A.J. (2015). 3D culture assays of murine mammary branching morphogenesis and epithelial invasion. Methods in molecular biology (Clifton, NJ) *1189*, 135-162.

Nielsen, T.O., Hsu, F.D., Jensen, K., Cheang, M., Karaca, G., Hu, Z., Hernandez-Boussard, T., Livasy, C., Cowan, D., Dressler, L.*, et al.* (2004). Immunohistochemical and clinical characterization of the basal-like subtype of invasive breast carcinoma. Clinical cancer research : an official journal of the American Association for Cancer Research *10*, 5367-5374.

Nieto, M.A., Huang, R.Y., Jackson, R.A., and Thiery, J.P. (2016). EMT: 2016. Cell *166*, 21-45.

Obiditsch-Mayer, I., and Breitfellner, G. (1968). Electron microscopy in cancer of the lung. Cancer *21*, 945-951.

Okegawa, T., Ninomiya, N., Masuda, K., Nakamura, Y., Tambo, M., and Nutahara, K. (2018). AR-V7 in circulating tumor cells cluster as a predictive biomarker of abiraterone acetate and enzalutamide treatment in castration-resistant prostate cancer patients. Prostate *78*, 576-582.

Osswald, M., Jung, E., Sahm, F., Solecki, G., Venkataramani, V., Blaes, J., Weil, S., Horstmann, H., Wiestler, B., Syed, M.*, et al.* (2015). Brain tumour cells interconnect to a functional and resistant network. Nature *528*, 93-98.

Padmanaban, V., Grasset, E.M., Neumann, N.M., Fraser, A.K., Henriet, E., Matsui, W., Tran, P.T., Cheung, K.J., Georgess, D., and Ewald, A.J. (2020). Organotypic culture assays for murine and human primary and metastatic-site tumors. Nat Protoc *15*, 2413-2442.

Padmanaban, V., Krol, I., Suhail, Y., Szczerba, B.M., Aceto, N., Bader, J.S., and Ewald, A.J. (2019). E-cadherin is required for metastasis in multiple models of breast cancer. Nature *573*, 439-444.

Paine, I.S., and Lewis, M.T. (2017). The Terminal End Bud: the Little Engine that Could. J Mammary Gland Biol Neoplasia *22*, 93-108.

Pantel, K., and Alix-Panabières, C. (2019). Liquid biopsy and minimal residual disease — latest advances and implications for cure. Nature Reviews Clinical Oncology *16*, 409-424.

Paoletti, C., Li, Y., Muñiz, M.C., Kidwell, K.M., Aung, K., Thomas, D.G., Brown, M.E., Abramson, V.G., Irvin, W.J., Jr., Lin, N.U.*, et al.* (2015). Significance of Circulating Tumor Cells in Metastatic Triple-Negative Breast Cancer Patients within a Randomized, Phase II Trial: TBCRC 019. Clin Cancer Res *21*, 2771-2779.

Paoletti, C., Miao, J., Dolce, E.M., Darga, E.P., Repollet, M.I., Doyle, G.V., Gralow, J.R., Hortobagyi, G.N., Smerage, J.B., Barlow, W.E.*, et al.* (2019). Circulating Tumor Cell Clusters in Patients with Metastatic Breast Cancer: a SWOG S0500 Translational Medicine Study. Clin Cancer Res *25*, 6089-6097.

Papenfort, K., and Bassler, B.L. (2016). Quorum sensing signal-response systems in Gram-negative bacteria. Nature reviews Microbiology *14*, 576-588.

Pareja, F., Brown, D.N., Lee, J.Y., Da Cruz Paula, A., Selenica, P., Bi, R., Geyer, F.C., Gazzo, A., da Silva, E.M., Vahdatinia, M.*, et al.* (2020). Whole-Exome Sequencing Analysis of the Progression from Non–Low-Grade Ductal Carcinoma In Situ to Invasive Ductal Carcinoma. Clinical Cancer Research *26*, 3682-3693.

Park, S., Greco, V., and Cockburn, K. (2016). Live imaging of stem cells: answering old questions and raising new ones. Current opinion in cell biology *43*, 30-37.

Patil, R., Tan, X., Bartosik, P., Detappe, A., Runnels, J.M., Ghobrial, I., Lin, C.P., and Niedre, M. (2019). Fluorescence monitoring of rare circulating tumor cell and cluster dissemination in a multiple myeloma xenograft model in vivo. J Biomed Opt *24*, 1-11.

Patsialou, A., Wyckoff, J., Wang, Y., Goswami, S., Stanley, E.R., and Condeelis, J.S. (2009). Invasion of Human Breast Cancer Cells In vivo Requires Both Paracrine and Autocrine Loops Involving the Colony-Stimulating Factor-1 Receptor. Cancer research *69*, 9498-9506.

Pavlova, N.N., Pallasch, C., Elia, A.E.H., Braun, C.J., Westbrook, T.F., Hemann, M., and Elledge, S.J. (2013). A role for PVRL4-driven cell-cell interactions in tumorigenesis. eLife *2*, e00358-e00358.

Pegram, H.J., Andrews, D.M., Smyth, M.J., Darcy, P.K., and Kershaw, M.H. (2011). Activating and inhibitory receptors of natural killer cells. Immunology and cell biology *89*, 216-224.

Pei, D., Shu, X., Gassama-Diagne, A., and Thiery, J.P. (2019). Mesenchymal-epithelial transition in development and reprogramming. Nat Cell Biol *21*, 44-53.

Peinado, H., Zhang, H., Matei, I.R., Costa-Silva, B., Hoshino, A., Rodrigues, G., Psaila, B., Kaplan, R.N., Bromberg, J.F., Kang, Y.*, et al.* (2017). Pre-metastatic niches: organ-specific homes for metastases. Nature Reviews Cancer *17*, 302-317.

Pettigrew, C.A., Asp, E., and Emerson, C.P., Jr. (2014). A new role for Hedgehogs in juxtacrine signaling. Mech Dev *131*, 137-149.

Pignatelli, J., Bravo-Cordero, J.J., Roh-Johnson, M., Gandhi, S.J., Wang, Y., Chen, X., Eddy, R.J., Xue, A., Singer, R.H., Hodgson, L.*, et al.* (2016). Macrophage-dependent tumor cell transendothelial migration is mediated by Notch1/Mena(INV)-initiated invadopodium formation. Sci Rep *6*, 37874.

Pimentel, H., Bray, N.L., Puente, S., Melsted, P., and Pachter, L. (2017). Differential analysis of RNA-seq incorporating quantification uncertainty. Nature Methods *14*, 687-690.

Piskounova, E., Agathocleous, M., Murphy, M.M., Hu, Z., Huddlestun, S.E., Zhao, Z., Leitch, A.M., Johnson, T.M., DeBerardinis, R.J., and Morrison, S.J. (2015). Oxidative stress inhibits distant metastasis by human melanoma cells. Nature *527*, 186-191.

Polonsky, M., Rimer, J., Kern-Perets, A., Zaretsky, I., Miller, S., Bornstein, C., David, E., Kopelman, N.M., Stelzer, G., Porat, Z.*, et al.* (2018). Induction of CD4 T cell memory by local cellular collectivity. Science (New York, NY) *360*.

Przepiorski, A., Sander, V., Tran, T., Hollywood, J.A., Sorrenson, B., Shih, J.-H., Wolvetang, E.J., McMahon, A.P., Holm, T.M., and Davidson, A.J. (2018). A Simple Bioreactor-Based Method to Generate Kidney Organoids from Pluripotent Stem Cells. Stem Cell Reports *11*, 470-484.

Quan, Q., Wang, X., Lu, C., Ma, W., Wang, Y., Xia, G., Wang, C., and Yang, G. (2020). Cancer stem-like cells with hybrid epithelial/mesenchymal phenotype leading the collective invasion. Cancer Sci *111*, 467-476.

Raff, M.C. (1992). Social controls on cell survival and cell death. Nature *356*, 397-400.

Rayavarapu, R.R., Heiden, B., Pagani, N., Shaw, M.M., Shuff, S., Zhang, S., and Schafer, Z.T. (2015). The role of multicellular aggregation in the survival of ErbB2-positive breast cancer cells during extracellular matrix detachment. The Journal of biological chemistry *290*, 8722-8733.

Reddy, P., Liu, L., Ren, C., Lindgren, P., Boman, K., Shen, Y., Lundin, E., Ottander, U., Rytinki, M., and Liu, K. (2005). Formation of E-cadherin-mediated cell-cell adhesion activates AKT and mitogen activated protein kinase via phosphatidylinositol 3 kinase and ligand-independent activation of epidermal growth factor receptor in ovarian cancer cells. Molecular Endocrinology *19*, 2564-2578.

Reffay, M., Parrini, M.C., Cochet-Escartin, O., Ladoux, B., Buguin, A., Coscoy, S., Amblard, F., Camonis, J., and Silberzan, P. (2014). Interplay of RhoA and mechanical forces in collective cell migration driven by leader cells. Nature cell biology *16*, 217-223.

Rennhack, J.P., To, B., Swiatnicki, M., Dulak, C., Ogrodzinski, M.P., Zhang, Y., Li, C., Bylett, E., Ross, C., Szczepanek, K.*, et al.* (2019). Integrated analyses of murine breast cancer models reveal critical parallels with human disease. Nature communications *10*, 3261.

Reymond, N., d'Água, B.B., and Ridley, A.J. (2013). Crossing the endothelial barrier during metastasis. Nature Reviews Cancer *13*, 858-870.

Riahi, R., Sun, J., Wang, S., Long, M., Zhang, D.D., and Wong, P.K. (2015). Notch1-Dll4 signalling and mechanical force regulate leader cell formation during collective cell migration. Nature communications *6*, 6556.

Riley, R.S., June, C.H., Langer, R., and Mitchell, M.J. (2019). Delivery technologies for cancer immunotherapy. Nature reviews Drug discovery *18*, 175-196.

Ring, B.Z., Hout, D.R., Morris, S.W., Lawrence, K., Schweitzer, B.L., Bailey, D.B., Lehmann, B.D., Pietenpol, J.A., and Seitz, R.S. (2016). Generation of an algorithm based on minimal gene sets to clinically subtype triple negative breast cancer patients. BMC Cancer *16*, 143.

Rinkenberger, J., and Werb, Z. (2000). The labyrinthine placenta. Nat Genet *25*, 248-250.

Riquelme, P.A., Drapeau, E., and Doetsch, F. (2008). Brain micro-ecologies: neural stem cell niches in the adult mammalian brain. Philosophical Transactions of the Royal Society B: Biological Sciences *363*, 123-137.

Risson, E., Nobre, A.R., Maguer-Satta, V., and Aguirre-Ghiso, J.A. (2020). The current paradigm and challenges ahead for the dormancy of disseminated tumor cells. Nature Cancer *1*, 672-680.

Robertson, F.M., Bondy, M., Yang, W., Yamauchi, H., Wiggins, S., Kamrudin, S., Krishnamurthy, S., Le-Petross, H., Bidaut, L., and Player, A.N. (2010). Inflammatory breast cancer: the disease, the biology, the treatment. CA: a cancer journal for clinicians *60*, 351-375.

Robinson, D.R., Wu, Y.-M., Lonigro, R.J., Vats, P., Cobain, E., Everett, J., Cao, X., Rabban, E., Kumar-Sinha, C., Raymond, V.*, et al.* (2017). Integrative clinical genomics of metastatic cancer. Nature *548*, 297.

Roh-Johnson, M., Bravo-Cordero, J.J., Patsialou, A., Sharma, V.P., Guo, P., Liu, H., Hodgson, L., and Condeelis, J. (2014). Macrophage contact induces RhoA GTPase signaling to trigger tumor cell intravasation. Oncogene *33*, 4203-4212.

Roh-Johnson, M., Shah, A.N., Stonick, J.A., Poudel, K.R., Kargl, J., Yang, G.H., di Martino, J., Hernandez, R.E., Gast, C.E., Zarour, L.R.*, et al.* (2017). Macrophage-Dependent Cytoplasmic Transfer during Melanoma Invasion In Vivo. Developmental cell *43*, 549-562.e546.

Röhrig, F., and Schulze, A. (2016). The multifaceted roles of fatty acid synthesis in cancer. Nature Reviews Cancer *16*, 732.

Rosenbluth, J.M., Schackmann, R.C.J., Gray, G.K., Selfors, L.M., Li, C.M.-C., Boedicker, M., Kuiken, H.J., Richardson, A., Brock, J., Garber, J.*, et al.* (2020). Organoid cultures from normal and cancer-prone human breast tissues preserve complex epithelial lineages. Nature communications *11*, 1711.

Roussos, E.T., Balsamo, M., Alford, S.K., Wyckoff, J.B., Gligorijevic, B., Wang, Y., Pozzuto, M., Stobezki, R., Goswami, S., Segall, J.E.*, et al.* (2011). Mena invasive (MenaINV) promotes multicellular streaming motility and transendothelial migration in a mouse model of breast cancer. J Cell Sci *124*, 2120-2131.

Ruppender, N., Larson, S., Lakely, B., Kollath, L., Brown, L., Coleman, I., Coleman, R., Nguyen, H., Nelson, P.S., Corey, E.*, et al.* (2015). Cellular Adhesion Promotes Prostate Cancer Cells Escape from Dormancy. PLoS One *10*, e0130565.

Sachs, N., de Ligt, J., Kopper, O., Gogola, E., Bounova, G., Weeber, F., Balgobind, A.V., Wind, K., Gracanin, A., Begthel, H.*, et al.* (2018). A Living Biobank of Breast Cancer Organoids Captures Disease Heterogeneity. Cell *172*, 373-386.e310.

Sachs, N., Papaspyropoulos, A., Zomer-van Ommen, D.D., Heo, I., Böttinger, L., Klay, D., Weeber, F., Huelsz-Prince, G., Iakobachvili, N., Amatngalim, G.D.*, et al.* (2019). Long-term expanding human airway organoids for disease modeling. Embo j *38*.

Sahai, E., Astsaturov, I., Cukierman, E., DeNardo, D.G., Egeblad, M., Evans, R.M., Fearon, D., Greten, F.R., Hingorani, S.R., Hunter, T.*, et al.* (2020). A framework for advancing our understanding of cancer-associated fibroblasts. Nature reviews Cancer *20*, 174-186.

Sanchez, L.R., Borriello, L., Entenberg, D., Condeelis, J.S., Oktay, M.H., and Karagiannis, G.S. (2019). The emerging roles of macrophages in cancer metastasis and response to chemotherapy. J Leukoc Biol *106*, 259-274.

Sanjana, N.E., Shalem, O., and Zhang, F. (2014). Improved vectors and genome-wide libraries for CRISPR screening. Nat Methods *11*, 783-784.

Sarioglu, A.F., Aceto, N., Kojic, N., Donaldson, M.C., Zeinali, M., Hamza, B., Engstrom, A., Zhu, H., Sundaresan, T.K., Miyamoto, D.T.*, et al.* (2015). A microfluidic device for label-free, physical capture of circulating tumor cell clusters. Nat Methods *12*, 685-691.

Sasportas, L.S., and Gambhir, S.S. (2014). Imaging Circulating Tumor Cells in Freely Moving Awake Small Animals Using a Miniaturized Intravital Microscope. PLOS ONE *9*, e86759.

Savage, P., Blanchet-Cohen, A., Revil, T., Badescu, D., Saleh, S.M.I., Wang, Y.C., Zuo, D., Liu, L., Bertos, N.R., Munoz-Ramos, V.*, et al.* (2017). A Targetable EGFR-Dependent Tumor-Initiating Program in Breast Cancer. Cell reports *21*, 1140-1149.

Sawabata, N., Susaki, Y., Nakamura, T., Kawaguchi, T., Yasukawa, M., and Taniguchi, S. (2020). Cluster circulating tumor cells in surgical cases of lung cancer. General Thoracic and Cardiovascular Surgery *68*, 975-983.

Saxena, K., Jolly, M.K., and Balamurugan, K. (2020). Hypoxia, partial EMT and collective migration: Emerging culprits in metastasis. Translational Oncology *13*, 100845.

Schafer, Z.T., Grassian, A.R., Song, L., Jiang, Z., Gerhart-Hines, Z., Irie, H.Y., Gao, S., Puigserver, P., and Brugge, J.S. (2009). Antioxidant and oncogene rescue of metabolic defects caused by loss of matrix attachment. Nature *461*, 109-113.

Scheele, C.L.G.J., Hannezo, E., Muraro, M.J., Zomer, A., Langedijk, N.S.M., van Oudenaarden, A., Simons, B.D., and van Rheenen, J. (2017). Identity and dynamics of mammary stem cells during branching morphogenesis. Nature *542*, 313-317.

Schindelin, J., Arganda-Carreras, I., Frise, E., Kaynig, V., Longair, M., Pietzsch, T., Preibisch, S., Rueden, C., Saalfeld, S., Schmid, B.*, et al.* (2012). Fiji: an open-source platform for biological-image analysis. Nature Methods *9*, 676-682.

Schoppmann, S.F., Bayer, G., Aumayr, K., Taucher, S., Geleff, S., Rudas, M., Kubista, E., Hausmaninger, H., Samonigg, H., Gnant, M.*, et al.* (2004). Prognostic value of lymphangiogenesis and lymphovascular invasion in invasive breast cancer. Ann Surg *240*, 306-312.

Seeley, T.D., and Visscher, P.K. (2004). Quorum sensing during nest-site selection by honeybee swarms. Behavioral Ecology and Sociobiology *56*, 594-601.

Senga, K., Mostov, K.E., Mitaka, T., Miyajima, A., and Tanimizu, N. (2012). Grainyhead-like 2 regulates epithelial morphogenesis by establishing functional tight junctions through the organization of a molecular network among claudin3, claudin4, and Rab25. Mol Biol Cell *23*, 2845-2855.

Shahbazi, M.N., Jedrusik, A., Vuoristo, S., Recher, G., Hupalowska, A., Bolton, V., Fogarty, N.N.M., Campbell, A., Devito, L., Ilic, D.*, et al.* (2016). Self-organization of the human embryo in the absence of maternal tissues. Nature cell biology *18*, 700-708.

Shalem, O., Sanjana, N.E., Hartenian, E., Shi, X., Scott, D.A., Mikkelsen, T.S., Heckl, D., Ebert, B.L., Root, D.E., Doench, J.G.*, et al.* (2014). Genome-Scale CRISPR-Cas9 Knockout Screening in Human Cells. Science (New York, NY) *343*, 84-87.

Shamir, E.R., and Ewald, A.J. (2014). Three-dimensional organotypic culture: experimental models of mammalian biology and disease. Nature reviews Molecular cell biology *15*, 647-664.

Shen, L., and Turner, J.R. (2005). Actin depolymerization disrupts tight junctions via caveolae-mediated endocytosis. Mol Biol Cell *16*, 3919-3936.

Sheridan, J.M., Ritchie, M.E., Best, S.A., Jiang, K., Beck, T.J., Vaillant, F., Liu, K., Dickins, R.A., Smyth, G.K., Lindeman, G.J.*, et al.* (2015). A pooled shRNA screen for regulators of primary mammary stem and progenitor cells identifies roles for Asap1 and Prox1. BMC Cancer *15*, 221.

Shimasaki, N., Jain, A., and Campana, D. (2020). NK cells for cancer immunotherapy. Nature Reviews Drug Discovery *19*, 200-218.

Shyer, A.E., Huycke, T.R., Lee, C., Mahadevan, L., and Tabin, C.J. (2015). Bending gradients: how the intestinal stem cell gets its home. Cell *161*, 569-580.

Siebel, C., and Lendahl, U. (2017). Notch Signaling in Development, Tissue Homeostasis, and Disease. Physiol Rev *97*, 1235-1294.

Siegel, M.B., He, X., Hoadley, K.A., Hoyle, A., Pearce, J.B., Garrett, A.L., Kumar, S., Moylan, V.J., Brady, C.M., Van Swearingen, A.E.*, et al.* (2018). Integrated RNA and DNA sequencing reveals early drivers of metastatic breast cancer. J Clin Invest *128*, 1371-1383.

Silver, D.L., and Montell, D.J. (2001). Paracrine Signaling through the JAK/STAT Pathway Activates Invasive Behavior of Ovarian Epithelial Cells in Drosophila. Cell *107*, 831-841.

Silvestri, V.L., Henriet, E., Linville, R.M., Wong, A.D., Searson, P.C., and Ewald, A.J. (2020). A tissue-engineered 3D microvessel model reveals the dynamics of mosaic vessel formation in breast cancer. Cancer Research, canres.1564.2019.

Simian, M., and Bissell, M.J. (2017). Organoids: A historical perspective of thinking in three dimensions. J Cell Biol *216*, 31-40.

Singh, A.B., and Harris, R.C. (2005). Autocrine, paracrine and juxtacrine signaling by EGFR ligands. Cellular Signalling *17*, 1183-1193.

Smith, H.W., and Marshall, C.J. (2010). Regulation of cell signalling by uPAR. Nature reviews Molecular cell biology *11*, 23-36.

Smits, L.M., Reinhardt, L., Reinhardt, P., Glatza, M., Monzel, A.S., Stanslowsky, N., Rosato-Siri, M.D., Zanon, A., Antony, P.M., Bellmann, J.*, et al.* (2019). Modeling Parkinson's disease in midbrain-like organoids. npj Parkinson's Disease *5*, 5.

Souza-Fonseca-Guimaraes, F., Cursons, J., and Huntington, N.D. (2019). The Emergence of Natural Killer Cells as a Major Target in Cancer Immunotherapy. Trends in immunology *40*, 142-158.

Strilic, B., and Offermanns, S. (2017). Intravascular Survival and Extravasation of Tumor Cells. Cancer cell *32*, 282-293.

Summerbell, E.R., Mouw, J.K., Bell, J.S.K., Knippler, C.M., Pedro, B., Arnst, J.L., Khatib, T.O., Commander, R., Barwick, B.G., Konen, J.*, et al.* (2020). Epigenetically heterogeneous tumor cells direct collective invasion through filopodia-driven fibronectin micropatterning. Science Advances *6*, eaaz6197.

Sun, C., Mezzadra, R., and Schumacher, T.N. (2018). Regulation and Function of the PD-L1 Checkpoint. Immunity *48*, 434-452.

Szczerba, B.M., Castro-Giner, F., Vetter, M., Krol, I., Gkountela, S., Landin, J., Scheidmann, M.C., Donato, C., Scherrer, R., Singer, J.*, et al.* (2019). Neutrophils escort circulating tumour cells to enable cell cycle progression. Nature *566*, 553-557.

Tabassum, D.P., and Polyak, K. (2015). Tumorigenesis: it takes a village. Nature reviews Cancer *15*, 473-483.

Taddei, M.L., Giannoni, E., Fiaschi, T., and Chiarugi, P. (2012). Anoikis: an emerging hallmark in health and diseases. The Journal of Pathology *226*, 380-393.

Takahashi, H., Katsuta, E., Yan, L., Tokumaru, Y., Katz, M.H.G., and Takabe, K. (2020). Transcriptomic Profile of Lymphovascular Invasion, a Known Risk Factor of Pancreatic Ductal Adenocarcinoma Metastasis. Cancers (Basel) *12*.

Takebe, T., and Wells, J.M. (2019). Organoids by design. Science (New York, NY) *364*, 956-959.

Talmadge, J.E., and Fidler, I.J. (2010). AACR centennial series: the biology of cancer metastasis: historical perspective. Cancer research *70*, 5649-5669.

Tarin, D. (1969). Fine structure of murine mammary tumours: the relationship between epithelium and connective tissue in neoplasms induced by various agents. British Journal of Cancer *23*, 417-425.

Tasdogan, A., Faubert, B., Ramesh, V., Ubellacker, J.M., Shen, B., Solmonson, A., Murphy, M.M., Gu, Z., Gu, W., Martin, M.*, et al.* (2020). Metabolic heterogeneity confers differences in melanoma metastatic potential. Nature *577*, 115-120.

Taube, J.H., Herschkowitz, J.I., Komurov, K., Zhou, A.Y., Gupta, S., Yang, J., Hartwell, K., Onder, T.T., Gupta, P.B., Evans, K.W.*, et al.* (2010). Core epithelial-to-mesenchymal transition interactome gene-expression signature is associated with claudin-low and metaplastic breast cancer subtypes. Proceedings of the National Academy of Sciences *107*, 15449-15454.

TCGA (2012). Comprehensive molecular portraits of human breast tumours. Nature *490*, 61-70.

Theveneau, E., and Linker, C. (2017). Leaders in collective migration: are front cells really endowed with a particular set of skills? [version 1; peer review: 2 approved]. F1000Research *6*.

Theveneau, E., and Mayor, R. (2012). Neural crest delamination and migration: from epithelium-to-mesenchyme transition to collective cell migration. Dev Biol *366*, 34-54.

Tian, J., Qian, B., Zhang, S., Guo, R., Zhang, H., Jeannon, J.P., Jin, R., Feng, X., Zhan, Y., Liu, J.*, et al.* (2020). Three-dimensional reconstruction of laryngeal cancer with whole organ serial immunohistochemical sections. Sci Rep *10*, 18962.

Toda, S., Blauch, L.R., Tang, S.K.Y., Morsut, L., and Lim, W.A. (2018). Programming self-organizing multicellular structures with synthetic cell-cell signaling. Science (New York, NY) *361*, 156-162.

Toda, S., Frankel, N.W., and Lim, W.A. (2019). Engineering cell–cell communication networks: programming multicellular behaviors. Current Opinion in Chemical Biology *52*, 31-38.

Trepat, X., Wasserman, M.R., Angelini, T.E., Millet, E., Weitz, D.A., Butler, J.P., and Fredberg, J.J. (2009). Physical forces during collective cell migration. Nature Physics *5*, 426-430.

Turner, J.R. (2009). Intestinal mucosal barrier function in health and disease. Nature reviews Immunology *9*, 799-809.

Tuveson, D., and Clevers, H. (2019). Cancer modeling meets human organoid technology. Science (New York, NY) *364*, 952-955.

Ulintz, P.J., Greenson, J.K., Wu, R., Fearon, E.R., and Hardiman, K.M. (2018). Lymph Node Metastases in Colon Cancer Are Polyclonal. Clin Cancer Res *24*, 2214-2224.

Ullah, I., Karthik, G.M., Alkodsi, A., Kjällquist, U., Stålhammar, G., Lövrot, J., Martinez, N.F., Lagergren, J., Hautaniemi, S., Hartman, J.*, et al.* (2018). Evolutionary history of metastatic breast cancer reveals minimal seeding from axillary lymph nodes. J Clin Invest *128*, 1355-1370.

van de Wetering, M., Francies, H.E., Francis, J.M., Bounova, G., Iorio, F., Pronk, A., van Houdt, W., van Gorp, J., Taylor-Weiner, A., Kester, L.*, et al.* (2015). Prospective derivation of a living organoid biobank of colorectal cancer patients. Cell *161*, 933-945.

Villasenor, A., Chong, D.C., Henkemeyer, M., and Cleaver, O. (2010). Epithelial dynamics of pancreatic branching morphogenesis. Development *137*, 4295-4305.

Vona, G., Estepa, L., Béroud, C., Damotte, D., Capron, F., Nalpas, B., Mineur, A., Franco, D., Lacour, B., Pol, S.*, et al.* (2004). Impact of cytomorphological detection of circulating tumor cells in patients with liver cancer. Hepatology *39*, 792-797.

Walker, M.T., and Kapoor, V. (2007). Neuroimaging of parenchymal brain metastases. Cancer Treat Res *136*, 31-51.

Wang, C., Mu, Z., Chervoneva, I., Austin, L., Ye, Z., Rossi, G., Palazzo, J.P., Sun, C., Abu-Khalaf, M., Myers, R.E.*, et al.* (2017). Longitudinally collected CTCs and CTC-clusters and clinical outcomes of metastatic breast cancer. Breast Cancer Res Treat *161*, 83-94.

Wang, D.-Y., Jiang, Z., Ben-David, Y., Woodgett, J.R., and Zacksenhaus, E. (2019). Molecular stratification within triple-negative breast cancer subtypes. Scientific Reports *9*, 19107.

Wartlick, O., Mumcu, P., Jülicher, F., and Gonzalez-Gaitan, M. (2011). Understanding morphogenetic growth control — lessons from flies. Nature Reviews Molecular Cell Biology *12*, 594-604.

Watanabe, S. (1954). The metastasizability of tumor cells. Cancer *7*, 215-223.

Watson, S.S., Dane, M., Chin, K., Tatarova, Z., Liu, M., Liby, T., Thompson, W., Smith, R., Nederlof, M., Bucher, E.*, et al.* (2018). Microenvironment-Mediated Mechanisms of Resistance to HER2 Inhibitors Differ between HER2+ Breast Cancer Subtypes. Cell systems *6*, 329-342.e326.

Wei, Q., Ye, Z., Zhong, X., Li, L., Wang, C., Myers, R.E., Palazzo, J.P., Fortuna, D., Yan, A., Waldman, S.A.*, et al.* (2017). Multiregion whole-exome sequencing of matched primary and metastatic tumors revealed genomic heterogeneity and suggested polyclonal seeding in colorectal cancer metastasis. Ann Oncol *28*, 2135-2141.

Wei, R.-r., Sun, D.-n., Yang, H., Yan, J., Zhang, X., Zheng, X.-l., Fu, X.-h., Geng, M.-y., Huang, X., and Ding, J. (2018). CTC clusters induced by heparanase enhance breast cancer metastasis. Acta Pharmacologica Sinica *39*, 1326-1337.

Weigelt, B., Geyer, F.C., and Reis-Filho, J.S. (2010). Histological types of breast cancer: how special are they? Molecular oncology *4*, 192-208.

White, M.D., and Plachta, N. (2015). How adhesion forms the early mammalian embryo. Curr Top Dev Biol *112*, 1-17.

Wiseman, B.S., Sternlicht, M.D., Lund, L.R., Alexander, C.M., Mott, J., Bissell, M.J., Soloway, P., Itohara, S., and Werb, Z. (2003). Site-specific inductive and inhibitory activities of MMP-2 and MMP-3 orchestrate mammary gland branching morphogenesis. The Journal of cell biology *162*, 1123-1133.

Wolf, K., Te Lindert, M., Krause, M., Alexander, S., Te Riet, J., Willis, A.L., Hoffman, R.M., Figdor, C.G., Weiss, S.J., and Friedl, P. (2013). Physical limits of cell migration: control by ECM space and nuclear deformation and tuning by proteolysis and traction force. Journal of Cell Biology *201*, 1069-1084.

Wong, C.W., Lee, A., Shientag, L., Yu, J., Dong, Y., Kao, G., Al-Mehdi, A.B., Bernhard, E.J., and Muschel, R.J. (2001). Apoptosis: An Early Event in Metastatic Inefficiency. Cancer research *61*, 333-338.

Wrenn, E.D., Moore, B.M., Greenwood, E., McBirney, M., and Cheung, K.J. (2020a). Optimal, Large-Scale Propagation of Mouse Mammary Tumor Organoids. J Mammary Gland Biol Neoplasia, 1-14.

Wrenn, E.W., Yamamoto, A., Moore, B.M., Huang, Y., McBirney, M., Thomas, A.J., Greenwood, E., Rabena, Y.F., Rahbar, H., Partridge, S.C*., et al.* (2020b). Regulation of collective metastasis by nanolumenal signaling. Cell *in press*.

Xavier da Silveira Dos Santos, A., and Liberali, P. (2018). From single cells to tissue self-organization. The FEBS journal.

Xiang, L., Yin, Y., Zheng, Y., Ma, Y., Li, Y., Zhao, Z., Guo, J., Ai, Z., Niu, Y., Duan, K*., et al.* (2020). A developmental landscape of 3D-cultured human pre-gastrulation embryos. Nature *577*, 537-542.

Xiang, X., Deng, Z., Zhuang, X., Ju, S., Mu, J., Jiang, H., Zhang, L., Yan, J., Miller, D., and Zhang, H.G. (2012). Grhl2 determines the epithelial phenotype of breast cancers and promotes tumor progression. PLoS One *7*, e50781.

Xie, C., and Tammi, M.T. (2009). CNV-seq, a new method to detect copy number variation using high-throughput sequencing. BMC Bioinformatics *10*, 80.

Xin, T., Greco, V., and Myung, P. (2016). Hardwiring Stem Cell Communication through Tissue Structure. Cell *164*, 1212-1225.

Xiong, G., Chen, J., Zhang, G., Wang, S., Kawasaki, K., Zhu, J., Zhang, Y., Nagata, K., Li, Z., Zhou, B.P*., et al.* (2020). Hsp47 promotes cancer metastasis by enhancing collagen-dependent cancer cell-platelet interaction. Proceedings of the National Academy of Sciences *117*, 3748-3758.

Yamada, K.M., and Sixt, M. (2019). Mechanisms of 3D cell migration. Nature Reviews Molecular Cell Biology *20*, 738-752.

Yang, C., Cao, M., Liu, Y., He, Y., Du, Y., Zhang, G., and Gao, F. (2019). Inducible formation of leader cells driven by CD44 switching gives rise to collective invasion and metastases in luminal breast carcinomas. Oncogene *38*, 7113-7132.

Yang, J., Antin, P., Berx, G., Blanpain, C., Brabletz, T., Bronner, M., Campbell, K., Cano, A., Casanova, J., Christofori, G*., et al.* (2020). Guidelines and definitions for research on epithelial–mesenchymal transition. Nature Reviews Molecular Cell Biology *21*, 341-352.

Yoshida, K., Fujikawa, T., Tanabe, A., and Sakurai, K. (1993). Quantitative analysis of distribution and fate of human lung cancer emboli labeled with 125I-5-iodo-2'-deoxyuridine in nude mice. Surg Today *23*, 979-983.

Yoshizawa, T., Hong, S.-M., Jung, D., Noë, M., Kiemen, A., Wu, P.-H., Wirtz, D., Hruban, R.H., Wood, L.D., and Oshima, K. (2020). Three-dimensional analysis of extrahepatic cholangiocarcinoma and tumor budding. The Journal of Pathology *251*, e5474.

Youk, H., and Lim, W.A. (2014). Secreting and sensing the same molecule allows cells to achieve versatile social behaviors. Science (New York, NY) *343*, 1242782.

Yu, K.-D., Wu, L.-M., Liu, G.-Y., Wu, J., Di, G.-H., Shen, Z.-Z., and Shao, Z.-M. (2011). Different Distribution of Breast Cancer Subtypes in Breast Ductal Carcinoma in situ (DCIS), DCIS with Microinvasion, and DCIS with Invasion Component. Annals of Surgical Oncology *18*, 1342-1348.

Yu, M., Bardia, A., Wittner, B.S., Stott, S.L., Smas, M.E., Ting, D.T., Isakoff, S.J., Ciciliano, J.C., Wells, M.N., Shah, A.M.*, et al.* (2013). Circulating breast tumor cells exhibit dynamic changes in epithelial and mesenchymal composition. Science (New York, NY) *339*, 580-584.

Yu, X., Harden, K., C Gonzalez, L., Francesco, M., Chiang, E., Irving, B., Tom, I., Ivelja, S., Refino, C.J., Clark, H.*, et al.* (2009). The surface protein TIGIT suppresses T cell activation by promoting the generation of mature immunoregulatory dendritic cells. Nature Immunology *10*, 48-57.

Yu, X., Miyamoto, S., and Mekada, E. (2000). Integrin alpha 2 beta 1-dependent EGF receptor activation at cell-cell contact sites. Journal of Cell Science *113*, 2139-2147.

Zajac, O., Raingeaud, J., Libanje, F., Lefebvre, C., Sabino, D., Martins, I., Roy, P., Benatar, C., Canet-Jourdan, C., Azorin, P.*, et al.* (2018). Tumour spheres with inverted polarity drive the formation of peritoneal metastases in patients with hypermethylated colorectal carcinomas. Nature cell biology *20*, 296-306.

Zhang, A., Hitomi, M., Bar-Shain, N., Dalimov, Z., Ellis, L., Velpula, K.K., Fraizer, G.C., Gourdie, R.G., and Lathia, J.D. (2015). Connexin 43 expression is associated with increased malignancy in prostate cancer cell lines and functions to promote migration. Oncotarget *6*, 11640-11651.

Zhang, D., Zhao, L., Zhou, P., Ma, H., Huang, F., Jin, M., Dai, X., Zheng, X., Huang, S., and Zhang, T. (2017). Circulating tumor microemboli (CTM) and vimentin+ circulating tumor cells (CTCs) detected by a size-based platform predict worse prognosis in advanced colorectal cancer patients during chemotherapy. Cancer Cell Int *17*, 6.

Zhang, J., Goliwas, K.F., Wang, W., Taufalele, P.V., Bordeleau, F., and Reinhart-King, C.A. (2019). Energetic regulation of coordinated leader-follower dynamics during collective invasion of breast cancer cells. Proceedings of the National Academy of Sciences of the United States of America *116*, 7867-7872.

Zhao, Q., Barclay, M., Hilkens, J., Guo, X., Barrow, H., Rhodes, J.M., and Yu, L.-G. (2010). Interaction between circulating galectin-3 and cancer-associated MUC1 enhances tumour cell homotypic aggregation and prevents anoikis. Molecular Cancer *9*, 154.

Zheng, X., Fan, L., Zhou, P., Ma, H., Huang, S., Yu, D., Zhao, L., Yang, S., Liu, J., Huang, A.*, et al.* (2017). Detection of Circulating Tumor Cells and Circulating Tumor Microemboli in Gastric Cancer. Transl Oncol *10*, 431-441.

Zhou, H., Neelakantan, D., and Ford, H.L. (2017). Clonal cooperativity in heterogenous cancers. Seminars in cell & developmental biology *64*, 79-89.

Zhou, J., Li, C., Liu, X., Chiu, M.C., Zhao, X., Wang, D., Wei, Y., Lee, A., Zhang, A.J., Chu, H.*, et al.* (2020). Infection of bat and human intestinal organoids by SARS-CoV-2. Nature Medicine.

Zhou, Y., Zhou, B., Pache, L., Chang, M., Khodabakhshi, A.H., Tanaseichuk, O., Benner, C., and Chanda, S.K. (2019). Metascape provides a biologist-oriented resource for the analysis of systems-level datasets. Nat Commun *10*, 1523.

Zoeller, E.L., Pedro, B., Konen, J., Dwivedi, B., Rupji, M., Sundararaman, N., Wang, L., Horton, J.R., Zhong, C., Barwick, B.G.*, et al.* (2019). Genetic heterogeneity within collective invasion packs drives leader and follower cell phenotypes. Journal of Cell Science *132*, jcs231514.

CURRICULUM VITAE

Emma Wrenn

EDUCATION

Molecular & Cellular Biology Graduate Program, University of Washington **Sep 2015-Mar 2021**

- Progressed to candidacy December 2017, Ph.D. conferred March 2021
- Supervisory committee: Cyrus Ghajar, Barry Gumbiner, Patrick Paddison, Valeri Vasioukhin

University of California, Santa Barbara **Sep 2011-Dec 2014**

- Bachelor of Science degree in Biological Sciences with High Honors

AWARDS and HONORS

- Harold M. Weintraub Graduate Student Award (2021)
- Chen Hu Endowment Fund PHS Trainee Travel Award (2019)
- UCSB Distinction in the Major (2014)
- UCSB Award for Academic Excellence (2014)
- Undergraduate Research and Creative Activities Grant Awardee (2014)
- Phi Beta Kappa Honor Society (2014)
- University of California Regents Scholarship (2011-2014)

RESEARCH EXPERIENCE

UW Molecular and Cellular Biology Graduate Program **Jun 2016-Mar 2021**

Dissertation Advisor: Kevin Cheung, Translational Research Program, Human Biology and Public Health Sciences Divisions, Fred Hutchinson Cancer Research Center

Project: Dissecting the molecular mechanisms driving enhanced metastatic seeding of tumor cell clusters in breast cancer

UW MCB Spring Rotation **Mar-Jun 2016**

Principal Investigator: Robert Bradley, Basic Sciences and Human Biology Divisions, Fred Hutchinson Cancer Research Center

Project: Identifying changes in nonsense-mediated decay efficiency during the cell cycle

UW MCB Winter Rotation **Jan-Mar 2016**

Principal Investigator: Kevin Cheung, Translational Research Program, Human Biology and Public Health Sciences Divisions, Fred Hutchinson Cancer Research Center

Project: Assessing differences in apoptosis induction in single and clustered tumor cells

UW MCB Fall Rotation **Sep-Dec 2015**

Principal Investigator: Dana Miller, Biochemistry Department, University of Washington

Project: Neuronal transcriptional response to hydrogen sulfide in *C. elegans*

Undergraduate Research **May 2013-Dec 2014**

Principal Investigator: Thomas Weimbs: Molecular, Cellular, and Developmental Biology Department; University of California, Santa Barbara

Project: Stabilization of polycystic kidney disease associated protein PC-1 under hypoxic conditions

PUBLICATIONS

Wrenn ED, Moore BM, Greenwood E, McBirney M, Cheung KJ. Optimal, large-scale propagation of mouse mammary tumor organoids. J Mammary Gland Biol Neoplasia. 2020 Oct 26:1–14. doi: 10.1007/s10911-020-09464-1. Epub ahead of print. PMID: 33106923; PMCID: PMC7587543.

Wrenn ED, Yamamoto A, Moore BM, Huang Y, McBirney M, Thomas AJ, Greenwood E, Rabena YF, Rahbar H, Partridge SC, Cheung KJ. Regulation of Collective Metastasis by Nanolumenal Signaling. Cell. 2020 Sep 25:S0092-8674(20)31087-4. doi: 10.1016/j.cell.2020.08.045. Epub ahead of print. PMID: 33007268.

Wrenn ED, Cheung KJ. FoxP1 "Tspans" Quiescence and Activation of Mammary Stem Cells. Dev Cell. 2018 Dec 3;47(5):539-540. doi: 10.1016/j.devcel.2018.11.017. PMID: 30513297. Comment on Fu et al. Developmental Cell 2018.

*Greenwood E**, *Wrenn ED**, Cheung KJ. Un(MaSC)ing Stem Cell Dynamics in Mammary Branching Morphogenesis. Dev Cell. 2017 Feb 27;40(4):328-330. doi: 10.1016/j.devcel.2017.02.014. PMID: 28245919. Comment on Scheele et al. Nature 2017. **equal contribution*

POSTERS and PRESENTATIONS

Seminar presentations

Wrenn E. Cell-cell contact induced EGFR signaling promotes the survival and growth of highly metastatic tumor cell clusters. 2018 ASCB|EMBO meeting; Topic - Morphogenesis and Multicellular Interactions, Patterning Tissue Morphogenesis minisymposium; San Diego, CA (12/10/2018).

Wrenn E. Cell-cell contact induced EGFR signaling promotes the survival and growth of highly metastatic tumor cell clusters. Pacific Northwest Tumor Microenvironment Symposium; Portland, OR (10/8/2018).

Wrenn E. EGFR-Fra1 growth signaling in highly metastatic tumor cell clusters. University of Washington Molecular & Cellular Biology Program Retreat; Seattle, WA (6/2/18).

Wrenn E. Targeting cluster-driven metastasis: Identifying and disrupting pro-metastatic signaling in tumor cell clusters**.** Fred Hutchinson Human Biology Division Friday Science Seminar; Seattle, WA (5/11/18)

Wrenn E. Apoptosis in single cells and cell clusters derived from a mouse model of breast cancer. University of Washington Molecular & Cellular Biology Winter Rotation Talks; Seattle, WA (3/15/2015).

Wrenn E. *C. elegans* neuronal response to hydrogen sulfide. University of Washington Molecular & Cellular Biology Fall Rotation Talks; Seattle, WA (12/15/2015).

Poster presentations
** denotes presenter*

***Wrenn E,** Yamamoto A, Moore BM, Thomas A, McBirney M, Greenwood E, Cheung KJ. Clustered tumor cells concentrate metastasis promoting growth factors in quorum sensing microlumina. Hallmarks of Cancer Symposium; Seattle, WA (11/19/19)

***Wrenn E,** Yamamoto A, Moore BM, Thomas A, McBirney M, Greenwood E, Cheung KJ. Microlumenal Signaling between clustered tumor cells drives metastatic outgrowth. Cold Spring Harbor Biology of Cancer: Microenvironment & Metastasis; Cold Spring Harbor, NY (9/26/19)

Wrenn E, Yamamoto A, Moore BM, Thomas A, McBirney M, Greenwood E, *Cheung KJ. Collectively disseminated tumor cell clusters rely on short-range cell-contact dependent EGFR signaling for metastatic colonization. Directed Cell Migration Gordon Research Conference; Galveston, TX (1/20/2019)

***Wrenn E,** Moore BM, McBirney M, Yamamoto A, Thomas A, Greenwood E, Cheung KJ. Cell-cell contact induced EGFR signaling promotes the survival and growth of highly metastatic tumor cell clusters. Presented at 2018 ASCB|EMBO meeting; San Diego, CA (12/10/2018)

Wrenn E, Greenwood E, Yamamoto A, Moore BM, Thomas A, *Cheung KJ. Tumor cell clustering promotes breast cancer metastasis by increasing apoptosis resistance and cell proliferation. American Society for Clinical Investigation Annual Meeting; Chicago, IL (4/20/2018)

Wrenn E, Moore BM, *Cheung KJ. Tumor cell clustering and ROCK inhibition promote apoptosis resistance in an ex-vivo model of metastatic colonization. Directed Cell Migration Gordon Research Conference; Galveston, TX (1/22/2017)

***Wrenn E**, Bradley RK. Nonsense mediated decay of SRSF3 varies across the cell cycle. University of Washington Molecular & Cellular Biology Spring Poster Session; Seattle, WA (6/7/2016).

***Wrenn E.** Kipp K, Weimbs T. Developing doxycycline inducible MDCK cell lines expressing polycystin-1 variants. UCSB Undergraduate Research Colloquium; Santa Barbara, CA (5/2014).

TEACHING EXPERIENCE

Rotation Mentor **2018-2019**
Cheung Laboratory, Fred Hutchinson Cancer Research Center
Supervised two 10-week rotations from first-year Ph.D. students in the UW Molecular & Cellular Biology program

Teaching Assistant, BIOL 355 – Foundations in Cell Biology **Sep-Dec 2016**
University of Washington

Teaching Assistant, BioQuest Academy **Jun-Jul 2016**
Center for Infectious Disease Research

ACADEMIC SERVICE

Co-chair, Tumor Microenvironment Student and Post-doc Group **2018-2019**
Member, UW MCB Hooding Ceremony Committee **2018**
Volunteer and Session Moderator, Fred Hutch Human Biology Retreat **2017**
Volunteer, UW MCB Annual Recruitment Events **2015-2018**